A HIGH RESOLUTION OPTICAL/NEAR-INFRARED STUDY OF THE EVOLUTIONARY LINK BETWEEN ULTRALUMINOUS INFRARED GALAXIES AND OPTICAL QSOS

A DISSERTATION SUBMITTED TO THE GRADUATE DIVISION OF THE UNIVERSITY OF HAWAII IN PARTIAL FULFILLMENT OF THE REQUIREMENTS FOR THE DEGREE OF

DOCTOR OF PHILOSOPHY

IN

ASTRONOMY

August 1998

By

Jason A. Surace

Dissertation Committee:

David Sanders, Chairperson

Joshua Barnes

Alan Stockton

Gerry Luppino

Martin Rayner

We certify that we have read this dissertation and that, in our opinion, it is satisfactory in scope and quality as a dissertation for the degree of Doctor of Philosophy in Astronomy.

DISSERTATION COMMITTEE

_____

Chairperson

_____

_____

_____

_____

This work is dedicated to my wife Atiya who suffered through a full decade of my self-centered obsession with infrared galaxies.

Acknowledgements

Many people have helped contribute to the success of this work.

I should thank my advisor, Dave Sanders, who provided me with plenty of advice and a wealth of financial support and computer hardware, and was kind enough to send me to two other continents while I was a student. I should also thank my various collaborators: Joe Mazzarella (for many years!), Sylvain Veilleux, D-C Kim, Bill Vacca, John Hibbard, and Aaron Evans. I also thank my thesis committee, in particular Alan Stockton and Josh Barnes for their comments on scattering and merger morphologies.

This thesis would have been impossible without the advanced instrumentation of the UH 2.2m. Gerry Luppino, John Tonry, Kevin Jim, Mark Metzger, and Klaus Hodapp, among others, should be credited with the creation of the cameras, spectrographs, and tip/tilt system on which this project so critically depended. I also thank the UH 2.2m telescope operators, John Dvorak and Chris Stewart, for their late-night attentiveness. Also, despite a sometime rocky relationship, I thank the IfA Adaptive Optics group (the Roddiers, Alan Tokunaga, Buzz Graves, and Malcolm Northcott) for getting me deeply involved in high resolution work and instrumentation.

I would like to thank various other IfA people: the grad students (Jim Deane, Doug Clowe, Mike Nassir, Rob Whitely, Marni Krismer, Joe Jensen, Byron Han, and a cast of thousands) for their help and support during my graduate career. The same goes for a few other post-docs like Gillian Wilson and Kathy Roth. In particular, I could never have finished this thesis in a timely fashion without borrowing a considerable amount of observing time out of Cathy Ishida.

I would also like to thank the Caltech Infrared Army, whose initial observations at Palomar during the late 80's and early 90's, which I reduced during my stay at Caltech, directly led to this thesis topic. In particular, I thank Lee Armus for all of his work on our first aborted attempt to tackle this subject. Similarly, I thank Tom Soifer and Gerry Neugebauer for years of support, Rob Knop and James Larkin for writing a great deal of handy software (particularly for the Amiga, a truly superior computing platform), and finally Alycia Weinberger, Dominic Benford, and Todd Hunter, who (along with all the others) certainly provided a lot of entertainment.

Abstract

The possible evolutionary connection between ultraluminous infrared galaxies (ULIGs: $L_{\rm bol} > 10^{12}$ L$_\odot$) and optically selected quasi-stellar objects (QSOs) was investigated. Three complete samples were examined: (1) "warm" ULIGs with mid-infrared colors characteristic of active galactic nuclei ($f_{25\mu{\rm m}}/f_{60\mu{\rm m}}$ >0.2), which appear to represent a critical transition phase between the second and third samples (2) "cool" ULIGs ($f_{25\mu{\rm m}}/f_{60\mu{\rm m}}$ <0.2) which appear to be the progenitors of warm ULIGs and which have many active star-formation characteristics, and (3) far-IR excess QSOs which have infrared to blue luminosity ratios at least as great as those of the "warm" ULIGs.

High spatial resolution observations (FWHM$\approx$ 0.3-0.8$''$) were made at wavelengths ranging from the near-ultraviolet (λ=3200Å) to near-infrared (λ=2.1μm). The following are the major findings: (1) all ULIGs have small scale structure in their central few kiloparsecs, (2) this structure is consistent in most cases with knots of powerful star formation which are insignificant in terms of their contribution to the high bolometric luminosity of the systems, (3) some of these knots have colors and luminosities consistent with QSO nuclei seen through patchy emission and extinction, (4) both ULIGs and QSOs have similar total mass host galaxies, (5) mergers are implicated in at least 22% of far-IR excess QSOs; 50% also have nuclear disturbances, and (6) there is evidence that the fraction of active nuclei detectable in the optical and near-infrared increases with the estimated dynamical age of the systems.

These results are consistent with the idea that at least *some* ($\approx$ 30%) QSOs like those examined here evolve via mergers from progenitors similar to the ULIGs, and that the ultimate fate of most ULIGs is to form systems similar in properties to optical QSOs. Implications for the evolution of active nuclei and clustered star formation in merging far-infrared active galaxies are discussed.

Table of Contents

List of Tables

List of Figures

Chapter 1

Introduction[1]

1.1. Historical Background

Over the past 30 years, our understanding of galaxy formation and the role of interactions between galaxies has undergone considerable change; galaxies are now understood to be dynamic, evolving entities, and that sometimes these interactions can be cataclysmic, violent events. Arp compiled his now famous "Atlas of Peculiar Galaxies" (Arp 1966), the vast majority of which are now understood to be interacting systems. Early n-body experiments (Toomre & Toomre 1972) showed how colliding spiral galaxies could be transformed in just the way seen in the Arp Atlas systems, and also that this could result in considerable changes in the circumnuclear environments of the merged galaxies, as large amount of gas would be funneled into the galaxy centers. Larson & Tinsley (1978) showed that the peculiar galaxies of the Arp Atlas showed evidence for having undergone a recent burst of star formation, and suggested that these bursts were due to galaxy interactions like those described by Toomre. All of these early works increasingly suggested that galaxy interactions, rather than being rare curiosities, might actually play an important role in galaxy formation and evolution.

The launch of the Infrared Astronomical Satellite (*IRAS*) in 1983 proved to be a major turning point in the study of galaxy interactions. One of the most important results of the IRAS mission was the discovery of a class of galaxies that emit the bulk of their luminosity in the far-infrared (Soifer et al. 1984, 1989). This far-infrared radiation appeared to be due to dust re-radiation of UV photons; in the majority of infrared luminous galaxies this dust appears to be heated by star-formation activity, a result expected from pre-*IRAS* studies. Initial studies of these galaxies indicated that a significant fraction of these galaxies appeared to be in groups or in morphologically disturbed systems indicative of galaxy interactions (Soifer et al. 1984). Although most studies to date have had relatively low resolution and short integration times, they have nonetheless generated considerable evidence that tidal interactions between galaxies in close association with each other are somehow associated with unusual infrared activity (Bushouse et al. 1988; Haynes & Herter 1988; Surace et al. 1994).

Some of these galaxies have luminosities similar to that of classical optically- selected quasars (i.e., $L_{\rm bol}$ $>10^{12}$ $L_{\odot}$), and have been dubbed "ultraluminous infrared galaxies" (hereafter referred to as ULIGs). Sanders (1988a) found that the ULIGs show a distinct trend towards non-thermal, AGN-like spectra as opposed to lower luminosity systems; this result has been more precisely quantified by Kim (1995). This increasing Seyfert fraction, combined with the high space density of ULIGs relative to optical QSOs (Soifer et al. 1986) led to the suggestion that ULIGs were evolutionary predecessors of optically selected quasars (Sanders et al. 1988a). In this scenario, a merger between two gas-rich spiral disks leads to the formation and/or fueling of an active galactic nucleus (AGN); reprocessing of the AGN

[1] This introductory chapter borrows heavily from the original proposal for this dissertation. As a result, it is written in such a way as to anticipate, but not know, the final conclusions.

light by dust in the merger core results in the ultraluminous infrared emission. Over time, powerful winds would blow away the shroud of reprocessing dust, enabling direct lines of sight to the central engine which would then have the appearance of an optical quasar.

Many additional studies have helped support this scenario. Sanders (1988b) used a far-infrared color criterion ($f_{25\mu m}$ / $f_{60\mu m} > 0.2$), known to select AGN-like systems (de Grijp et al. 1985), to select a complete sample of ULIGs with "warm" colors (the Warm Galaxy Sample, hereafter WGS). The WGS would therefore represent a transitional state between the BGS ULIGs and optically selected quasars. It was shown that these transition objects all exhibited evidence for an AGN in the form of Seyfert spectra, and that most appeared to have advanced interaction morphologies suggesting that they were more evolved forms of the BGS ULIGs. Observations by Heckman et al. (1990) provided evidence for the winds that would be needed to clear the dust away from the merger remnant. More recent work has shown that indeed most ULIGs do appear to be systems with disturbed morphologies indicative of current or past interactions (Clements et al. 1996, Murphy et al. 1996). Finally, much theoretical work, primarily in the form of n-body simulations, has continued to work out the expected details for the merger process (Barnes & Hernquist 1992 and references therein). For a detailed review of luminous and ultraluminous infrared galaxies, see Sanders & Mirabel (1996).

Optically selected quasars have also been found to have significant infrared activity. Neugebauer et al. (1984) found evidence that many of the quasars in the Palomar-Green Bright Quasar Sample (BQS) (Schmidt & Green 1983) were extended in the near-IR, a result recently confirmed by direct imaging (McLeod & Rieke 1995a,b). Sanders et al. (1989) found that the spectral energy distributions (SEDs) of PG QSOs were characterized not only by a blue peak but by a second infrared peak, which they concluded was due to reradiation by dust from a warped disk surrounding the quasar nucleus. Implicating dust in the SEDs of QSOs helped further claims of SED evolution between the dusty ULIGs and optically-selected QSOs. Other evidence has shown that some quasars lie in host galaxies that are similar to the merger remnants expected of evolved ULIG systems, and that mergers must play some role in the fueling of optical QSOs (Hutchings & Neff 1992, Stockton 1990 and references therein). Surprisingly, early *HST* results seemed to contradict the ground-based observations by failing to find the expected bright host galaxies (Bachall et al. 1995). The controversy continuing to surround the interpretation of the *HST* results have indicated that the space-based observations are not the panacea they might have been, and highlights the need for further ground- based follow-up work (McLeod & Rieke 1995, Neugebauer et al. 1995, Bahcall et al. 1997).

Several problems remain to be solved in the hypothetical merger time sequence. While many ULIGs and QSO host galaxies appear to be mergers, it is not clear if this is true for *all* ULIGs (especially the WGS) and QSO hosts. QSO progenitors, like QSOs, must contain compact central engines; however, results are inconclusive on the presence of AGN in the ULIGs and many authors have argued that the high infrared luminosities of the ULIGs are actually due to star formation (Kim 1995; Leech et al. 1989; Lonsdale et al. 1995; Condon et al. 1991). Similarly, it is not clear if the observed QSO host galaxy properties are compatible with their being major mergers of spiral galaxies (McLeod & Rieke 1994a,b). Even if they are, it is not clear what fraction are the result of major mergers in light of

the apparent diversity in QSO host environments (Bahcall et al. 1997). Finally, it has not been shown that the QSO mergers are actually older than ULIGs, thus establishing a time sequence, nor has it actually been shown that time evolution exists within the ULIGs themselves; some workers argue that the observed properties of ULIGs (particularly the apparent "warm" galaxy – AGN correlation) actually represent a range of properties, and not an evolutionary sequence.

1.2. The Need for High Spatial Resolution

At the distance of typical ULIGs (z=0.05-0.15), 1″ corresponds to a physical scale of 1–3 kpc. Since it is expected that most of the activity occurs within the central few kiloparsecs (Carico et al. 1990), previous studies have been hampered by an inability to spatially resolve this nuclear activity. The resulting spatial confusion has prevented a detailed understanding of the star formation and possible AGN activity within the nuclei. Additionally, current observations have not been able to clearly resolve extended morphological features such as tidal tails, loops, and multiple nuclei. It is this shortcoming in resolution that this dissertation intends to address.

Astronomy in the late 1980s and early 1990s enjoyed a renaissance in high spatial resolution observing. Perhaps the most significant development was the launch of the Hubble Space Telescope (*HST*). Since ground-based observations are hampered by the intrinsic seeing of the atmosphere, the placement of an optical telescope in earth orbit immediately resulted in resolution improvements as high as 20× at optical wavelengths. Although initially plagued by defects in manufacture, the refurbished telescope currently provides (with WFPC2) spatial resolution with a degree of stability and sky coverage unmatchable from the ground.

However, the situation on the ground was also rapidly changing. It was recognized that a handful of ground-based sites such as Mauna Kea offered considerable improvements in both seeing and transparency (particularly in the near-infrared) over older sites, which led to their rapid development as new astronomical centers. Even at these sites, it became apparent that the telescopes themselves were major sources of image degradation (Roddier et al. 1990), and several facilities began vigorous programs to minimize telescope- based seeing defects (Pickles et al. 1994, Hawarden et al. 1994).

More important, however, was the development of adaptive optics. Spurred in part by the expense, delays, and difficulties in acquiring time associated with *HST* as well as the desire to improve already existing facilities, many groups pursued projects aimed at correcting for ground-based atmospheric distortions (see Beckers 1993 and references therein, Roddier et al. 1994, Rousset et al. 1994, Olivier et al. 1994). Unfortunately, most of these adaptive optics implementations were incapable of providing high order corrections with natural guide stars fainter than m_V=15. However, lower- order tip/tilt corrections were possible; in the near-infrared on a small telescope like the UH 2.2m such corrections are capable of providing nearly all the resolution enhancement provided by a full adaptive optics system (Roddier et al. 1991).

Advances were also made in detector technology. In particular, major improvements were made in near-infrared detectors that made them much more similar in size, performance, and usability to optical charge-coupled devices (CCDs) (McLean 1994 and references therein, Hodapp et al. 1996). Between the time when data for this dissertation was initially taken and the time it was completed (a span of roughly 10 years), the imaging area of the near-infrared detectors used increased by nearly three-hundred fold. These developments vastly improved the efficiency of near-infrared observations, both by improving the quality of the raw data through better responsivity and lower dark current and through improved telescope efficiency due to the larger field of view with adequate spatial sampling. Similar improvements in the size and quantum efficiency of CCDs allowed observations to be extended to very short ($\lambda \approx 3000$Å) wavelengths, thus improving detectability of very blue emission like that expected from young stars.

1.3. Scientific Objectives

This dissertation is an attempt to examine whether or not an evolutionary connection exists between ultraluminous infrared galaxies and optically selected quasars. In order to this issue, several key points must be examined.

The first is to determine whether or not merger activity exists in each of the samples. If mergers can be implicated in the formation history of both ULIGs and QSOs, this would be strong circumstantial evidence that they have had similar histories. Morphological diagnostics of merger activity (tidal tails, multiple nuclei, etc.) have already been identified in many of the ULIGs (Sanders et al. 1988ab, Murphy et al. 1996, Kim 1995, Surace 1993). It is likely that deep, high resolution imaging will show that all of the ULIGs are merger products. It is believed that the QSOs will also show some evidence for merger activity when similar observations are made of them.

Second, it is necessary to determine the age of any merger processes in each of the samples. This will be carried out by several means. The first is through observation of the merger morphologies of the systems. As the merger remnants age, we expect them to undergo morphological changes. For example, mean nuclear separations should decrease, tidal tails should expand and fade, and the extended envelope should become more relaxed. Second, current HST observations are revealing the presence of knots or clusters of star formation in many interacting galaxies (Whitmore & Schweizer 1995, Meurer et al. 1995). Assuming that these knots form as a result of the merger process, it should be possible to set an age for a given system by measuring the luminosities and colors of these knots, since these will evolve with time. Comparisons will be made to spectral synthesis starburst models, models of various emission mechanisms, and to empirical observations of other known starbursts. Because the spatial resolution will be high enough to spatially separate the starburst knots from the underlying galaxy, the burst age/strength degeneracy will be eliminated.

Third, the emission mechanisms present in the optical and near-infrared will be identified and characterized. In particular, since QSOs all contain a compact central source, we would expect their hypothetical progenitors, the ULIGs, to also contain compact central

sources. A search will be made for evidence of an AGN in each of the ULIGs. Additionally, the nature of the compact star formation in the ULIGs will be examined with the particular question of determining their contribution to the high bolometric luminosity, possibly obviating the need for an AGN. This will be accomplished by a multi- wavelength high-resolution imaging campaign. Observations will include near-infrared, optical, and U′data. The many wavelengths will enable us to penetrate to varying degrees the heavy extinction seen in the IRAS galaxies. The resulting broad-band colors and high resolution maps of the nuclear morphology should be diagnostic of the different contributions of the (possibly starburst) stellar populations and AGN. We will attempt to show that the luminosity and colors of the QSO hosts are consistent with their being evolved versions of the ULIG hosts. Similarly we hope to show that the ULIGs have compact central engines which are consistent in terms of size, bolometric luminosity, and color with being heavily obscured QSO nuclei.

1.4. Sample Selection

Three complete samples have been chosen in order to test the possible connection between ultraluminous galaxies and optically selected QSOs. These samples are composed of the nearest examples of three presumably distinct evolutionary stages. All three samples lie in roughly the same region of the sky, as originally defined by the BGS: declination $\delta > -30$ °(in order to be visible from the northern hemisphere) and $|b| > 30$ °(in order to avoid confusion in the galactic plane, which is very severe in the far-infrared). All three samples are furthermore volume-limited with $z < 0.16$, for reasons discussed below.

1.4.1. "Warm" ULIGs

This sample was originally defined by Sanders et al. (1988b), and consists of all 12 ultraluminous galaxies characterized by having $f_{25\mu\mathrm{m}}/f_{60\mu\mathrm{m}} > 0.2$ and within the volume defined by z<0.16, corresponding to a 60 μm flux limit of 1.5 Jy. Since only a fraction (approximately 1/5) of ULIGS meet this "warmness" criterion (Kim 1995), this sample was naturally extended to higher redshifts and lower flux limits than the original BGS ULIG sample in order to get sufficient numbers of objects. This volume is also very near the completeness limit for ultraluminous galaxies in the deepest existing *IRAS*-based surveys, and is therefore a logical limiting volume. Finally, at these distances the physical spatial resolution obtainable may be enough to detect interesting features.

It is believed that these galaxies represent a transition state from the "cool" ULIGs to traditional optically selected QSOs (see §1.4.2–1.4.3); their properties are intermediate between the two other samples. Most have some evidence for merger activity and star formation like the greater body of ULIGs, but they also have evidence for compact nuclei (as seen in ground-based images) and Seyfert spectra similar to those of QSOs.

Table 1.1. Warm ULIG Sample

Name	RA (J2000.0)	DEC (J2000.0)	z
IZw1	00:53:34.9	12:41:36.2	0.061
IRAS 01003−2238	01:02:49.8	−22:21:56.3	0.118
Mrk 1014	01:59:50.1	00:23:41.5	0.163
IRAS 05189−2524	05:21:01.5	−25:21:46.7	0.042
IRAS 07598+6508	08:04:30.5	64:59:52.8	0.149
IRAS 08572+3915	09:00:25.4	39:03:54.2	0.058
IRAS 12071−0444	12:09:45.1	−05:01:13.7	0.129
3C273	12:29:06.7	02:03:08.6	0.158
Mrk 231	12:56:14.2	56:52:26.1	0.042
Pks 1345+12	13:47:33.5	12:17:24.5	0.122
Mrk 463	13:56:02.7	18:22:18.3	0.051
IRAS 15206+3342	15:22:37.9	33:31:36.6	0.125

1.4.2. "Cool" ULIGs

We define "cool" ULIGs as the complementary set to the "warm" sample having $f_{25\mu m}/f_{60\mu m} < 0.2$ and which therefore would not be expected to have characteristics similar to AGN. This sample includes all 7 "cool" ULIGs from the original BGS, as well as 7 additional objects drawn from the IRAS 1 Jy ULIG survey (Kim 1995). The 7 BGS ULIGs are all fairly well studied, and hence form an important base group from which to extend this study. However, it was felt that since the "warm" sample extends to much higher redshift than the "cool" BGS ULIGs, this would necessarily bias the study towards finding more resolvable structure in the relatively nearby systems. Therefore, 7 additional higher redshift ULIGs were selected from the 1 Jy Survey such that the resulting "cool" sample has a redshift distribution similar to the "warm" sample. Additionally, it was intentionally biased towards being observable in the summer months, thus decreasing the crowding of the observing program in the winter and spring. Although this sample is technically incomplete, it must be stressed that no additional infrared, optical, or morphological criteria were applied in the selection of these 7 systems — only their location on the sky, which should be uncorrelated with their other properties, was considered.

1.4.3. Infrared-Excess Optically Selected QSOs

A complete comparison sample of QSOs was chosen from the optically selected Palomar-Green Bright Quasar Survey (PG-BQS; Schmidt & Green 1983) to lie in the same volume of space as the two ULIG samples ($z < 0.16$) and to have the same bolometric luminosity as the ultraluminous galaxies ($L_{\rm bol} > 10^{12}\ L_{\odot}$, which corresponds to $M_{\rm bol} < -22.18$ when adjusted to $H_0 = 75$ km s^{-1} Mpc $^{-1}$ (Schmidt & Green 1983)). Given that the space density of ULIGs is similar to that of optical QSOs, there are 32 PG QSOs within this volume. In

Table 1.2. Cool ULIG Sample

Name	RA (J2000.0)	DEC (J2000.0)	z	Log $L_{\rm ir}$ $L_\odot$
IRAS 00091−0738	00:11:43.2	−07:22:07.8	0.119	12.17
IRAS 01199−2307	01:22:21.4	−22:51:59.5	0.156	12.23
IRAS 03521+0028	03:54:42.1	00:37:05.9	0.152	12.44
UGC 5101	09:35:51.7	61:21:11.3	0.039	11.99
IRAS 12112+0305	12:13:46.1	02:48:41.4	0.072	12.24
Mrk 273	13:44:42.1	55:53:12.7	0.038	12.13
IRAS 14348−1447	14:37:38.7	−15:00:22.8	0.082	12.24
IRAS 15250+3609	15:26:59.4	35:58:37.5	0.055	11.99
Arp 220	15:34:57.3	23:30:11.9	0.018	12.17
IRAS 20414−1651	20:44:17.4	−16:40:13.7	0.086	12.12
IRAS 22206−2715	22:23:28.8	−27:00:03.3	0.131	12.15
IRAS 22491−1808	22:51:49.3	−17:52:23.5	0.078	12.08
IRAS 23233+0946	23:25:55.6	10:02:45.1	0.128	12.02
IRAS 23365+3604	23:39:01.3	36:21:09.8	0.064	12.10

order to pre-select for systems likely to be at a closer evolutionary stage to the ULIGs, an additional criterion was imposed such that they have infrared excesses ($L_{\rm ir}/L_{\rm blue}$) as great or greater than the "warm" system with the lowest such ratio (3c273; $L_{\rm ir}/L_{\rm blue} > 0.46$). Of the 18 such PG QSOs, 3 are also WGS ULIGs. Although many of these PG QSOs have been observed before (McLeod & Rieke 1995a,b, Hutchings & Neff 1992), there have been no systematic multiwavelength surveys made with the required depth or resolution to detect the features we are looking for.

In summary, there are 14 "cool" ULIGS, 12 "warm" ULIGS, and 18 infrared- excess PG QSOs. However, the PG QSOs and "warm" ULIGs overlap by 3. Most of this study will focus on the "warm" ULIGs, which are believed to represent the critical transition objects. The remaining two samples are primarily for comparison purposes.

1.5. Organization of Dissertation

This dissertation is organized into several chapters based on the three different samples and the types of data obtained. Following Chapter 1, the Introduction, will be a chapter discussing the warm ULIG sample and the optical data obtained for it with *HST*. The next chapter will deal with ground-based near-infrared imaging of the same sample. The next chapters will present results for the cool ULIG and PG QSO samples, respectively, using the techniques outlined in chapters 2 & 3. Chapter 6 will present the first U′-band imaging of these systems. The final chapter will synthesize the results of the previous chapters into a merger time sequence and discuss it's implications for ULIG evolution. Appendix A details an auxiliary study of widely separated interacting galaxy pairs using

Table 1.3. Infrared-Excess PG QSO Sample

Name	RA (J2000.0)	DEC (J2000.0)	z	$L_{\rm ir}/L_{\rm blue}$
PG 0007+106	00:10:31.0	10:58:29.5	0.089	0.48
IZw1	00:53:34.9	12:41:36.2	0.061	2.01
Mrk 1014	01:59:50.1	00:23:41.5	0.163	2.57
PG 0838+770	08:44:45.6	76:53:09.4	0.131	0.66
PG 1001+054	10:04:20.1	05:13:00.5	0.161	0.48
PG 1114+445	11:17:06.4	44:13:32.6	0.144	0.98
PG 1119+120	11:21:47.1	11:44:18.3	0.050	0.69
PG 1126−041	11:29:16.7	−04:24:07.6	0.060	0.79
PG 1202+281	12:04:42.2	27:54:11.4	0.165	1.04
3C273	12:29:06.7	02:03:08.6	0.158	0.46
PG 1229+204	12:32:03.6	20:09:29.2	0.064	0.54
PG 1351+640	13:53:15.8	63:45:44.8	0.088	0.81
PG 1402+261	14:05:16.2	25:55:33.7	0.164	0.55
PG 1411+442	14:13:48.4	44:00:13.6	0.090	0.69
PG 1415+451	14:17:00.6	44:56:06.4	0.114	0.73
PG 1440+356	14:42:07.5	35:26:22.9	0.079	0.83
PG 1613+658	16:13:57.2	65:43:09.6	0.129	1.25
PG 2130+099	21:32:27.8	10:08:19.5	0.062	0.52

IRAS data combined with high spatial resolution techniques in an attempt to clarify the starburst fueling timescale and its dependence on the galaxy merger progenitors. Appendix B discusses the deconvolution algorithms used in this thesis and their applicability under different circumstances to ground-based data. Finally, Appendix C will provide a detailed discussion of the techniques used to derive colors from spectral synthesis data and the detectors available at the Institute for Astronomy (IfA). As per departmental guidelines, each chapter is designed to be self-contained within the larger framework of the dissertation itself, and as such will feature its own brief introduction with relevant background material, a discussion of the data, conclusions, and references.

REFERENCES

Arp, Halton. 1966, ApJS, 123, 1

Bahcall, J.N., Kirhakos, S., & Schneider, D.P. 1995, ApJ, 450, 486

Bahcall, J.N., Kirhakos, S., Saxe, D.H., & Schneider, D.P. 1997, ApJ, 479, 642

Barnes, J. & Henrquist, L. 1992. ARA&A, 30, 705

Beckers, J.M. 1993. ARA&A, 31, 13

Bushouse, H.A., Lamb, & Werner, M.W. 1988. ApJ, 335, 74

Carico, D.P., Sanders, D.B., Soifer, B.T., Matthews, K., & Neugebauer, G. 1990, AJ, 100, 70

Clements, D.L., Sutherland, W.J., McMahon, R.G., & Saunders, W. 1996, MNRAS, 279, 477

Condon, J.J., Huang, Z., Yin, Q., & Tranh, T.X., 1991, ApJ, 378, 65

de Grijp, M.H., Miley, G.K., Lub, J., & de Jong, T., 1985, Nature, 314, 240

Hawarden, T.G., Cavedoni, C.P., Rees, N.P., Chuter, T.C., et al. 1994, Proceedings of the SPIE, 2199, 494

Haynes, M.P. & Herter, T.1988, AJ, 96, 504

Heckman, T., Armus, L., & Miley, G, 1990, ApJS, 74, 833

Hodapp, K.W., Hora, J.L., Hall, D.N., Cowie, L.L. et al. 1996, New Astronomy, 1, 176

Hutchings, J.B., & Neff, S.G., 1992, AJ, 104, 1

Kim, D-C., 1995, PhD. Thesis, University of Hawaii

Larson, R.B., & Tinsley, B.M. 1978, ApJ, 219, 46

Leech, K.J., Penston, M.V., Terlevich, R., Lawrence, A. et al. 1989, MNRAS, 240, 349

Lonsdale, C.J., Smith, H.E., & Lonsdale, C.J., 1995, ApJ, 438, 632

McLean, I., editor, *Infrared Astronomy with Arrays: The Next Generation*, 1994, (Dordrecht, Netherlands: Kluwer Academic Publishers)

McLeod, K.K. & Rieke, G.H. 1994a, ApJ, 420, 58

McLeod, K.K. & Rieke, G.H. 1994b, ApJ, 431, 137

McLeod, K.K. & Rieke, G.H. 1995, ApJ, 454, L77

Meurer, G., Heckman, T., Leitherer, C., Kinney, A., Robert, C., & Garnett, D. 1995, ApJ, 110, 2665

Murphy, T., Armus, L., Matthews, K., Soifer, B.T., Mazzarella, J.M., Shupe, D.L., Strauss, M.A., & Neugebauer, G. 1996, AJ, 111, 1025

Neugebauer, G., Green, R.F., Matthews, K., Schmidt, M., Soifer, B.T., & Bennett, J. 1987, ApJS, 63, 615

Neugebauer, G., Matthews, K., & Armus, L. 1995, ApJ, 455, L123

Olivier, S.S., An, J., Avicola, K., Bissinger, D., et al. 1994, Proceedings of the SPIE, 2201, 1110

Pickles, A.J., Young, T.T., Nakamura, W., Cowie, L.L., et al. 1994, Proceedings of the SPIE, 2199, 504

Roddier, F.J., Anuskiewicz, J., Graves, J.E., Northcott, M.J., & Roddier, C.A. 1994, Proceedings of the SPIE, 2201, 2

Roddier, F.J., Cowie, L.L., Graves, J.E., Songaila, A., et al. 1990, Proceedings of the SPIE, 1236, 485

Roddier, F.J., Northcott, M., & Graves, J.E., 1991, PASP, 103, 131

Rousset, G., Beuzit, J-L., Hubin, N., Gendron, E., et al. 1994, Proceedings of the SPIE, 2201, 1088

Sanders, D.B. & Mirabel, I.F. 1996, ARA&A, 34, 749

Sanders, D.B., Soifer, B.T., Elias, J.H., Madore, B.F., Matthews, K., Neugebauer, G., & Scoville, N.Z. 1988a, ApJ, 325, 74

Sanders, D.B., Phinney, E.S., Neugebauer, G., Soifer, B.T., & Matthews, K., 1989, ApJ, 347, 29

Sanders, D.B., Soifer, B.T., Elias, J.H., Neugebauer, G.,& Matthews, K. 1988b, ApJ, 328, 35

Schmidt, M & Green, R.F. 1983, ApJ, 269, 352

Soifer, B.T., Boehmer, L., Neugebauer, G., & Sanders, D.B., 1989, AJ, 98, 766

Soifer, B.T., Rowan-Robinson, M., Houck, J.R., de Jong, T., Neugebauer, G., & Aumann, H.H. 1984, ApJ, 278, L71

Soifer, B.T., Sanders, D.B., Neugebauer, G., Danielson, G.E., Lonsdale, C.J., et al. 1986, ApJ, 303, L41

Stockton, A. in "Dynamics and Interactions of Galaxies", 1990, (Springer-Verlag: New York), 440

Surace, J.A., Armus, L., Graham, J.R., Matthews, K. et al. 1994, *Infrared Astronomy with Arrays: The Next Generation*, 1994, (Dordrecht, Netherlands: Kluwer Academic Publishers), 157

Surace, J.A., Mazzarella, J.M, Soifer, B.T., & Wehrle, A.E. 1993, AJ, 105, 864

Toomre, A., & Toomre, J. 1972, ApJ, 178, 623

Whitmore, B., & Schwiezer, F. 1995, AJ, 109, 960

Chapter 2

HST/WFPC2 Observations of Warm Ultraluminous Infrared Galaxies [1]

ABSTRACT

We present new high resolution *B*- and *I*-band images of a nearly complete sample of 9 "warm" ($f_{25}/f_{60} > 0.2$) ultraluminous infrared galaxies (ULIGs) obtained with the Wide Field Planetary Camera (WFPC2) of the *Hubble Space Telescope* (*HST*). The *HST* images clearly reveal the presence of tidal tails and other features associated with merging galaxies. All of the warm ULIGs show evidence for complex structures such as dust lanes and spiral features in their inner few kiloparsecs. Additionally, they show compact, blue "knots" of star formation (between 4 and 31 knots per object) which appear similar to those seen in more nearby merger systems. Spectral synthesis modeling is used to estimate mean upper age limits and masses: the median upper age limit for the knots in individual galaxies is $\sim 3\times10^8$ yr (ranging from $\sim 10^7$–1×10^9 yr) and the range of knot masses is $\sim 10^5 - 10^9$ $M_\odot$. We also argue that these starburst knots cannot be significant contributors to the extremely high bolometric luminosity of these galaxies. Additionally, each object contains one or two knots whose luminosity and color are implausible in terms of star formation, and which we identify as putative active nuclei. These observations are consistent with the hypothesis that warm ULIGs may represent a critical transition stage in the evolution of ULIGs into optical quasistellar objects (QSOs).

2.1. Introduction

One of the most important results of the *Infrared Astronomical Satellite*[2] (*IRAS*) all-sky survey was the discovery of a significant population of galaxies that emit the bulk of their luminosity in the far-infrared (e.g. Soifer et al. 1984). Studies of the properties of these "infrared" galaxies showed systematic trends coupled to the total far-infrared luminosity; more luminous systems were more likely to appear to be merger remnants or interacting pairs, and were more likely to possess AGN- like emission line features. A more complete review of the properties of luminous infrared galaxies can be found in Sanders & Mirabel (1996). Much recent attention has been focused on ultraluminous infrared

[1] Chapter 2 appeared in a modified form as "HST/WFPC2 Observations of Warm Ultraluminous Infrared Galaxies" by Surace, J.A., Sanders, D.B., Vacca, W.D., Veilleux, S., & Mazzarella, J.M., 1998, ApJ, 492, 116

[2] The Infrared Astronomical Satellite was developed and operated by the US National Aeronautics and Space Administration (NASA), the Netherlands Agency for Aerospace Programs (NIVR), and the UK Science and Engineering Research Council (SERC).

galaxies (ULIGs), objects with infrared luminosities, $L_{\rm ir}$[3], greater than 10^{12} $L_{\odot}$, which corresponds to the bolometric luminosity of QSOs (i.e. $M_B < -22.1$: Schmidt & Green 1983). Multiwavelength observations of a complete sample of 10 ULIGs led Sanders et al. (1988a) to suggest that these objects might plausibly represent the initial dust- enshrouded stage in the evolution of optically selected QSOs, and that the majority, if not all QSOs may begin their lives in such an intense infrared phase.

An important subset of ULIGs are those objects with "warm" ($f_{25}/f_{60} > 0.2$) [4], mid-infrared colors. These warm objects, which represent $\sim$20–25 % of the total population of ULIGs, appear to represent a critical transition stage in the evolution of the larger population of "cool" ULIGs into optical QSOs. Studies of several small but complete samples of warm ULIGs have shown that many of these objects have a point-like optical appearance on the Palomar Sky Survey and that they exhibit broad (Seyfert 1) optical emission lines, characteristics that have led them to be referred to as "infrared QSOs" (e.g. Low et al. 1988, Sanders et al. 1988b). Particularly useful for study has been the complete flux-limited sample of 12 warm ULIGs from the survey of Sanders et al. (1988b). As the nearest and brightest warm ULIGs, these objects are the most amenable to studies at other wavelengths.

This chapter presents the first *HST* images obtained with WFPC2 of the majority of the warm ULIGs in the sample of Sanders et al. (1988b). The sample, observations, and data reduction techniques are described in Sections 2.2, 2.3, and 2.4 respectively. Section 2.5 presents the main results including descriptions of the large-scale morphology and colors revealed by the new *HST* images, and the somewhat surprising discovery of a large population of extremely luminous "knots" which appear to be a common feature of all warm ULIGs. Section 2.6 discusses the properties of these knots in terms of starburst models, and in addition, identifies one or two putative nuclei in each object. Both the large-scale structure and knot properties of warm ULIGs are then compared to features that have been detected recently in *HST* images of nearby optically selected QSOs.

2.2. The Sample

Of the twelve warm ULIGs in our complete sample, nine were observed with *HST* in our Cycle 5 GO program, the remaining three sources having already been included in previously approved GTO and/or GO programs – 3C273 (various Cycles: Bahcall et al. 1995), IRAS 07598+6508 (Cycle 5: Boyce et al. 1996), and I Zw I (several GO programs in Cycles 3–5). The nine targets observed by us are listed in Table 2.1 along with the target coordinates, redshift, infrared and bolometric luminosity, and the *HST* exposure times.

---

[3] $L_{\rm ir} \equiv L(8 - 1000\mu{\rm m})$ is computed using the flux in all four *IRAS* bands according to the prescription given in Perault (1987); see also Sanders & Mirabel (1996). Throughout this paper we use $H_{\circ} = 75$ km s^{-1}Mpc^{-1}, $q_{\circ} = 0.5$ (unless otherwise noted).

[4] The quantities f_{12}, f_{25}, f_{60}, and f_{100} represent the *IRAS* flux densities (non- color-corrected) in Jy at 12 μm, 25 μm, 60 μm, and 100 μm respectively.

Table 2.1. Warm ULIGs observed by *HST*

Name	RA (J2000.0)	Dec	z	$\log\frac{L_{ir}}{L_\odot}$	$\log\frac{L_{bol}}{L_\odot}$	F439W (sec)	F814W (sec)
IRAS 01003−2238	01:02:49.83	−22:21:56.3	0.118	12.22	12.28	3030	1100
Mrk 1014	01:59:50.18	00:23:41.5	0.163	12.50	12.80	1380	480
IRAS 05189−2524	05:21:01.53	−25:21:46.7	0.042	12.08	12.17	2830	1313
IRAS 08572+3915	09:00:25.42	39:03:54.2	0.058	12.10	12.19	2830	1320
IRAS 12071−0444	12:09:45.10	−05:01:13.7	0.129	12.32	12.38	2500	1200
Mrk 231	12:56:14.24	56:52:26.1	0.042	12.52	12.67	2226	712
Pks 1345+12	13:47:33.55	12:17:24.5	0.122	12.25	12.41	2700	985
Mrk 463	13:56:02.74	18:22:18.3	0.051	11.77	12.03	1030	360
IRAS 15206+3342	15:22:37.96	33:31:36.6	0.125	12.16	12.24	3000	1030

Note. — names as given in Sanders et al. (1988b), with new astrometric positions derived from the STScI Digital Sky Survey.

Note. — redshift and L_{ir} from Kim & Sanders (1996), with additional luminosity needed to compute L_{bol} taken from Sanders *et al.* (1988b)

An initial description of the properties of the complete sample as determined from ground-based studies – including optical morphology, optical spectral type, and the radio-to-UV spectral energy distribution (SED) – was presented in Sanders et al. (1988b). Three of the 12 warm ULIGs (I Zw I, Mrk 1014, and 3C273) were previously classified as optical QSOs, while the remainder are type 1 or 2 Seyferts. Six of the 12 objects have a dominant pointlike optical nucleus on the Palomar Sky Survey plates, similar in appearance to optically selected QSOs. Deep ground-based optical images show that three of the 12 have double nuclei while most of the remaining objects exhibit large-scale tidal features characteristic of advanced mergers. A more complete description of each the nine objects observed by us and the remaining three observed by others with *HST* is given in §2.8. Ground-based images are also shown in Figure 2.1.

Since all of the warm ULIGs in our sample are at redshifts 0.05-0.15, the physical resolution achievable optically from the ground is only about 1–2 kpc, which is clearly insufficient to disentangle such structures as nuclear bars or rings that, for example, might be associated with a circumnuclear starburst, or to disentangle the relative contributions of such a starburst from any AGN component that might be present. The higher resolution of *HST* also permits much more accurate photometry, allowing for example, a more detailed examination of stellar populations. Finally, the low background in space, accompanied by the increase in point source detectability due to higher spatial resolution, enables us to search for very faint high spatial frequency structure.

2.3. Observations

The *HST* data were taken in Cycle 5 between September, 1995 and March, 1996 with the WFPC2 camera. In all cases the apparent optical nucleus of the target was centered on the PC chip at the position listed in Table 2.1. The PC was chosen for its superior spatial sampling ($0.''046$ pixel^{-1}) compared to the WFC CCDs. The PC field-of-view (FOV) is shown in Figure 2.1 superimposed on deep ground-based images of each target. In most cases all of the detectable structure fell within the $36''$ FOV of the PC, although in the case of Mrk 231 and IRAS 05189−2524 some additional structure was detected in the flanking WFC fields. Because of the non-symmetric orientation of the WFC fields in relation to the PC, the random rotation angle introduced by the spacecraft, and the geometry of the galaxies, it was not possible in all cases to arrange to observe both the inner galaxy with the PC and simultaneously capture the full extent of the outer disk and large scale tidal features with the WFC fields. In any case, as shown by the PC data, the outer regions of these galaxies are of too low a surface brightness to be imaged with WFPC2 without much longer integration times.

For each galaxy, exposures were made using the F439W and F814W filters, which correspond closely to the standard Johnson-B and Cousins-I filters (see Holtzman et al. 1995). In the remainder of this paper we refer to these filters simply as B and I. In each filter, one short exposure was made to image any bright features without saturation, and then the remaining time was split into two or three long exposures in order to identify cosmic rays. The ratio of exposure times in the B and I filters was approximately 3:1 (see Table 2.1) in an attempt to ensure a similar S/N at both wavelengths, although scheduling constraints often necessitated somewhat varying times. In general, each target was observed during one or two consecutive orbits, with a time interval of several weeks between targets.

2.4. Data Reduction

Dark subtraction, bias subtraction, and flat-fielding were carried out using the standard data reduction pipeline procedures at STScI. The spacecraft was commanded to keep the field in a fixed position and orientation throughout the observations, eliminating the need for later registration. This was confirmed by examining the location of the centroids of the nuclei, stars in the frame, and the extended structure. The image rotation introduced by the roll angle of the spacecraft was removed by rotating the image using linear interpolation according to the amount specified by STScI based on spacecraft telemetry. All photometric analysis was carried out on the unrotated images in order to avoid the small uncertainties introduced by the rotation process. Images were combined using the IRAF/STSDAS routine GCOMBINE which includes an algorithm for removal of cosmic rays from individual frames (effectively filling them in with good pixels from other frames). Saturated pixels in the bright nuclei were similarly replaced with data from the short exposures. Remaining bad pixels were identified by eye and by fabrication of comparison images constructed from only the lowest-valued pixels in an image stack. These pixels were filled in by linear interpolation from surrounding pixels.

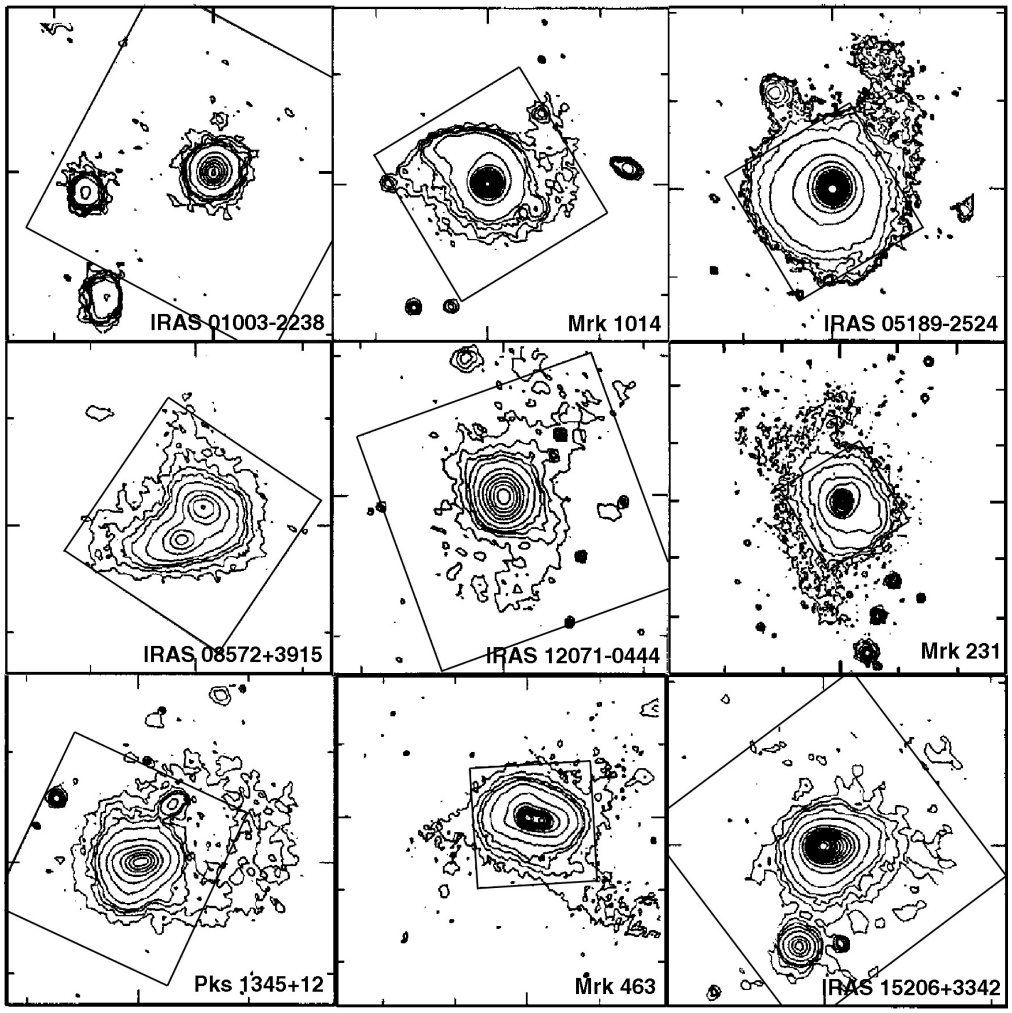

Fig. 2.1.— The PC field-of- view ($36''$x $36''$) superimposed on contour maps of the ground-based Gunn-r images of the nine warm ULIGs. The ground-based data are from Sanders et al. (1988b). The galaxies are ordered by increasing R.A., from left to right, top to bottom. All images are displayed with North at the top and East to the left.

For each galaxy, additional observations were made of nearby stars within several arcminutes in order to accurately determine the PSF. In some cases this was not entirely successful due to their low brightness in the B and I filters (as no previous observations in our filters existed, and their spectral types were unknown). Therefore, these observations were supplemented with models of the PSF made using the Tiny TIM software available from STScI (Krist 1994). Because of the PC undersampling and the considerable pixel-to-pixel scattering within the PC CCD, the actual PSF is somewhat variant depending on the exact location of the peak within a given pixel. Ten times oversampled models of the point spread function were generated, then shifted and rebinned to the actual data resolution and convolved with the pixel-pixel scattering function in order to derive a more accurate PSF model (Krist 1994). In most cases it was found that the observed PSF, while qualitatively very similar to the Tiny TIM model, had some significant deviations at the 10–15% level, which seemed to vary from target to target. In general, the resolution and strehl ratio predicted by Tiny TIM was higher than actually observed.

Photometric calibration was performed using published photometric solutions for WFPC2 and the F439W and F814W filters. Corrections were made for charge transfer efficiency (Whitmore 1996), aperture size (Table 2a of Holtzman et al. 1995a), and detector gain (Holtzman et al. 1995b). Zero-points and color-corrections for conversion from the *HST* flight filter system to ground-based Johnson filters were taken from Table 7 of Holtzman et al. (1995b) and checked against those of Whitmore (1996). The derived magnitudes have an uncertainty associated with calibration of approximately 4%. Absolute magnitudes were derived from the expression:

$$\mathrm{M'=m\text{-}15.62\text{-}5\ Log(cz)\ +\ 1.086\ (q_0\text{-}1)\ z} \tag{2.1}$$

which is correct for $H_0 = 75$ km s^{-1} and c in km s^{-1} (Peebles 1993). At these low redshifts, the choice of cosmology is relatively unimportant. M' is used to indicate that this expression corrects only for distance, and does not include K-corrections (bandpass-stretching and spectral dependence) or corrections for reddening. The most distant target is at redshift $z = 0.16$ and the median redshift for the sample is only $z = 0.09$; thus K-corrections are likely to be quite small. Based on stellar synthesis models which are believed to be representative of some of the components described below, theoretical K-corrections were computed and found to indeed be generally very small, typically $\Delta m = 0.1$ in the B and I filters at $z = 0.16$ for systems 10^7– 10^8 yrs old, with extremes of $\Delta m = 0.4$ for extremely blue or red systems. K-corrections are not believed to affect derived colors by more than $\Delta(B - I) = 0.4$. Finally, since no actual observational spectral energy distributions (SEDs) exist for the features in these objects, it was felt that the uncertainties in assigning K-corrections probably outweighed any real benefit.

More importantly, no reddening corrections have been made to any magnitudes reported in this paper. The reddening in some regions of these galaxies may be quite large; Kim (1995) reports typical extinctions based on optical spectroscopy of A_V=2-6 mag for the central ($2''$) regions of these systems, and of A_V=4.5 mag for Seyfert-like ULIGs in general. The effects of reddening are more thoroughly discussed in §6.2.

2.5. Results

2.5.1. Large-Scale Morphology and Colors

Figure 2.2 displays the large scale structure seen in the PC observations of each of the observed ULIGs. Of the nine ULIGs, all except IRAS 01003−2238 show clear signs of recent merger activity in the form of tidal tails and loops. Additionally, IRAS 08572+3915, PKS 1345+12, and Mrk 463 have clear double nuclei. Further details can be seen in the near-truecolor image of Figure 2.3 for each of the 9 objects. Figures 2.4 & 2.5 show close-ups of the individual nuclear regions in each ULIG (small boxes in Figure 2.2) at B and I respectively. Most of the ULIGs show evidence of structure in the form of filaments, knots, and fans in their inner few kiloparsecs. Also, the *HST* images show evidence for small spatial scale features in the more extended structures that were previously observed from the ground (e.g. tidal tails). Section 2.8 discusses these features on an individual galaxy basis and their connection to previous ground-based images.

Figure 2.6 shows color maps (B–I) constructed by dividing the images for each object as shown in Figures 2.4 and 2.5. The effect of the wavelength-variant PSF on the derived colors was examined. Normally the higher resolution at B would lead to colormaps with excessively blue point sources, however, it appears that this is not actually a significant effect for these data. Color maps were constructed for the observed PSF stars which show a uniform color across the star's entire profile. Stars visible in the actual data frames were also used to confirm that the PSFs were well- matched, although in a few cases convolution with a narrow Gaussian was needed in order to broaden the B-profile in order to more completely remove this color gradient. Although PSF mismatch must be present to some degree in all the colormaps, it appears to be small compared to the pixel-to-pixel variation in the colormaps due to noise in the original images and blurring due to pixel- pixel scattering within the CCDs. Only in Mrk 1014 and Mrk 231, which are dominated by very bright point sources and which therefore have very high S/N even at the first diffraction ring, are major distortions of the colormap due to PSF structure seen.

Since low S/N regions in the B and I images result in very noisy color map regions, the color maps have been masked such that only regions with a S/N ≥ 5 are displayed. As a result, very red regions are not displayed in the color maps since the S/N of the B images is usually lower than those at I. This effect can be seen in IRAS 08572+3915 (NW) and IRAS 15206+3342, where some regions become increasingly red and are then masked off. In these masked regions, B–I is at least 3.

IRAS 01003−2238, Mrk 1014, and PKS 1345+12 have a reasonably simple color structure, perhaps indicating the presence of a uniform (if any) dust screen. The other six galaxies have a variety of different features. This varies from organized structures like the face-on spiral pattern of Mrk 231 and the dust lane which seems to bisect IRAS 05189−2524, to the rather chaotic pattern seen in IRAS 12071−0444 and the northwest nucleus of IRAS 08572+3915. Typical colors for spiral galaxies are B–I= 1.8 (Lu et al. 1993). As expected, in most cases the detectable background light in these galaxies is similar to this value. It is also apparent from the colormaps that many of the ULIGs (notably

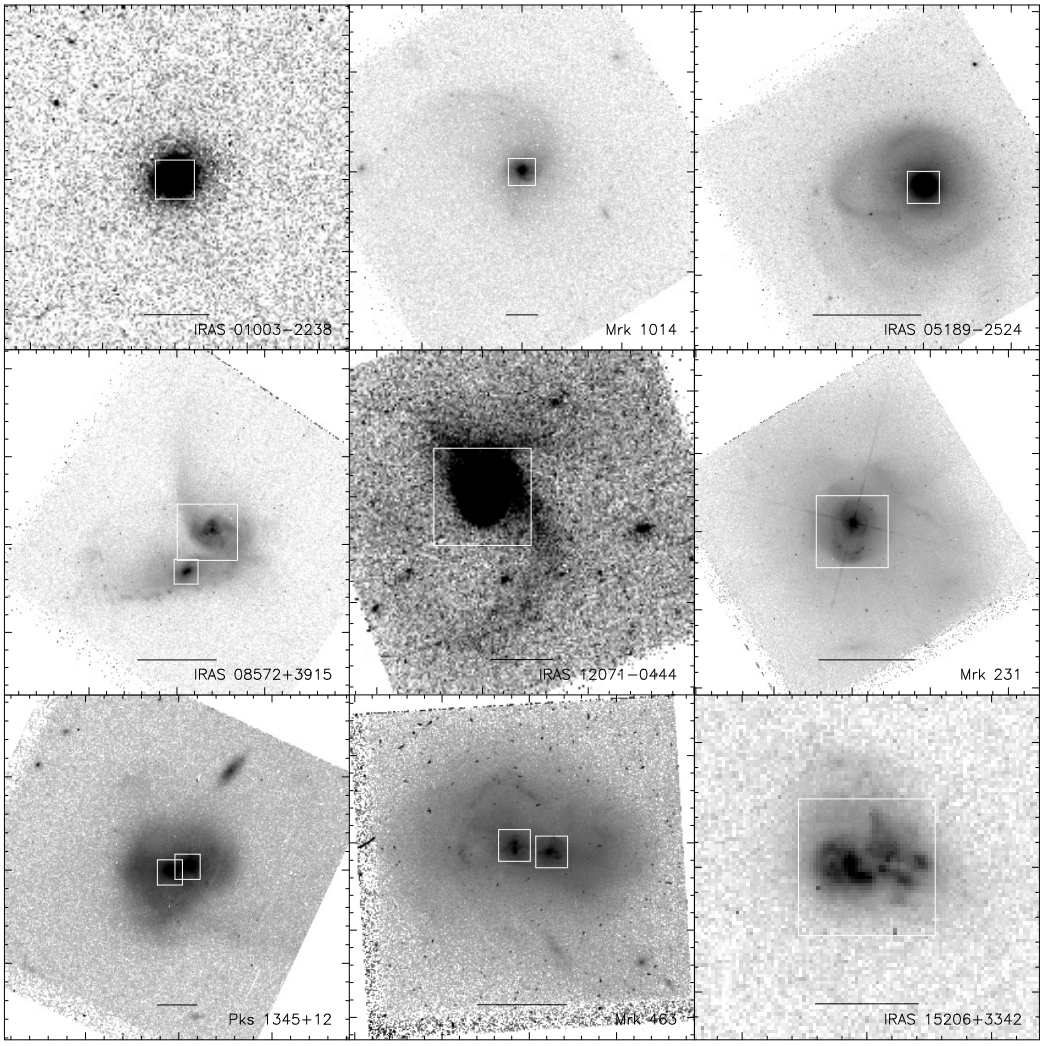

Fig. 2.2.— Large-scale structure of the nine warm ULIGs observed with the PC2 in *I*-band (F814W). In order to emphasize both faint and bright features, all images are block-averaged (3x3) and displayed with a non-linear stretch. Major ticks are $10''$, except for IRAS 01003−2238 and IRAS 15206+3342 where each major tick is $5''$. The scale bar represents 10 kpc. The white boxes indicate the individual nuclear regions that will be displayed in Figures 2.4–2.6.

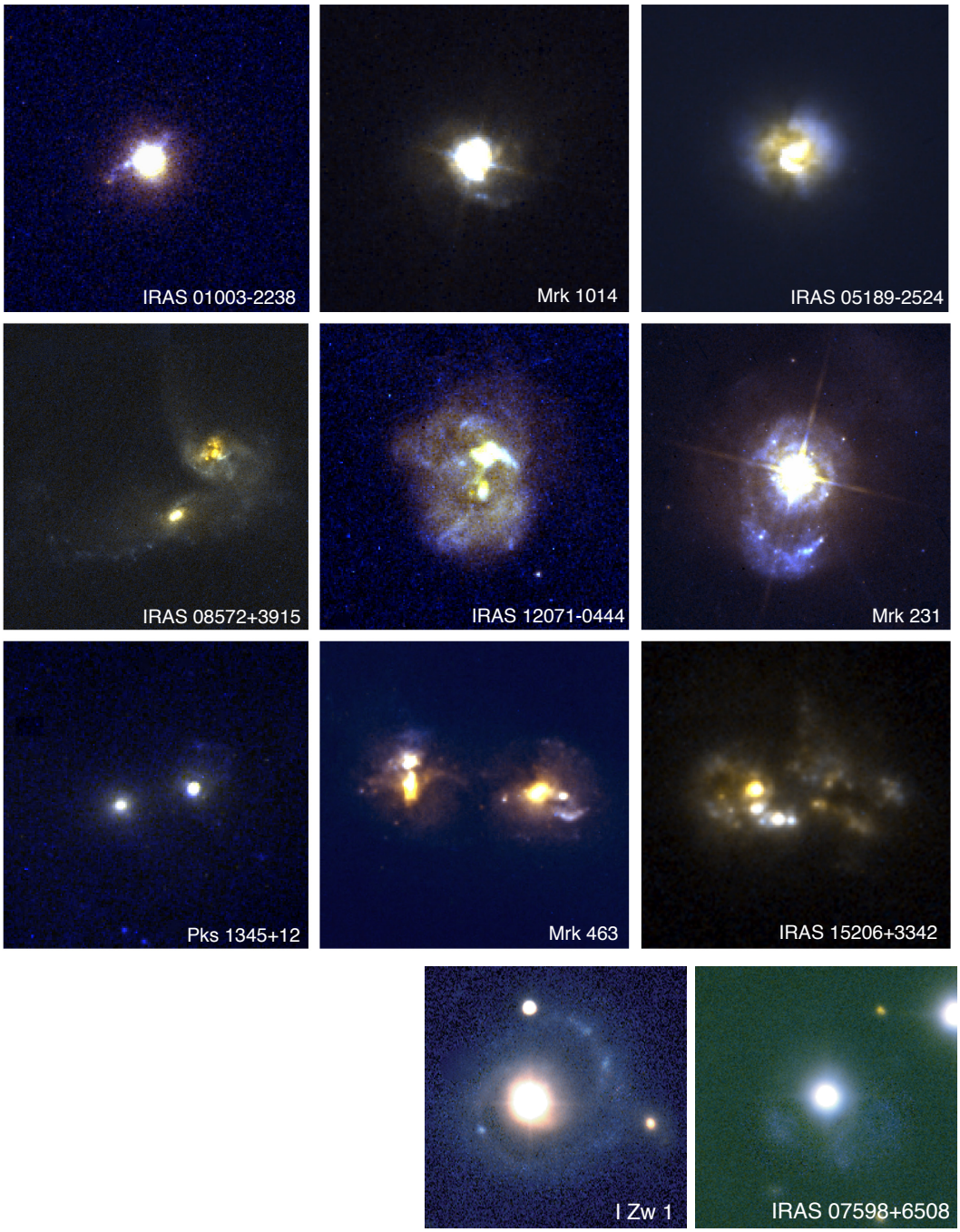

Fig. 2.3. - "Near-truecolor" images of the nine warm ULIGs. Order and orientation are the same as in Figure 2.1. For these images, we have linearly interpolated the galaxy SED and then presented it as a color image. The result should be similar to the actual color, as *I* is mapped to red, and *B* to blue. Both color and intensity information are presented simultaneously. Note that the colors are *not absolute* i.e., the color balance changes from image to image depending on the S/N in the different observations. Additionally, ground-based images of two of the warm ULIGs not observed by *HST* are presented.

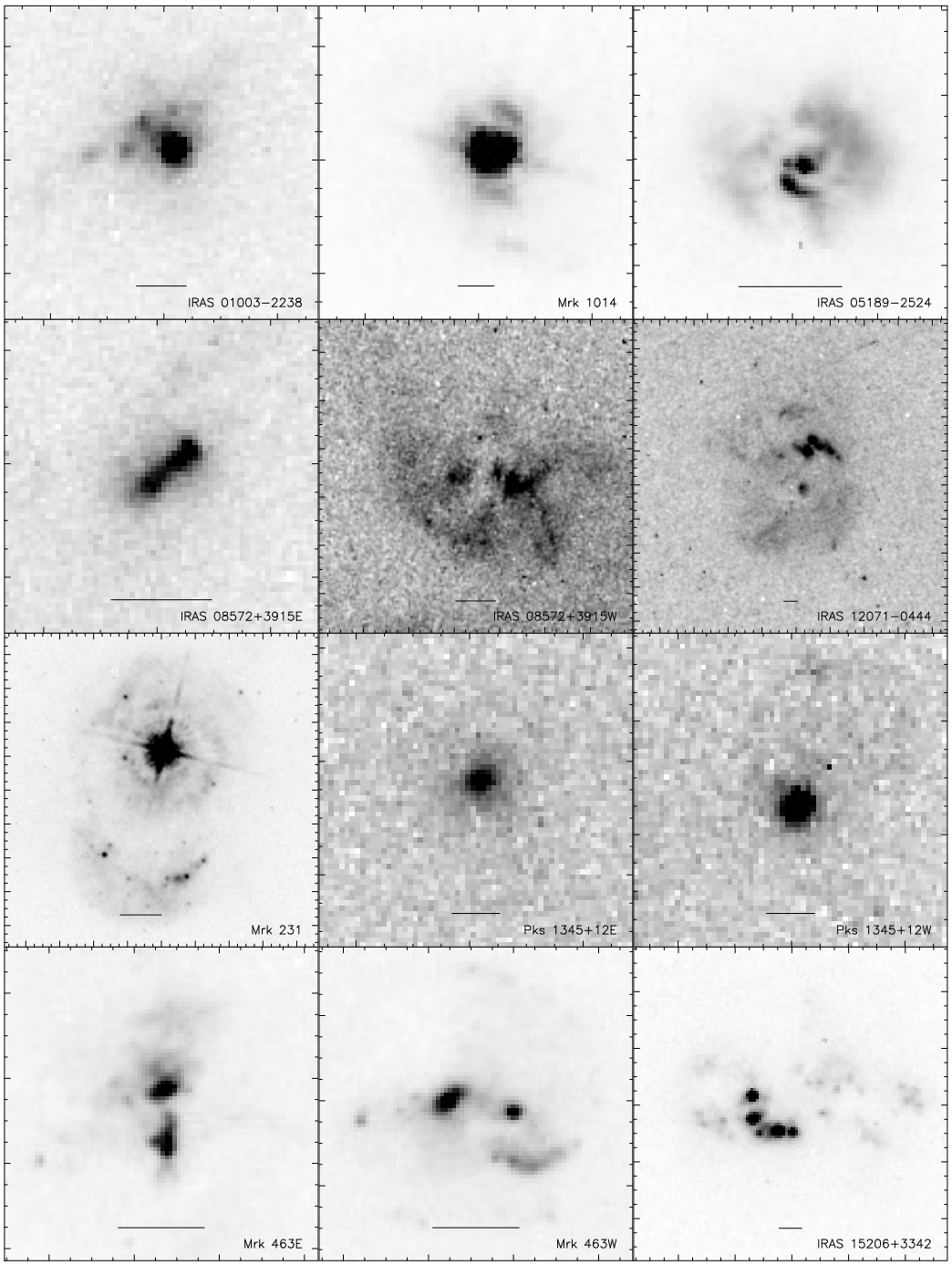

Fig. 2.4.— Close-up view of the nuclear regions of the warm ULIGs at *B*-band (F439W). The double nuclei in IRAS 08572+3915, PKS 1345+12, and Mrk 463 are displayed in separate panels labeled E (East) and W (West). The field of view represented by each of the 12 panels for the nine warm ULIGs is identical to the overlay boxes displayed in Figure 2.2. The major ticks are in arcseconds, and the scale bar represents 1 kpc.

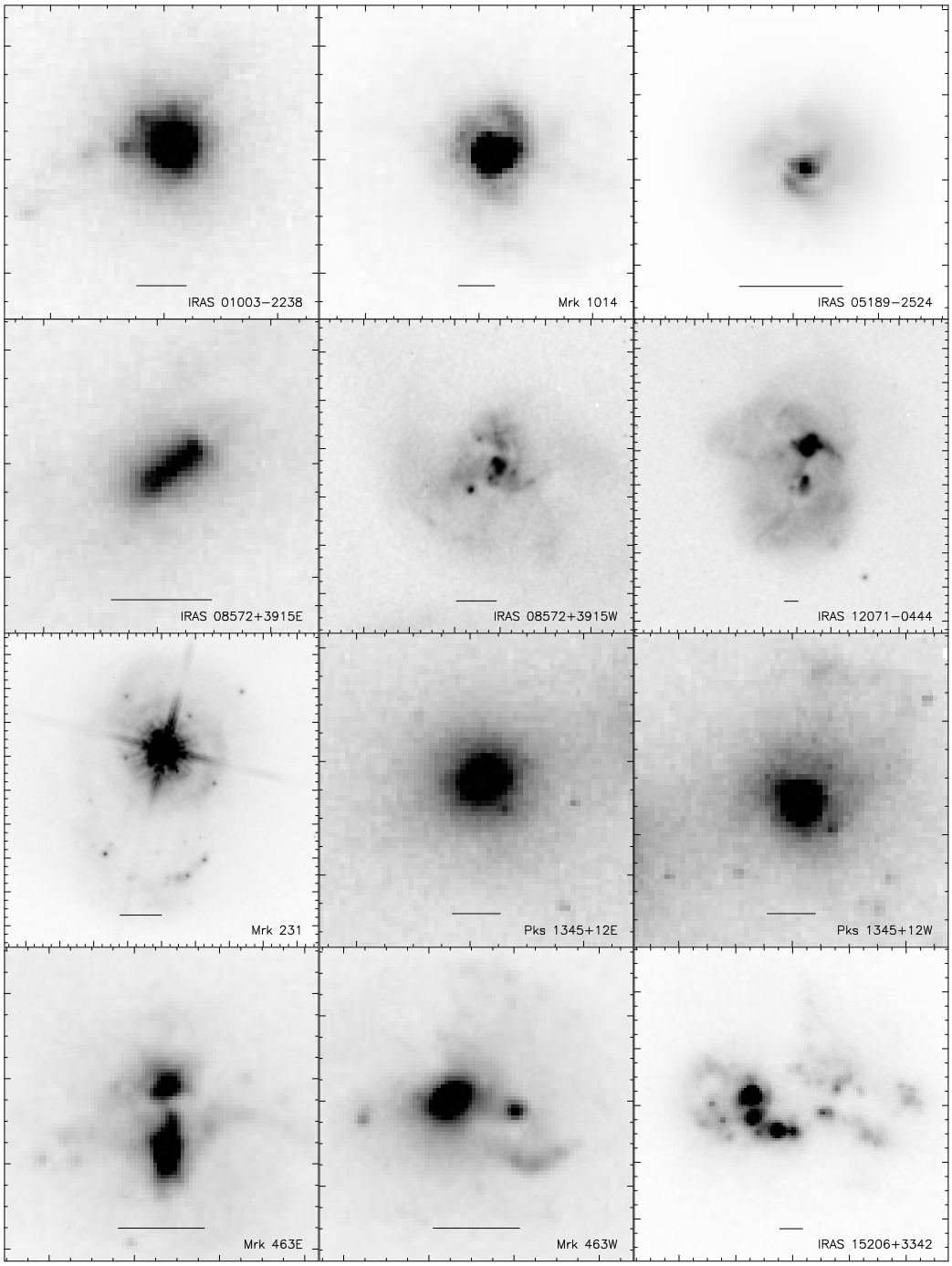

Fig. 2.5.— Close-up view of the nuclear regions of the warm ULIGs at *I*- band (F814W). The layout is the same as in Figure 2.4.

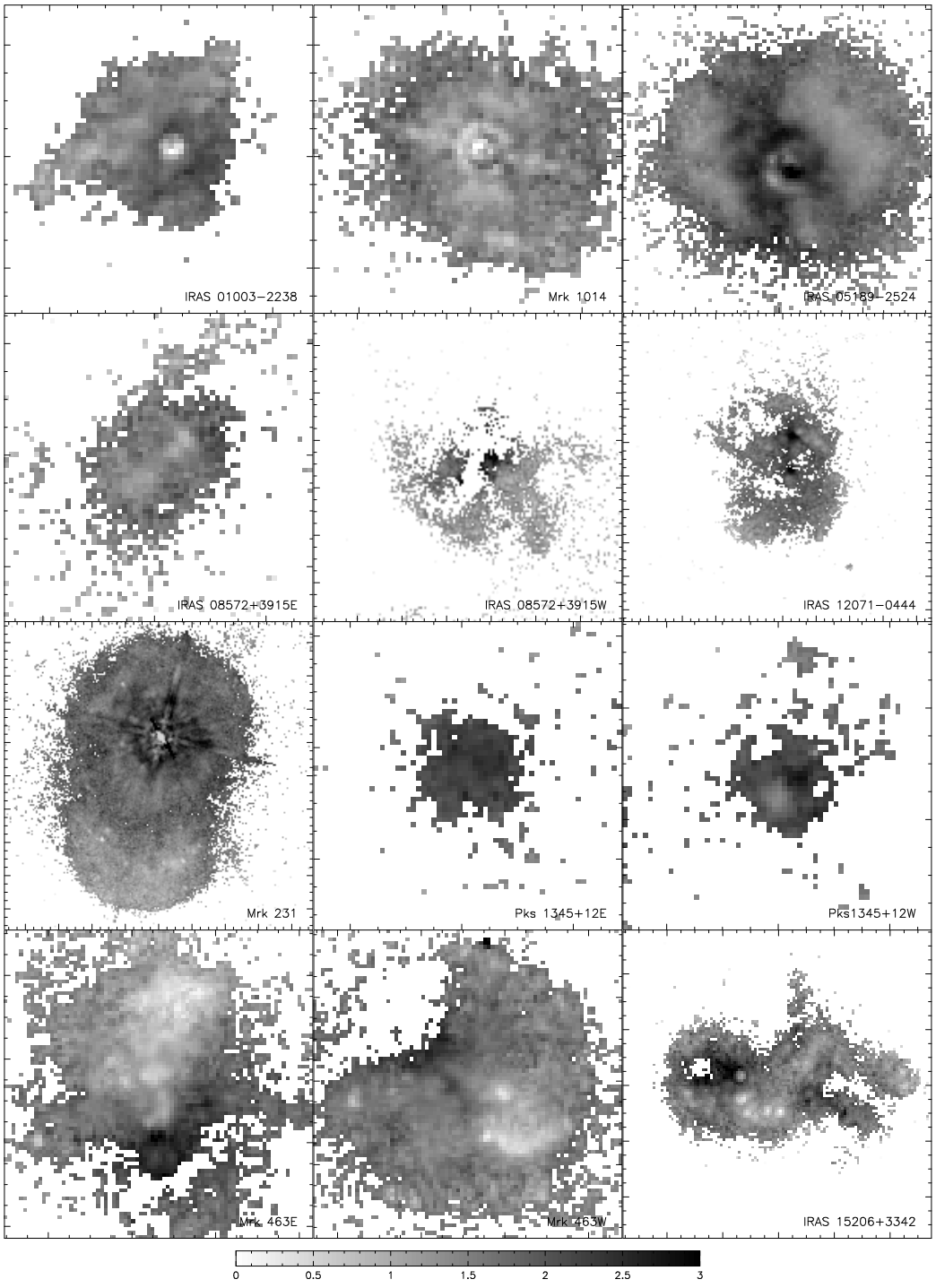

Fig. 2.6.— *B–I* colormaps of the nuclear regions of the warm ULIGs. The scalebar is the same as in Figures 2.4 and 2.5. *B–I* colors range from 0 to 3 (blue to red), except for PKS 1345+12, where they range from 0 to 4.

Mrk 231, Mrk 463, and IRAS 15206+3342) show evidence of large numbers of blue (B-$I \leq 1.0$) pointlike features.

2.5.2. Knots

We have identified in each of the galaxies bright compact regions which are usually bluer than the underlying galaxy and which appear similar to the bright blue knots found in other interacting galaxies (e.g. NGC 4038/9 – Whitmore & Schweizer 1995). These knots were identified on the basis of their peak surface brightness being three or more times the local background in either filter and being roughly circular, with closed isophotal contours (thereby differentiating them from the tidal streamers seen in some systems like Mrk 231 and IRAS 12071-0444). While three of the observed galaxies (Mrk 1014, IRAS 05189−2524, and PKS 1345 +12) seem to have very few of these "knots", the remaining six have as many as 30 each (in the cases of Mrk 231 and Mrk 463). The mean number of knots per galaxy is 13. Their locations are illustrated in Figure 2.7 and given in Table 2.2. For those systems with many knots, approximately half lie within 2 kpc of what appear to be nuclei (see § 5.3) while the remainder are spread along what appear to be inner tidal features (e.g. IRAS 08572+3915 and Mrk 463). The knots often appear to be arranged in linear structures or "strings" one or two knot widths wide and 4–5 knots long (the best examples can be found in IRAS 01003−2238, IRAS 12071−0444, Mrk 231, and IRAS 15206+3342).

The apparent magnitudes were measured for each of the identified knots. Initially, we attempted to derive fluxes by fitting them with the observed PSF. However, the uncertainties associated with this technique were very large (typically 1 magnitude). This was primarily because the marginal sampling of the PC2, especially at B, made it difficult to constrain the fitted PSFs. Additionally, many of the knots appear to be slightly resolved, which renders this technique inappropriate. Magnitudes were therefore derived from aperture photometry. Most of the photometry was derived from circular apertures typically 4–7 pixels in radius, although in some cases the irregular shape of the knots necessitated the use of polygonal apertures. These apertures varied in size depending on the knot brightness, but were always made large enough (> 10 times the width of the PSF) so that aperture corrections for point sources tended to be fairly small. Additional aperture corrections due to the extended nature of the knots were computed after the knot sizes were measured (see below), although these corrections were generally small. Estimates were made of the underlying background galaxy flux by using the mean of the pixels in an 3-pixel annulus immediately outside the photometric aperture. In some cases sections of the annuli had to be deleted due to confusion with nearby structure. Most of the knots are isolated from one another by > 7 pixels, and hence confusion does not seem to be a serious problem (with the exception of IRAS 15206+3342). The measured magnitudes for each of the knots, after correction for the background and aperture effects, are given in Table 2.2.

Simulations were performed in order to estimate the uncertainty of the measured fluxes. The observed point spread function was rescaled to the range of observed knot magnitudes and then added into various regions of the actual data for Mrk 231 and IRAS 05189−2524. Poisson noise and the effects of the detector gain and readout were all modeled using

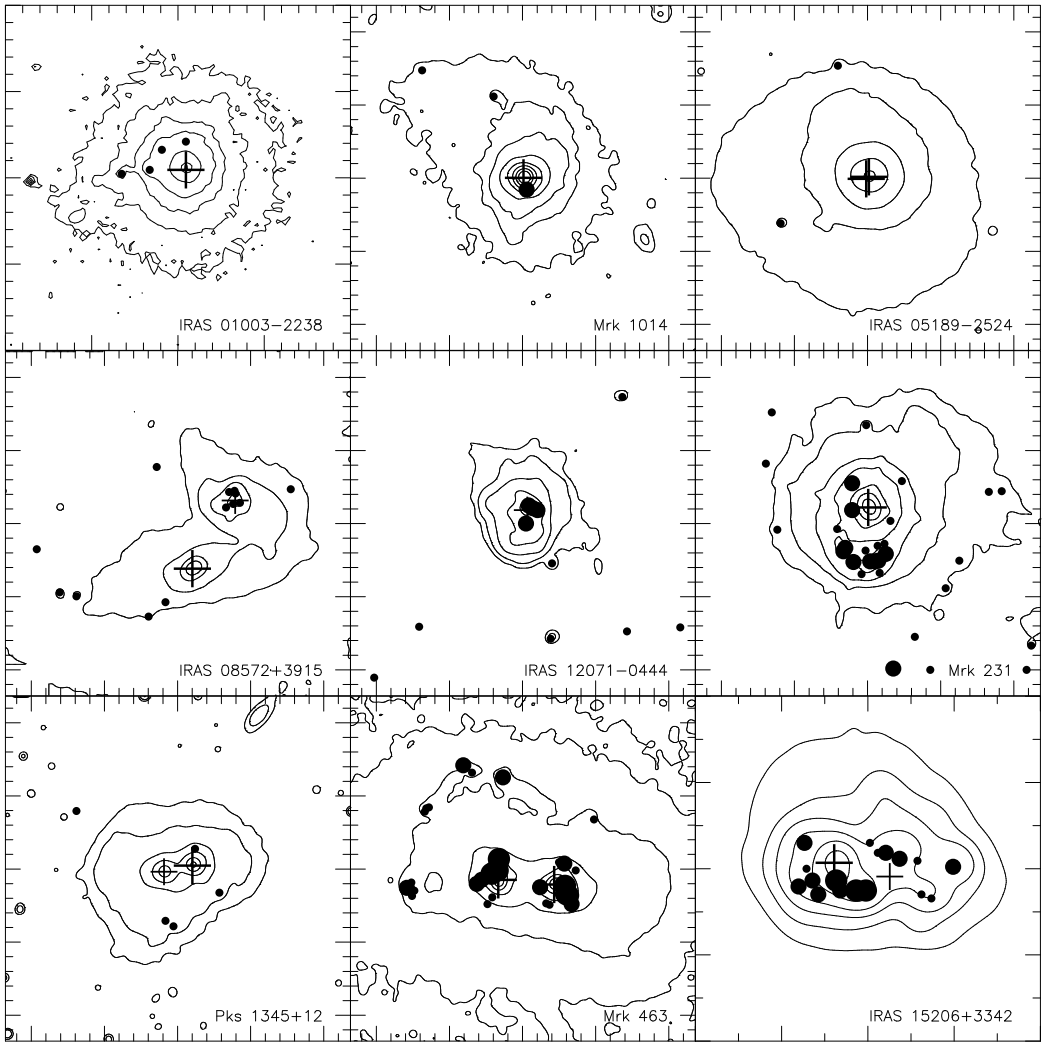

Fig. 2.7.— Locations of the identified blue knots superimposed on I-band contour maps of the warm ULIGs. Putative nuclei are indicated by '+' signs and all other knots by filled circles. The contours have been smoothed for clarity. Orientation is the same as in Figure 2.2.

the parameters given for the PC in the WFPC2 instrument handbook. In this way, the uncertainty in point fluxes derived from real-data conditions, with fully simulated noise and confusion, could be examined. Attempts were then made to recover the known flux using the described aperture photometry technique. It was found that the magnitudes derived in this fashion had an associated uncertainty of about 0.25 between 24–26 magnitudes, and decreased to about 0.05 magnitudes at 23 magnitudes and brighter. This is similar to the expected result based on the image noise statistics. Since most of the knots fall in the magnitude range from 22 to 26 (the 3σ limiting magnitude based on image noise statistics is generally between 26–27), a reliable uncertainty from measurement is about 0.15. Systematics due to calibration problems (see §4) and aperture effects contribute another 0.1 magnitudes. Since the systematics probably affect both filters nearly equally, the associated uncertainty in color is only a function of measurement uncertainties, and is around 0.2–0.3.

In almost every case, the knots appear to be resolved in comparison both to the observed PSF and the Tiny TIM models. Size measurements were performed by fitting radial Gaussians to the data using the IMEXAMINE task in IRAF. Each knot was fit by hand in order to ensure that the centroiding and background estimation were reasonable, and that the actual fits were realistic. An effective radius, $R_{\rm eff}$, was derived which is equal to the HWHM of a Gaussian which, when convolved with the observed PSF, reproduces the measured width. These effective radii are given in Table 2.2.

The technique of using Gaussian fits to estimate effective radii has been employed by several workers (Whitmore & Schweizer 1995, Meurer et al. 1995), although others have argued that Hubble profiles with characteristic core and half-light radii may be more appropriate for knot measurements (Holtzman et al. 1996). Given that only rarely do the data have sufficient signal-to-noise to detect the low, broad wings of the Hubble profile and that radial Gaussians seem to provide very good fits to the detected knot profiles, use of Gaussians seems well- motivated. The total luminosities of the knots will, of course, be affected by the actual form of the fitting function.

Simulations were performed in order to estimate the uncertainties of this technique. Gaussian distributions with sizes similar to the derived sizes were convolved with the observed PSF and rescaled to match the range of magnitudes of the observed knots. These were then added (with appropriate noise modeling) to the actual data in Mrk 231. In all cases, it was found that the derived width *overestimates* the real width, with this tendency increasing slightly as the signal-to-noise ratio decreases. It is likely that the actual knot sizes are somewhat smaller than those reported, although the simulations indicate that the uncertainty is probably not more than 40%. No significant correlation was found for observed width vs. apparent magnitude; it is thus likely that the correlation found in the simulations between derived width and S/N are not significant in the actual data. The tendency of this method to overestimate the true width has been noticed before (Schweizer et al. 1996).

Table 2.2. Warm Galaxy Knots

Number	Δ RA ($''$)	Δ Dec ($''$)	m_B (mag)	m_I (mag)	M'_B [a] (mag)	R_{eff} [b] (pc)	Mass ($M_\odot$)
IRAS 01003-2238							
1	0.74	-0.05	24.25	23.43	-14.17	65	2E+07
2	0.41	0.00	23.50	23.16	-14.92	106	2E+06
3	0.28	0.23	23.27	22.78	-15.15	161	2E+06
4	0.00	0.32	23.82	23.77	-14.60	55	1E+06
5†	0.00	0.00	19.27	18.32	-19.15	28	3E+08
Mrk 1014							
1	2.04	5.54	23.79	23.07	-15.37	70	3E+06
2	6.91	7.34	23.90	23.29	-15.26	80	3E+06
3	-0.22	-0.81	22.47	21.50	-16.69	150	4E+08
4†	0	0	16.40	15.90	-22.76	<15	3E+09
IRAS 05189-2524							
1	5.93	-3.08	23.04	21.92	-13.14	12	2E+07
2	2.02	7.68	<24.68	23.13	<-11.15	64	···
3*	-0.09	0.14	18.78	16.55	-17.40	25	2E+10
4*	0.09	-0.09	19.01	17.37	-17.17	27	1E+09
IRAS 08572+3915							
1	13.55	-3.33	26.00	24.50	-10.86	74	4E+06
2	11.98	-6.27	24.14	23.38	-12.72	48	5E+06
3	10.83	-6.55	24.57	24.10	-12.29	49	2E+05
4	5.91	-7.93	24.58	24.35	-12.28	67	2E+05
5	4.76	-6.95	23.52	22.98	-13.34	65	4E+05
6	-3.80	0.76	24.92	24.23	-11.94	55	1E+05
7	5.36	2.28	24.08	24.08	-12.78	140	2E+05
8	0.62	-0.48	23.85	21.58	-13.01	26	3E+08
9	0.13	-0.25	24.59	22.28	-12.27	75	2E+08
10	-0.33	-0.16	23.43	22.75	-13.43	55	5E+05
11†	0.00	0.00	22.90	20.59	-13.96	114	1E+09
12	-0.02	0.47	24.68	22.42	-12.18	102	1E+08
13	0.05	0.65	24.79	22.66	-12.07	71	9E+07
14	0.41	0.57	24.44	23.07	-12.42	40	1E+07
15†	2.88	-4.66	20.54	19.26	-16.32	···	···
IRAS 12071-0444							
1	10.45	-11.44	<27.50	23.53	<-11.11	142	···
2	7.38	-7.96	27.41	24.04	-11.20	82	2E+09
3	-1.69	-3.64	23.55	22.78	-15.06	54	5E+07
4	-1.60	-8.79	<27.50	22.32	<-11.11	104	···
5	-6.81	-8.28	24.70	24.06	-13.91	17	8E+05
6	-10.44	-8.00	25.19	23.74	-13.42	120	4E+07
7	-6.49	7.73	25.71	23.24	-12.90	150	6E+08

Table 2.2—Continued

Number	Δ RA ($''$)	Δ Dec ($''$)	m_B (mag)	m_I (mag)	M'_B [a] (mag)	R_{eff} [b] (pc)	Mass ($M_\odot$)
8	0.09	-0.92	22.75	20.52	-15.86	202	4E+09
9†	0.00	0.00	21.59	19.00	-17.02	244	4E+10
10	-0.09	0.32	21.61	20.19	-17.00	112	1E+09
11	-0.37	0.14	22.02	20.40	-16.59	126	8E+08
12	-0.69	0.00	22.66	21.59	-15.95	181	2E+08
13	-0.92	-0.23	23.55	22.33	-15.06	112	1E+08
			Mrk 231				
1	1.10	1.68	22.23	21.12	-13.92	66	3E+07
2	-1.52	-0.90	23.27	20.86	-12.88	< 20	5E+08
3	1.10	-0.16	22.38	20.86	-13.77	62	5E+07
4	2.12	-1.45	23.98	22.60	-12.17	42	1E+07
5	1.70	-2.97	21.31	20.50	-14.84	< 20	4E+07
6	1.56	-2.74	22.97	22.28	-13.19	71	4E+05
7	1.01	-3.70	22.69	21.47	-13.47	38	3E+07
8	0.18	-2.92	24.60	23.10	-11.55	46	7E+06
9	0.46	-4.53	23.52	22.15	-12.63	51	2E+07
10	-0.14	-3.66	22.57	21.88	-13.58	46	6E+05
11	-0.46	-3.66	21.17	20.66	-14.98	136	2E+06
12	-0.69	-3.61	21.46	20.70	-14.69	31	3E+07
13	-0.78	-4.44	23.65	22.75	-12.50	25	6E+06
14	-1.20	-3.15	21.79	20.33	-14.36	40	9E+07
15	-0.64	-2.60	24.05	22.59	-12.10	< 20	1E+07
16	-1.10	-2.46	24.15	23.54	-12.00	42	1E+05
17	6.58	6.51	24.80	24.12	-11.35	91	8E+04
18	0.14	5.64	23.28	21.64	-12.87	44	2E+07
19	6.21	-1.50	24.10	22.44	-12.05	46	2E+07
20	-1.70	-10.97	22.51	21.79	-13.64	44	7E+05
21	-4.23	-11.06	23.64	23.48	-12.51	46	2E+05
22	-3.17	-8.81	25.53	24.71	-10.62	65	8E+05
23	-10.81	-11.06	23.40	22.60	-12.75	43	5E+06
24	-11.13	-9.41	24.15	23.21	-12.00	< 30	4E+06
25	-5.29	-5.50	25.49	23.71	-10.66	< 20	7E+06
26	-6.21	-3.61	23.64	23.35	-12.51	43	2E+05
27	-8.23	1.08	23.34	22.69	-12.81	35	3E+05
28	-9.11	1.13	24.39	23.15	-11.76	183	5E+06
29	-2.30	1.82	23.26	21.06	-12.89	46	2E+08
30	6.99	3.01	26.08	24.59	-10.07	< 20	2E+06
31†	0.00	0.00	14.54	12.99	-21.61	< 20	7E+10
			Pks 1345+12				
1	1.85	-3.76	23.64	22.86	-14.84	69	4E+07
2	1.29	-4.13	23.92	23.10	-14.56	97	3E+07
3	-1.83	-1.83	24.04	23.19	-14.44	162	3E+07
4	-0.18	1.16	24.23	22.52	-14.25	134	2E+08
5	7.92	3.74	<26.70	23.44	<-11.78	102	···
6†	1.93	-0.41	21.76	18.66	-16.72	165	1E+11
7†	0.00	0.00	20.64	17.91	-17.84	84	1E+11

Table 2.2—Continued

Number	Δ RA ($''$)	Δ Dec ($''$)	m_B (mag)	m_I (mag)	M'_B [a] (mag)	R_{eff} [b] (pc)	Mass ($M_\odot$)
			Mrk 463				
1	9.79	0.11	23.23	22.58	-13.34	60	5E+05
2	10.10	-0.26	22.80	22.32	-13.77	48	6E+05
3	9.59	-0.45	24.30	23.24	-12.27	23	7E+06
4	9.74	-0.81	23.17	22.95	-13.40	39	4E+05
5	6.25	8.11	22.87	22.65	-13.70	82	5E+05
6	5.65	7.60	23.05	22.78	-13.52	52	4E+05
7	3.54	7.28	22.48	21.96	-14.09	48	9E+05
8	8.59	5.23	23.38	23.15	-13.19	42	3E+05
9	8.78	5.17	23.28	23.35	-13.29	49	3E+05
10	8.87	4.94	23.79	24.05	-12.78	48	2E+05
11	4.59	-1.37	24.24	24.13	-12.33	42	1E+05
12	4.27	-0.91	25.86	23.21	-10.71	25	1E+08
13	5.33	0.01	22.48	21.74	-14.09	36	2E+07
14	5.00	0.29	22.54	21.08	-14.03	121	6E+07
15†	3.85	0.29	18.83	16.95	-17.74	69	6E+09
16	4.31	0.70	20.87	20.78	-15.70	16	3E+06
17	3.81	1.72	20.28	20.52	-16.29	< 20	4E+06
18	3.90	0.93	18.50	17.78	-18.07	83	4E+07
19	1.00	-0.22	21.69	20.68	-14.88	47	7E+07
20†	0.00	0.00	18.82	16.76	-17.75	58	1E+10
21	-0.70	-0.12	19.83	19.07	-16.74	50	2E+08
22	0.59	-1.32	23.47	23.21	-13.10	38	3E+05
23	0.36	-1.41	23.53	23.44	-13.04	24	2E+05
24	-0.29	1.49	22.81	22.34	-13.76	62	6E+05
25	-0.65	1.39	22.67	21.93	-13.90	65	1E+07
26	-1.44	0.93	24.00	23.00	-12.57	81	8E+06
27	-1.15	-1.37	22.95	23.08	-13.62	62	4E+05
28	-0.56	-0.68	21.50	21.41	-15.07	100	1E+06
29	-0.93	-0.77	20.88	20.82	-15.69	109	3E+06
30	-0.79	-0.72	20.86	20.82	-15.71	77	3E+06
			IRAS 15206+3342				
1	0.69	0.46	21.77	21.96	-16.79	206	7E+06
2	0.64	-0.14	23.00	20.37	-15.56	73	3E+09
3	0.83	-0.55	22.30	20.94	-16.26	159	4E+08
4	0.51	-0.41	22.08	20.18	-16.48	76	2E+09
5	0.37	-0.74	22.60	21.23	-15.96	107	3E+08
6†	0.00	0.00	19.29	17.37	-19.27	57	3E+10
7	-0.05	-0.41	19.50	18.68	-19.06	104	2E+09
8	-0.14	-0.64	21.54	21.78	-17.02	84	8E+06
9	-0.51	-0.64	19.45	18.54	-19.11	88	3E+09
10	-0.74	-0.64	20.43	20.17	-18.13	67	3E+07
11†	-1.29	-0.32	22.87	20.10	-15.69	93	2E+10
12	-2.02	-0.74	22.66	20.83	-15.90	233	1E+09
13	-2.25	-0.83	22.64	20.81	-15.92	221	1E+09
14	-0.83	0.46	23.33	21.79	-15.23	152	2E+08

Table 2.2—Continued

Number	Δ RA ($''$)	Δ Dec ($''$)	m_B (mag)	m_I (mag)	M'_B [a] (mag)	R_{eff} [b] (pc)	Mass ($M_\odot$)
15	-1.01	0.23	23.28	22.07	-15.28	90	1E+08
16	-1.20	0.23	22.37	21.75	-16.19	101	7E+06
17	-1.52	0.09	22.44	20.46	-16.12	108	2E+09
18	-1.93	0.05	23.73	21.91	-14.83	87	3E+08
19	-2.76	-0.09	21.74	20.55	-16.82	233	6E+08

† putative nucleus - identified on the basis of *B*–*I* color, size, and absolute *B* magnitude (in all cases the brightest object at *B*).

* the two listed nuclei appear to actually be a single nucleus split by a dust lane.

[a] absolute magnitude, uncorrected for redshift, as given by Eqn.1.

[b] effective radius defined by half-width half-intensity.

Note. — Reference to the knots should be made in accordance with the IAU naming convention (galaxy name):SSVVM(number).

Additionally, tests were performed to determine the effect of source extension on the derived magnitude. Assuming Gaussian radial distributions with the effective radii observed (typically 1.25–2 pixels), the additional aperture corrections needed compared to those derived from point source models are very small (< 0.05 magnitudes) for the 4–7 pixel radius apertures used to determine the photometry.

2.5.3. Identification of Putative Nuclei

Within the general population of knots that were identified for each object there were one or two knots which we believe plausibly represent putative nuclei. Not only are these the brightest knots at B, but they are also usually the most pointlike, are connected to morphological features such as tidal tails (in the case of the double nucleus systems), and more importantly they are spatially coincident with dominant K-band peaks in high-resolution K-band images that have recently been obtained with the University of Hawaii 2.2m telescope (see Chapter 3). The properties of these putative nuclei can be found in Table 2.2, including the implausibly large masses that would be implied if these if these objects were interpreted as starbursts (see §2.6.2 below).

2.6. Discussion

2.6.1. Large-scale Features

Of the 9 warm ULIGs observed by us with *HST*, all but IRAS 01003-2238 are unmistakably advanced merger systems. This is perhaps expected since several recent studies have shown that $> 95\,\%$ of ULIGs are strongly interacting/merger systems (Sanders et al. 1988a, Melnick & Mirabel 1990, Kim 1995, Murphy et al. 1996, Clements et al. 1996). More interesting perhaps, (and indeed what our *HST* observations were designed to show), is the mean separation of the nuclei of the parent disks. Although our statistics are obviously limited by the small sample size, we find that the warm ULIG double nuclei fraction is considerably lower than that of "cold" ULIGS. As will be shown later, following our discussion of the knots observed in each object, only 4 of the nine observed warm galaxies have obvious double nuclei (44%), as opposed to $\gtrsim 60\%$ found by Murphy et al. (1996) for his ground-based images of cold ULIGs. Three of the four double-nucleus warm ULIGs were already known to be double from lower-resolution ground-based observations. What the enhanced resolution of *HST* has primarily revealed is that what were previously thought to be possible doubles (e.g. based on oval shaped inner contours in r-band images) in the case of IRAS 12071−0444 and IRAS 05189−2524 are more plausibly explained as complex clumps of many star-forming knots in the former and dust bifurcation in the latter. This lack of additional galaxy nuclei at very small separations may indicate either that the progenitor nuclei rapidly coalesce during the warm ULIG phase, or that obscuration due to dust and/or confusion with star-forming regions can hide the second nucleus, however we argue against this latter interpretation below. In general, the smaller fraction of double nuclei seems to support the idea that the warm ULIGs are more advanced mergers than the majority of ULIGs which have cooler far-infrared colors.

2.6.2. Knot Ages and Masses

Figure 2.8 shows the M'_B vs (B–I) color-magnitude diagram for the individual knots in each of the 9 warm ULIGs. (Those knots that were flagged in Table 2.2 as representing possible nuclei have been excluded from this plot, and will be discussed separately in Section 2.6.6). Typically, $0 < (B - I) < 2.5$. The limiting magnitude at B varies typically between $M'_B = -10$ (for Mrk 231) to $M'_B = -12.5$ (PKS 1345+12), although not all knots this faint are detected due to confusion with the complex structure of the underlying galaxies. Detection is believed to be complete in all systems to about $M'_B < -12.5$.

Stellar synthesis models created by the GISSEL package (detailed in Bruzual & Charlot 1993; the updated version is hereafter called BC95) are the basis for our estimates of the knot ages and masses. These models compute complete spectral energy distributions for different stellar ensembles with different star formation histories in timesteps ranging from 0.5 Myr to 20 Gyr and produce absolute magnitudes in many standard filters. These models are based on solar metallicity; no attempt has been made to explore metallicity effects as they are most likely unimportant compared to other uncertainties. A Salpeter IMF and a stellar mass distribution from 0.1 to 125 $M_\odot$ is assumed, although the actual

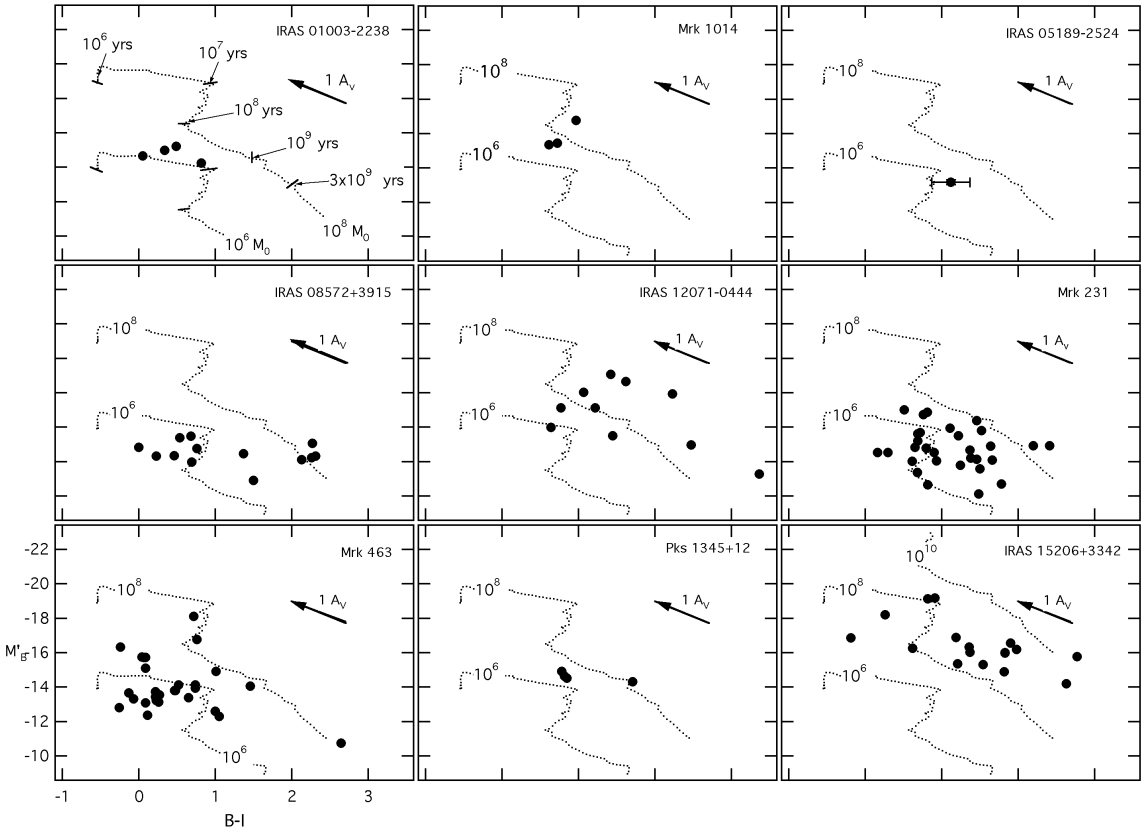

Fig. 2.8.— Color-magnitude diagrams, M'_B vs. (B–I), for identified knots in the warm ULIGs. The dotted lines represent evolutionary tracks for instantaneous starbursts of 10^6 $M_\odot$ and 10^8 $M_\odot$. The upper left box (IRAS 01003−2238) marks the locations on the evolutionary tracks corresponding to the starburst age in years. The data in the upper right box (IRAS 05189−2524) show error bars which are typical of the uncertanties in the B–I colors of the knots in all of the warm ULIGs. These error bars are omitted on the remaining graphs for sake of clarity. The dereddening vector ($A_V = 1$) is shown in the upper right of each panel.

mass distribution has little effect after an age of a few Myrs. This model is probably applicable to the majority of starburst regions (Leitherer 1996). The models were used to construct color-magnitude, M'_B vs. (B–I), evolutionary tracks as a function of time for an instantaneous starburst of different total masses (Figure 2.8). They illustrate that the knot age is a nearly monotonically increasing function of B–I color, although there is a degeneracy in B–I colors from approximately 10^7 to 10^8 yrs during which the color remains essentially fixed (B–$I = 0.7$). Perhaps not surprisingly, the mean knot color is very close to this value (Figure 2.9). Our knot ages are determined entirely from the B–I color since the constraints on the intrinsic knot luminosity are relatively weak. Knot masses are derived from the BC95 models by scaling a 1 $M_\odot$ stellar ensemble to the observed absolute magnitude. The evolutionary tracks in Figure 2.8 are for knots of a fixed mass.

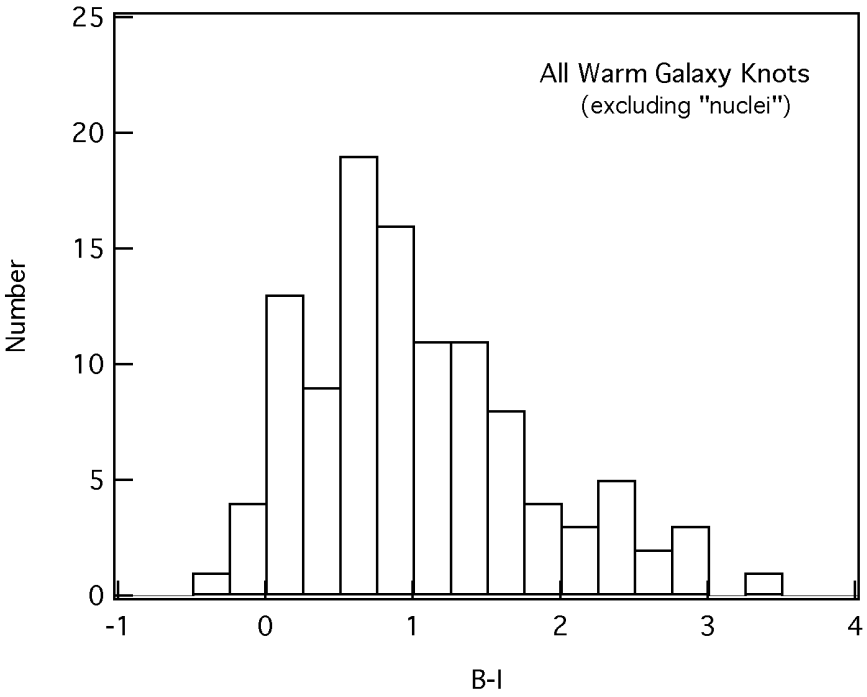

Fig. 2.9.— Distribution of B–I colors for all of the knots (excluding putative nuclei) identified in all of the warm ULIGs.

Also shown in Figure 2.8 are the effects of 1 visual magnitude of dereddening (Sapar & Kuusik 1978). Kim (1995) examined optical spectra of 5 of the nine galaxies in our sample and concluded that the reddening varied typically from A_V=2 mag (IRAS 15206+3342) to A_V=6 mag (IRAS 08572+3915). Unfortunately, the slit size and extraction apertures of these spectra are so large that they are averaged over the entire central ($\approx 2''$) regions of the galaxies. The complex morphology in the *HST* images suggests that the actual extinction is likely to be patchy in many cases. Additionally, an examination of the *HST* data in the apertures used for these spectra shows that the knots typically account for 10–40% of the wide-band optical emission; they do not dominate it, and hence the reddening indicated by the spectra applies at least in part to either the underlying galaxy or the nucleus. It is unlikely that the reddening of the knots can be as large as that estimated by Kim (1995)

since this would imply that the knots are intrinsically much bluer than even a zero-age starburst. Some authors (Whitmore & Schweizer 1995) have argued that the dust clearing time is likely to be very short, with a 100 pc region (roughly the size of our knots) being cleared in only 10^6 yr. Since we believe that these systems are at least 10–100 Myr or more in age, possibly very few of them still have substantial foreground dust screens and may not be very reddened. However, at least a handful (5) of the knots must be highly reddened, since they are redder than stellar aging can account for.

The dereddening vector lies nearly parallel to the evolutionary track. Hence, it is difficult, from *B*- and *I*-band observations alone, to distinguish between stellar aging and reddening, particularly in the absence of any knowledge of the intrinsic knot luminosities. The derived ages are thus upper limits. Only for the very youngest knots are the ages well constrained, as they cannot be very reddened. However, the dereddening vector nearly parallels lines of constant mass, and hence dereddening has very little effect on the derived mass. The only difficulty arises when the knots have apparent colors of $(B–I) > 0.7$ yet have true (dereddened) colors of $(B–I) < 0.7$. In this case our mass estimates based on the reddened colors will be too large by a factor of nearly 10. Otherwise, estimating the mass based on reddened colors will overestimate it by at most a factor of 2. All of the masses listed in Table 2.2 are therefore upper mass limits. Both the time degeneracy and uncertainties due to reddening can be addressed with additional observations at shorter wavelengths (e.g. *U*-band). From 10-100 Myr, (*B–I*) (and all combinations of *B* and longer wavelengths) remains essentially fixed, while (*U–B*) is evolving rapidly (Figure 2.8). Furthermore, while in almost all 2-color diagrams of *B* and longer wavelengths the evolutionary tracks parallel the reddening vector, the (*U–B*) vs (*B–I*) track is nearly perpendicular to the reddening vector. Alternately, high spatial resolution spectra would allow a direct measurement of each knot's reddening and stellar population.

Since we expect the properties of the knots to be connected to the galaxy merger system as a whole, we discuss below the mean properties of the knots on a *per galaxy basis*. Following Whitmore & Schweizer (1995), if it is assumed that the spread in knot colors is due equally to the effects of reddening and intrinsic color due to age, then the mean reddening is $\sim 25\,\%$ of the spread in knot colors. The estimated mean reddening then varies from $A_V = 0.41$ mag in IRAS 15206+3342 to $A_V = 0.08$ mag in Mrk 1014. Applying no reddening correction, the knot colors imply ages varying from a mean of 7 Myr in Mrk 463 and IRAS 01003- 2238 (corresponding to $< B - I >= 0.4$) to 1.4 Gyr in IRAS 12071−0444 (corresponding to $< B - I >= 1.63$). These represent upper limits to the mean knot ages in each galaxy. Applying the mean reddening correction shortens these ages to 6 and 370 Myr, respectively. The 6 remaining galaxies have upper limits to their mean knot ages of $\sim 6\times10^8$ yr (with no reddening correction). Note that if a reddening correction is applied to these 6 apparently older systems, then their ages may drop to as little as 0.6×10^8 yr due to the degeneracy in *B–I* colors from 10^7 to 10^8 yr. Due to the uncertainties involved, no further corrections will be made for reddening. The mean age for *all* knots in all warm ULIGs is 5.7×10^8 yr, while the median age is $0.1\text{-}2.5\times10^8$ (the range being due to the color-age degeneracy). This latter figure is dominated by the large numbers of blue knots in Mrk 463 and IRAS 01003-2238.

The five galaxies IRAS 01003−2238, IRAS 08572+3915, Mrk 231, Mrk 463, and IRAS 15206+3342 each contain at least a few knots whose ages cannot exceed 10 Myr. However, at the same time the total span of colors is very large for some galaxies. The five galaxies IRAS 08572+3915, IRAS 12071−0444, Mrk 231, Mrk 463, and IRAS 15206+3342 all have many apparently old knots with ages 0.5–2 Gyr. This would seem to imply either that the knots are not all coeval or highly variable reddening is present. In the former case, some process initiated cluster formation (presumably the galaxy merger), but knot formation is then seen to continue for $> 10^8$ yr afterwards. Meurer (1995b) argues that NGC 4038/9 exhibits a cluster formation history similar to this.

Knots close to the galaxy centers seem to be much redder than those farther out. In particular, the two galaxies with the most well-developed, bright tidal tails (IRAS 08572+3915 and Mrk 463) both seem to have extremely blue knots ($< B-I > \approx 0.34$ and 0.60, respectively) in the tails which have age upper limits of only 6–10 Myr. The knots in the central regions of the galaxies are much redder with implied ages of 30 Myr and 2 Gyr. This may either reflect differences in knot age, radially variable extinction ranging from A_V=0.5–2 mag, or both.

There is a fairly wide range of derived knot masses spanning nearly 4 orders of magnitude, from a few times 10^5 $M_\odot$ to a few times 10^9 $M_\odot$. Individual globular clusters typically have masses of 10^5 $M_\odot$ (van den Bergh 1995), while for the Whitmore & Schweizer (1995) knots and/or clusters we derive masses (based on the BC95 models) ranging from $10^{4.5} - 10^{6.5}$ $M_\odot$. Even considering reddening effects, there are several galaxies that have knots which cannot be less than 10^8 $M_\odot$ (IRAS 12071−0444 and IRAS 15206+3342), and other galaxies have knots which cannot be less than 10^7 $M_\odot$. Figure 2.8 shows that the distribution of colors for any single object covers a wide range of color with a significantly smaller range in luminosity. This implies that the older knots are generally the most massive. If the spread in knot colors is primarily due to reddening, then the more massive knots must be preferentially more reddened than the less massive ones. This may be a selection effect: low-mass knots with extreme ages ($> 10^9$ yrs) or reddening are too faint at B to still be detected. However, it is the case that in the systems with many knots *there are no young, blue knots with estimated masses as large as the older, redder knots.* The above discussion of the correlation between color and radial distribution also extends to the knot masses: the most massive knots appear preferentially distributed closer to the galaxy nuclei.

2.6.3. Knot Sizes

There appears to be a considerable range in knot sizes. The resolution limit varied from around 10 to 30 pc, depending on the distance to the galaxy, and so a handful were unresolved, and it is not possible to rule out that these are stars. The remaining knots have an average $R_{\rm eff}$ of 65 pc, with the very largest being nearly 250 pc in radius. This is 2–3 times larger than the largest knots found in other systems, and many times larger than their mean knot radii: 18 pc in NGC 4038/9 (Whitmore & Schweizer 1995) and $\approx$ 10 pc in 9 starburst galaxies (Meurer et al. 1995). Schweizer derives a median upper limit of 5 pc for the clusters/knots in NGC 3921 (Schweizer et al. 1996) and Holtzman et al. (1996)

finds typically 2–10 pc. Our largest knots are nearly 50 times larger than these and the 1.5–5 pc half-light radii of globular clusters (van den Bergh et al. 1991).

2.6.4. Luminosity Function of Knots

Figure 2.10 presents the luminosity functions of the knots in Mrk 231 and Mrk 463, the two systems with the largest number of knots. These functions appear similar to the bright tail of the cluster/knot luminosity functions found in more nearby interacting galaxies such as NGC 4038/9 and NGC 7252. The data were binned into 0.5 mag bins, which are sufficiently large that photometric uncertainties should have little effect on the form of the distribution. Additionally, the putative "nuclei" have not been included, since they are believed to be of non-stellar origin (see §6.5). A lower magnitude limit cutoff of $M'_B = -12.5$ was chosen to ensure completeness in both systems. There is no direct evidence of a turnover in the knot luminosity function. This is not surprising: if we assume an age of 600 Myr for most of the knots, and a peak in the current galactic globular cluster distribution near $M_B \approx -8$, then the peak would occur in our (younger cluster) data near $M_B = -12$, which is just fainter than our completeness limit. This makes the assumption that all the clusters are the same age; Meurer (1995b) argues that the luminosity function of burst-model clusters with continuous cluster formation more closely resembles the power-law observed by Whitmore & Schweizer (1995).

A power-law fit of the form

$$d\Phi/dL'_B \propto {L'_B}^{-\alpha} \tag{2.2}$$

yields indices of $\alpha = -1.80 \pm 0.20$ and $\alpha = -1.63 \pm 0.11$ for Mrk 231 and Mrk 463, respectively. This index is surprisingly robust; moving the magnitude limit higher or removing the brightest objects seems to have little effect. This is similar to those found for compact knots/clusters in other systems: $\alpha = -1.78 \pm 0.05$ for NGC 4038/9 (Whitmore & Schweizer 1995), $\alpha = -2.1 \pm 0.3$ for NGC 3921 (Schweizer et al. 1996) and $\alpha = -1.64 \pm 0.07$ for NGC 1275 (Holtzman et al. 1996). However, combining the data for all the warm galaxies and choosing an appropriate limiting magnitude that ensures completeness in every system, we find $\alpha = -1.39 \pm 0.08$. This is appreciably more positive than that found in other systems, and is due to an overabundance of bright knots. This may be partly contaminated by confusion due to an inability to properly resolve the knots, as described below. Both Whitmore & Schweizer (1995) and Holtzman et al. (1996) report that their brightest clusters/knots have $M_V \approx -15.5$. We expect $(B\text{–}V) \leq 0.5$ based on BC95 for clusters of the ages determined by those authors, hence the brightest observed knots in Mrk 231 are similar to those seen in more nearby systems. However, there are knots in Mrk 463 which are nearly 2.5 mag brighter than this, and in the warm ULIGs as a whole there are many knots (see IRAS 15206+3342 in Figure 2.8) that are nearly 4 mag brighter than the brightest clusters/knots seen in other systems. Thus, there is a population of knots in the warm ULIGs which are nearly 100 times brighter at B than the brightest clusters/knots found in

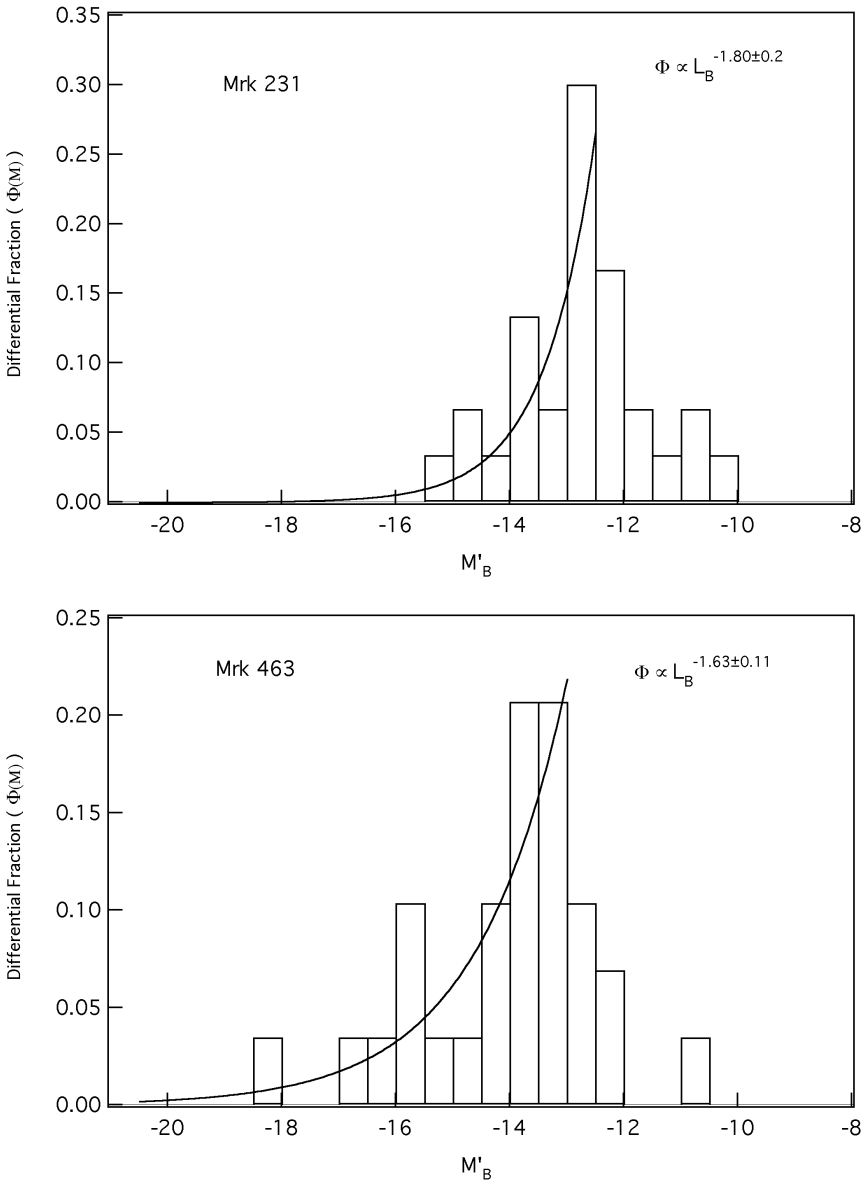

Fig. 2.10.— Luminosity functions for the knots (excluding putative nuclei) identified in Mrk 231 and Mrk 463.

much closer interacting galaxies. The distribution of these knots is noticeably skewed such that there is an overabundance of bright knots, compared to the knots in nearby galaxies. Also, with typical estimated knot masses ranging from 10^5 $M_\odot$ to as high as 10^9 $M_\odot$, they vary from 10–500 times more massive than that estimated for the clusters/knots observed in other galaxies. If the brightest observed knots are single physical entities, then they lie on the extreme tail of the cluster/knot distribution seen in other galaxies, which is apparently normally unpopulated.

A more likely explanation is that the knots are associations of many of the clusters seen in nearer systems. Meurer (1995b) notes that the typical intercluster separation in some starburst regions may be ≤ 18 pc, which is too small to resolve in our observations. We note that the seeing-limited resolution of NGC 4038/9 from the ground ($1''$= 90 pc for H_o = 75 km s^{-1}) is similar to the diffraction-limited resolution of the warm ULIGs that can be achieved with *HST* ($\approx$ 90 pc FWHM for IRAS 15206+3342). Ground-based images of the central regions of NGC 4038/9 at B show a loop-like structure with bright embedded knots (Rubin et al. 1970). These knots (excluding the regions of the galaxy nuclei) have mean radii of $\approx$ 75 pc (derived from the 45 pc HWHM spatial resolution ground-based data using the methods described above) , varying from nearly unresolved to as large as 150 pc. This is very similar to the range seen in the warm ULIGs. Whitmore & Schweizer (1995) have determined that each of these knots in NGC 4038/9 is actually composed of many smaller clusters. The mean number of clusters per knot is 13, and correspondingly the knot as a whole is on average 2.8 mag brighter than the individual clusters. Assuming that the clusters associate in knots in an essentially random way, then shifting the NGC 4038/9 luminosity function by this amount results in the brightest knots being equivalent to $M_B \approx -18.5$. This is only a magnitude difference from the brightest of the knots seen in the warm ULIGs. The derived masses of the warm ULIGs are still somewhat too large. While the lowest mass knots in the ULIGs can be explained as aggregates of tens of typical clusters with spatial distributions of the kind seen in NGC 4038/9, the most massive ULIG knots like those in IRAS 15206+3342, approach 10^9 $M_\odot$. This would require some 10^4 globular clusters or 50 of the most massive clusters observed by Whitmore & Schweizer (1995). This could be explained either by a very large reddening correction which would reduce the knot mass estimate by a factor of 15, by knots with larger total numbers of clusters due to a higher density than those seen in galaxies like NGC 4038/9, or by a preferential spatial distribution wherein extremely massive clusters tend to form together. The smaller luminosity function index (with corresponding overabundance of bright knots) may similarly be due either to an intrinsic difference in underlying cluster luminosity distribution between the ULIGs and nearby interacting and starburst systems, or to a preferential spatial grouping of clusters in knots (whereby the brightest knots have a disproportionate share of bright clusters, either because they are young or they are massive).

There is no observable relationship between knot size and mass; the intrinsic scatter in these two properties masks any expected $M \propto D^3$ relationship for constant density. There is a strong correlation between knot mass and color (and hence age). As was noted earlier, there are no young knots as massive as the older knots. By extension, there are no young (blue) knots as dense as the older (red) knots. The knot densities vary from $0.1 - 1000 M_\odot$

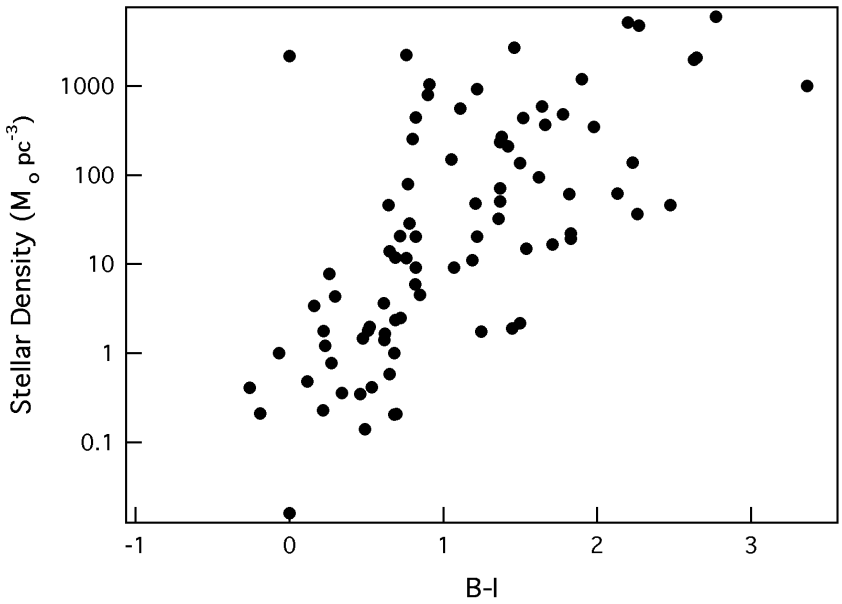

Fig. 2.11.— Mean stellar densities computed for all of the knots (excluding putative nuclei) identified in the warm ULIGs. There is a noticeable trend in that there are no blue knots with estimated masses or densities as large as the reddened knots.

pc^{-3} (Figure 2.11). This range is below that of globular clusters, which is perhaps not surprising if the knots are indeed composed of associations of clusters.

2.6.5. Contribution of Star-Forming Knots to Galaxy Luminosity

It is possible to address the relationship of the observed knots to the high bolometric luminosity of these systems. The mean integrated B magnitude of the observed knots in individual warm ULIGs in our sample is $M_B = -16.4$, ranging from -13.16 in IRAS 05189-2524 to a maximum of -20.4 for IRAS 15206+3342. A bolometric correction of 0.7 is derived from BC95 by assuming a starburst 600 Myr in age, consistent with the mean age previously derived on the basis of B–I colors. Thus, to generate the observed $\geq 10^{12}\ L_{\odot}$ in the far-infrared via the modeled starburst would require over 10^3 times more star formation than is presently observed in the B-band in all of the starburst knots combined. Even in the most extreme example, IRAS 15206+3342, the total starburst bolometric luminosity derived from the observed B-band luminosity falls short by more than a factor of 40. Under the assumption of a younger, more luminous starburst (with an accompanying increase in the bolometric correction), which could be allowed by invoking the maximum allowable extinction of $2\,A_V$, it would still require 100 times as much total star formation than currently exists in the observable knots in order to account for the observed far-infrared luminosity. Only in the case of IRAS 15206+3342 would it be possible to approach within a factor of 10 the necessary luminosity. This result assumes that the knot SED is well modeled at non-optical wavelengths by the spectral synthesis starburst model with uniform

dust extinction. Local, unresolved regions of high extinction internal to the knots will result in our underestimating the bolometric knot luminosity. Similar observations in the near-IR will be required to determine the near-IR excess, if any, of the knots.

Based on radio and far-infrared data, Condon et al. (1991) concluded that ULIGs contained ultraluminous starbursts in an environment so dense as to be optically thick even at 25 μm. A deeply embedded ultraluminous starburst composed of star-forming knots with properties (luminosities and radii) similar to those optically observed would have to be at least 600-1200 pc in diameter. This is sufficiently large that it should be detectable in our images and color maps as a large region with a considerable color gradient (B-$I \geq 4$) or no detectable optical luminosity at all, although it might be possible to mask the presence of such a region with a peculiar overlying stellar distribution at lower optical depth. Such a large color gradient is detected only in IRAS 08572+3915 and IRAS 15206+3342, but only in the latter does this region approach a kiloparsec in size. That such a large region is not generally observed in our data suggests that any ultraluminous starburst must be far more compact than the observed starburst knots, and that the spatially extended optical starburst is unlikely to share many properties with it. This is not surprising, considering that Condon et al. (1991) finds that ULIGs with $L_{\rm fir} > 10^{12}$ L$_\odot$ have radio emission typically dominated by compact radio sources. The three targets in the warm sample which he specifically examined have characteristic radio core sizes ranging from 0.1 to 80 pc in radius; additionally Mrk 1014 (Kellerman et al. 1994), PKS 1345+12 (Shaw et al. 1992) and Mrk 463 (Mazzarella et al. 1991) are also known to have compact cores. Based on the radio/far-infrared correlation it is argued that the starburst energy source is of a similar size. The minimum blackbody radii Condon derived from the far-infrared luminosities, which presumably are representative of the size of the enshrouding dust, are $0.15''$= 150 pc for IRAS 05189−2524, $0.09''$= 85 pc for IRAS 08572+3915, and $0.25''$= 200 pc for Mrk 231. A single observed optical knot is similar to or larger than the expected size of the starburst region, and is nearly one- tenth as large as the volume of the dust shroud. Although such an obscured region containing very extreme star-formation is not clearly seen, its detection is complicated by the uncertainties in coordinate precession and in the relationship between the radio and optical coordinate systems (Taff et al. 1990). These uncertainties prevent the registration of the radio and optical images with a precision greater than the typical spatial scale of the structure seen with *HST* ($\leq 0.3''$), making it impossible to pinpoint the location of the putative ultraluminous starburst. Thus, it is not possible to conclusively rule out an extremely compact, deeply embedded ultraluminous starburst, but it is possible to constrain its position and size, and to show that it cannot have properties similar to the starburst which we have actually been able to detect.

2.6.6. Putative Nuclei

Most of the warm ULIGs possess optical sources which are more luminous than the general knot population. The presence in these systems of optical emission lines typical of Seyferts suggests the presence of optically detectable active nuclei, thus providing an initial physical motivation for singling out these regions as putative "nuclei". The magnitudes, sizes, and positions of the putative nuclei were measured, and appear in Table 2.2 marked

with a dagger. In the cases of IRAS 08572+3915 (West), IRAS 12071−0444, Mrk 463 (East and West), and IRAS 15206+3342, it is not clear what constitutes an optical "nucleus"; in these cases, the brightest object seen at B was used. IRAS 05189−2524 lists both blue knots seen in the center of the galaxy. In most cases the putative nuclei are also more pointlike than the general knot population. In the apparent double nucleus systems (IRAS 08572+3915, PKS 1345+12, Mrk 463, and IRAS 15206+3342), one of these nuclei is more extended than the other and is likely to be the stellar core of one of the merging galaxies, as opposed to an active nucleus.

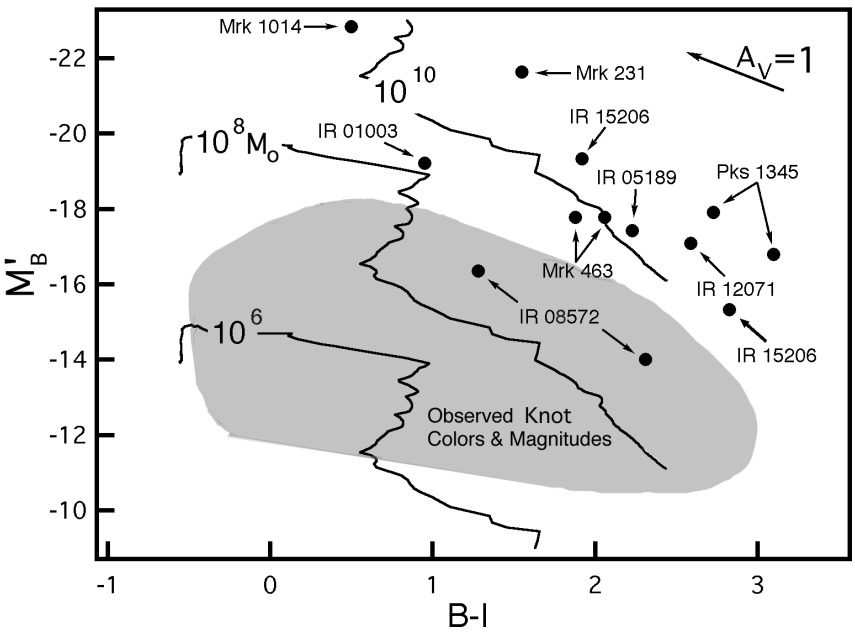

Fig. 2.12.— Color-magnitude diagram, M'_B vs. (B–I) , for the putative nuclei identified in each of the warm ULIGs. For comparison with the remaining knots the shaded region indicates the locus of points for the data used in Figure 2.8. Extinction ($A_V = 1$) is indicated by the dereddening vector at upper right. Mrk 1014, a PG QSO, is typical of the colors found in optically selected QSOs. The nuclei for the remaining warm ULIGs in our sample fall roughly along what can be described as a QSO reddening line.

Figure 2.12 shows a color-magnitude diagram for the nuclei with the same scaling as Figure 2.8. QSOs have $< B - I >= 1.2 \pm 0.3$ (Elvis et al. 1994) with a B magnitude classically defined as $M_B < -23$ (Schmidt & Green 1983). Mrk 1014, a classical optically selected QSO, falls roughly within this region, and represents a "zeropoint" in the color-magnitude diagram for "infrared-loud" classical QSOs. Three of the eight galaxies (Mrk 231, IRAS 15206+3342, and PKS 1345+12) have nuclei which fall very nearly on a reddening line extending through the data point for Mrk 1014 (see Figure 2.12), and which therefore have QSO-like luminosities ($L_{bol} > 10^{12}$ $L_\odot$), assuming they also have similar SEDs. In the case of Mrk 231, this is not surprising, since optically it appears much like a classical QSO. Morphologically, these nuclei share a common trait: all of them are very nearly radially symmetric in profile, which suggests that the underlying QSO nucleus is seen through a uniform foreground dust screen. We note that the reddening derived by Kim (1995) for PKS 1345+12, which has almost no knots and therefore has an optical spectrum

probably dominated by the nucleus, is $A_V = 3.8$. This is similar to the reddening derived by assuming a reddened QSO nucleus ($A_V = 3.5$).The nuclei of Mrk 463, IRAS 12071−0444, IRAS 05189−2524, and IRAS 08572+3915 all show clear signs of complex extinction and scattering. Since the nuclei were defined to be a single component at B, any true nucleus affected by variable extinction and scattering would be both fainter and bluer than it would if the extinction were uniform. This would move it to the lower left of the color-magnitude diagram, in the manner seen. IRAS 01003−2238 cannot be easily explained in this scenario, as it has a nearly stellar radial profile, yet falls considerably short of QSO-like luminosity. If the knots identified as nuclei are not actually QSO-like active nuclei but are instead compact, luminous starbursts, then their derived bolometric luminosity (excluding Mrk 1014 and Mrk 231) is only about 10^{10} $L_\odot$. Under the most extreme assumption that they are very young starbursts (1 Myr), their dereddened luminosities are as high as 2×10^{11} $L_\odot$.

We also note that the masses derived for the nuclei, under the assumption that they are a starburst of the sort modeled for the blue knots, are typically $> 10^{10}$ $M_\odot$. This seems unreasonably large in light of the measured radii. In the case of Mrk 231 and Mrk 1014, this would result in average stellar densities of nearly 10^7 and 2×10^5 $M_\odot \mathrm{pc}^{-3}$, respectively. Similarly, IRAS 01003−2238, IRAS 05189−2524, and PKS 1345+12 all have derived stellar densities $> 10^5$ $M_\odot \mathrm{pc}^{-3}$. Elliptical galaxy cores typically have masses as high as 10^{10} $M_\odot$, but they also have much smaller densities of $\approx 10^2 - 10^3$ $M_\odot \mathrm{pc}^{-3}$. Similarly, although nuclear star clusters in galaxy cores may have very high densities ($> 10^5$ $M_\odot \mathrm{pc}^{-3}$), they have smaller masses ranging from $10^6 - 10^8$ $M_\odot$ (Lauer 1989). The remainder of the warm ULIG nuclei would require stellar densities of 10^3 $M_\odot \mathrm{pc}^{-3}$ and higher, which makes them denser than all but 7 of the knots and at the high end of elliptical core densities. The only exception is the eastern nucleus of IRAS 08572+3915, whose luminosity and color are consistent with a typical galaxy core, which it strongly resembles (see §2.8).

Until high spatial resolution spectra are obtained, it will not be possible to determine whether the observed optical Seyfert activity is related to the putative nuclei that have been identified here. An interesting prediction of Condon et al. (1991) is that the observed broad optical emission line regions are a result of starburst/superwind activity and must be extended on size scales larger than the minimum far-infrared size (≥ 0.25 arcseconds). This minimum size is larger than the observed sizes of the putative nuclei. If the optical emission features are spatially coincident with and have size scales similar to the putative nuclei, then this may be strongly suggestive of a true active nucleus, rather than a spatially extended wind.

2.6.7. Relationship to optical QSOs

One of the original motivations for studying our complete sample of warm ULIGs was that they might plausibly represent an important "transition stage" in the evolution of cooler ULIGs into optically selected QSOs. While the connection between the cool and warm ULIG samples seems fairly secure due the fact that ground-based observations have clearly shown that both samples are dominated by molecular gas-rich mergers (c.f. review by Sanders & Mirabel 1996), the connection between warm ULIGs and optically selected

QSOs is much less secure. This has been due in large part to a lack of sensitive high-resolution observations of QSO hosts coupled with the fact that the merger features, which are already hard to detect in many of the warm ULIGs, may fade to undetectability by the time these objects emerge as optical QSOs.

HST images of the three objects in our complete sample of 12 warm ULIGs that were not observed in our Cycle 5 GO program have either recently been published or can be found in the *HST* archive. These three have the smallest far-infrared/submillimeter excess of the 12 warm ULIGs and all of them exhibit Seyfert 1 optical spectra. Of the three, I Zw 1 and 3C273 are well-known optical QSOs, while *IRAS* 07598+6508 has a Seyfert 1 optical spectrum which has led it to be featured as an "infrared quasar" in several recent publications (e.g. Low et al. 1988). These three (along with Mrk 1014) are both "warm" ULIGs and optical QSOs, and represent the clearest transition between the two. Although the exposure times for these three sources were generally shorter than those used in our Cycle 5 observations and different filters were used, it is still instructive to compare their properties with what has been described above for the other nine sources observed by us in our complete sample. In addition to the *HST* images, Figure 2.3 also presents near-truecolor optical imaging obtained with the UH 2.2m telescope for I Zw 1 and IRAS 07598+6508. This data was obtained in the manner described in Chapter 4, and is discussed in Chapters 3 and 5. In particular, *IRAS* 07598+6508 and I Zw 1 have several properties in common with our data, including luminous knots and arm-like circumnuclear features, as well as luminous hosts, although 3C273, other than its jet and the presence of a luminous host, has yet to reveal knots or other large scale features.

Additional recently published *HST* images of other nearby optically selected QSOs (Bahcall et al. 1997) further strengthen the evolutionary connection between warm ULIGs and QSOs. In particular, "arcs", "loops", and "chains of emission nebulae" seen in some of the 20 QSO hosts imaged by Bahcall et al. (e.g. PKS 2349-014, PG 0316-346), the double nuclei and/or partially merged disks seen in a few objects (e.g. PG 1012+008), and the "knots" of emission close to the QSO nucleus seen in the majority of the sample of QSOs, all suggest a continuity of morphological properties with our sample of warm ULIGs. Further evidence for a connection comes from the fact that the mean absolute magnitude at both r-band and K-band of the host galaxies in the two samples appears to be nearly equal (e.g. Sanders & Mirabel 1996). Additional *HST* data, in particular spectroscopy of the emission knots discovered in both samples, may provide sufficient evidence to show whether or not the features observed in QSO hosts are indeed aged versions of those observed in the warm ULIGs.

2.7. Conclusions

From our new *HST* WFPC2 images of a nearly complete sample of warm ULIGs we draw the following conclusions:

1. Eight of the nine objects imaged show evidence that they are advanced merger systems. Three have clearly identified double nuclei, while an additional five objects show

circumnuclear features that connect to larger scale tidal tails, fans and/or bridges that were previously identified in lower resolution ground-based images.

2. A population of compact, blue star-forming knots has been discovered in all of the warm ULIGs. These knots appear similar in radius and luminosity to the most luminous knots found in ground-based images of nearby merger LIGs such as NGC 4038/9 and Mrk 171. *HST* imaging shows that the luminous knots in these nearby systems break up into groups of several massive star-clusters that are assumed to be proto globular clusters. However, the warm ULIGs are too distant to be similarly resolved with *HST*.

3. The masses of the star-forming knots in the warm ULIGs are estimated to be in the range $10^5 - 10^9\ M_\odot$. There is some evidence that the warm ULIGs have an overabundance of luminous (massive) knots compared to other nearby, less luminous merger systems. Their (extinction uncorrected) colors yield a median upper age for the starburst knots in a given system of $\sim 3 \times 10^8$ yrs. Regardless of reddening effects, several of the systems have knots which must be very young ($\approx 0.5 - 1 \times 10^7$ yrs). These young, blue knots are often found at larger radii, whereas those found closer to the centers are often redder. This color difference may be due either to radially variable extinction or knot age.

4. The combined total luminosity of the knots identified in our *HST* images of each system is generally too small by factors of 100 or more to account for the total observed far-infrared luminosity. If the far-infrared luminosity were the result of starburst activity in a large population of hidden knots similar to the ones detected optically, they would need to occupy a volume so large that it should be detectable in our observations. Any ultraluminous starburst is therefore likely to be very different from the starburst that is detected optically. Most likely it will be much more luminous, massive, and dense than the identified starbursts knots.

5. We have identified in each system one or more candidate knots as putative nuclei. These nuclei appear to have properties substantially different from the starburst knots. Their luminosities and colors would only be consistent with starburst models with an extremely biased high-mass IMF, and even then their relatively small apparent physical sizes would imply extraordinarily high stellar densities. Nearly all of these knots have colors and luminosities which can be more easily explained as reddened AGN. High spatial resolution spectroscopy with *HST* could help prove that these extremely luminous knots are indeed the active nuclei which dominate the ground-based optical spectra of these objects.

We would like to thank Dong-Chan Kim for lending us his ground-based images and spectra of the ULIGs, John Hibbard for his images of NGC 4038/9, Alan Stockton for some useful comments on our presentation, and Stephane Charlot for use of his GISSEL spectral synthesis libraries. We also thank an anonymous referee for his or her comments that have helped us clarify our results. DBS and JAS were supported in part by NASA through grant number GO-05982, and NASA grant NAGW-3938. WDV acknowledges support in the form of a Fellowship from the Beatrice Watson Parrent Foundation. SV gratefully acknowledges the financial support of NASA through grant number HF- 1039.01-92A awarded by the Space Telescope Science Institute which is operated by the AURA, Inc. for NASA under

contract No. NAS5-26555. This work has made use of the NASA/IPAC Extragalactic Database (NED) which is operated by the Jet Propulsion Laboratory, California Institute of Technology, under contract with the National Aeronautics and Space Administration, and the Digitized Sky Survey (DSS), which was produced at the Space Telescope Science Institute under U.S. Government grant NAGW-2166. The DSS was produced using photographic data obtained with the Oschin Schmidt Telescope on Palomar Mountain, operated by the California Institute of Technology, and the UK Schmidt Telescope, which was operated by the Royal Observatory Edinburgh and the Anglo-Australian Observatory.

2.8. Notes on Individual Objects

The following notes on individual objects are added here to further help understand the relationship of the new *HST* imaging data (e.g. Figures 2.2 – 2.4) to previous ground-based observations (e.g. Figure 1), as well as provide additional information on features that can be identified in the digital images (available from the *HST* archive), but which may not be so obvious in the hardcopy figures.

I Zw 1 — Optical images of I Zw 1 that exist in the *HST* archive reveal spiral arm-like features in the nuclear regions of the surrounding host galaxy, but these images are generally not deep enough to easily compare with our data. We have obtained ground-based optical images using tip-tilt optics on the UH 2.2m telescope (Surace et al. 1997) which show more clearly the presence of features such as those seen in our *HST* images of Mrk 231, but there is no other obvious large-scale evidence of tidal structure. Such spiral structure has been imaged previously (Sargent 1970, Bothun et al. 1984), as has a small companion galaxy which may be tidally interacting with host galaxy of I Zw 1 itself (Stockton 1982).

IRAS 01003−2238 — This galaxy is the most pointlike of any in the sample. The only easily identifiable circumnuclear feature is a chain of knots extending from SE to NW, less than 1″ away from the apparent nucleus. These knots are embedded in a plateau of extended emission. IRAS 01003−2238 is known to be an unusually powerful Wolf-Rayet galaxy (Armus *et al.* 1988), which is consistent with the young ages that can be assigned to the extremely blue knots.

Mrk 1014 = PG 0157+001 — An optically identified QSO (Schmidt & Green 1983) with a strong infrared excess (e.g. Sanders, Scoville & Soifer 1988) and described in MacKenty & Stockton (1984). The WFPC2 images of the underlying host galaxy is dominated by what appears to be a prominent tidal arm which curves toward the East (a total length of 60 kpc), and a weaker counterarm which extends from the southwest and then curves to the North. There are two extremely blue knots, as well as several linear structures within 1 kpc of the QSO nucleus. Several other knots are found in the outer regions of the host.

IRAS 05189−2524 — Optically classified as a Seyfert 2 (Veilleux et al. 1995). The *HST* images clearly show that the plateau of emission seen in ground-based images to the southeast of the nucleus is resolved into at least 2 loops $\approx$ 15 kpc in total length at right angles to each other; there additionally appear to be loop or shell-like structures at slightly fainter levels. Although not visible here, careful analysis of the PC and adjoining WFC frames reveals the two "hornlike" tidal features to the north seen in the groundbased image (see Figure 2.1), and indicates that they are actually the high surface brightness base of a complete loop. There is no obvious connecting feature in the *HST* images which would connect the inner disk structure to the counter tidal tail previously identified by Sanders et al. (1988a) which extends to the South from the western edge of the disk.

IRAS 07598+6508 — The *HST B*-band image of *IRAS* 07598+6508 obtained by Boyce et al. (1997) clearly shows several 'chains' of 'knots' surrounding the prominent optical nucleus, similar to the features seen by us in Mrk 231. In addition, large-scale tidal features have been detected in deep ground-based optical images obtained at the UH 2.2m telescope

(A. Stockton, private communication 1997), leading us to describe this object as a clear case of an advanced merger.

IRAS 08572+3915 — The new *HST* images clearly show the interaction of two spiral galaxies which have not yet merged. The eastern nucleus is morphologically similar to a spiral bulge from which a tidal tail 30 kpc in length emerges to the East and then wraps entirely around the system to the NW. Another tidal tail at least 15 kpc in length emerges from the western nucleus and extends directly north. A bridge of material is seen connecting the two nuclei. Unlike the nondescript eastern nucleus for which we find no published reference as to spectral type, the LINER western nucleus (Veilleux et al. 1995) is morphologically complex, with several bright blue knots as well as highly reddened regions. This disparity in optical appearance is not surprising and probably reflects very real differences in the environments of these two nuclei. This is supported by studies at 3.4μm (Zhou *et al.* 1993), 10μm (Sanders et al. 1988b), and 1.66 Ghz (Sopp & Alexander 1991) which indicate that most of the bolometric luminosity of this object originates in the northwest nucleus.

IRAS 12071−0444 — Sanders et al. (1988b) classify this galaxy on the basis of optical spectra as a Seyfert 2. In addition Veilleux, Sanders & Kim (1997) find strong evidence for a 'buried QSO' on the basis of detection of [Si VI] emission in the near infrared. The *HST* images show two tidal tails extending to the North and South. The southern tail loops back around to the northeast (although it is difficult to see in Figure 2.2) and appears to almost return to the nucleus, a total distance of 60 kpc; our *HST* images are not deep enough to tell if it reconnects. The inner 5 kpc region has a high surface brightness and is chaotic in appearance. A central, highly reddened compact source dominates this region. A string of blue knots 2.5 kpc in length runs to the West of the central source.

3C273 — *HST* images of the radio-loud QSO 3C273 (Bahcall et al. 1997), as well as previous ground-based images by us and others (Röser & Meisenheimer 1991, McLeod & Rieke 1994), clearly show an optical jet extending to the southwest from the optical nucleus and reveal the presence of a fairly luminous host galaxy. However, there is no obvious evidence of a previous interaction/merger, and the extreme brightness of the nucleus as well as the relatively short *HST* exposure times make the identification of any circumnuclear knots that might be present extremely difficult.

Mrk 231 = UGC 8058 — This optically classified Seyfert 1 galaxy is the most luminous object in the local ($z < 0.1$) Universe (Sanders et al. 1988a). The *HST* data clearly show a diffuse linear structure to the NW of the Seyfert nucleus. The central kiloparsec shows the compact ($R_{\rm eff} < 20\,{\rm pc}$) Seyfert nucleus surrounded by a system of concentric spiral features similar to spiral arms. However, these features appear to be off-center and cross each other on the eastern side where they then connect to the outer tidal features, allowing one to trace the outer tidal arms all the way into the central kpc. Armus et al. (1994) claimed detection of a second nucleus in the near-infrared lying 3″ to the South. However, the new *HST* images show this feature to be a dense arc of star forming knots with a total estimated luminosity compatible with the extreme luminosities cited in that paper. Most of the compact blue knots detected by *HST* occur either in this arc or in the "plateau" to

the West (Hutchings & Neff 1987). The galaxy itself has twin tidal tails extending on the eastern side approximately 34 kpc to the north and south.

PKS 1345+12 = 4C12.50 — The western nucleus is optically classified as a Seyfert 2 (Gilmore & Shaw 1986). More recently, Veilleux et al. (1997) have reported the detection of very broad Paα emission in the near infrared indicating the likely presence of a 'buried QSO'. The system also contains a compact gigahertz-peaked, compact-steep-spectrum radio source with a characteristic double-lobed shape in VLBI images which Shaw et al. (1992) associates with the eastern nucleus [although Stanghellini et al. (1993) associates it with the western nucleus !]. Shaw et al (1992) also interpret this object as a merger between a spiral Seyfert galaxy and a powerful radio elliptical galaxy. The extremely red color of this source (B-$I \approx 3.5$) has been attributed to dust obscuration (Smith & Heckman 1989). Our images show two radially symmetric nuclei with only a few additional compact blue knots. The western nucleus shows a slightly asymmetric color profile, whereas the eastern nucleus shows almost no color gradient at all.

Mrk 463 = UGC 8850 — The eastern nucleus is optically classified as a Seyfert 1 (Miller & Goodrich 1990). Associated with this nucleus are a radio luminosity density, aligned radio structures, and optical/near-infrared colors which have been interpreted by Mazzarella et al. (1991) as representative of a dusty QSO. An optical "jet" seen by Uomoto et al. (1993) resembles in our data an "X"-shaped structure dominated by a central peak. Tremonti et al. (1996) report that the bright object to its north is highly polarized and reflects a hidden Seyfert 1 nucleus lying in this "X"-structure. This is confirmed by high resolution near-infrared observations (Surace et al. 1997) which indicate that the near-infrared luminosity is centered on the "X". The entire eastern nucleus lies on a plateau of extended emission in which there are several bright knots. The western nucleus is optically classified as a Seyfert 2. There seem to be two principal components to the western nucleus: a dominant source which is distinctly elongated in the E-W direction, and a more compact, very blue source 1″ to its West. Also in this region are two arcs of star-forming knots to the North and South of the two dominant components of the western nucleus. Both of these arcs form a sharp edge to a fan of emission centered on the dominant nuclear components. Overall, the system has two faint tails extending SE and SW approximately 54 kpc each (Hutchings & Neff 1989).

IRAS 15206+3342 — Sanders et al. (1988b) classify this galaxy as a Seyfert 2 on the basis of optical spectra, although Veilleux et al. (1997) find it to be HII-like. The inner few kiloparsecs are characterized by many chains of knots, some of which are extremely luminous. Several of the knots have luminosities and colors compatible with being extremely massive starbursts, but there are two which make good candidates for being nuclei. Additional spectroscopic observations will be needed to identify unambiguously the source of the putative Seyfert activity.

REFERENCES

Armus, L., Heckman, T.M., & Miley, G.K. 1988, ApJ, 326, 45

Armus, L., Surace, J.A., Soifer, B.T., Matthews, K., Graham, J.R., & Larkin, J.E. 1994, AJ, 108, 76

Bahcall, J.N., Kirhakos, S., Saxe, D.H., & Schneider, D.P. 1997, ApJ, in press

Bahcall, J.N., Kirhakos, S., & Schneider, D.P. 1995, ApJ, 450, 486

Bothun, G.D., Heckman, T.M., Schommer, R.A., & Balick, B. 1984, AJ, 89, 1293

Boyce, P.J., et al. 1997, ApJ, in press

Bruzual, G., & Charlot, S. 1993, ApJ, 405, 538

Clements, D.L., Sutherland, W.J., McMahon, R.G., & Saunders, W. 1996, MNRAS, 279, 477

Condon, J.J., Huang, Z-P., Yin, Q.F., & Thuan, T.X. 1991, ApJ, 378, 65

Elvis, M., et al. 1994, ApJS, 95, 1

Gilmore, G. F., & Shaw, M. A. 1986, Nature, 321, 750

Holtzman, J., et al. 1995a, PASP, 107, 156

Holtzman, J., et al. 1995b, PASP, 107, 1065

Holtzman, J., et al. 1996, AJ, 112, 416

Hutchings, J.B., & Neff, S.G. 1987, AJ, 93, 14

Hutchings, J.B., & Neff, S.G. 1989, AJ, 97, 1306

Kellerman, K., Sramek, R., Schmidt, M., Green, R., & Shaffer. D. 1994, AJ, 108, 1163

Kim, D.-C. 1995, PhD Thesis, Univeristy of Hawaii

Kim, D.-C., & Sanders, D. B. 1997, ApJ, submitted

Krist, J. 1994, The Tiny Tim User's Manual, (Baltimore: STScI)

Lauer, T. 1989, Cores and Nuclear Star Clusters in Galaxies (Cambridge: Cambridge University Press), 3

Leitherer, C. 1996, in From Stars to Galaxies, eds. C. Leitherer, U. Fritze-vonAlvensleben, J. Huchra (San Francisco: ASP), 373

Low, F. J., Huchra, J. P., Kleinmann, S. G., & Cutri, R. M. 1988, ApJ, 287, 95

Lu, N.Y., Hoffman, G.L., Groff, T., Roos, T., & Lamphier, C. 1993, ApJS, 88, 383

MacKenty, J.W., & Stockton, A. 1984, ApJ, 283, 64

Mazzarella, J., Gaume, R., Soifer, B.T., et al, 1991, AJ, 102, 1241

McLeod, KK., & Rieke, G.H., 1994, ApJ, 431, 137

Melnick, J., & Mirabel, I.F. 1990, A&A, 231, L9

Meurer, G., Heckman, T., Leitherer, C., Kinney, A., Robert, C., & Garnett, D. 1995, ApJ, 110, 2665

Meurer, G. 1995b Nature, 375, 742

Miller, J.S., & Goodrich, R.W. 1990, ApJ, 355, 456

Murphy, T., Armus, L., Matthews, K., et al., 1996, AJ, 111, 1025

Peebles, J. Principles of Physical Cosmology, 1993 (Princeton: Princeton Univ. Press)

Perault, M. 1987, Ph.D. Thesis, University of Paris

Röser, H-J., & Meisenheimer, K., 1991, A&A, 252, 458

Rubin, V., Ford, W., & D'Odorico, S. 1970, ApJ, 160, 801

Sanders, D.B., Scoville, N.Z., & Soifer, B. T. 1988, ApJ, 335, 1

Sanders, D.B., & Mirabel, I.F. 1996, ARA&A, 34, 749

Sanders, D.B., Soifer, B.T., Elias, J.H., et al., 1988a, ApJ, 325, 74

Sanders, D.B., Soifer, B.T., Elias, J.H., Neugebauer, G., & Matthews, K. 1988b, ApJ, 328, 35

Sapar, A., & Kuusik, I. 1978, Publ. Tartu. Astrophys. Obs., 46, 71

Sargent, W. 1970, ApJ, 160, 405

Schmidt, M. & Green, R.F. 1983, ApJ, 269, 352

Schweizer, F., Miller, B.M., Whitmore, B.C., & Fall, S.M. 1996, AJ, 112, 1839

Shaw, M.A., Tzioumis, A.K., & Pedlar, A. 1992, MNRAS, 256, 6

Smith, E. P., & Heckman, T. M. 1989, ApJS, 69, 365

Soifer, B.T., Boehmer, L., Neugebauer, G., & Sanders, D.B. 1989, ApJ, 98, 766

Soifer, B.T., Rowan-Robinson, M., Houck, J.R., de Jong, T., Neugebauer, G., et al., 1984, ApJ, 278, L71

Sopp, H.M. & Alexander, P. 1991, MNRAS, 251, 112

Stanghellini, C., O'Dea, C.P., Baum, S.A., & Laurikainen, E., 1993, ApJS, 88, 1

Stockton, A. 1982, ApJ, 257, 33

Surace, J.A., et al. 1997, in preparation

Taff, L.G., Lattanzi, M.G., Bucciarelli, B. Gilmozzi, R., et al. 1990, ApJ, 353, L45

Tremonti, C.A., Uomoto, A., Antonucci, R., Tsvetanov, Z., Ford, H.C., & Kriss, G.A. 1996, BAAS, 28, 1287

Uomoto, A., Caganoff, S., Ford, H.C., et al., 1993, AJ, 105, 1308

Veilleux, S., Kim, D-C., Sanders, D.B., Mazzarella, J.M., & Soifer, B.T. 1995, ApJS, 98, 171

Veilleux, S., Sanders, D.B., & Kim, D-C. 1997, ApJ, 484, 92

van den Bergh, S. 1995, Nature, 374, 215

van den Bergh, S., Morbey, C., & Pazder, J. 1991, ApJ, 375, 594

Whitmore, B. 1996, Photometry with the WFPC2 (Baltimore: STSCI)

Whitmore, B., & Schwiezer, F. 1995, AJ, 109, 960

Zhou, S., Wynn-Williams, C.G., & Sanders, D.B. 1993, ApJ, 409, 149

Chapter 3

High Resolution Tip/Tilt Near-Infrared Imaging of Warm Ultraluminous Infrared Galaxies[1]

ABSTRACT

We present high spatial resolution (FWHM $\approx$ 0.3–0.5″) H (1.6μm) and K′(2.1μm) images of a complete sample (12) of ultraluminous infrared galaxies (ULIGs) chosen to have "warm" mid-infrared colors ($f_{25}/f_{60} > 0.2$) known to be characteristic of active galaxies. The extended underlying galaxy is detected in each system at H and K′, as are tidal features and many of the star forming knots seen at optical wavelengths. While some of these knots have a considerable near-infrared excess, we show that they are likely to have bolometric luminosities more similar to that of the extended starbursts with similar optical morphology seen in less far-infrared luminous interacting systems. We find that each ULIG has increasing contributions at long wavelengths by a very compact source which we identify as an active galactic nucleus (AGN). We show that the optical/near-infrared colors of these putative nuclei are much more extreme than the most active starburst IRAS galaxies, yet are identical to "far-infrared loud" quasars which are in turn similar to optical quasars combined with large quantities of hot ($\approx$800 K) dust. Half of the ULIGs have nuclei with dereddened near-infrared luminosities comparable to those of QSOs, while the other half have dereddened luminosities more similar to Seyferts, although this may be an effect of patchy extinction and scattering.

3.1. Introduction

One of the most important results from the *Infrared Astronomical Satellite*[2] (*IRAS*) all-sky survey was the discovery of a significant population of galaxies that emit the bulk of their luminosity in the far-infrared (e.g. Soifer et al. 1984). Studies of the properties of these "infrared galaxies" showed systematic trends coupled to the total far-infrared luminosity; more luminous systems were more likely to appear to be merger remnants or interacting pairs, and were more likely to possess AGN- like emission line features. A more complete review of the properties of luminous infrared galaxies can be found in Sanders & Mirabel (1996). Much recent attention has been focused on ultraluminous infrared galaxies (ULIGs),

[1]Chapter 3 has been submitted to ApJ as "High Resolution Tip/Tilt Near-Infrared Imaging of Warm Ultraluminous Infrared Galaxies" by Surace, J.A. & Sanders, D.B.

[2]The Infrared Astronomical Satellite was developed and operated by the US National Aeronautics and Space Administration (NASA), the Netherlands Agency for Aerospace Programs (NIVR), and the UK Science and Engineering Research Council (SERC).

objects with infrared luminosities, $L_{\rm ir}$[3], greater than 10^{12} $L_{\odot}$, which corresponds to the bolometric luminosity of QSOs (i.e. $M_{\rm B} < -22.1$: Schmidt & Green 1983). Multiwavelength observations of a complete sample of 10 ULIGs led Sanders et al. (1988a) to suggest that these objects might plausibly represent the initial dust- enshrouded stage in the evolution of optically selected QSOs, and that the majority, if not all QSOs may begin their lives in such an intense infrared phase.

An important subset of ULIGs are those objects with "warm" mid-infrared colors ($f_{25}/f_{60} > 0.2$). [4] These warm objects, which represent $\sim$20–25 % of the total population of ULIGs discovered by *IRAS*, appear to represent a critical transition stage in the evolution of the larger population of "cool" ULIGs into optical QSOs. Studies of several small but complete samples of warm ULIGs have shown that many of these objects have a point-like optical appearance on the Palomar Sky Survey and that they exhibit broad (i.e. Seyfert 1) optical emission lines, characteristics that have led them to be referred to as "infrared QSOs" (e.g. Low et al. 1988, Sanders et al. 1988b). Particularly useful for study has been the complete flux-limited sample of 12 warm ULIGs from the survey of Sanders et al. (1988b). As the nearest and brightest warm ULIGs, these objects are the most amenable to studies at other wavelengths.

Surace et al. (1998; Paper I; Chapter 2) examined the warm ULIG sample of Sanders (1988b) using *HST*/WFPC2 and found that nearly all were advanced merger remnants with extremely complex optical morphologies in their central few kiloparsecs. These central regions were dominated by knots of powerful star formation plus one or two compact emission sources whose optical colors, luminosities, and physical sizes appeared similar to reddened quasars, and were therefore presumed to be putative active galactic nuclei (AGN). Unfortunately, the unknown effects of extinction on small spatial scales resulted in considerable uncertainty in the properties of the star-forming knots and putative AGN, and optical colors alone could not effectively differentiate between the two phenomena.

Extending wavelength coverage to the near-infrared offers several potential improvements over previous studies at optical wavelengths. The most important of these is lowered sensitivity to extinction effects; the extinction at 2.1μm is only one-tenth that at 0.5 μm. In these objects, which are expected to have some regions of significant dust obscuration, the near-infrared offers a much greater opportunity to detect additional emission regions which may have been so heavily obscured as to have been invisible at optical wavelengths. While some recent studies of ULIGs have found that their central regions are opaque even at near-infrared wavelengths (e.g. Goldader et al. 1995), these studies have concentrated primarily on "cooler" systems which are likely to be more heavily obscured. The presence of optical Seyfert lines in the warm ULIG sample would seem to indicate that extinction is much less severe than in the cooler ULIGs. Also, determination

---

[3] $L_{\rm ir} \equiv L(8 - -1000\mu{\rm m})$ is computed using the flux in all four *IRAS* bands according to the prescription given in Perault (1987); see also Sanders & Mirabel (1996). Throughout this paper we use $H_{\circ} = 75$ km s^{-1}Mpc^{-1}, $q_{\circ} = 0.5$ (unless otherwise noted).

[4] The quantities f_{12}, f_{25}, f_{60}, and f_{100} represent the *IRAS* flux densities in Jy at 12 μm, 25 μm, 60 μm, and 100 μm respectively.

of the near-infrared spectral energy distribution (SED) of the optically observed small-scale structure allows a disentanglement of the effects of extinction, star-formation, and AGN activity. Color information at longer wavelengths is particularly important since this is where normal stellar populations and AGN have very different colors, plus thermal emission from hot dust first becomes detectable longward of H-band.

High resolution observations greatly increase point source sensitivity; in the background limited case doubling the spatial resolution is twice as effective as doubling the telescope aperture. The increased point source sensitivity in turn enhances the detectability of features such as star-forming knots. The distributed spatial morphology of these star-forming knots allows them to be distinguished from AGN. By identifying these star-forming regions (some of which may be hidden from optical detection by dust extinction) and characterizing their SEDs in the near-infrared, a more accurate assessment of the contribution of star-formation to the total ULIG energy budget may be obtained. Unfortunately, the characteristic separation of the optical structure is too small ($\approx$0.2–0.4″) to be resolved by conventional means even at the best of ground-based sites. However, recent advances in adaptive optics (AO) techniques and deconvolution, which compensate for local and atmospheric image distortions, allow this kind of resolution to be achieved from the ground. We report here the results of such a high spatial resolution near-infrared imaging study using a low-order tip/tilt system.

3.2. Data

The data were taken between October, 1995 and May, 1997 using the UH 2.2m telescope on Mauna Kea. The observations were made at H (1.6μm) and K′(2.1μm). The H filter was chosen since it is the longest wavelength filter which is still relatively unaffected by thermal dust emission; dust hot enough to emit significantly at this wavelength would be above the dust sublimation temperature. The choice of the University of Hawaii K′ filter over the K filter was motivated by the lower thermal sky background in the K′-band (Wainscoat & Cowie 1992), thereby improving the detectability of faint features as star-forming knots. Throughout this paper we exclusively refer to K′. Comparison to work by other authors is made using the conversions (Wainscoat & Cowie 1992):

$$K - K' = 0.18\ (H - K) \tag{3.1}$$

$$(H - K') = 0.82\ (H - K) \tag{3.2}$$

A fast tip/tilt f/31 secondary, capable of correcting for image motion at a rate of 10–100 Hz, was used to stabilize the images against both correlated seeing effects such as telescope wind shake as well as some atmospheric seeing (Jim 1995). The detector was the QUIRC 1024x1024 camera utilizing a HAWAII HgCdTe array (Hodapp et al. 1996). At the f/31 focus, it's 0.06″/pixel scale ideally samples the focal plane under diffraction-limited conditions (0.21″at 2.1μm). Because of the camera's relatively large field of view

($\approx 61''$), it was possible to dither and subtract successive exposures in order to correct for the sky background, thus doubling the telescope efficiency. Pixel-pixel response variations were corrected by dividing by high S/N normalized dome flats. The dithered frames were registered using the centroids of the background stars and galaxies in the frames, or in some cases with cross- correlation using the extended features in the ULIGs themselves. The images were scaled by their exposure times and any residual background was subtracted. The images were then combined using a clipping algorithm that rejects high-sigma outliers and weights the images by their exposure times. Typical total exposure times were 30–120 minutes per target per filter.

The data were flux calibrated by observing several photometric standards (Elias et al. 1982, Casali & Hawarden 1992) throughout the night at the same airmass as the targets. In most cases the nights were photometric. For those where they were not, we calibrated the data using either earlier photometric observations at the Palomar 5m (taken with a 58x62 InSb array between October 1988 and March 1992) or the aperture photometry of Neugebauer et al. (1987) and Sanders (1988a). The K$'$ filter was calibrated using the same infrared standards and the above $K-K'$ correction.

The point spread function (PSF) was calibrated in most cases by using actual stars in the final combined image. Point sources were identified by eye and the DAOPHOT package in IRAF was then used to construct a model PSF for each image. This models consists of a theoretical elliptical gaussian core and a "correction image" representing the observed variations from the theoretical model. In a few cases there were no suitable stars in the vicinity of the target. In these cases, a PSF was obtained by interleaving observations of the ULIG and nearby bright stars by using the same guide star (and by extension, nearly the same degree of image stabilization) for both sets of observations. Although the derived PSF is not necessarily identical to that of the ULIG data, there is evidence that the atmospheric variability on Mauna Kea is stable on timescales of tens of minutes (Ramsay et al. 1992), comparable to the interleave times used. Typical of most AO systems, the observed PSF consists of two components: a diffraction-limited core and an extended halo approximately 0.5–1$''$ in diameter, equivalent to the uncorrected PSF width (Figure 3.1). This extended halo is due to scattered light in second- order and higher distortion modes, which cannot be compensated for by a tip/tilt-type system (Beckers 1993). Although on a small telescope (such as the UH 2.2m) tip/tilt is capable of delivering nearly all the gain in resolving power that can be achieved with higher-order systems, this uncompensated extended halo can still contain a significant fraction ($\approx 30\%$) of the total flux, thus complicating photometry. All photometry was performed using aperture photometry in circular or polygonal apertures, depending on the shape of the observed structure. Aperture corrections were derived from the observed PSF.

In several cases, deconvolution was applied. This was particularly necessary in those cases where structure was seen on very small spatial scales ($< 0.5''$). Deconvolution is able to increase the contrast and detectability of small-scale structure and improve the photometry by eliminating confusion resulting from the extended scattered halo. We chose to employ the Richardson-Lucy algorithm (R-L) implemented in IRAF. The algorithm was allowed to iterate 25 times. As a check on the validity of the deconvolved structure, we

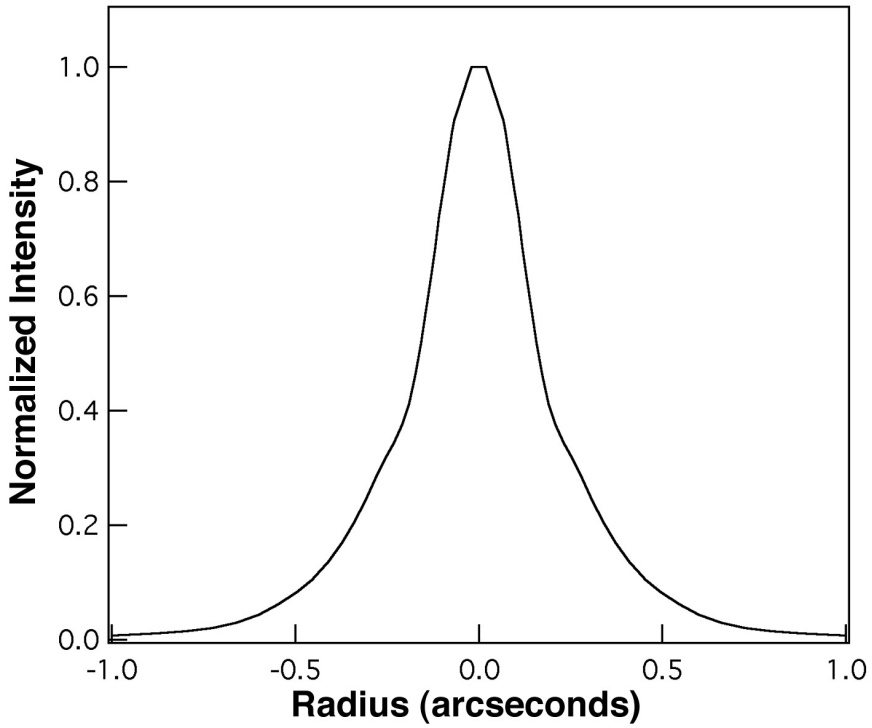

Fig. 3.1.— Typical radial profile of the point spread function at K′ achievable with fast tip/tilt guiding. Note that the central core is nearly diffraction-limited in width, but that a considerable amount of power remains in the wings due to higher-order scattering modes.

compared the deconvolved images with the *HST* optical images, which are of much higher resolution.

In the case of one galaxy, IRAS 07598+6508, it has not been possible to obtain complete, high quality data at H & K′. Therefore, while images and radial profiles at J and K-band are presented, it will be excluded from further discussion. It has a Seyfert 1 optical nucleus, leading some authors to describe it as an "infrared quasar" (Low et al. 1988), as well as considerable tidal debris in the surrounding host galaxy (Boyce et al. 1996). Since it is widely regarded as a QSO, it will therefore be considered similar to the three "infrared-loud" QSOs newly observed at H & K′and discussed in §3.3.4.

3.3. Analysis

3.3.1. Near-Infrared Morphology

HST/WFPC2 imaging indicates that the optical emission of these warm ULIGs is characterized by a dominant nucleus which is the most compact (generally unresolved by *HST*) and luminous source at B and which has been identified as a putative AGN, as well as by compact star-forming regions (with the exception of 3C273) found predominantly in the inner few kpc (Paper I). In most cases these star- forming regions seem to have ages based on their optical colors of less than $\approx 5\times 10^8$ years. The near-infrared, however, traces primarily the late-type stellar population at H-band with increasing sensitivity to emission from hot dust at K′-band (Aaronson 1977). Figure 3.2 shows the large scale structure observed at H-band for the complete sample of warm ULIGs. The near-infrared morphology generally appears to be much simpler than that seen optically. In every object, the extended emission of the surrounding galaxy is detected. In several cases, we can even trace the tidal structure (e.g. Mrk 1014, IRAS 05189−2524, IRAS 08572+3915, Mrk 231, Pks 1345+12, and Mrk 463). Three of the objects (IRAS 08572+3915, Pks 1345+12, and Mrk 463) show clear double galaxy nuclei, a result known from previous optical and near-infrared imaging (Sanders 1988a; Carico et al. 1990). Additionally, we can detect the spiral arms and star forming knots of the host galaxy of I Zw 1, the star-forming knots in the outer regions of Mrk 463 and IRAS 15206+3342, and the extended host of IRAS 12071−0444. However, only in a few cases (IRAS 15206+3342, Mrk 231, and Mrk 463w) is there any indication of complex near-infrared structure in the immediate vicinity of the nuclei, and even then this structure is comparatively faint compared to the nuclei themselves (Figure 3.3). This smoothness is in part due to the lower resolution of the near- infrared images. However, the typical size scale of the optical knots is 150 pc, with a knot separation of 300–500 pc. In this case we would expect many of the knots to be separated. Typical $B-K'$ colors for a starburst lie in the range 0–4, with $B-K'\approx 2.5$ for a starburst 10^8–10^9 years in age. Given that the starburst knots detected in Paper I were typically $m_{\rm B}$=22–24, then most of the knots should be $m_{\rm K'}$ ≈19.5–21.5. The detection limit for point sources is typically $m_{\rm K'}$=22–23; most of the optical knots should therefore be detectable. Unfortunately, matters are complicated by the more limited spatial resolution in the near-infrared, which limits the dynamic range in the vicinity of very strong point sources, and also by confusion due to the much stronger emission in the near-infrared from the underlying host galaxy. The former

may not actually be very significant, given the nearly unresolved nature of the K-band peaks (see below).

Despite the more limited spatial resolution in the near-infrared, the star- forming knots seen optically are clearly detected in Mrk 231, Mrk 463, and IRAS 15206+3342. Figure 3.3 displays these high spatial-resolution, high surface brightness features, which have been enhanced by Richardson-Lucy deconvolution. These bright, compact emission regions are spatially coincident with the optical knots, and it seems likely that the near-infrared emission also arises from these knots. The many knots detected optically in IRAS 08572+3915 were not detected in the near-infrared, despite the near-infrared observations being deep enough to see well- defined tidal tails. It seems likely that this is due to heavy obscuration in this nucleus. Even at optical wavelengths, it's appearance at B and I is so different as to preclude easy registration of features. At near-infrared wavelengths, it's appearance is so different from the optical as to prevent identification of any knots.

Perhaps most surprising is that almost no *new* knots have been discovered in the warm ULIGs. It was argued in Paper I that the optically observed star-forming knots were insufficiently luminous to be a significant contributor to the high bolometric luminosity in these ULIGs. However, one possibility is that a significantly larger population of star-forming knots exists, yet is embedded deeply enough so as to be undetectable in the WFPC2 data (limiting magnitude $m_{\rm B} < 27$). Assuming that most of the knots have a similar intrinsic luminosity, any knot extinguished by more than 4 $A_{\rm V}$ would have been undetectable by *HST*. However, the extinction at K′is only 1/12 that at B; knots which were extinguished just enough to be undetectable at B would be extinguished by only 0.3 magnitudes at K′. Given the K′detection limit and an expected K′magnitude of 20 for the brightest knots, similar knots would be seen even if they were obscured by 25 $A_{\rm V}$. This leads to the conclusion that either there is no population of moderately embedded star-forming knots in these galaxies or that any moderately embedded clusters are intrinsically less luminous than those seen optically. If any more knots exist like those seen optically, then they have line-of-sight extinctions greater than 25 $A_{\rm V}$. The failure to find any large populations of spatially distributed, moderately embedded knots lends credence to the idea that the dust-clearing time in the vicinity of the knots is short compared to the current starburst lifetime. It additionally supports the finding of Paper I that the knots do not contribute greatly to the bolometric luminosity, since there are relatively few of them, at least to an optical depth of 25 $A_{\rm V}$.

An examination of the radial profiles in both bands (Figure 3.4) is particularly instructive. In nearly all cases, the ULIGs are extended on large scales (1 $''\approx$ 1 kpc) at H. The underlying old stellar population of the merger remnant thus seems to contribute strongly at H. The only notable exceptions are three systems already known to be dominated even at optical wavelengths by an unresolved central source: Mrk 1014, IRAS 07598+6508, and 3C273. All three are QSOs (Schmidt & Green 1983), and even in these cases, all three are known to possess sizable host galaxies (McLeod & Rieke 1994b, Boyce et al. 1996). The high luminosity of their central peaks is sufficient to effectively mask the low surface brightness hosts at the depth and radii illustrated in Figure 3.4. In contrast to H, at K′many of the ULIGs are dominated by a single, essentially unresolved point source. This difference in compactness between H and K′is particularly evident in IRAS 05189−2524,

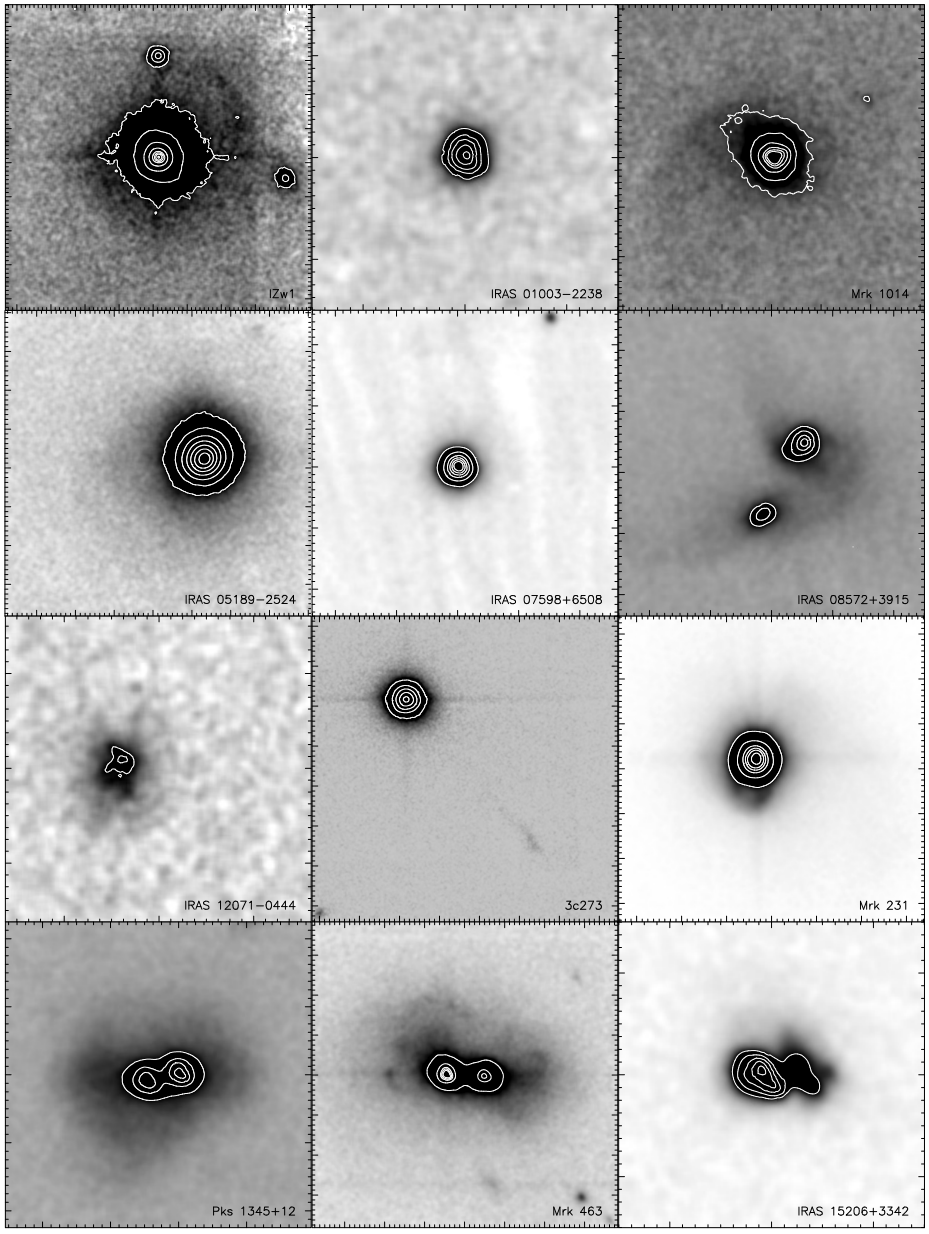

Fig. 3.2.— The large-scale structure observed at H. The data have been adaptively smoothed, a process which applies greater smoothing to regions with low signal-to- noise in order to increase contrast. The data are displayed such that the gray- scale part of the image illustrates low surface brightness features, while the white logarithmic contours show the high surface brightness structure. Tick marks are 0.5 $''$apart, with major ticks every 4 $''$. Northeast is at top left.

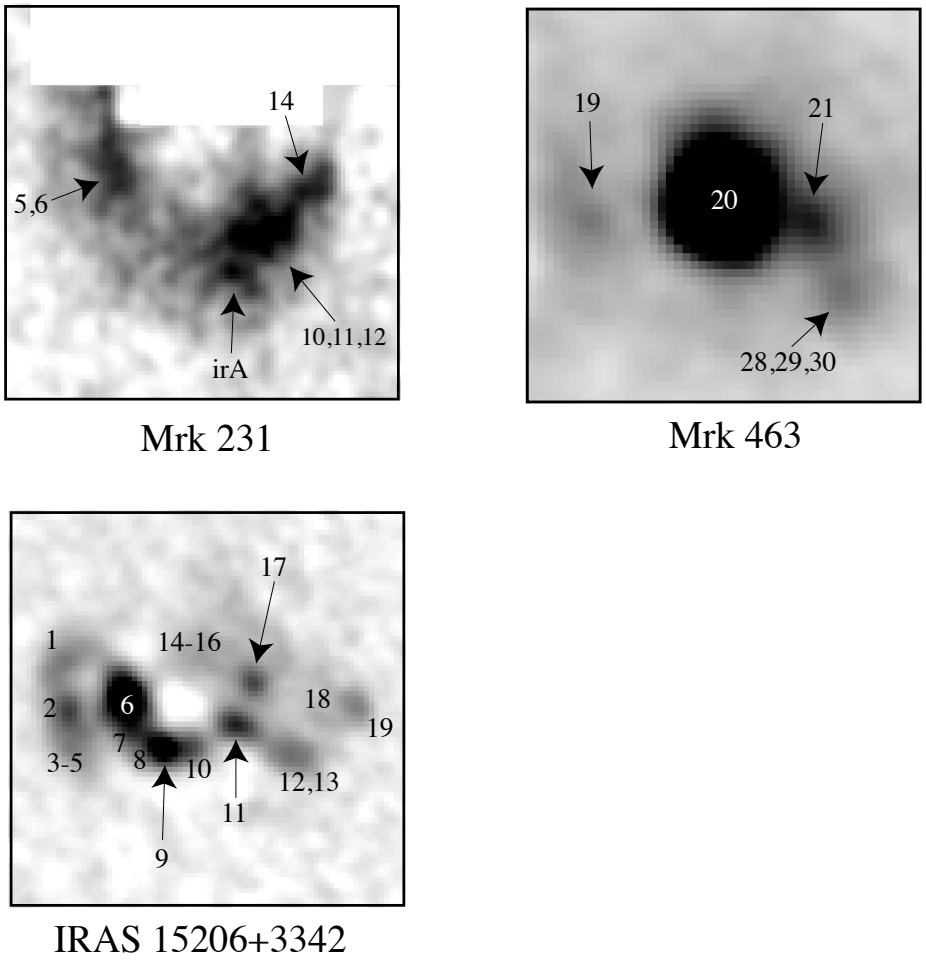

Fig. 3.3.— Selected K′ (Mrk 231 and IRAS 15206+3342) and H-band (Mrk 463) data deconvolved with the Richardson-Lucy algorithm to show high spatial frequency structure near the nuclei. The indicated knots are spatially coincident with the optical knots of Surace et al. (1998), and have been labeled with their optical names. The one new infrared knot is labeled "irA". Northeast is at top left.

IRAS 08572+3915w, IRAS 12071−0444, Pks 1345+12w, and Mrk 463e. The three QSOs (Mrk 1014, IRAS 07598+6508, and 3C273) show this effect to a lesser degree as they are already dominated by a central point source at H and K′. Of the remaining galaxies, I Zw 1, also a QSO (Schmidt & Green 1983), is superimposed on an extremely large and luminous host, and hence has a considerable host contribution even at small radii. The Seyfert 1 galaxy Mrk 231 is similarly known to possess a central "monster", yet it is also superimposed on an extremely luminous host. This leaves IRAS 15206+3342 as the only warm ULIG which is either not already known to be dominated by a central point-like source, or does not show increasing compactness at long wavelengths indicating that the majority of the bolometric luminosity is probably also compact. However, a single peak (the putative nucleus in Paper I) does have noticeably redder near-infrared colors than the other dozen or so detected knots. This may suggest that while this "nucleus" does not yet dominate as strongly at 2.1μm as in the other ULIGs, it may begin to do so at slightly longer wavelengths.

The physical FWHM of the PSF at K′ ranges from 300 pc in Mrk 231 to nearly 1.5 kpc in Mrk 1014, with a median of 600 pc, and in most cases the emitting region at K′ (which appears to be spatially coincident with the optical nucleus) is at least as small as the PSF. This is not surprising since the emission region is expected to be very small if the ULIGs harbor a dust-enshrouded QSO. Similarly, the ultracompact starbursts postulated by Condon et al. (1991) are also smaller than we can resolve in the near- infrared and the putative nuclei identified in Paper I also have size scales much smaller than the near-infrared resolution limit. This result implies that the majority of the H and K′-band flux in the warm ULIGs is emitted from spatially distinct regions. This increasing compactness at long wavelengths indicates a strong infrared excess on small spatial scales, which we show in §3.3.3 is most easily explained by the presence of hot dust.

3.3.2. Near-Infrared Luminosities

The photometry for the total integrated galaxy light and the putative nuclei are presented in Table 3.1. The integrated galaxy magnitude represents all of the light from both the galaxy and the putative nuclei. It was measured using a 30″ diameter aperture, corresponding to 30–100 kpc; in all cases this was sufficiently large that the observed galaxy emission at the edge of the aperture was no longer visible against the background noise. The H-band luminosity of the putative nucleus was determined in two ways. First, detailed two-dimensional PSFs were fit to the galaxies; the resulting fitted PSFs were integrated in order to estimate the nuclear flux. This technique has several shortcomings; in particular, the fit is complicated by an ignorance of the underlying intrinsic galaxy profile. As an estimate, the fit was made by scaling the PSF until the galaxy profile reversed itself, i.e. a "hole" was dug in the nuclear regions. The other technique was simply to measure the total flux inside a fixed (2.5 kpc diameter). Although this technique ignores the underlying nuclear galaxy emission, it is fairly successful in situations where the central regions are dominated by a bright point source. In these cases, the surface brightness of the underlying galaxy is so low inside the fixed aperture compared to that of the nucleus such that it represents only a small fraction of the total flux. It was found that in nearly all cases, the

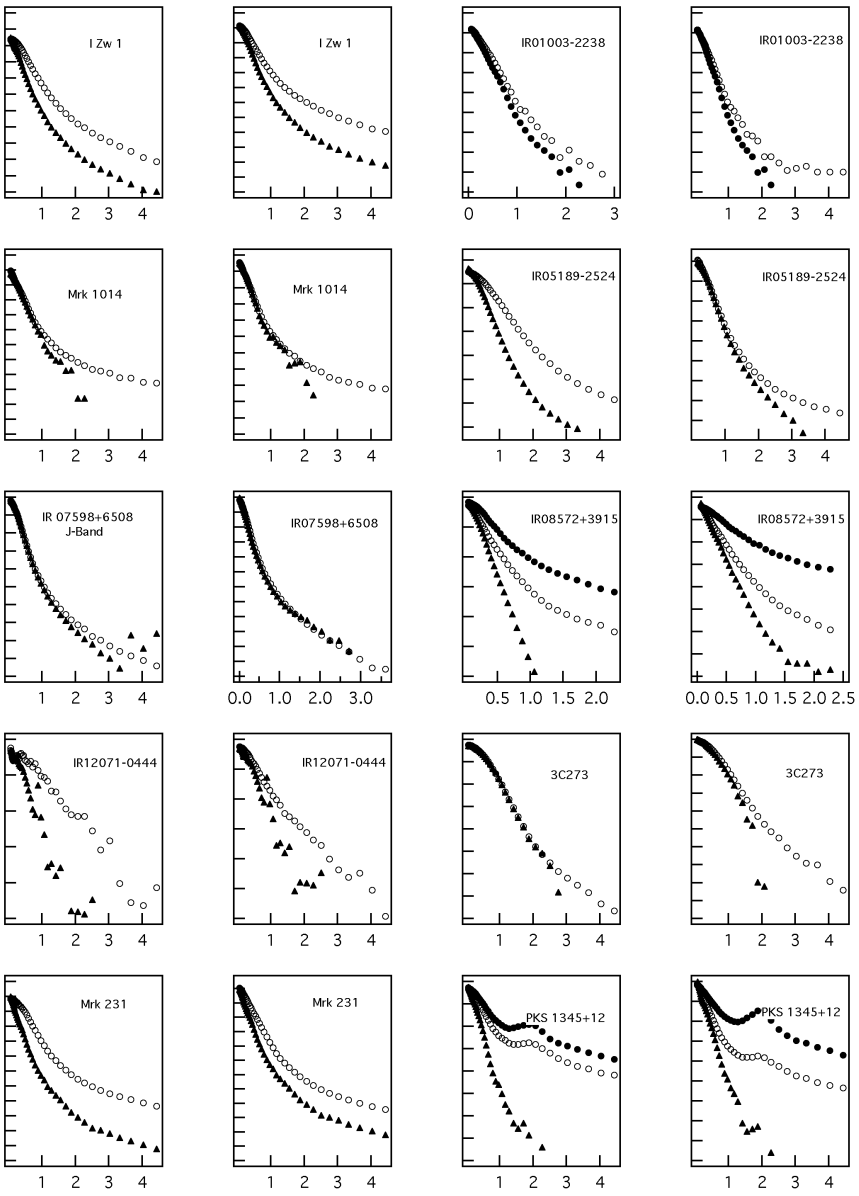

Fig. 3.4.— Radial profiles at H and K′ of the warm ULIGs (eastern nuclei=filled circles; western nuclei=open circles) and the associated point spread functions (triangles), plotted as surface intensity (in magnitudes) versus radius (in arcseconds). The galaxies are all noticeably extended at H, while they are essentially unresolved at K. Note that in terms of surface brightness, FWHM intensity occurs at just 0.3 mag/″ below the peak.

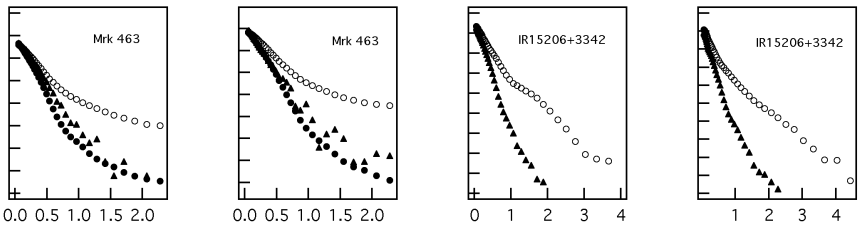

Fig. 3.4.— (continued)

two techniques agreed with each other at approximately the 10% level. Comparison of the photometry with that of previous studies (Sanders et al. 1988, Mcleod et al. 1994a, 1994b) shows that it is the same to within 15% .

Table 3.1. Warm ULIG Total and Nuclear Photometry

Name	$m_{\rm H,total}$	$m_{\rm H,nuclear}$	$\frac{L_{\rm nuclear}}{L_{\rm total}}$	$M_{\rm H,host}$	$m_{\rm K',total}$	$m_{\rm K',nuclear}$	$\frac{L_{\rm nuclear}}{L_{\rm total}}$
I Zw 1†	11.19	11.69	0.63	−24.5	9.94	10.52	0.53
IRAS 01003−2238	15.03	15.80	0.49	−22.7	14.30	15.33	0.39
Mrk 1014†	12.84	13.53	0.53	−25.6	11.67	12.28	0.57
IRAS 05189−2524	11.21	11.93	0.52	−24.2	10.23	10.44	0.82
IRAS 07598+6508	13.01	...	...	...	10.45	...	...
IRAS 08572+3915W	13.65	15.17	0.25	−22.9	12.73	13.75	0.39
IRAS 12071−0444	14.28	15.35	0.37	−23.9	13.42	13.91	0.64
3c273†	10.88	11.04	0.86	−26.1	9.70	9.85	0.87
Mrk 231	9.91	10.13	0.82	−24.4	8.87	8.98	0.90
Pks 1345+12W	12.99	15.36	0.11	−25.5	12.62	14.21	0.23
Mrk 463E	11.19	12.05	0.45	−24.8	10.20	10.50	0.76
IRAS 15206+3342	14.14	15.40	0.29	−24.1	13.47	14.58	0.36

Note. — † calibrated using photometry of Neugebauer et al. 1987. IRAS 07598+6508 of poor quality.

The emission at H-band is dominated by the old stellar population. The presence of double nuclei and well-formed tidal tails in these systems indicates that the merger process is not yet complete, and simulations indicate that they are unlikely to be more than 1–2 Gyr in age. Therefore the H-band emission is indicative of the current state of the stars which predated the merger itself, and the integrated H-band luminosity can be used to characterize the progenitors' masses by assuming a common $M/L_{\rm H}$ ratio and comparing them to a typical spiral galaxy. Characterization of the mass of the underlying "host" in the warm ULIGs is interesting for several reasons (here we define the word "host" to mean the smooth component of the galaxy luminosity profile which is unlikely to be a result of clustered star-formation or non-stellar nuclear activity). In particular, it will allow us to determine if the ULIGs represent the collision of typical gas-rich spirals, or whether they

are peculiar. For example, the ULIGs might be scaled- up versions of their less luminous counterparts, and simply represent the chance collision of unusually massive galaxies, in which case we would expect to find an unusually luminous host galaxy at H. Similarly, it may be that in order to drive enough material into the merger nucleus to trigger ULIG activity, the colliding galaxies must have very large masses. This is also important in testing any possible evolutionary scenario linking ULIGs and optically-selected QSOs; if QSOs are the evolved remnants of ULIGs, then they must have similar total old stellar masses and hence H-band luminosities.

Table 3.1 presents the derived photometric quantities: the nuclear fraction of emission at H and K′, and the H-band luminosity. McLeod & Rieke (1994a) estimate that for an L^* galaxy $M_{\rm H}$=−23.9; adjusting to H_0=75 kms^{-1}, this is $M_{\rm H}$=−24.04 . Using $M_{\rm V}$=−21.14 for an L^* galaxy with H_0=75 kms^{-1} and an estimate of (V-H)=2.7 for an aged stellar population with a Salpeter IMF (BC 93), we similarly derive M$_H$=−23.84. The range in host galaxy luminosities is ∼0.4 L^* (IRAS 01003-2238) to nearly 7 L^* (3C273), with a mean of 2.4 L^*. Six of the ULIGs have hosts in the range 1–2 L^*, while three (2 QSOs and a powerful radio galaxy) are in the range 5–7 L^*. This seems to be consistent with the idea that most of the ULIGs are the result of mergers between typical (i.e. L^*) or perhaps slightly more luminous than normal galaxies. Previous studies have derived similar results: ∼2.5 $L^*_{\rm B}$ (Armus et al. 1990, Jensen et al. 1997) and 2.5 $L^*_{\rm K'}$ (Jensen et al. 1997) for the BGS ULIGs and "Arp 220-like" objects, and ∼3 $L^*_{\rm r}$ (ranging from ∼ 1–24 $L^*_{\rm r}$) for the ULIG 2 Jy sample (Murphy et al. 1996). Finally, the range and distribution in $M_{\rm H}$ for the "warm" ULIGs is very similar to that of the host galaxies of PG QSOs (McLeod & Rieke 1994a,b), which typically range from 0.5–7 $L^*_{\rm H}$, with a mean of 1.5 $L^*_{\rm H}$. Additionally, McLeod & Rieke (1994a,b) note that the host galaxies of luminous quasars are more similar to 2 $L^*_{\rm H}$, and are more likely to have tidal features indicative of past galaxy-galaxy interactions.

IRAS 08572+3915 is surprisingly underluminous (≈0.5 L^*) at H considering that it's morphology is clearly that of two merging spiral galaxies (Surace et al. 1998). A possible explanation for this is the extremely high optical depth throughout the western galaxy component. Very red near-infrared colors ($0.7 < H - K' < 1.4$) within 2 kpc of the even redder nucleus (H- K' >2) indicate that dust obscuration may be very spatially widespread. Assuming a typical old stellar population color of ($H-K'$)=0.16, then this would imply $A_{\rm H} \approx 2 - -3$. Dereddening this region by 2 magnitudes at H would increase the total galaxy brightness by 1.2 magnitudes, making the estimated luminosity of the underlying old stellar population much more similar to the range found for the other ULIGs at ≈ 1.2 L^*. We note that the derived luminosity for IRAS 08572+3915 in K′-band is nearly 0.7 L^*, further indicating that substantial extinction may obscure the old stars.

This illustrates an important point: the luminosities given in Table 3.1 are *lower limits* to the true H-band luminosity. As illustrated by IRAS 08572+3915 above, there may still be considerable extinction at H due to spatially extended dust. This may affect all the ULIGs which have large, spatially extended regions that are redder than expected for late-type stars: notably, IRAS 05189−2524, IRAS 08572+3915, IRAS 12071-0444, and Mrk 463. IRAS 08572+3915 is the most extreme example. There may also be very low surface brightness, very extended emission on physical scales greater than 50 kpc (e.g. in tidal tails) which we fail to detect in the near- infrared. This can be evaluated by comparing

the spatial extent of the near- infrared data to previous optical data (Sanders et al. 1988a, Surace et al. 1998). In the cases of IRAS 05189−2524, IRAS 12071−0444, Mrk 231, and IRAS 15206+3342 there is extended structure seen optically which cannot be detected in the near-infrared data. In the remainder of the galaxies, all of the optically detected extended structure is detected in the near-infrared, and hence this is probably unlikely to affect them. Finally, the techniques used to determine the nuclear emission component will always result in over-subtracting from the underlying galaxy. This effect is most pronounced when the contrast between the nuclear component and underlying galaxy core is minimal, for example as in IRAS 05189−2524, IRAS 08572+3915, IRAS 12071−0444, and Pks 1345+12.

It is interesting to note that none of these sources of error is likely to affect IRAS 01003−2238. This object is very blue and pointlike, does not have a high surface brightness background host, and has only a few knots of star formation visible optically, with no extended tidal features. The presence of strong Wolf-Rayet emission possibly associated with the optical star-forming knots would seem to preclude this being a merger so advanced as to have no visible tidal remnants. It is under- luminous at H ($\approx$ 0.3–0.5 L^*), and this, combined with the above, would seem to indicate that unlike the other ULIGs it is either not a merger system or it is a merger involving under-luminous (and probably low-mass) galaxies.

3.3.3. Optical/Near-Infrared Colors

It is possible to examine the spectral energy distribution in the optical/near- infrared as characterized by the ($B-I$), ($I-H$), and ($H-K'$) colors by combining the new near-infrared data with the optical data of Paper I. This makes possible the disentanglement of the effects of extinction and dust emission. As has been noted previously, 2-color diagrams suffer a degeneracy in that many different combinations of extinction and thermal dust emission can produce similar results. This makes it difficult to determine uniquely the underlying emission mechanism. It additionally complicates questions such as the age-dating of knots based on colors alone, since even modest amounts of reddening can result in large variations in age estimates.

3.3.3.1. Modeled Colors

The stellar colors are based on the spectral synthesis models of Bruzual & Charlot (1993; the updated version used is hereafter called BC95). The particular model we have chosen is an instantaneous starburst with a Salpeter IMF and lower and upper mass cutoffs of 0.1 and 125 $M_\odot$. Of particular importance is that stellar ($H-K'$) colors reach a maximum of roughly 0.16, which corresponds to an extremely old age ($> 10^9$ yrs) for a stellar ensemble. This is very similar to the observed colors of typical galaxies (Aaronson 1977).

The QSO colors are based on a model of a typical QSO optical/near-infrared SED. The continuum emission is modeled with a two-part broken power law derived from Neugebauer et al. (1987) for the Bright Quasar Survey (BQS):

$$F_\lambda \propto \lambda^{-(2+\alpha)} \quad \begin{array}{r} \text{where } \alpha = -1.4; \lambda > 1\mu\text{m} \\ \alpha = -0.2; \lambda < 1\mu\text{m} \end{array} \tag{3.3}$$

Broad line emission based on the line widths, equivalent widths, and line strengths determined by Baldwin (1975), Davidson & Netzer (1979), Wills et al. (1985) and Osterbrock (1989) was also modeled. The derived QSO colors as a function of redshift are given in Table 3.2. The colors derived from this model are in good agreement with the observational results of the Elvis (1994: UVSX) sample, whose average colors are $(B-I)$=1.1±0.3, $(I-H)$=1.3±0.3, and $(H-K')$=0.78±0.2 at a median redshift of 0.15. The presence of strong line emission is the cause of most of the dependency of the color on redshift. In particular, Hα, Hβ, and MgII are shifted through the B and I filters in the redshift range $0 < z < 0.16$. The considerable scatter in QSO colors is likely to be intrinsic. Neugebauer (1987) noted a considerable scatter in the continuum power-law indices; these alone can easily account for the observed color variances.

Table 3.2. Synthetic QSO optical/near-infrared Colors

z	$(B-I)$	$(I-H)$	$(H-K')$
0.00	0.54	1.75	0.78
0.05	0.61	1.68	0.78
0.10	0.75	1.50	0.78
0.15	0.93	1.20	0.78

The effects of line-of-sight extinction, i.e. a simple foreground dust screen, were derived from Rieke & Lebofsky (1985). The reddening law was linearly interpolated to the rest frame wavelength of the galaxy in order to account for redshift.

The spectrum of hot dust with a characteristic temperature, T, and a λ^{-2} emissivity law was modeled according to the prescription given by Aaronson (1977):

$$F_\lambda \propto \lambda^{-2} B_\lambda \propto \lambda^{-7} (E^{\frac{\mathrm{hc}}{\lambda k T}} - 1)^{-1} \tag{3.4}$$

Modeled dust temperatures were in the range 600–1000 K. The effects of cooler thermal dust emission at long wavelengths on color are degenerate since the dust emission is so red that it only increases the K′-band flux, and hence the $(H-K')$ color. Only at temperatures above 600 K can dust emission contribute appreciably at wavelengths shorter than 2 μm. 1000 K is near the realistic ceiling for dust temperatures; at temperatures above ∼1500 K, the dust evaporates (Spitzer 1978). In any case, such a hot dust model does not fit the data well as even 1000 K is clearly hotter than needed.

Free-free emission was modeled according to (Spitzer 1978)

$$F_\lambda \propto \lambda^{-2} e^{-\frac{hc}{\lambda kT}} \tag{3.5}$$

Finally, the case of mixed stars and dust was considered. The spatial extent of the knots is such that they must be very large associations of many stars. It is both possible and likely that there are local, unresolved regions of high extinction inside the knots. An example of this might be a small region of star-formation containing several embedded protostars. The result of the presence of such unresolved regions inside the knots is to increase the thermal near-infrared component of the SED relative to that of a naked starburst, in a manner similar to that of the hot dust modeled above. Note that this is different from the effects of uniform line-of-sight extinction as modeled above.

We have modeled the effect of mixed stars and dust by assuming an underlying power-law distribution for the unreddened luminosity L_{A_V} obscured by a given extinction A_V:

$$L_{A_V} = L_{A=0}(A_V + 1)^\alpha \tag{3.6}$$

This is an "onion-skin" model; it peels away each optical depth and computes the total luminosity in each filter from all emission at that optical depth. The colors were derived by computing a numerical model of the observed luminosity at each optical depth, and then summing over all optical depths from A_V=0 to A_V=A_{max}. The resulting colors are displayed in Figure 3.5. The α=0 case corresponds to dust mixed uniformly with the emitting source, and is similar to that of Aaronson (1977) and Carico et al. (1990). The (B–I) colors rapidly converge on a fixed value determined by α, since the effective optical depth rises very rapidly at short wavelengths and hence stars at A_V >10 cannot contribute more than a tiny fraction to the observed short wavelength emission. At $A_V > 50$ this becomes true even at K′, and thus each model converges at high optical depth on a color dictated by α. This behaviour can be most easily described by the statement that the colors are fixed by the total stellar luminosity at optical depths less than one for any given wavelength, i.e. only the relatively unobscured stars in the outer regions of the dust/star mixture contribute noticeably to what is observed. This is similar to the result of Witt et al. (1992) that any extended stellar distribution mixed with a scattering and absorbing interstellar medium reaches a maximum reddening value at sufficiently high optical depths. While models with large amounts of stars at high optical depth (e.g. α=2) have fairly large (H–K') colors, they are accompanied by a similar increase in (B–I) and (I–H) which is not entirely dissimilar to the effects of reddening. In the reddening- orthogonal color basis discussed below, nearly all four models lie in essentially the same color location, and hence only the α=0 case will be illustrated. We have assumed that the luminosity source has the same colors as an intermediate age starburst (B–I, I–H, H–K' = 0.62, 0.97, 0.2), and that the dust obeys the same reddening law discussed above. The former assumption is almost certainly unrealistic, since it ignores the thermal dust emission associated with protostars found inside star-forming regions. However, this will be discussed using an additional observational model presented in §3.3.4.

The treatment described above ignores the effects of scattering, which may be quite important for an extended distribution of stars and dust. Witt et al. (1992) present models for various spherical distributions of dust and stars, with a full treatment of scattering. Of

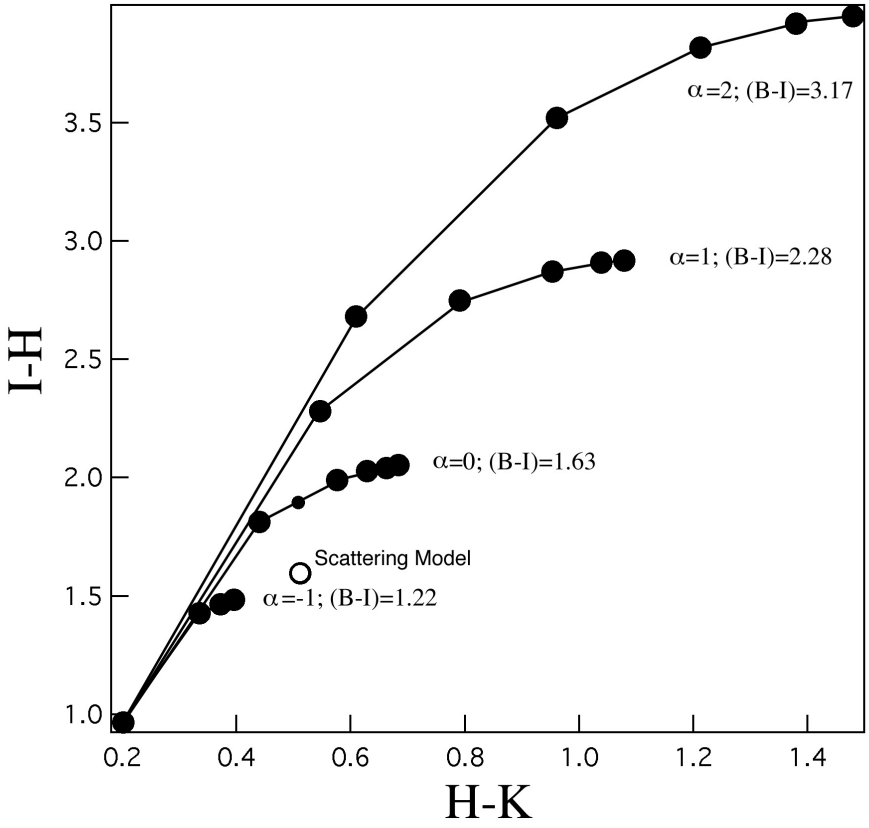

Fig. 3.5.— $(I-H)$ and $(H-K')$ colors for models of mixed stars and local dust extinction, with the luminosity at each optical depth characterized by a power-law of index α. The marked intervals are the maximum optical depth in units of 10 A_V. The $(B-I)$ colors for a given model become fixed rapidly since only stars at low optical depth contribute significantly to the short wavelength emission. This is true even at K$'$-band at high optical depth, hence the colors converge on a model- dependent value. The open circle indicates colors for mixed star and dust models including scattering with $A_V = 16$ magnitudes, although $(B-I)$ is lower (1.46 for evenly mixed stars and dust, and 0.77 for centrally concentrated stars and dust). The same point in the non-scattering models is marked with a small filled circle.

particular interest here are those models for "dusty" galaxies in which dust and stars are uniformly mixed. This corresponds to the model generated above, and is the most likely to represent the situation within the starburst knots (other models which represent dusty starburst cores or obscured AGN are more similar to the galaxies taken as a whole, rather than as small-scale individual knots). The addition of scattering leads to an increase in the fraction of emergent light, particularly at short wavelengths. The evolution of optical/near-infrared colors for both models is similar under the assumption of an intermediate age burst as described above. With a total extinction of $A_V = 16.2$ magnitudes, the non- scattering model predicts ($B-I$, $I-H$, $H-K'$) = (1.63, 1.96, 0.54), while the scattering model predicts ($B-I$, $I-H$, $H-K'$) = (1.46, 1.60, 0.42).

A more important change, however, is that scattering reduces the effective optical depth by increasing the fraction of light originally emitted by the stars which actually emerges from the model. This is particularly valuable because the mixed stars and dust model without scattering developed above cannot easily constrain the total bolometric luminosity of the stellar ensemble; it is relatively easy to hide luminosity at high optical depth where it cannot be seen in comparison to the stars at lower optical depth. One can therefore easily increase the "geometric" correction (the difference in magnitude between the true luminosity and that observed) at any given wavelength by simply specifying a sufficiently large total optical depth for the star/dust mixture. In the uniformly mixed stars and dust model without scattering and with a total optical depth of $A_V = 50$ mag, for example, the geometric correction to convert between the actual total stellar luminosity and that observed is nearly 4.8 magnitudes at B and 3.5 at K. For an ensemble with $A_V = 16$ mag these numbers drop to 3.1 and 0.8, respectively. For the "dusty" galaxy model with scattering, however, even if the total optical depth at B is as high as τ=20 (corresponding to the A_V =16 mag case described above), the geometric correction is only 2.4, and at K is 0.7. This effect is even more pronounced for other dust geometries; at $A_V = 16$ magnitudes the geometric correction at B is 0.4 for stars with dust lying interior to the stars and 1.8 for a "starburst" system with a centrally concentrated stellar distribution and dust mixed with the stars. Witt & Gordon (1996) showed that this effect becomes even more pronounced when the scattering medium is assumed to be clumpy instead of homogeneous, in which case the effective optical depth may be decreased by additional factors of 2–4. The addition of the scattered light to the total observed light therefore makes the observed luminosity more indicative of the actual total luminosity.

Figures 3.6 and 3.7 show the three-dimensional space occupied by the three colors ($B-I$), ($I-H$), and ($H-K'$). The resulting cube has been rotated by roughly 90° in order to illustrate the orthogonal nature of the extinction and dust emission curves. Note that stellar and QSO nuclear emission are well separated in the three-color representation. The "dusty" galaxy scattering model occupies nearly the same color space as the free-free emission model. The ($B-I$) colors of QSOs are similar to the expected colors of moderate age (10–100 Myr) starburst clusters. The largest distinguishing characteristic between the two is that QSO nuclei are more luminous at long wavelengths. As a result, the primary advantage of the short wavelength ($B-I$) data is to allow the disentanglement of extinction effects.

The following discussion will concentrate primarily on Figure 3.7, which has been rotated such that the color basis projected onto the page is orthogonal to extinction

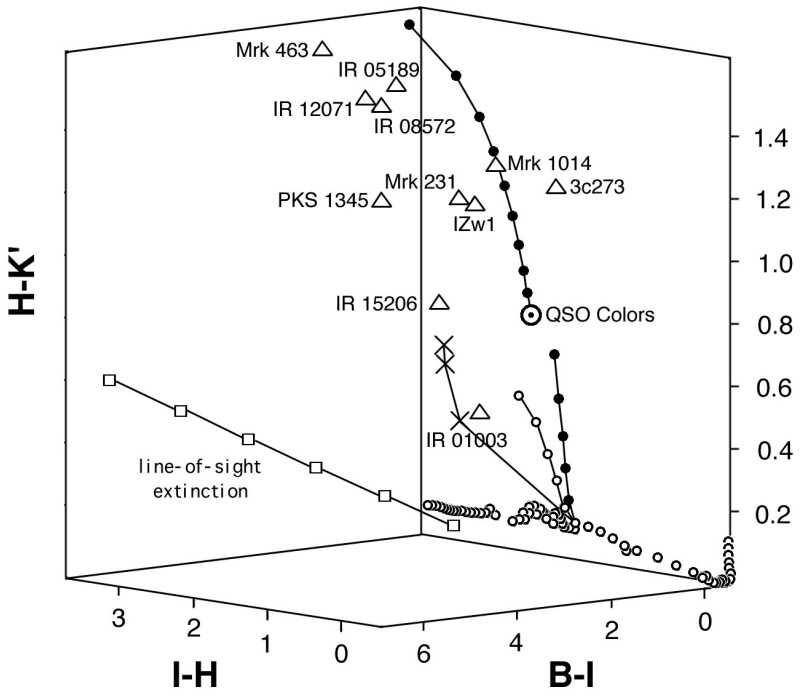

Fig. 3.6.— $(B-I)$, $(I-H)$, $(H-K)$ color cube illustrating the colors of the following emission sources: (1) optical QSO nuclear colors indicated by the large, dotted circle and (2) the evolutionary track of an instantaneous starburst aging from 0 to 15 Gyrs, indicated by the open circles. It also shows the effects of the following physical processes on the colors of stars and QSOs: (1) line-of-sight dust extinction in units of 1 A_V (open squares), (2) free-free emission in increments of 20% of the total flux at K′ (open joined circles), (3) emission from 800 K dust in increments of 10% of the total flux at K′ (filled circles), and (4) emission from uniformly mixed stars and dust, in units of A_V=10, 30, and 50 magnitudes. Note that the line-of-sight dust extinction and thermal dust reddening curves are nearly orthogonal.

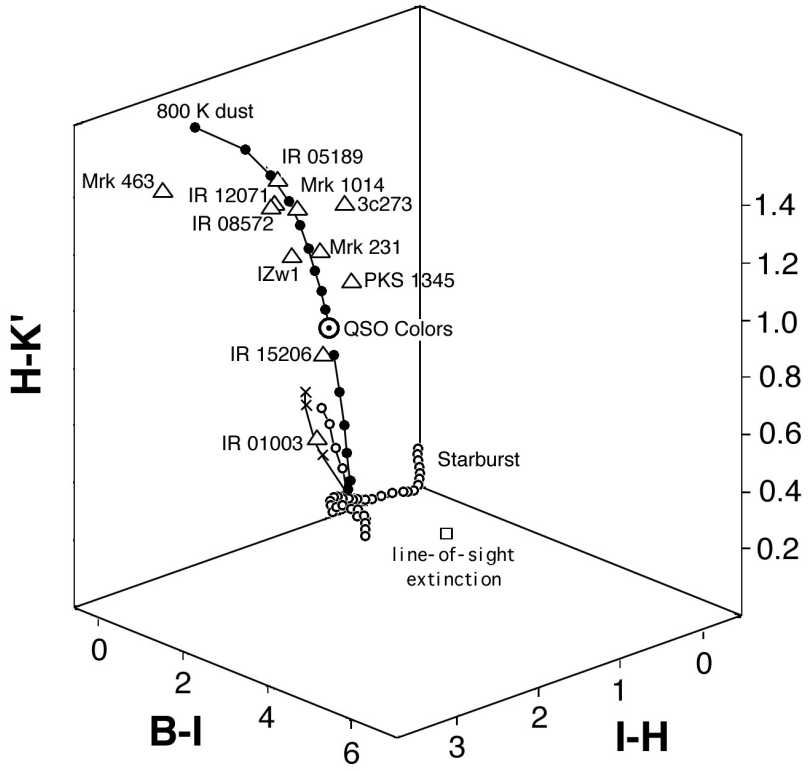

Fig. 3.7.— Same as Figure 3.6, but rotated such that the projected color basis is orthogonal to the line-of-sight dust extinction, i.e. line-of-sight extinction does not affect the position of points in this graph. Note the separation between QSO and stellar colors. Also, nearly all the warm ULIG nuclear colors are very similar to that of the infrared-loud QSOs, with the exception of IRAS 01003−2238.

(i.e. line-of- sight extinction does not change the apparent position of the points). Since extinction is almost certainly present to a varying degree throughout these galaxies, it is important to eliminate as much as possible extinction effects. To distinguish between stellar emission and QSO activity, any processes capable of producing similar optical/near- infrared colors must be considered. In the following discussion, "reddening" will be used to mean processes which move points upward in the projected basis of Figure 3.7, primarily giving them larger values of ($H-K'$), as opposed to the reddening caused by extinction. There are few processes which can make the QSO emission bluer. Large amounts of free-free emission (open circles, the last of which is pure free- free emission) can decrease ($H-K'$) by only as much as 0.2. Likewise, free- free emission can redden the stellar colors only slightly. The most important effects are clearly that of hot dust and dust mixed with stars. The overall effect of mixed dust and stars is to redden the basic stellar colors. As discussed above, however, this reddening saturates when sufficiently high optical depths are reached. Furthermore, models of distributed stars and dust with both scattering and absorption indicate that it is difficult to redden the starlight even with very high total optical depths (Witt et al. 1992,1996), and hence it is difficult to mimic the very red near-infrared QSO colors.

Since the QSO and stellar colors differ primarily at long wavelengths, the most serious problem occurs with reddening processes that affect only K′ and longer wavelength bands, such as thermal dust emission. If 800 K dust contributes as much as 55– 60% of the emission at K′, then the resulting stellar/hot dust ensemble will have colors nearly identical to that of optically selected QSOs. Thankfully, some reprieve is noted in that the extremely red colors of hot dust can also redden the QSO nuclei, and hence any hot dust component around a QSO moves it even further away from the basic starburst colors. Unfortunately, the very red dust colors also imply that the stellar-hot dust emission will converge on the same colors as QSO-hot dust emission as the percentage of hot dust increases. For stellar colors, this effect is noticeable when hot dust accounts for $> 70\%$ of the emission at K′. Carico et al. (1990) found that for far-infrared bright and luminous ($f_{60} > 5$ Jy; $L_{\rm ir} > 10^{11}$ $L_{\odot}$) galaxies which do not show signs of Seyfert activity, typically (H-K')= 0.40 (ranging from 0.16 to 0.57). Since these galaxies are believed to be powered predominantly by star formation, this represents the typical near-infrared colors observed for the most powerful of clearly identifiable starbursts.

Because the detailed SEDs of the high spatial frequency structure in the warm ULIGs are unknown, particularly at short rest wavelengths, it is not possible to apply K- corrections to them. However, since the models of the emission processes, starbursts, and QSOs do have detailed SEDs, inverse K-corrections can be made to their rest-frame colors at the redshift of our targets. This is done by convolving the synthetic spectra with the known detector and filter bandpasses. The magnitude zeropoint calibration of the filters is derived using the Kurucz model spectrum of Vega (BC95). For brevity, Figures 3.6 and 3.7 are calibrated to the median ULIG redshift, z=0.12. The K- corrections affect the modeled stellar colors by $\delta(B-I, I-H, H-K')$=(0.05,0.07,0.18) for a young (10 Myr) starburst, and by (0.40,0.11,−0.08) for an old (2 Gyr) population. The effects of K-corrections can therefore be quite large depending on the modeled population, and hence the representation of stellar colors can be considered to have a sizable uncertainty attached. Larger redshift values

also shift the dust emission curves to a more vertical orientation, as the rest frame filter bandpasses become bluer.

3.3.3.2. Nuclear Colors

Also shown in Figures 3.6 and 3.7 are the colors of the ULIG nuclear regions (open triangles). IRAS 01003−2238 seems to be unique in that it is most consistent with a young (10^7 yrs) stellar population mixed with local dust extinction with an optical depth of 15 A_V. It could also be a combination of hot young stars with 20% hot dust at K′ and 1 A_V of extinction. IRAS 15206+3342 has an SED similar to that of a QSO reddened by 1 A_V, but it is also similar to a young stellar population with a very large thermal dust component and 1–2 A_V of line-of-sight extinction. Given the large range of QSO colors it is not possible to differentiate between these two possibilities based on the optical/near- infrared colors alone.

The remaining 9 galaxies all have SEDs characterized by large K′ excesses. The three optically identified QSOs (I Zw 1, Mrk 1014, and 3C273) may be taken as representative of a subclass of "infrared loud" QSOs. Mrk 231, the most QSO- like of the ULIGs, has an SED nearly identical to that of the infrared-loud QSOs. Similarly, IRAS 05189−2524, IRAS 08572+3915w, and IRAS 12071−0444 also have colors essentially identical to that of the infrared-loud QSOs seen through $\approx 2A_V$ of extinction. PKS 1345+12w has a smaller near- infrared excess than the infrared-loud QSOs, but has the same colors as a typical QSO (characterized by our synthetic colors) seen through $2A_V$ of extinction. Mrk 463e has a larger excess at both H & K′ than the others. This can be explained by emission from 800–900 K thermal dust which contributes 20–30% more of the K- band flux than exists in the infrared-loud QSOs.

Compared to the synthetic optically-selected QSO colors, both the ULIGs and the subsample of three infrared-loud QSOs have a noticeable K′-band excess. This excess is 2–3σ greater than that expected considering the normal range of QSO colors ($\sigma_{H-K'}$=0.2; Elvis et al. 1994). However, it is likely that previous near-infrared and optical surveys have underestimated the ($H-K'$) color of the QSO nuclei. Given that normal galaxy colors ($H-K'<0.2$; Aaronson 1977) are almost always bluer than QSO nuclei ($H-K'>0.8$), studies that used large apertures to measure the QSO nuclear contribution are contaminated by underlying host galaxy light and therefore derive colors bluer than the actual nuclei. Also, several authors (Neugebauer et al. 1987, Sanders et al. 1989) have suggested that a hot dust component already contributes significantly to the near-infrared emission in optically selected QSOs. Given the presence of a strong far-infrared dust emission component and significant molecular gas content (see Sanders 1991), it would not be surprising if a larger reservoir of dust has also given rise to an enhanced hot dust emission component.

3.3.3.3. Knot Colors

In Table 3.3, we present photometry for the additional compact sources observed in the warm ULIGs. This includes both the galaxy "nuclei" which do not appear to have AGN-

like characteristics (i.e. IRAS 08572+3915e) and are likely to be the true stellar cores of galaxies, and the clumps of near-infrared emission which we associate with the compact star-forming "knots" observed in Paper I. The galaxy nuclei were measured using aperture photometry and the undeconvolved images, and have an uncertainty of 0.1 magnitudes. The knot magnitudes were measured from the R-L deconvolved images in order to minimize confusion. Uncertainties in the photometry are introduced by the non- linear nature of the deconvolution algorithm; these were checked by comparison with aperture photometry of the raw images. The knot magnitudes are uncertain by 0.15– 0.2 magnitudes.

The colors of the starburst "knots" found in Paper I were examined and initially revealed anomalous colors: while the knots had $(B{-}I)$ and $(H{-}K')$ colors that were consistent with stars, the $(I{-}H)$ colors were far larger (typically $(I{-}\ H){>}\ 2.5$) than could be explained by any plausible combination of stellar colors and reddening effects. A careful examination of the data revealed that this was most likely due to aperture effects. The resolution of the optical data is typically 5-10 times higher than that of the infrared data. As a result, the apertures used to measure the optical data are much smaller. It is likely that the larger apertures used for the near- infrared data also include some additional underlying emission that may not be related to the optical knots, hence the apparent increase in luminosity between the optical and near-infrared data. However, as noted previously, the largest differences in emission and obscuration mechanisms lie in the optical $(B{-}I)$ and near-infrared $(H{-}K')$ colors. The purely optical and purely infrared knot colors should be fairly certain since data of different resolutions are not mixed. Therefore, the knot colors in the 2-color $(B{-}\ I)$ vs. $(H{-}K')$ plane are presented in Figure 3.8.

The colors of the galaxy nuclei appear very similar to that of stars with mild reddening. Pks 1345+12e has colors similar to that of an old stellar population with A_V=1–2. IRAS 08572+3915e and Mrk 463w appear similar to a somewhat younger stellar population (1–2 Gyrs), but have a slight near- infrared excess. In the case of Mrk 463w this may not be surprising as this galaxy core shows both Seyfert 2 activity and numerous knots of star formation near it, indicating that there may be considerable new star formation in it, resulting in a thermal dust contribution. There is a surprisingly wide range in $(H{-}K')$ colors for the putative starburst knots themselves. For comparison, we consider larger samples of luminous infrared galaxies (LIGs; $10^{11} < L_{\rm ir} < 10^{12}\ L_{\odot}$; Carico 1988, 1990). These are the most far-infrared luminous galaxies in which it is fairly certain that star formation is the primary contributor to the far- infrared luminosity, and as such represent the most extreme known starburst galaxies. The distribution in knot colors is very similar to that of the LIG nuclear regions, $(H{-}K')$= 0.25–0.6, not counting the few LIGs known to be Seyferts and which are therefore likely to have a strong non-stellar component.

Carico et al. (1990) found that the "disk" $(H{-}K')$ colors of luminous IRAS galaxies were typically $(H{-}K')$=0.25 (ranging from 0.08 to 0.37). It is unclear what stellar components were integrated into this "disk" light — clearly there must be some contamination by star-forming regions, which probably accounts for the difference between these colors and the value of $H{-}K'$=0.16 found by Aaronson (1977). The colors of the underlying host galaxies of the warm ULIGs were examined by subtracting the contribution of the putative nucleus as well as any additional contribution from identified point-like sources from the integrated galaxy flux. In this case the contribution from the putative

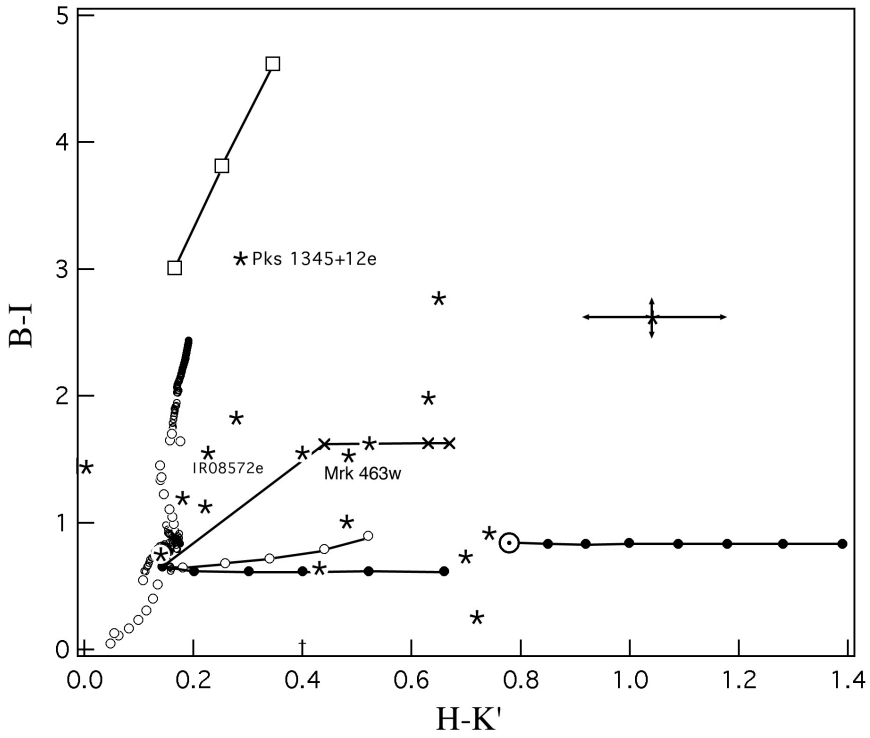

Fig. 3.8.— The $(B-I)$,$(H-K')$ color plane, with the same reddening mechanisms, stellar and QSO colors as in Figure 3.6. The star-forming knots are marked with stars and the stellar galaxy nuclei are labeled.

nucleus was taken as the flux inside the central 2.5 kpc. This should ensure that all the nuclear contamination of the underlying galaxy colors is removed and, although this process also eliminates some of the host galaxy's flux, should leave the colors unchanged. Most of the colors so derived for the warm ULIGs appear similar to those found by Carico et al. (1990), ranging from $H-K'=0.09$ in IRAS 05189−2524 to nearly $H-K'=0.7$ in IRAS 08572+3915 (the latter probably being strongly affected by dust) with a median of $H-K'=0.4$. However, a few of the systems seem to show peculiarly red colors, namely the optically selected QSOs. This is probably the result of residual nuclear contamination caused by the extended wings of the bright nuclei.

3.3.4. Contribution of putative "nuclei" to the bolometric luminosity

ULIGs are defined by their extremely high infrared luminosities ($L_{\rm ir}$ $>10^{12}L_{\odot}$, equivalent to the bolometric luminosities of optically selected QSOs). If the source of the majority of this luminosity were an AGN, then it is likely that after expulsion of the enshrouding dust the AGN would appear similar to an optical QSO. Although the broad-band optical/near-infrared colors of the warm ULIG nuclei (as in §3.3.1, the dominant compact emission sources at K′ spatially coincident with previously identified optical nuclei) appear very similar to that of QSOs, many of the nuclei are less luminous at these wavelengths than QSOs. Three of our 12 ULIGs (the optically identified QSOs I Zw 1, Mrk 1014, and 3C273) already have a substantial fraction of their $L_{\rm bol}$ in a QSO-like SED at short wavelengths (i.e. "the blue bump"). The nucleus of the broad-line object IRAS 07598+6508 also meets the minimum B-band luminosity criterion for QSOs (Surace, unpublished). Dereddening of the observed optical emission by the optically estimated extinction (typically 2 $A_{\rm V}$, Surace et al. 1998) is insufficient to raise the estimated optical luminosity of the remaining eight AGN to the canonical $M_{\rm B}=-22.1$ luminosity criterion for optical QSOs except in the case of the nucleus of Mrk 231 (dereddened $M_{\rm B}=-23$). Dereddened B-band luminosities of the remaining seven range from $M_{\rm B}=-15.5$ for IRAS 08572+3915 to $M_{\rm B}=-22$ for IRAS 15206+3342. The median value is $M_{\rm B}=-20.2$, which is typical of Seyferts (Osterbrock 1989).

Due to the much lower extinction in the near-infrared, it is possible that the nuclei in many cases are seen directly in the near-infrared (which is supported by their essentially unresolved near-infrared morphology) and hence the observed K′-band luminosity may be more indicative of their true luminosity, although it is also sensitive to hot dust emission, as in §3.2. Using the observed colors for I Zw 1, Mrk 1014, and 3C273 (the infrared-loud optically-selected QSOs), $M_{\rm B}=-22.1$ is equivalent to a QSO K′ magnitude of $M_{\rm K'}=-25.8$; using the synthetic optical QSO colors it is $M_{\rm K'}=-25.2$ at the median redshift $z=0.12$. IRAS 05189−2524 and Mrk 463e (which are also broad-line objects) now qualify as QSOs based on their K′ luminosity. The remaining five of the warm ULIGs still fall short of QSO near-infrared luminosities; their infrared luminosities range from $M_{\rm K'}=-23$ (IRAS 01003-2238) to $M_{\rm K'}=-24.7$ (IRAS 12071-0444), with a mean of $M_{\rm K'}=-23.8$. Therefore, while in 58% (7/12) of the warm ULIGs the dereddened near-infrared nuclear luminosity is similar to an optically selected QSO and is probably the source of the majority of the bolometric luminosity, if we assume only a simple foreground reddening screen then the remaining five

warm ULIG nuclei appear similar to lower luminosity Seyferts and fall an order of magnitude short of QSO luminosities. It is notable, however, that in these underluminous systems both the nuclei and the star-forming knots are insufficiently luminous at optical/near-infrared wavelengths (even after dereddening) to account for the high bolometric luminosity. Either a large fraction of the total luminosity must arise in a source or sources so heavily extinguished as to escape detection at *both* optical and near-infrared wavelengths, or alternatively the "knots"/nuclei we have already detected must have intrinsic SEDs with an unusually strong far-infrared component in comparison to the putative nuclei in the seven ULIGs which have dereddened optical/near-infrared luminosities consistent with QSOs.

Until now we have assumed that both the optical and near-infrared emission reached the observer through a common path. The apparent optical and near-infrared underluminosity in five of the warm ULIGs relative to QSOs may be understood as a putative AGN being seen through a combination of patchy extinction and scattering. The nucleus might in some cases be seen directly in the near-infrared due to the lower near- infrared extinction, but primarily through scattered light in the optical (which may then be additionally reddened by extinction along the scattered path). In more extreme cases the line-of-sight column density may be so high that the AGN is seen only in scattered light even at near-infrared wavelengths. Since the extinction estimates are most heavily influenced by the short wavelength colors (where extinction effects are greatest) the extinction estimates would be dominated by that along the low- extinction scattered paths, leading to estimated extinctions that are much too low. Attempts to derive true luminosities based on the optical light would then be futile if they are dominated by scattered light which is dependent on the scattering geometry.

Polarization studies (Young et al. 1996) which included 6 of our warm ULIGs have actually found evidence for patchy obscuration in the vicinity of the scattering region. In particular, their conclusions for IRAS 05189−2524 agree with the conclusion presented in §3.3.1 based on morphology that the emitting region is seen directly in the near-infrared, but with an optical scattered component with mild optical extinction and a sizable contribution from starlight, which is probably a result of the circumnuclear starburst surrounding the AGN (Paper I). A similar result is found for Mrk 463e, whose optical/near-infrared morphology shows that the optical emission is dominated by a spatially distinct region to the north of the near-infrared nucleus. Recent HST results indicate that this emission is that of a highly polarized Seyfert 1 "hidden" nucleus (Tremonti et al. 1997). This agrees with the polarized SED found by Young et al. (1996) who concluded that the line-of-sight extinction to this nucleus was $A_V=17$; this high extinction agrees with our observed morphology. The steeply rising polarization in the near-infrared of IRAS 08572+3915w (Young et al. 1996) may indicate that it is so deeply buried that almost none of the optical emission arises from the AGN, and that even at near-infrared wavelengths the emission is predominantly scattered and not line-of-sight. The case of IRAS 08572+3915w reinforces the point that morphologically the galaxies with the least luminous nuclei also tend to have more complex optical morphology, suggestive of patchy scattering. Given that the far-infrared emission in the warm ULIGs is 50–90% of the bolometric luminosity, then this implies that the covering factor of a putative QSO must be of the same order. Patchy extinction must therefore be

present; only in those cases where the nuclei are seen along a direct line of sight would the unreddened luminosities be consistent with QSOs.

In terms of the previous color analysis which assumed a simple single-path model for the optical/near-infrared emission, correcting for the effects of patchy extinction and scattering would be to drive the nuclear colors even further from those of stars, thus further eliminating some of the degeneracy in the color diagram. The apparent enhancement at shorter wavelengths due to the addition of scattered light would result in the derivation of colors that are too blue — correction for this further reddens the colors. While most polarization studies detect only small fractional polarizations ($< 5\%$), they also use very large apertures (5–8″), which encompass large fractions of more distant galaxies like the warm ULIGs studied here (Young et al. 1996). The beam dilution can be estimated by comparing the B-band emission of the putative nuclei in the HST/WFPC data to the total flux encompassed in a 5″ aperture. If the polarized light is actually associated with the high surface brightness features observed with HST then the beam dilution correction may be anywhere from 5× in Mrk 463e to as high as 50× in IRAS 08572+3915, with 10–15× being more typical. In this case, a significant fraction of the observed optical nuclear emission may be scattered, affecting the analysis as mentioned previously.

3.3.5. Contribution of putative star-forming "knots" to the bolometric luminosity

In some of the objects in our sample of warm ULIGs the starburst knots (compact emission regions not identified as "nuclei") may additionally contribute as much as 25% of the bolometric luminosity. Since the ULIG knots appear to be powerful bursts of star-formation similar to the circumnuclear starbursts found in the LIGs, they may have similar SEDs. The relationship between K′and far-infrared luminosity in the LIGs can then be used to estimate a far-infrared luminosity of the ULIG knots based on their observed near-infrared luminosity. From Carico et al. (1990) the empirical relation

$$\log L_{\rm ir} = -\frac{M_{\rm K'} - 6.45}{2.63} \tag{3.7}$$

is derived for the subset of LIGs without any evidence for a strong AGN component which relates the "nuclear starburst" near-infrared luminosity to $L_{\rm ir}$. For those warm ULIGs where it is possible to observe bright near- infrared knots, the extrapolated total far-infrared knot luminosity ranges from $L_{\rm ir} = 10^{10.27}\ L_{\odot}$ in Mrk 231 to as high as $\log\ L_{\rm ir} = 10^{11.6}\ L_{\odot}$ in IRAS 15206+3342. Previous estimates of the knot bolometric luminosities (e.g. Surace et al. 1998) were appreciably lower ($0.1\text{–}2.5 \times 10^{10}\ L_{\odot}$) since they were based on their B magnitudes and a simple foreground reddening model applied to a purely stellar (no dust) starburst. The new near-infrared observations reveal a near- infrared excess in the knots similar to other infrared-luminous starbursts which result in higher estimated bolometric luminosities. Nevertheless, the net result is that the knot contribution to $L_{\rm bol}$ is much less than that of the putative nuclei, which are thus likely to be the dominant energy source in the warm ULIGs.

3.4. Conclusions

We have presented high spatial resolution images of a complete sample of "warm" ultraluminous galaxies. From these images we conclude the following:

1) The warm ULIGs have a near-infrared structure very similar to that seen optically, with tidal features and some clumpy emission coincident with the star- forming knots seen optically. Most of these knots have low line-of sight extinctions. We have failed to detect significant numbers of new near-infrared knots indicating that any additional knots are either extinguished by greater than A_V=25, are intrinsically less luminous, or are distributed differently from the optical knots.

2) The starburst knots have a wide range of ($H-K'$) infrared excesses. These excesses span the range seen in the less luminous LIGs. Adopting the SED of the LIGs as representative of the most luminous star-forming regions, then the knots seen in the warm ULIGs have total, estimated far-infrared luminosities in the range of 10^9– $10^{11.5}$ $L_\odot$.

2) A single "knot" of emission, spatially coincident with an optically identified "nucleus", increasingly dominates the emission at long wavelengths. This putative nucleus is generally unresolved at K′.

3) The colors of these putative nuclei are nearly identical to that of optically selected QSOs with an added hot (≈800 K) dust component contributing 10– 30% of the K′ emission seen through A_V=1–2 mag of extinction. These same colors are identical to "infrared loud" quasars. They could, however, also be produced by a powerful starburst 10–100 Myrs in age with 70% or more of the flux at K′ originating in hot dust. This would be a greater percentage than that observed in other, less luminous starburst galaxies.

4) Seven of the sample of 12 warm ULIGs have dereddened "nuclear" optical and near-infrared luminosities consistent with that of optically-selected QSOs. In the remaining five cases the dereddened luminosities of the putative nuclei are similar to that of Seyferts. If the underlying emission source is a QSO, then this could be explained by the optical emission being seen primarily through scattered light along less extinguished lines of sight.

5) The powerful Wolf-Rayet galaxy IRAS 01003−2238 appears unique among the warm ULIGs: it is pointlike, has no obvious tidal features or extended host, and is under- luminous at both optical/near-infrared wavelengths.

6) The dereddened "nuclear" luminosities of the sample of warm ULIGs are sufficiently high that in 58% (7/12) of the cases they could provide most of the bolometric luminosity. In all cases except IRAS 15206+3342 their contribution to the bolometric luminosity is likely to greatly exceed that of the more widespread star- formation detected so far.

We would like to thank Kevin Jim, Mark Metzger, Joe Hora and Klaus Hodapp for their advice and work on the fast tip/tilt secondary and the QUIRC infrared camera. We would also like to thank Buzz Graves and Malcolm Northcott for their knowledge on the characteristics of AO systems. We also thank Lee Armus and B.T. Soifer for helping with the early groundwork for this project. Finally, we thank Bill Vacca, Alan Stockton, Steve

Willner, and an anonymous referee whose useful comments helped strengthen both the material and presentation of this paper.

Table 3.3. Additonal Warm ULIG Structure

Name	$m_{\rm H}$	$m_{\rm K'}$
IRAS 08572+3915		
15(east)†	16.22	15.99
Mrk 231		
5,6	17.40	17.18
10,11,12	16.74	16.31
14	18.12	18.11
irA	17.79	17.64
Pks 1345+12		
6(east)†	15.79	15.50
Mrk 463		
19	17.31	16.83
20(west)†	14.32	13.84
21	16.86	16.72
28,29,30	18.01	17.60
IRAS 15206+3342		
1	17.63	17.36
2	18.03	16.99
3,4,5	17.62	17.10
7,8	18.07	17.37
9†	16.92	16.18
10	18.82	18.10
11	17.94	17.29
12,13	17.51	17.23
14	19.10	18.70
15,16	<20.60	<19.80
17	18.13	17.50
18	<20.40	<19.20
19	18.17	17.99

Note. — † denotes probable second (non-active) nucleus in double-nuclei systems. Names taken from Surace et al. (1997). Names with multiple numbers indicate the given magnitude is an integrated value for the named knots.

3.5. Notes on Individual Objects

I Zw 1 — a Palomar-Green (PG) QSO. Both spiral arms are clearly detected in the near-infrared. The QSO nucleus is situated on an extremely bright elongated stellar galaxy core.

IRAS 01003−2238 — A powerful Wolf-Rayet galaxy (Armus et al. 1988) with several small knots of star-formation seen optically. The near-infrared data reveals essentially no features at all.

Mrk 1014 — a PG QSO observed optically to have several knots and linear features very close to the nucleus, and a very large tidal arm. The single- armed tidal feature to the east of the optical nucleus is clearly detected.

IRAS 05189−2524 — the extended structure of the host galaxy is clearly detected at H. Under careful scrutiny, the eastern and southern loops can also be detected. Young et al. (1996) report broad polarized Hα and polarization evidence that the nucleus is seen directly in the near-infrared, confirmed by our detection of an apparently unresolved nucleus. This contrasts with the optical morphology presented in Paper I which showed a double peaked feature that appeared most consistent with a single object bisected by a dust lane.

IRAS 07598+6508 — our data for this object is poor. However, we do not readily detect the tidal structure and star-forming knots seen to the south and east of the nucleus, probably indicating very blue colors.

IRAS 08572+3915 — in the near-infrared, both nuclei can be clearly seen, as can the two tidal tails extending to the north and east. The western nucleus appears similar to a point superimposed on an extremely bright, extended background. The eastern nucleus is oval in shape and is very similar both in infrared and optical appearance.

Mrk 231 — this system is dominated in the near-infrared by the active nucleus seen optically. Additionally, the optical knots in the southern "horseshoe" are detected, and are even more distinct in the deconvolved images. Additionally, we seem to have detected at least one near-infrared knot not seen optically "irA".

Pks 1345+12 — the extended galaxy is clearly seen and is similar in appearance to previous optical images, and has no fine structure. The underlying host galaxy is very luminous and thus the nuclei are a contribute less than half to the total near-infrared luminosity.

Mrk 463 — this system is dominated at K′ by the eastern nucleus. The peak of the emission is located at knot 15 of Surace et al. (1998). This seems to imply that this knot is the true nucleus, and that the optically bright spot to the north is an excitation feature. This is probably the source of the polarized broad lines reported by Tremonti et al. (1997). The extended tidal remnants are detected, as are the star forming knots in these tails (primarily to the north and east).

IRAS 15206+3342 — as noted in Surace et al. (1998), this system possesses 4 extremely bright optical knots, as well as more than a dozen less luminous knots. In the deconvolved

near-infrared images, these knots are readily visible. The northeastern knot seems to dominate at K′. No additional knots are seen in the near- infrared.

REFERENCES

Aaronson, M. 1977, PhD. Thesis, Harvard

Armus, L., Heckman, T.M., & Miley, G.K. 1988, ApJ, 326, 45

Baldwin, J.A. 1975. ApJ, 201, 26

Beckers, J.M. 1993. ARA&A, 31, 13

Boyce, P.J., Disney, M., Blades, J.C., Boksenberg, A., Crane, P., et al. 1996, ApJ, 473, 760

Bruzual, G., & Charlot, S. 1993, ApJ, 405, 538

Carico, D.P., Sanders, D.B., Soifer, B.T., Elias, J.H., Matthews, K., & Neugebauer, G. 1988, AJ, 95, 356

Carico, D.P., Sanders, D.B., Soifer, B.T., Matthews, K., & Neugebauer, G. 1990, AJ, 100, 70

Carico, D.P., Soifer, B.T., Beichman, C., Elias, J.H., Matthews, K., & Neugebauer, G. 1986, AJ, 92,1254

Casali, M.M., & Hawarden, T.G. 1992, JCMT-UKIRT Newsletter, 3, 33

Condon, J.J., Huang, Z-P., Yin, Q.F., & Thuan, T.X. 1991, ApJ, 378, 65

Davidson, K. & Netzer, H. 1979. Rev.Mod.Phys. 51, 715

Elias, J.H., Frogel, J.A., Matthews, K., & Neugebauer, G. 1982, AJ, 87, 1029

Elvis, M., et al. 1994, ApJS, 95, 1

Goldader, J., Joseph, R.D., Doyon, R., & Sanders, D.B. 1995, ApJ, 444, 97

Hodapp, K.W., Hora, J.L., Hall, D.N., Cowie, L.L. et al. 1996, New Astronomy, 1, 176

Jensen, J., Sanders, D.B., & Wynn-Williams, C.G. 1997, in prep.

Jim, K.T. 1995, BAAS, 187, 1394

Low, F.J., Huchra, J.P., Kleinmann, S.G., & Cutri, R.M. 1988, ApJ, 327, L41

McLeod, K.K. & Rieke, G.H. 1994a, ApJ, 420, 58

McLeod, K.K. & Rieke, G.H. 1994b, ApJ, 431, 137

Neugebauer, G., Green, R.F., Matthews, K., Schmidt, M, Soifer, B.T., & Bennett, J. 1987, ApJS, 63, 615

Osterbrock, D. 1989. *Astrophysics of Gaseous Nebulae and Active Galactic Nuclei.*

Perault, M. 1987, Ph.D. Thesis, University of Paris

Ramsay, S.K., Mountain, C.M., & Geballe, T.R. 1992, MNRAS, 259, 751

Rieke, G.H. & Lebofsky, M.J. 1985, ApJ, 288, 619

Sanders, D.B., & Mirabel, I.F. 1996, ARA&A, 34, 749

Sanders, D.B., Soifer, B.T., Elias, J.H., Madore, B.F., Matthews, K., Neugebauer, G., & Scoville, N.Z. 1988a, ApJ, 325, 74

Sanders, D.B., Soifer, B.T., Elias, J.H., Neugebauer, G., & Matthews, K. 1988b, ApJ, 328, 35

Schmidt, M. & Green, R.F. 1983, ApJ, 269, 352

Spitzer, L. Physical Processes in the Interstellar Medium, 1978, (John Wiley & Sons, N.Y.), 57

Surace, J.A., Sanders, D.B. Vacca, W.D., Veilleux, S., & Mazzarella, J.M. 1998, ApJ, 492, 116 (Paper I)

Tremonti, C.A., Uomoto, A., Antonucci, R., Tsvetanov, Z., Ford, H.C., & Kriss, G.A. 1996, BAAS, 28, 1287

Wainscoat, R.J. & Cowie, L.L. 1992, AJ, 103, 332

Wills, B.J., Netzer, H., & Wills, D. 1985. ApJ, 288, 94

Witt, A.N., & Gordon, K.D. 1996, ApJ, 463, 681

Witt, A.N., Thronson, H.A., & Capuano, J.M. 1992, ApJ, 393, 611

Young, S., Hough, J.H., Efstathiou, A., Wills, B.J., Bailey, J.A., Ward, M.J., & Axon, D.J. 1996, MNRAS, 281, 1206

Chapter 4

Observations of "Cool" Ultraluminous Infrared Galaxies[1]

ABSTRACT

We present high spatial resolution (FWHM $\approx$ 0.3–0.8 $''$) BIHK$'$ imaging of a sample of ultraluminous infrared galaxies (ULIGs) with "cool" mid-infrared colors ($f_{25\mu\mathrm{m}}/f_{60\mu\mathrm{m}} < 0.2$) generally not characteristic of AGN and which form a complementary sample to the "warm" ULIGs of Chapters 2 & 3. We find that all of the cool ULIGs are either advanced mergers or pre-mergers with evidence for still-separate nuclei. Extended tidal features such as tails and loops as well as clustered star formation are observed in most systems. This extended tidal structure suggests a common progenitor geometry for most of the ULIGs: a plunging disk collision where the disks are highly inclined with respect to each other. The underlying host galaxies have H-band luminosities of 1–2.5 L^*, very similar to that found in the "warm" ULIGs. The nuclear regions of these galaxies have morphologies and colors characteristic of a recent burst of star formation mixed with hot dust and mildly extinguished by 2–5 A_V; only in one case (IRAS 22491$-$1808) is there evidence for a compact emission region with colors similar to an extinguished QSO. Most of the observed star-forming knots appear to have very young (10 Myr) ages based on their optical/near-infrared colors. These star-forming knots are insufficiently luminous to provide more than a fraction of the high bolometric luminosity.

4.1. Introduction

Chapter 1 has already presented much of the historical background surrounding ultraluminous infrared galaxies (ULIGs). An examination of deep far-infrared flux-limited samples such as the Kim 1 Jy survey (1995) shows that the majority (80% ; 90/115) of ULIGs are "cool" systems (i.e., $f_{25\mu m}/f_{60\mu m} < 0.2$). Thus, these galaxies are similar to the majority of systems previously studied by others (i.e. Sanders et al. 1988a, Kim 1995), rather than the smaller fraction of "warm" systems like those discussed in Chapters 2 & 3 (Sanders et al. 1988b). Results derived in this chapter are therefore likely to reflect the properties of ULIGs as a whole, and provide a valuable comparison sample. In Chapter 2 it was discussed that the warm ULIGs were possibly a transition state between cool ULIGs and QSOs. If this is true, then we expect the cool ULIGs to have properties similar to, yet less evolved, than the warm sample.

Many of the cool ULIGs have been imaged before at optical (Sanders et al. 1988, Kim 1995, Murphy et al. 1996) and near-infrared (Carico et al. 1990, Kim 1995, Murphy et al. 1996) wavelengths. However, these observations suffered from poor spatial resolution ($\geq$ 1.0 $''$) and lack of depth. Their wavelength coverage was insufficient (predominantly R and K-band) to disentangle reddening effects from intrinsic colors. Finally, they are incomplete; no one has imaged all of the objects in this cool sample. We present here new multiwavelength

[1] An expanded version of Chapter 4 incorporating elements of Chapter 1 will be submitted to ApJ as "Multiwavelength High Resolution Imaging of Ultraluminous Infrared Galaxies", by Surace & Sanders

observations with 1.5 and 4× the spatial resolution of previous observations at optical and near-infrared wavelengths; despite being ground-based, they allow us to isolate interesting features such as the star-forming knots detected in the warm ULIG sample.

4.2. Data

4.2.1. Sample

Details of the selection of the "cool" ULIG sample were presented previously in section 1.4.2. Briefly, these ULIGs are drawn from the *IRAS* BGS sample of Sanders et al. (1988) and the Kim 1 Jy sample (1995). They are chosen to have "cool" mid-infrared colors (i.e., $f_{25\mu m}/f_{60\mu m} < 0.2$). As such, they are the complementary sample to the "warm" sample discussed in Chapters 2 & 3. While the warmness criterion is known to select for AGN-like spectra (de Grijp et al. 1985), it can be demonstrated that coolness selects equally *against* AGN-like spectra. Given the Seyfert fraction in "warm" galaxies (70%; de Grijp et al. 1985), the Seyfert fraction in the 1 Jy ULIG survey (34%; Kim 1995), and the "warm" ULIG fraction in the same survey (20%), then the expected percentage of "cool" ULIGs with Seyfert spectra is 25%. This is substantially less than in the "warm" ULIGs. In actuality, only 11% (2/18) of our "cool" ULIG sample has Seyfert spectra (Mrk 273, UGC 5101).

All of the "cool" ULIGs have been chosen to lie within the volume $z < 0.16$. This is the same volume limit as the "warm" ULIG sample, and is very close to the completeness limit for ULIGs in deep *IRAS* surveys. Also, this is sufficiently nearby that the spatial resolution achievable from the ground can provide information on scales known from Chapters 2 & 3 to be physically meaningful (typically, a few hundred parsecs). Since there are over 100 such ULIGs known, this sample was selected first to include the original 7 cool ULIGs in the BGS sample, since these are most well-studied. The remaining cool ULIGs were selected such that their redshift distribution was similar to the "warm" ULIG and QSO samples. Specific objects were randomly chosen to lie in regions of the sky more amenable to observing from Mauna Kea and to ameliorate crowding of the observing program in spring. Since this selection criterion is unrelated to the physical properties of the ULIGs, it should not bias the sample.

4.2.2. Observations and Data Reduction

The data were taken between October, 1995 and March, 1998 at the f/31 focus of the UH 2.2m telescope. The near-infrared data was taken with the QUIRC camera in a manner identical to that of the "warm" ULIG sample in Chapter 3. The optical data was taken with several different instrument configurations. The UH Tektronix 2048 and Orbit 2048 cameras were used at the f/31 focus of the UH 2.2m. In both cases, the data were binned 2×2 in order to provide better spatial sampling (with adopted binned pixel sizes of 0.14″ and 0.09″, respectively). The Orbit 2048 was also used in conjunction with the HARIS spectrograph; by withdrawing the dispersion components it was possible to image through

the spectrograph. The telescope f/31 beam was reimaged at f/10 resulting in an unbinned image scale of $0.14''$pixel^{-1}.

Table 4.1. Cool ULIG Observation Details

Name	Inst.[a]	Exposure Time (sec)			
		B	I	H	K′
IRAS 00091−0738	QT	2520	1920	2520	1800
IRAS 01199−2307	QT	2880	2280	2400	2160
IRAS 03521+0028	QT	3600	2280	2400	3360
UGC 5101	WQT	1620	2160	2160	2040
IRAS 12112+0305	WQT	1440	1860	1920	1440
Mrk 273	W T	1200	2340	···	···
IRAS 14348−1447	WQH	720	720	1440	1680
IRAS 15250+3609	QH	1200	1680	2160	2160
Arp 220	NT	1080	1440	···	···
IRAS 20414−1651	WQH	1440	1560	1680	1800
IRAS 22206−2715	QT	480	1440	2400	2520
IRAS 22491−1808	WQT	2520	1440	2760	2520
IRAS 23233+0946	QT	2160	1800	2160	2160
IRAS 23365+3604	QH	240	240	1200	1560

[a] Q = UH2.2m f/31 QUIRC, T = UH2.2m f/31 Tektronix 2048, H = UH2.2m f/31 Orbit reimaged at f/10 through HARIS spectrograph, W = *HST*/WFPC2, N=*HST*/NICMOS

The optical data reduction involved several steps. First, the CCD bias pattern was removed by subtracting from each image a high S/N median bias frame constructed from sequences of 20-30 bias frames at the beginning and end of each night. Pixel-to-pixel response variations were then corrected by dividing each image by a high S/N flat produced by making dithered observations of the twilight sky in each filter. Typical twilight exposures were 2-3 seconds each; short enough to avoid getting detectable flux from field stars, yet long enough to avoid flat-field errors introduced by the radial shutter used at the UH 2.2m. Estimated S/N for the flats (based on poisson statistics and the gain of the CCD) was between 250-500. The images were then corrected to normal orientation by transposition and rotation using the ROTATE task in IRAF and the overscan regions were trimmed off using IMCOPY. The images were then aligned using the IMALIGN task in IRAF, which uses a marginal centroiding routine that calculates a best fit solution to a number of (user-supplied) reference stars in the field. Typical alignment errors were estimated (on the basis of the fit) to be about 0.25 pixels. Given that the data was typically sampled at 5 pixels FWHM for a point source, alignment errors are unlikely to be important. Images were scaled according to their exposure times and then, in order to account for any variable sky background, an offset was subtracted from each image based on the background actually measured in that frame. The images were then averaged using an algorithm that rejects pixels inconsistent with the known noise properties of the CCD, which allows for rejection

of cosmic rays. The shifted images were combined onto a larger image than the original data frames, thereby increasing the total field of view due to the dithering process.

The near-infrared data was reduced in the same manner as that described in Chapter 3. The data was initially sky-subtracted using consecutive, dithered frames; because the QUIRC field of view is so large, it is possible to dither the target on-chip, thereby increasing telescope efficiency by a factor of 2. The images were then flattened using median flats constructed from images of the illuminated dome interior. Each image was then masked by hand to exclude bad pixels and regions contaminated by negative emission introduced by the sky subtraction step. Images were shifted using IMALIGN, scaled by their exposure times, and the background was subtracted off each frame according to the measured background in the frame. The images were then combined by medianing using IMCOMB and rejecting pixels outside the linear regime of the array.

In those cases where the telescope cassegrain focus was rotated during the night in order to acquire better guide stars and thus improve the tip/tilt guiding (see Appendix B), additional flats were made whenever feasible at the rotation angles used. This was necessary since changes in the illumination of dust and other defects in the telescope optics tended to produce notable changes in the flat-field response, resulting in a strong background gradient in the vicinity of any optical defects such as dust.

The data were calibrated through observations of Landolt and Elias standard stars in the optical and near-infrared (Landolt 1983, 1992, Elias et al. 1982 ; see Appendix C). Typically 4–5 standard stars were observed throughout the night at airmasses similar to those of the science targets. The stars were interleaved with the science targets; such a strategy also enabled them to be used for refocussing the telescope between each target. In most cases the nights were photometric with $\sigma_{\rm M} < 0.05$. For data taken on non-photometric nights, we have calibrated the data by using large-aperture photometry already in the literature for the targets. In particular, the optical data for UGC 5101 was calibrated using Sanders et al. (1988a), while the IRAS 00091-0738 and IRAS 01199-2307 data were calibrated against Kim (1995).

The point-spread-function (PSF) was calibrated by using actual stars in the final combined science image using DAOPHOT in the manner described in Chapter 3. All of the stars were identified, scaled, shifted, and combined using a sigma-clipping algorithm and weighting according to total flux, thus creating as high a S/N PSF image as possible. In those few cases where no stars were found in the science images, the PSF was estimated by using the closest temporally adjacent PSF.

Additionally, some of the cool ULIGs have *HST* imaging data available for them. UGC 5101, IRAS 12112+0305, Mrk 273, IRAS 14348−1447, IRAS 20414−1651, and IRAS 22491−1808 were observed with WFPC2 through the F814W (I-band) filter as part of the Borne et al. (1997) ULIG snapshot survey. This data was retrieved from the STScI archive and reduced in the same manner as the WFPC2 data in Chapter 2.

In two cases we do not have complete data. Near-infrared data was not taken of Arp 220 because it had already been observed with NICMOS (Scoville et al. 1998), and that

data has been retrieved for use here. Mrk 273 was not observed in the near-infrared because it had already been observed with adaptive optics from CFHT (Knapen et al. 1997).

As in Chapter 3, in some cases high spatial resolution techniques were applied to the data in order to enhance detectability of features. The Richardson-Lucy algorithm implemented in IRAF/STSDAS was used along with the data-derived PSFs. It was allowed to iterate 20–50 times until noticeable artifacting appeared (see Appendix B for details). Other techniques used included CLEAN and radial model subtraction. In order to enhance non-radially symmetric features (mostly on the basis that the PSF and the galaxy cores are nearly so), circular isophotal models were fitted to and subtracted from the data. All radially symmetric features, such as the extended galaxy envelope, are subtracted out leaving only non-radially symmetric features behind. This technique will be discussed in more detail in Chapter 5.

4.3. Results

4.3.1. Morphology

4.3.1.1. Large-Scale Features

Images of each ULIG in the "cool" sample in each of the four observed filters are presented in Fig 4.1. Figure 4.2 gives near-truecolor images constructed in the same manner as those in Chapter 2; despite having higher spatial resolution, the near-infrared morphology is more featureless and therefore a near-infrared color image was not included. The cool ULIGs exhibit a wide variety of morphologies. At least 6 of the 14 systems (43%) have obvious double galaxy nuclei as evidenced by the manner in which tidal tails and spiral structure are centered on high surface brightness, extended emission regions. This is similar to the value of 47% found by Murphy et al. (1996) for a sample of 53 non-color-selected ULIGs. However, an additional 4 systems *may* have double nuclei, which would bring the total double nucleus fraction to as high as 72% (10/14). Specifically, IRAS 12112+0305 has a red, central, point-like emission region apparently within the common envelope of extended emission of the galaxy, and which is at the same redshift as the extended galaxy structure to its north (Surace, unpublished). This would seem to indicate that it is a nucleus like the putative active nuclei seen in the "warm" ULIGs. Several authors have shown evidence for an apparent double nucleus in Mrk 273 (Majewski et al. 1993 Condon et al. 1991), but more recent adaptive optics imaging at K indicates that this "nucleus" is more likely to be a luminous star-forming region (Knapen et al. 1997). Similarly, Graham et al. (1990) show evidence for a double "nucleus" in Arp 220, but more recent NICMOS imaging of the same galaxy has shown so much star-forming structure as to cloud this interpretation (Scoville et al. 1998). Finally, IRAS 20414−1651 appears to have multiple large, luminous condensations embedded in its tidal tails, but these may be superimposed background objects, or newly formed high density regions in the tails themselves.

Projected separations of the definite double nuclei span an order of magnitude from 25 kpc in IRAS 01199−2307 to just 2.5 kpc in IRAS 22491−1808. In all cases the double

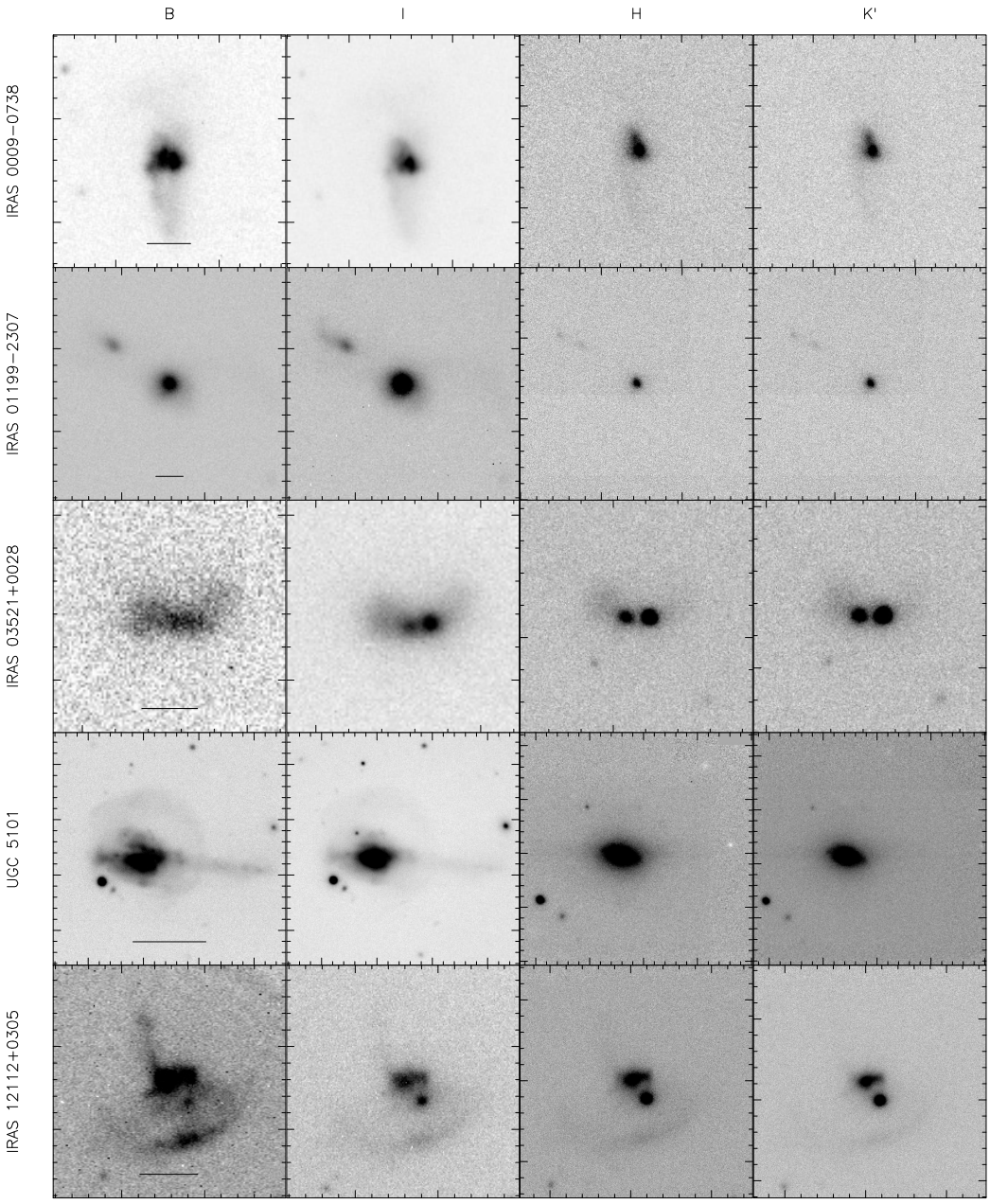

Fig. 4.1.— Optical (B,I) and near- infrared (H,K′) images of the "cool" ULIGs showing their large-scale structure. Northeast is at top left. All of the images for a given object except the NICMOS data for Arp 220 are at the same scale, with ticks 2 ″apart and major ticks every 10 ″. The physical scale bar on each of the B-band images is 10 kpc in length.

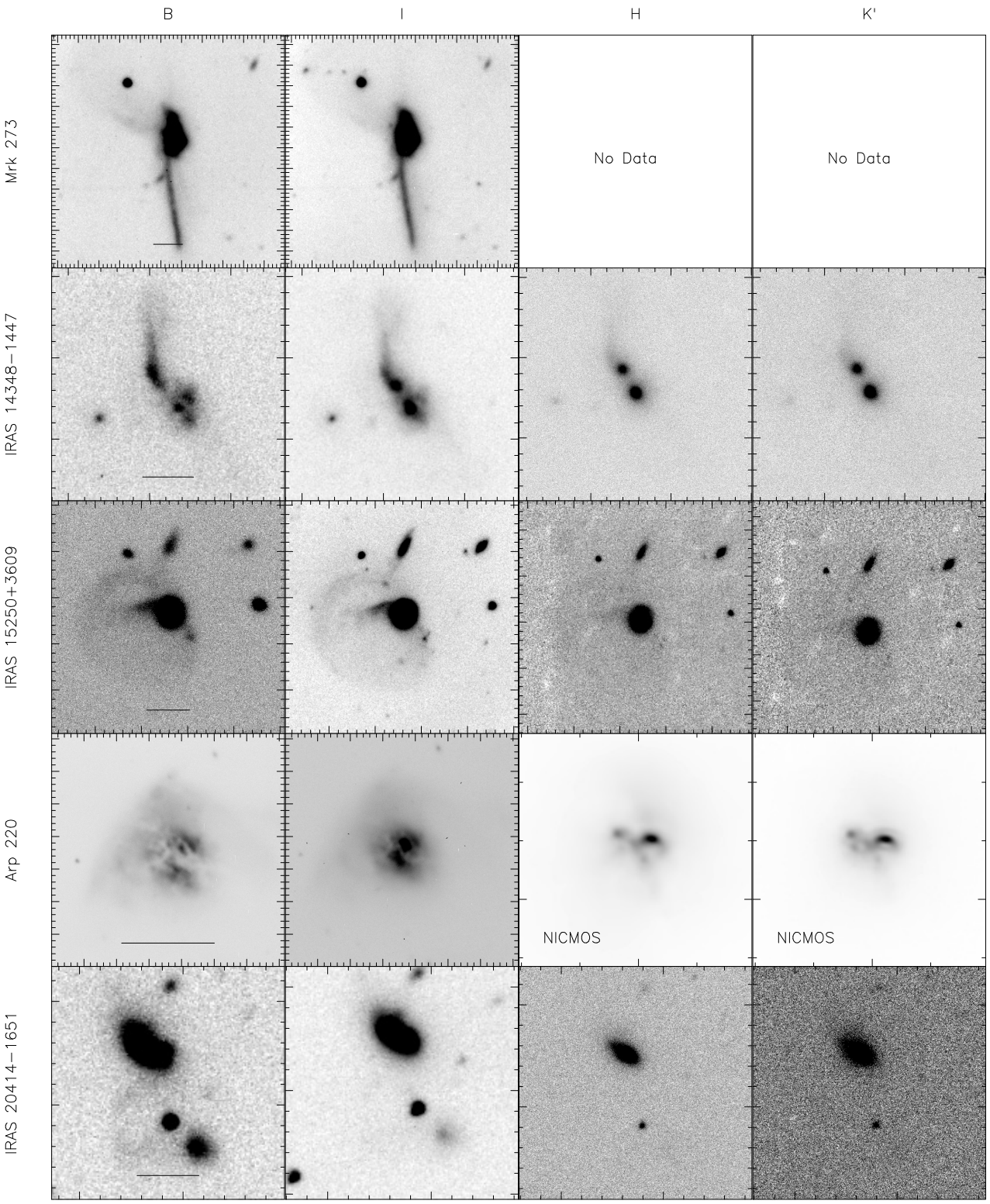

Fig. 4.1.— (continued)

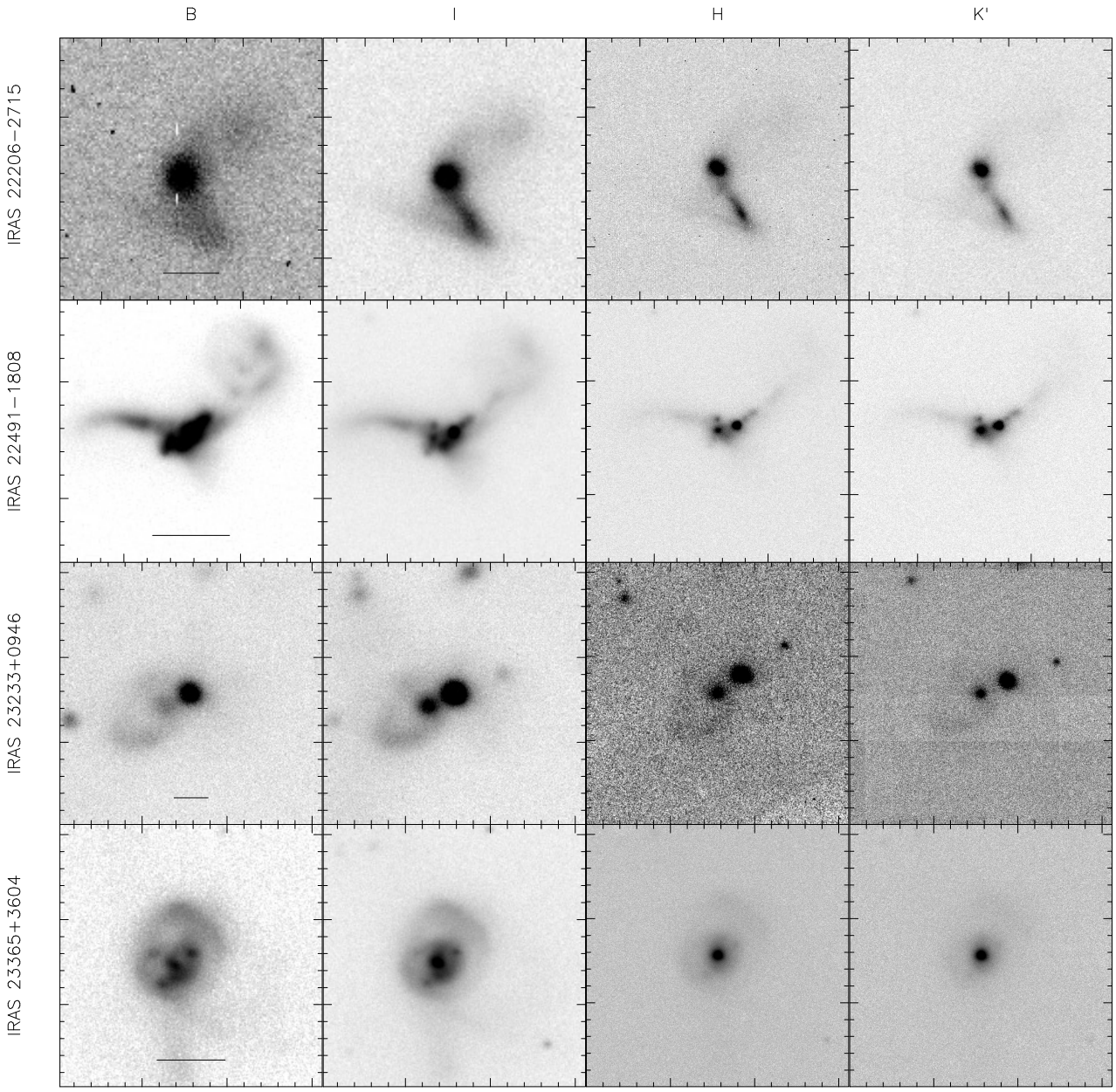

Fig. 4.1.— (continued)

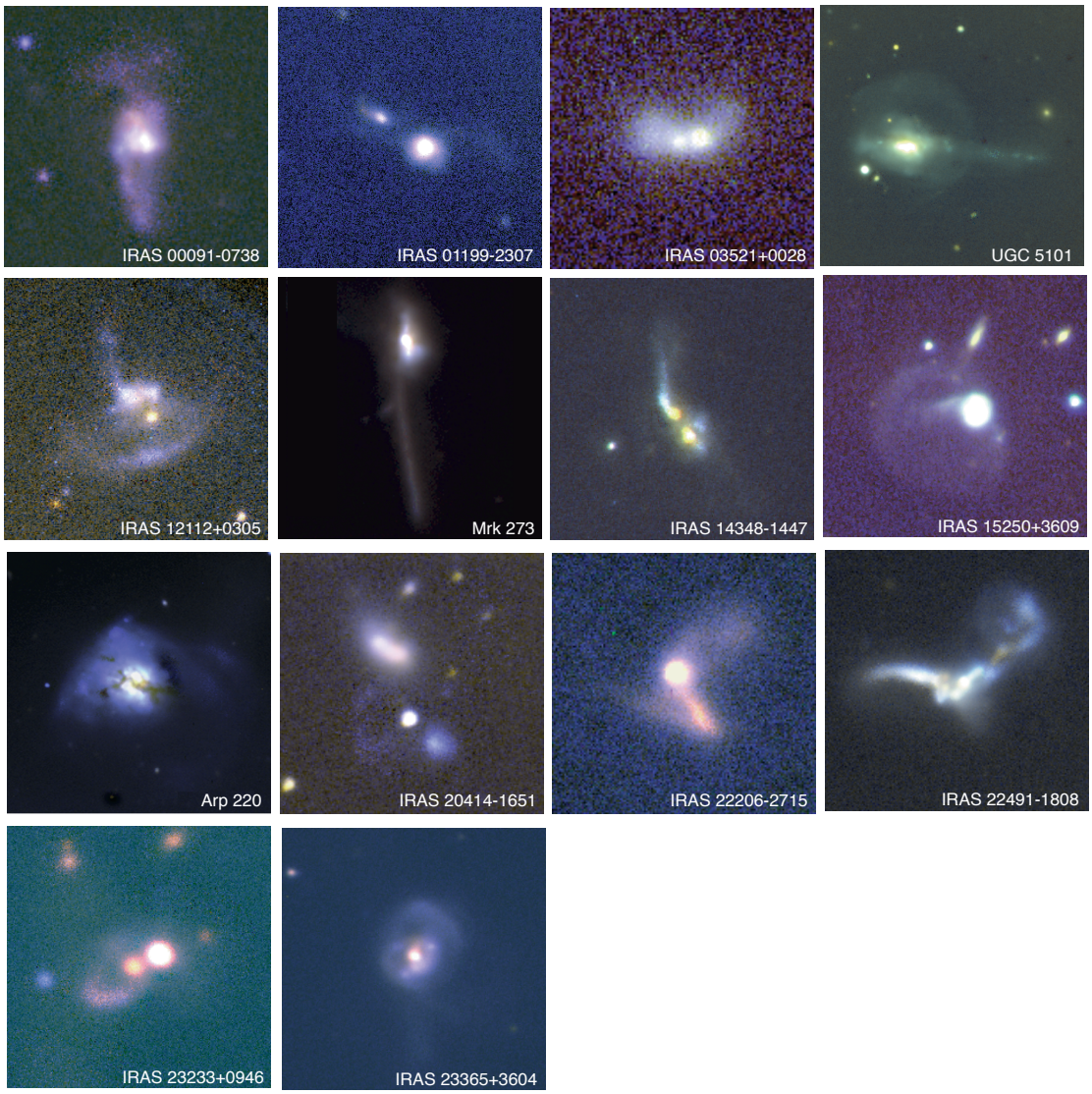

Fig. 4.2. - Near-truecolor images of the "cool" ULIGs constructed from the B & I-band data. As in Figure 2.3, we have linearly interpolated the galaxy SED from the *B* and *I* data; the color balance is not absolute.

nucleus systems have extended tidal structure indicating that these systems have already passed initial perigalacticon and are now in an advanced merger state. The lack of additional multiple nuclei is similar to the result found in Chapter 2 for warm ULIGs and may indicate that the timescale for final coalescence of the nuclei is comparatively short. However, this may also be an effect of confusion and limited spatial resolution. As noted in Chapter 2, it is difficult to differentiate true galactic nuclei (spiral bulge remnants) from unresolved aggregates of luminous, dusty young star- forming regions. Conversely, at the median redshift of the sample, typical spatial resolutions of 0.4″at K′ are $\approx$ 600 pc, so at least a few systems with projected separations of 0.5-2 kpc should be expected. Even in the most confused of cool ULIGs (IRAS 22491−1808), the two galaxy nuclei can be clearly differentiated from the star-forming clusters on the basis of their K′ emission. There are several apparently single nucleus systems which have extended nuclear regions with apparent bifurcating dust lanes (IRAS 00091−0738, IRAS 12112+0305, UGC 5101, Mrk 273, and Arp 220) which are very similar in appearance to the bifurcated core of IRAS 05189−2524. It seems possible that the original progenitor galaxy nuclei lie in this chaotic central region if they have not already coalesced. Indeed they must, because they aren't anywhere else in the system, and it seems unlikely that either heavy dust obscuration or a remarkable alignment along the line-of-sight could hide them.

None of the cool ULIGs shows evidence for the same kind of bright, extremely compact AGN-like nuclei as are found in several of the warm ULIGs such as Mrk 231. However, the *HST* images of Mrk 273 and UGC 5101 reveal that both of these systems have single, very compact (radius $\approx$ 100 pc) high surface brightness knots at I in their nuclear regions. Because there is also considerable structure in the nuclei of these systems, our ground-based optical images with limited spatial resolution cannot spatially separate these central nuclei from their luminous surroundings. Similarly, both our ground-based images and the *HST* data show the presence of a nearly unresolved object in IRAS 12112+0305. IRAS 23365+3604 also appears to have very compact nuclear structure, although it also has one of the lowest percentages of its total emission in its central 2.5 kpc region. These results point to the presence of "nuclei" in a small percentage (28%) of the cool ULIGs that are morphologically similar to some of the more extended, lower surface brightness "nuclei" in the warm ULIGs, such as IRAS 12071−0444 and IRAS 15206+3342. Three of these four are single nucleus systems, and all four have considerable numbers of star-forming knots visible near the nuclei in the *HST* data; all of these are suggestive of transition objects between the greater population of cool ULIGs (e.g., IRAS 14348−1447) and the AGN-like compact nucleus warm ULIGs (e.g., Mrk 231). That two of these systems (Mrk 273 and UGC 5101) are the only two cool ULIGs with known Seyfert spectra makes this explanation even more compelling (Sanders et al. 1988a, Khachikian & Weedman 1974).

All 14 systems show well-developed tidal tails and plumes. Many of these tails are curved to form circular or semi-circular ring-like structures (UGC 5101, IRAS 12112+0305, IRAS 15250+3609, IRAS 23233+0946). It is likely that many of the linear tails (UGC 5101, Mrk 273, IRAS 23365+3604) are similar structures seen edge-on. The tails have total projected lengths averaging 35 kpc and ranging from 9 kpc to 100 kpc; the ringlike structures are generally 15-30 kpc in radius. In almost every case, these tidal features appear to be circular rings or ring segments oriented nearly perpendicular to each other (i.e., Mrk 273,

UGC 5101, IRAS 23365+3604). In addition to these obvious cases where the disks and tails lie in a plane either parallel or orthogonal to the projected plane of the sky, many of the others can be explained as projections of this same geometry combined with additional rotation. In many cases it appears that the progenitor galaxies may have been rotating in opposite directions, judging from the opposing opening angles of the tidal tails, which have presumably inherited the angular momentum of their progenitors (e.g., IRAS 01199−2307, IRAS 23233+0946). Figure 4.3 shows UGC 5101 along with n-body simulations by Barnes (1992). The upper left panel shows the model disk encounter geometry, which is probably similar to that of many of the cool ULIGs. Two disks are inclined at nearly right angles to each other. The two meet in a slightly offcenter (non-zero impact parameter) plunging encounter. This type of encounter raises a nearly circular, off-center tail structure in the lower left galaxy as a result of the plunging orbit (Toomre 1978). The upper right panel shows the same system 1.4 Gyrs later (Barnes & Hernquist 1996). The lower left panel is the same as the upper right, only rotated to a different orientation. The bottom right panel shows the cool ULIG UGC 5101 at I-band for comparison.

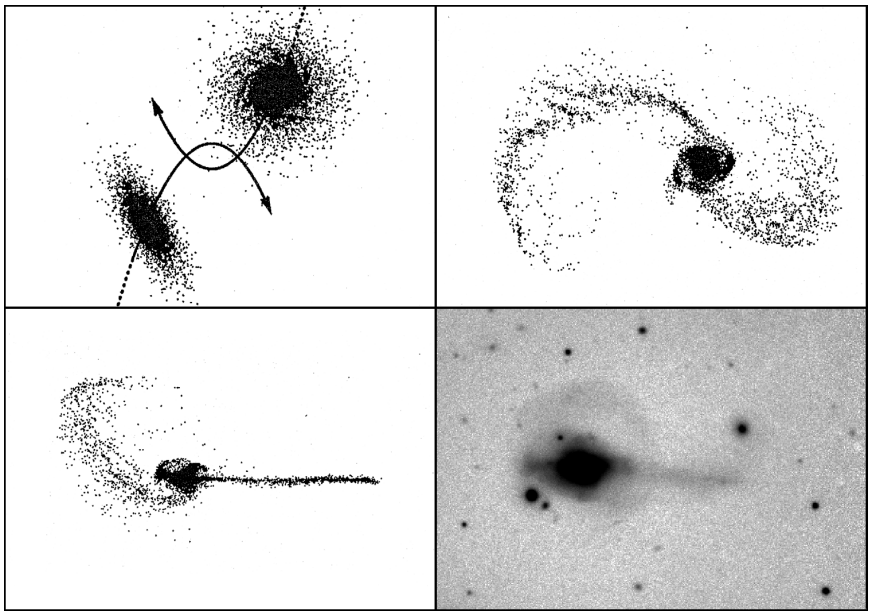

Fig. 4.3.— An illustration of the possible ULIG merger progenitor geometry: a plunging collision between two disks highly inclined to each other. At upper left is a schematic representation of such a collision. Upper right and bottom left show two orientations of the same 1.4 Gyr-old collision between two spiral galaxies, one of whose disks is in the orbital plane, and the other inclined to it by 71 °(Barnes 1992, Barnes & Hernquist 1996). At bottom right is an I-band image of UGC 5101, which strongly resembles the modeled remnant.

4.3.1.2. Star-Forming Knots and Small-Scale Structure

Many of the systems show evidence of the same clustered star formation seen in the "warm" ULIGs. Only IRAS 01199−2307, IRAS 03521+0028, IRAS 22206−2715, and IRAS 23233+0946 show no obvious high surface brightness compact knot-like features. Since

these are the four systems at the highest redshifts ($z > 0.13$), this may be an effect of the limited spatial resolution achievable from the ground; however, the physical spatial resolution for IRAS 00091−0738 is nearly as poor at $z = 0.12$, yet it shows considerable evidence for star-formation. Moreover, these systems are 4 of the 6 double nucleus systems and 3 of them have the largest projected separations, which may indicate a lack of clustered star formation at large nuclear separations. This is similar to other results which indicate that there may be a delay in star formation until some time after the first contact between galaxies (Joseph et al. 1984). The role of star-formation as characterized by far-infrared activity in very widely separated pairs is discussed in more detail in Appendix A. Figure 4.4 illustrates Richardson-Lucy deconvolved data for these star-forming regions. Figure 4.5 presents images of the *HST*/WFPC2 data for our sample objects, which can then be compared to the ground-based images in Figure 4.4.

In order to be recognized as real features in the deconvolved images, the small-scale structure must at least be recognizable in the undeconvolved images. This provides a means of allowing the real features to be discriminated from the amplified noise that produces the "mottling" effect in the deconvolved data. As in Chapter 2, the knots are defined as compact emission sources with closed isophotes that are more than 3σ above the local background. This distinction is made in an attempt to discriminate between the "knots", which appear to be compact bursts of star-formation, and the more extended "condensations" which appear to be a result of large-scale tidal structure. Examples of condensations can be seen in the southern arc of IRAS 12112+0305 and the western tail of UGC 5101. As was noted in Chapter 2, it is likely that all of the "knots" are actually unresolved aggregates of star- forming clusters like those seen in other, more nearby interacting galaxies. Given the even poorer spatial resolution of the ground based images (as opposed to those from *HST*), it is likely that many of the star-forming knots have become even more confused than in Chapter 2, and this confusion severely limits our ability to recognize the star-forming knots. Because of this, the analysis of the luminosity functions, etc., as were carried out in Chapter 2 cannot be repeated here meaningfully. Table 4.3 gives aperture photometry for the star-forming knots that could actually be recognized as such; it probably misses many more. It also does not list photometry for features that appeared to be more extended tidal structure, although in many cases there appears to be tidal structure in the form of arms and wisps even at very small scales. Details of this additional structure are discussed in §4.3.2. Positions are given relative to the brightest feature in I-band and corresponds to the aparrent stellar "nucleus".

Most of the star-forming knots are within a radius of a few kpc of the nuclei, a result suspected from previous aperture photometry studies which showed systematic color changes at small galactocentric radii (Carico et al. 1990). As in the warm ULIGs, knots and condensations are also seen along the tidal features; this is particularly apparent in IRAS 00091−0738, UGC 5101, Mrk 273, IRAS 12112+0305, IRAS 14348−1447, and IRAS 22491−1808.

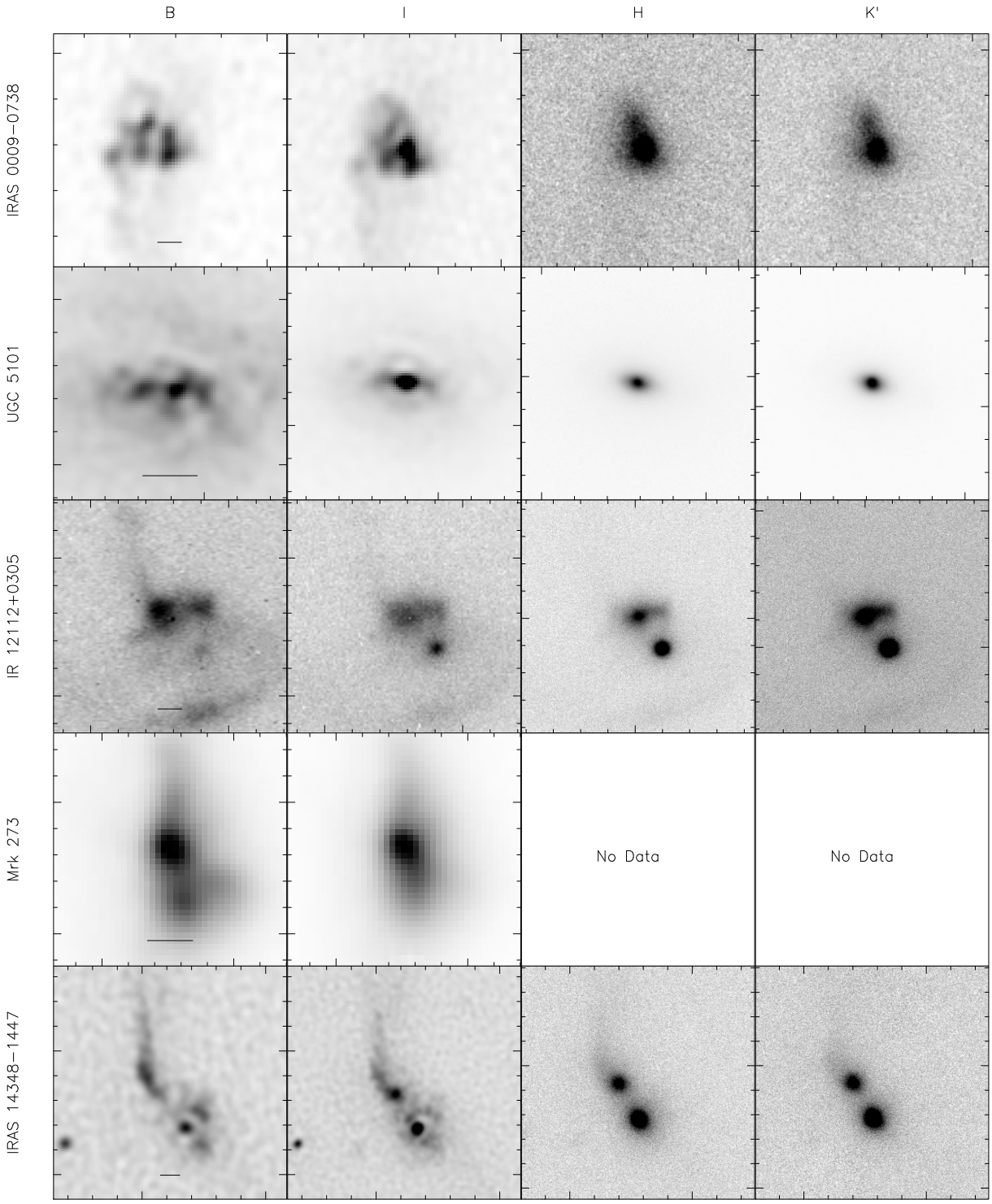

Fig. 4.4.— Selected images of high spatial resolution structure in the nuclear regions of the cool ULIGs. All of the optical data except IRAS 12112+0305 and Mrk 273 has been deconvolved with the Richardson-Lucy maximum likelihood algorithm. The physical scale-bar is 2.5 kpc in length. Tick marks are every $2''$with major ticks every $10''$.

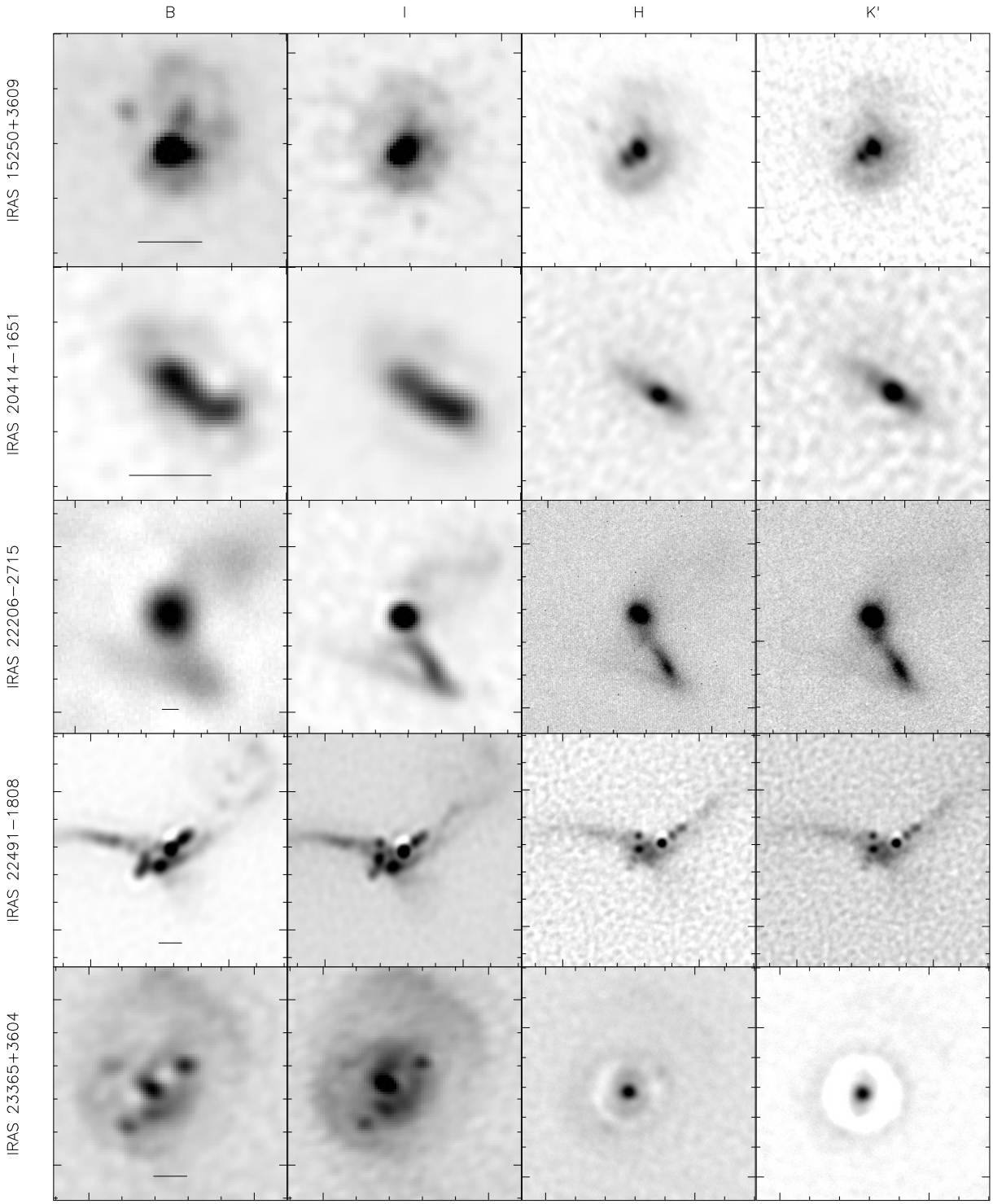

Fig. 4.4.— (continued)

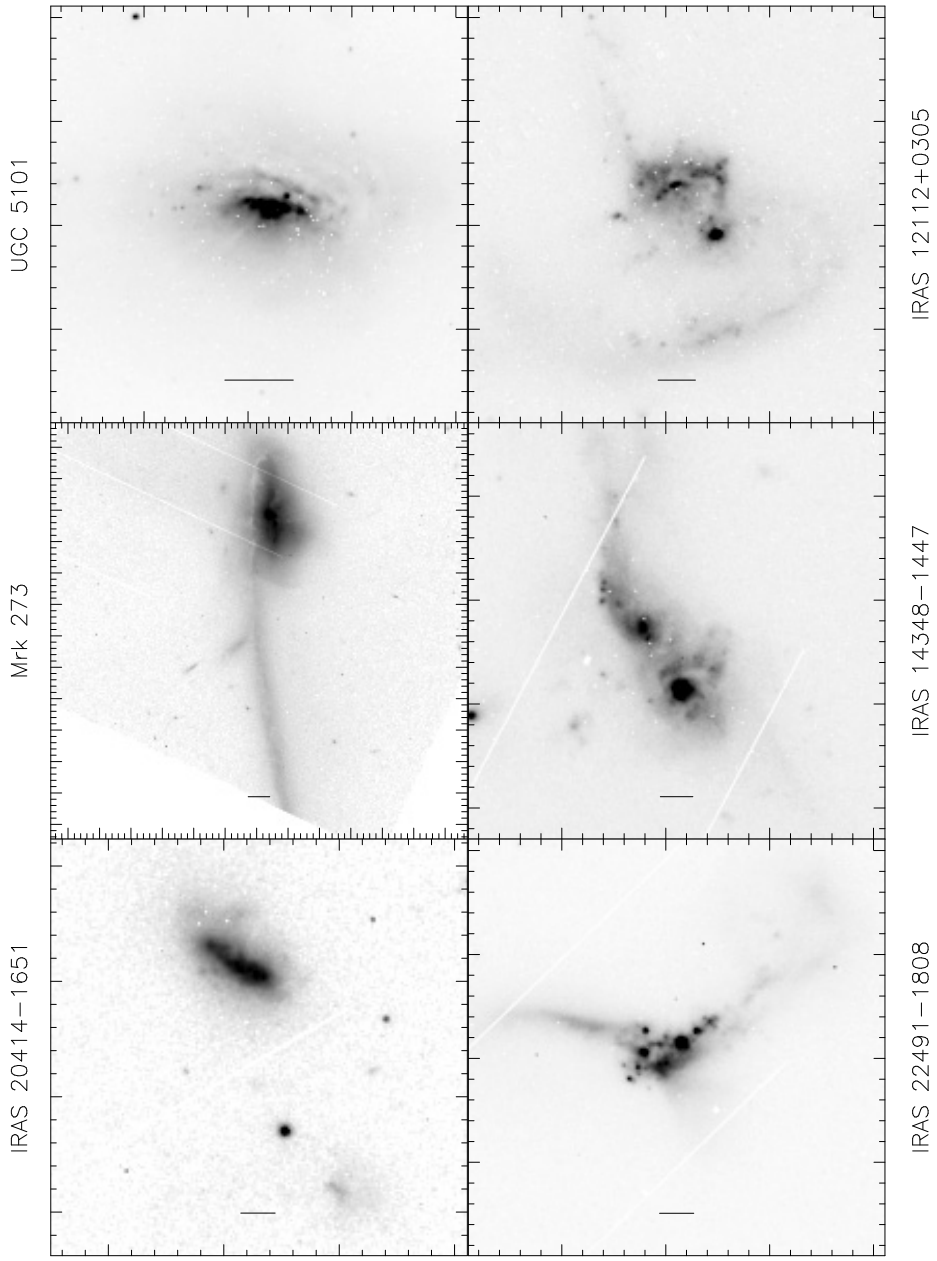

Fig. 4.5.— *HST*/WFPC2 archival F814W (I-band) images of ULIGs from the "cool" ULIG sample. Each tick mark is 1 $''$, and the physical scale-bar is 2.5 kpc. The very high spatial resolution (FWHM $\approx$ 0.1 $''$) *HST* is qualitatively very similar to the ground-based data. The observing strategy neccessitated by the snapshot survey resulted in the many bad pixels and data dropouts seen.

4.3.2. Luminosities

The "cool" ULIGs do not show morphological evidence for the compact putative AGN found in the "warm" ULIGs. Instead, most of the "nuclei" appear to be stellar in nature. Therefore, we discuss only the luminosities of the host galaxies and the star-forming knots.

4.3.2.1. Host Galaxies

Luminosities were computed using equation 2.1. As in Chapter 3, we consider the H-band luminosity as the best indicator of the total mass of the old stellar population, and hence the combined mass of the merger progenitors. It additionally is much less affected by extinction than shorter wavelength observations. Unfortunately, this is somewhat more complicated in the case of the cool ULIGs than it was for the warm ULIGs (and will be for the PG QSOs dealt with in the next chapter) . In particular, since the warm ULIGs each appeared to contain a compact AGN-like nucleus, it was easy to subtract this nuclear component, as well as any emission from compact star- forming knots, from the extended host galaxy. In the case of many of the cool ULIGs, there is not such a clear-cut "nuclear" component. Instead, the "nuclei" of the cool ULIGs often appear to be diffuse, extended regions with complex structure; a large fraction of the luminosity in the nuclear regions is likely to be old starlight, in which case it should not be subtracted from the global H-band luminosity.

Several approaches are considered in computing the total H-band luminosity of the host galaxy. First, the total flux at H-band, including any star-forming knots, galaxy nuclei, etc. is considered. It is expected that this will set an upper limit on the host galaxy luminosity, since it must necessarily include additional, young stellar population components. In this way it is found that the cool ULIGs are similar in luminosity to the warm ULIGs. In chapter 3 the H-band luminosity of an L^* galaxy was estimated to be between $M_{\rm H}=-23.8$–24.1; we adopt here $M_{\rm H}=-23.9$. The cool ULIGs are found to have total luminosities ranging from $M_{\rm H}=-23.38$ (Arp 220) to $M_{\rm H}=-24.7$ (IRAS 14348−1447, IRAS 22206−2715), with a mean value of $M_{\rm H}=-24.23$. This range is from 0.6–2.1 L^*, with a mean of 1.4 L^* and with roughly half of the ULIGs lying between 1.5–2.5 L^*. However, there are no 5–7 L^* systems as there were with the warm ULIGs.

However, this result is complicated by the finding that the colors of the nuclear regions of the cool ULIGs are consistent with reddening from 2–5 $A_{\rm V}$ (see §4.3). As was indicated in Chapter 3 for IRAS 08572+3915, it is therefore likely that the unreddened global values derived above are, in reality, slight underestimates. 1 $A_{\rm V}$ of reddening corresponds to 0.18 $A_{\rm H}$ (Reike & Lebofsky 1985). In the most extreme (hypothetical) case that all of the luminosity lay within the inner 2.5 kpc (since these reddening values were determined inside this region), then dereddening would at most increase the luminosity of the galaxies by 1 magnitude at H. In actuality this effect is much more modest, as can be demonstrated by dereddening just the observed luminosity in the nuclear regions and adding this to the outer galaxy luminosity; typically this increases the galaxy luminosity by 0.1 mag, ranging from 0.08 in IRAS 23233+0946 to 0.4 in UGC 5101. The dereddened luminosities

then range from $M_{\rm H}=-23.8$ to $M_{\rm H}=-24.9$ or 0.9–2.5 L^*. Excluding the anomalous case of IRAS 01003−2238, this is very similar to the range found for the warm ULIGs, and is consistent with the merger of two galaxies; a result also suggested by the extended morphologies of the ULIGs.

At the other extreme, it is possible to examine the luminosity of the outer galaxy by simply excluding all of the flux in the 2.5 kpc nuclear region. On average, 37% of the H-band flux lies within a radius of 1.25 kpc of the center of the galaxy, varying from 52% (IRAS 00091−0738) to 17% (IRAS 23365+3604). Excluding the central regions, the luminosity of the outer galaxies then range from $M_{\rm H}=-23$ (0.4 L^*) to $M_{\rm H}=-24.5$ (1.7 L*). Obviously, these are considerable underestimates — it is likely that the previous dereddened results are closer to the truth. Furthermore, the fraction of H-band light inside the central regions is similar to that found in the bulges of disk galaxies (Kent 1985), further indicating the likelihood that the central region contains a considerable amount of old starlight.

Table 4.2. Cool ULIG Global and Nuclear Photometry

Name	$m_{\rm B}$		$m_{\rm I}$		$m_{\rm H}$		$m_{\rm K'}$	
	Global	Nuclear[a]	Global	Nuclear	Global	Nuclear	Global	Nuclear
IRAS 00091−0738	18.37	19.41	16.36	17.26	14.81	15.29	14.31	14.86
IRAS 01199−2307	17.82	19.46	16.69	18.00	15.11	16.20	14.85	16.20
IRAS 03521+0028	20.50	22.91	17.49	19.32	14.91	16.10	14.11	15.32
UGC 5101	14.91	17.91	14.60	16.47	11.53	12.40	10.83	11.47
IRAS 12112+0305n	16.97	19.97	15.05	17.99	12.88	15.28	12.76	14.60
IRAS 12112+0305s		21.62		18.37		15.00		14.09
Mrk 273	14.69	17.07	13.16	15.25	...	...	...	...
IRAS 14348−1447e	16.51	20.58	14.58	18.09	12.92	15.45	12.19	14.67
IRAS 14348−1447w		20.13		17.64		14.85		14.04
IRAS 15250+3609	16.17	17.52	15.19	16.56	12.98	14.02	12.77	13.55
Arp 220	14.00	17.55	12.25	14.66	10.93	11.62	10.62	10.92
IRAS 20414−1651	17.94	20.18	16.11	17.72	14.02	14.84	13.49	14.05
IRAS 22206−2715e	17.26	18.72	15.78	16.94	14.01	15.26	13.45	14.68
IRAS 22206−2715w		19.33		17.24		15.91		15.49
IRAS 22491−1808e	16.44	18.59	15.00	17.05	13.26	15.67	12.97	15.15
IRAS 22491−1808w		19.90		18.13		16.33		15.07
IRAS 23233+0946e	18.12	20.85	15.80	18.31	14.16	16.39	13.80	16.17
IRAS 23233+0946w		19.72		17.41		14.94		14.71
IRAS 23365+3604	16.17	19.53	14.32	17.11	12.58	14.47	12.19	13.77

Note. — [a] central region 2.5 kpc in diameter. Global magnitudes are listed only under the first nucleus, but refer to the entire system. Ellipses indicate missing data.

4.3.2.2. Star-Forming Knots

The star-forming knots have B-band luminosities ranging from $M_{\rm B}=-14.4$ to $M_{\rm B}=-18.5$, which is similar to or slightly higher than those observed for the "warm" ULIGs. The higher values are likely to result from confusion. The more limited spatial resolution of the ground-based optical observations (typically 0.7–0.8 $''$at B) yields a physical resolution of 1 kpc at the median redshift. Any given knot optically detected from the ground is therefore likely to contain at least several of the knots detected by *HST*. An examination of Figure 4.5 confirms that in some cases (i.e., Mrk 273) this occurs, while in others (IRAS 22491−1808) this effect may be much less. Also, in Chapter 2 it was found that the luminosity function of the knots continued to increase until reaching the detection limit of $M_{\rm B}=-12$, but confusion and limited spatial resolution prevent our reaching such low detection limits. Finally, any differences in the ages of the stellar populations of the knots would be expected to change their luminosities by several magnitudes. The total integrated luminosity of the star- forming knots (the sum of all knot luminosities) at B-band ranges from $M_{\rm B}=-17.21$ in IRAS 00091−0738 to $M_{\rm B}=-19.50$ in IRAS 14348−1447, with a median value of $M_{\rm B}=-18.34$. This approximately 6 times more luminous than the mean integrated B-band luminosity of the knots in the warm ULIGs. The total fraction of the galaxy B-band luminosity found in the star-forming knots ranges from 6% to 25%, with a median of 11%. By comparison, the warm ULIGs vary from less than 1% (PKS 1345+12) to nearly 40% (IRAS 15206+3342), but this much larger spread in the total percentage is due to the presence of the putative active nuclei. The highest percentage (and total luminosity) are found in the two double nuclei with detectable star-forming knots: IRAS 22491−1808 and IRAS 14348−1447, which may be indicative of the increased luminosity of the knots with younger ages, if the presence of double nuclei actually implies younger age.

Very few of the knots are detected at near-infrared wavelengths. Significant numbers of detections occur only in IRAS 12112+0305, IRAS 15250+3609, and IRAS 22491−1808. The K-band luminosities for the detected knots range from $M_{\rm K'}=-17.97$ to $M_{\rm K'}=-23.04$, which again is similar to those found in most of the "warm" ULIGs. The implications of the non-detections are discussed below. The total integrated luminosity of the star-forming knots detected at K′ ranges from $M_{\rm K'}=-17.97$ to $M_{\rm K'}=-23.47$. Considering the upper limits imposed by the non-detections, the typical cool ULIG has an $M_{\rm K'}$ originating in the star-forming knots of no more than −21.24. In those warm ULIGs with knots detectable in the near-infrared, this same number ranged from −20.56 to −23.96, a very similar range.

4.3.3. Colors

The same confusion over the definition of "nuclei" that plagues the determination of the underlying galaxy luminosity also creates problems for the color analysis. In order to help eliminate redshift-dependence, we will define "nuclear" to mean the central region of the galaxy 2.5 kpc in diameter. At the redshift of the most distant object in our sample (z= 0.152), this corresponds to 0.8$''$, which under the worst conditions is roughly the size of one resolution element at optical wavelengths. Table 4.2 also gives "nuclear" magnitudes in each of the 4 observed filters.

Table 4.3. Star-Forming Knot Photometry

Number	ΔRA[a]	ΔDEC	$m_{\rm B}$	$m_{\rm I}$	$m_{\rm H}$	$m_{\rm K'}$
			IRAS 0009−0738			
1	1.1	0.3	21.23	19.11	> 18.50	> 18.61
			UGC 5101			
1	1.9	0.0	18.79	18.00	> 17.92	> 17.93
2	−5.6	−0.3	20.24	20.04	> 17.63	> 18.66
3	−4.6	0.7	20.03	19.85	> 17.63	> 18.66
4	−3.8	2.9	20.42	20.03	> 17.63	> 18.66
5	9.4	1.4	20.61	20.27	> 17.90	> 19.00
6	6.3	10.0	21.63	20.15	18.07	18.03
			IRAS 12112+0305			
1	−2.8	0.3	20.32	18.22	15.92	15.53
2	−2.7	−2.8	21.62	18.37	15.09	14.33
3	−2.8	−7.4	19.90	18.31	16.69	16.32
			Mrk 273			
1	−0.7	−3.64	17.61	16.09	...	...
			IRAS 14348−1447			
1	−1.1	1.3	19.31	18.42	> 17.75	> 17.17
2	−1.3	−1.4	19.69	18.42	> 17.75	> 17.17
3	3.2	4.1	19.12	18.25	> 18.00	> 17.03
			IRAS 15250+3609			
1	0.5	−0.4	...	...	14.39	13.96
2	1.5	1.4	20.50	17.86	18.50	18.33
3	−0.5	1.1	19.33	18.21	17.07	16.53
4	−2.0	0.7	20.18	19.61	18.43	18.13
5	−0.3	−1.1	19.97	18.74	16.88	16.55
			IRAS 20414−1651			
1	1.8	1.1	19.86	18.21	17.86	17.18
2	−3.8	−9.0	20.69	19.76	> 18.40	> 18.13
			IRAS 22491−1808			
1	0.0	1.0	21.44	18.46	16.98	16.65
2	−2.5	1.1	19.79	19.38	17.18	16.73
3	−3.2	1.5	20.35	19.38	17.19	16.73
4	−1.0	−0.6	19.07	18.00	16.92	> 17.19
5	0.4	−1.1	20.28	19.11	18.56	> 17.76

Table 4.3—Continued

Number	ΔRA[a]	ΔDEC	m_B	m_I	m_H	$m_{K'}$
			IRAS 23365+3604			
1	−1.9	1.4	19.93	18.45	> 18.00	> 17.65
2	2.2	1.3	21.55	20.62	> 18.88	> 18.69
3	1.4	−2.4	20.29	19.57	> 18.88	> 18.25
4	−0.3	−1.5	19.70	17.84	> 17.80	> 17.32

[a] RA and DEC offsets measured from the centroid of the "nucleus", i.e., the brightest emission source at I-band

The $(B-I)$,$(I-H)$,$(H-K')$ colors of the central 2.5 kpc regions of the cool ULIGs are shown in Figure 4.6 and 4.7. These figures are similar to Figures 3.6 and 3.7, and show the colors of an instantaneous starburst, a synthetic QSO spectrum, and several reddening mechanisms (hot dust emission, stars mixed with dust, and line-of-sight extinction). Also labeled are the median colors of the "warm" ULIGs, which for reasons presented in Chapter 3 are likely to be AGN viewed along a complex, lightly extinguished path. Most of the cool ULIG nuclei have colors characteristic of a young (10- 100 Myr) stellar population combined with hot (800K) dust emission that contributes 30–40% of the K′ flux, or of a mixture of stars and absorbing dust with a total optical depth approaching 30–50 A_V. However, the more complete mixed stars and dust model with scattering that was discussed in Chapter 3 indicates that it is difficult to acheive such reddened colors in this way, which strongly suggests that the $(H-K')$ excess is actually due to hot dust emission. These colors are similar to the range observed by Carico et al. (1990b) in the "LIGs" ($L_{IR} > 10^{11}\ L_\odot$). Whether they are stars mixed with hot dust emission or just stars mixed uniformly with extinguishing dust, they additionally appear to be reddened by a uniform foreground dust screen of 1–5 A_V, which is considerably higher than any foreground screen found in the "warm" ULIGs for either the nuclei or the star-forming knots. The presence of a greater foreground reddening screen than that in the warm ULIGs is qualitatively consistent with the evolution scenario in which an obscuring dust screen is blown away from the initial merger state. Alone among the cool ULIGs, IRAS 22491−1808e appears to have optical/near-infrared colors almost identical to that of the median "warm" ULIG colors. This is possible evidence that IRAS 22491−1808 harbors an AGN, although it's K′ luminosity ($M_{K'} = -22.37$) is more than an order of magnitude fainter than that of a QSO (see section 3.3.4). It is perhaps surprising that UGC 5101 does not also have AGN-like colors. However, the *HST* images reveal much structure in the vicinity of the compact *I*-band nucleus that cannot be resolved from the ground optically, and it is likely that this structure is contaminating our results.

The colors of the star-forming knots are more problematic to analyze. This is primarily because they are not as well determined as the nuclear colors due to their irregular shapes and small sizes, and because they are not detected in many cases in the near-infrared despite

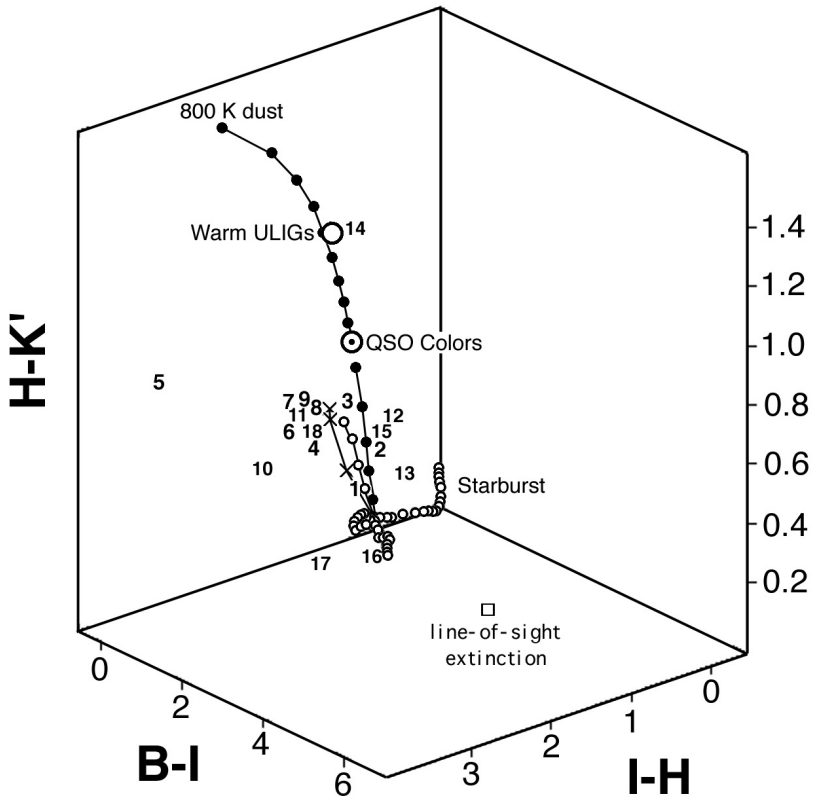

Fig. 4.6.— $(B-I)$,$(I-H)$,$(H-K')$ color cube as in Figure 3.7 illustrating the colors of the "cool" ULIG nuclear ($R < 1.25$ kpc) regions. For clarity, the ULIGs have been marked with numbers: (1) IRAS 00091−0738 (2) IRAS 01199−2307w (3,4) IRAS 03521+0028e,w (5) UGC 5101 (6,7) IRAS 12112+0305n,s (8,9) IRAS 14348−1447e,w (10) IRAS 15250+3609 (11) IRAS 20414−1651 (12,13) IRAS 22206−2715 (14,15) IRAS 22491−1448 (16,17) IRAS 23233+0946 and (18) IRAS 23365+3604. The cube is rotated to be orthogonal to the reddening vector. The median colors of the "warm" ULIGs are marked with a large circle. Other markings are the same as Figure 3.7. All of the ULIGs are consistent with stellar emission combined with dust extinction and hot dust emission, except for IRAS 22491−1808e.

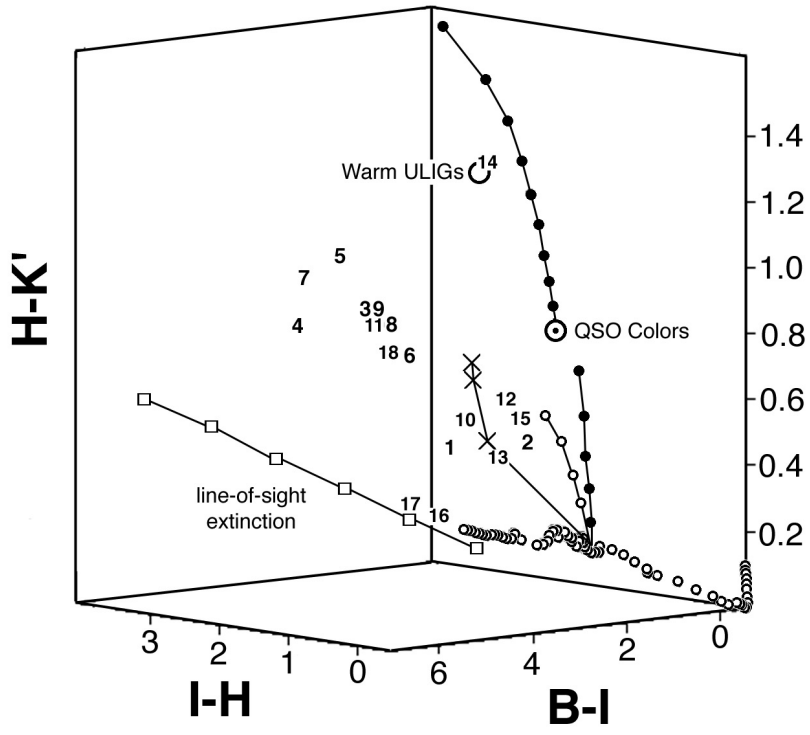

Fig. 4.7.— Same as Figure 4.6, but rotated as to be parallel to the reddening vector. It is apparent that most of the nuclei lie inside a narrow region of the three-color diagram and are most consistent with stellar emission reddened by 1–5 A_V.

the superior resolution at long wavelengths. For the non-detections, the upper limits on the near-infrared luminosities of the knots constrain their colors, and hence their ages. Fig 4.8 shows the ($B-I$),($I-H$) colors of the modeled starburst used in the previous chapters (BC 95). It is apparent that for starburst colors of ($I-H$) < 1 the modeled starburst age is constrained to less than 10 Myrs. As noted in Chapter 2, with detections only at B and I, and upper limits in the near-infrared, it is only possible to set upper limits to the knot ages; dereddening will always *decrease* the estimated ages. Many of the cool ULIGs with detectable star-forming knots (IRAS 00091−0738, UGC 5101, IRAS 14348−1447, IRAS 20414−1651, IRAS 22491−1808 and IRAS 23365+3604) have at least several knots whose ages cannot be more than 5–7 Myrs. However, several also have knots that are sufficiently red that their age limits can only be estimated to be less than 1 Gyr (UGC 5101, IRAS 12112+0305, Mrk 273, IRAS 22491−1808) or a few hundred Myrs (IRAS 15250+3609 and IRAS 22491−1808). Thus, while we can show the presence of young stars, we cannot easily fix a lower age limit, thereby demonstrating the presence of intermediate age stars. We do, however, note that presence of young stars seems to be much more prevalent among cool ULIGs than among warm ULIGs. While this could arguably be an effect of greater reddening in the warm ULIGs, the results presented here run counter to this in that the cool ULIG nuclei seem to suffer greater foreground reddening than that found in the warm ULIGs.

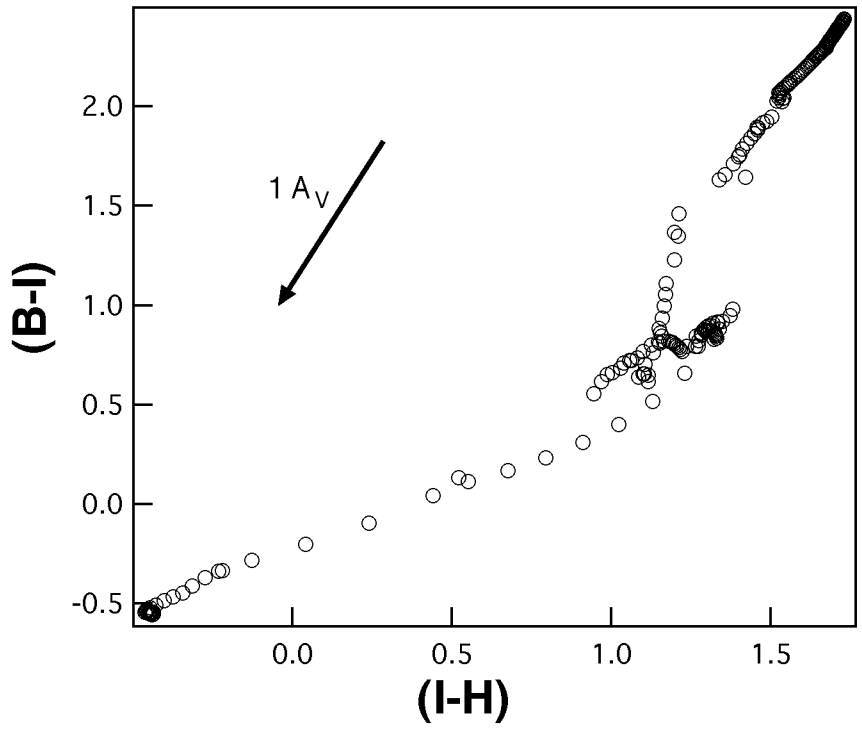

Fig. 4.8.— ($B-I$),($I-H$) color-color diagram for an instantaneous starburst having a Salpeter IMF and a mass range from 0.1–125 $M_\odot$. Systems with (I-H) < 1 are constrained to be less than 10 Myrs in age.

4.4. Relationship of Optical/Near-Infrared Emission to Bolometric Luminosity

In Chapter 3 it was found that in many cases the putative AGN in the warm ULIGs could be made to account for the high bolometric luminosities of the systems by assuming a QSO-like SED and extrapolating from the observed optical/near-infrared luminosities. It is possible to apply similar techniques to the emission in the cool ULIGs. Starburst models are chosen since the optical/near-infrared colors appear to be characteristic of young stars. The bolometric luminosity will then be determined based on both empirical and theoretical models.

The theoretical SED models are based on the BC95 models. As before, a modeled instantaneous starburst with a Salpeter IMF and upper and lower mass cutoffs of 0.1 and 125 $M_{\odot}$was used. For any given age, a bolometric correction (BC) can be determined from the models to derive a bolometric luminosity based on the luminosity at some other waveband. Fig 4.9 shows the bolometric correction as a function of age for K-band. It is immediately apparent that the bolometric correction hinges critically on the age of the starburst. Prior to 5 Myrs, the luminosity is dominated by short-wavelength emission from high mass OB stars; very little of the bolometric luminosity originates in the late- type stars that emit strongly at long wavelengths. At 10 Myrs this changes radically as the most massive stars age and emit the bulk of their luminosity at progressively longer wavelengths, and hence the bolometric correction spans fully 6 magnitudes depending on the age. With this model, an ultraluminous starburst could have $M_K < -21.2$ for a young burst, or $M_K = -27$ for an old one. Ironically, the change in bolometric correction with age is much less at shorter wavelengths (Fig 4.9 also shows the BC as a function of age for B- band), but the uncertainty in luminosity caused by dust extinction at short wavelengths may offset any gain. It can be argued that ages of 10 Myrs and shorter for *all* of the knots are unlikely for several reasons. The cool ULIGs span a considerable range in interaction morphology. The presence of star-forming knots in most of these systems (as well as the more dynamically evolved, based on presence of single nuclei, warm ULIGs presented in chapter 2), however, indicates that the star formation history for the knots as a whole must be similar to the dynamical timescale, i.e., hundreds of Myrs. Similarly, the wide range in colors seen in many of the knots in the ULIGs may be evidence for a spread in knot ages, although this may also be due to reddening.

While B-band observations are strongly affected by dust extinction (as noted earlier), we can constrain the maximum amount of foreground extinction on the basis that the starlight can only be dereddened to the colors of the bluest young starbursts. Most of the star-forming knots, therefore, cannot be dereddened by more than 2 magnitudes. This yields a fraction of the bolometric luminosity contributed by star-formation detected at B-band with a young (less than 10 Myr), dereddened starburst between 1% (IRAS 00091−0738) and 100% (IRAS 22491−1808), with a median value of 6%. If the starburst is older (100 Myrs), then these percentages fall by a factor of 6. An additional uncertainty results from the large geometric corrections to the luminosity discussed in Chapter 3. However, the scattering models indicate that it is relatively difficult to acheive the red colors observed in Figures 4.6–4.7 via a stellar ensemble mixed with dust alone, and that they are more likely

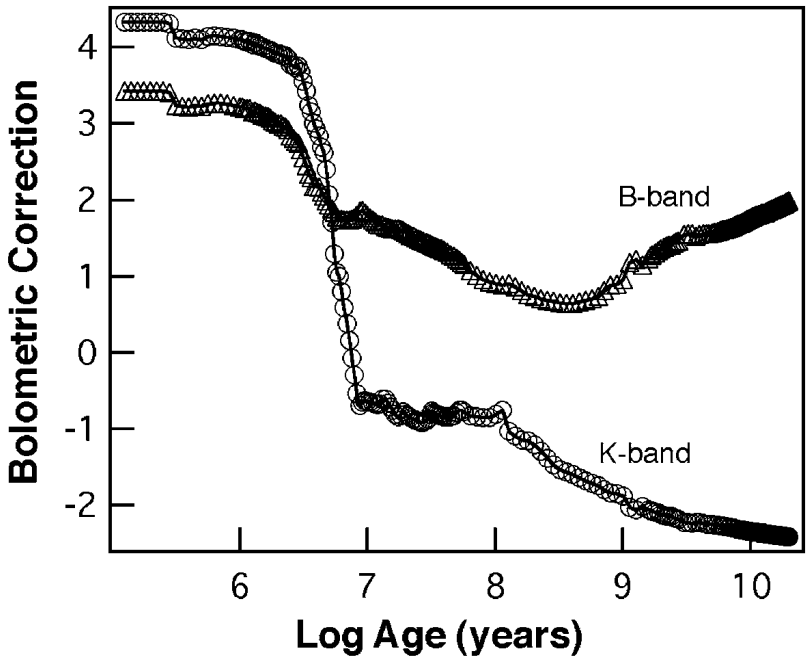

Fig. 4.9.— Bolometric corrections for K-band (circles) and B-band (triangles) for an instantaneous starburst with a Salpeter IMF ranging from 0.1 to 125 $M_{\odot}$ (BC95).

to be a result of hot dust emission and foreground extinction. If the stars are embedded in a thick dusty medium then this would typically increase their luminosity by factors of 3–6.

Results for the K-band are least affected by uncertainties in dust extinction, and hence should give the best luminosity estimate. We have examined those cases where star formation can be morphologically separated from the underlying host galaxy stellar population, i.e. those systems that show evidence for star-forming knots. The total K-band flux was dereddened by the amount indicated by the nuclear optical/near-infrared colors and then the portion attributable to starlight (typically 50–70%, again determined by the colors) was separated out. These extinction estimates are likely to be overestimates, given the high extinctions derived from the nuclear colors and the maximum extinctions derived from just the knot optical colors. As discussed above, the BC95 models cannot readily constrain the bolometric luminosity based on the K-band luminosity due to the enormous age dependence of the BC. If the star-forming knots are very young, (less than 1 Myr), then every cool ULIG with detectable knots at K′could conceivably derive its entire bolometric luminosity from the star-forming knots alone. The upper limits for the knots not detected at K′can only constrain the bolometric luminosity under this assumption of extremely young stellar age to being just under the emasured ULIG bolometric luminosities. If the knots are more than 10 Myrs in age, then it is likely that none of the ULIGs could have contributions to their bolometric luminosities by star-forming knots much above 50%, and in most cases it would be less than 10%.

The empirical model is again based on the BC from K-band to $L_{\rm ir}$ found in the LIGs (Carico et al. 1990; equation 3.7). Assuming that 75% of the bolometric luminosity is emitted in the far-infrared (Sanders et al. 1988a), then this is equivalent to a bolometric correction of 0-0.5 for $M_{K'}=-20$ – -25, or roughly equivalent to the modeled value for a starburst 10 Myrs old (i.e. a BC of 0–0.5 will convert between $M_{K'}$ to $M_{\rm bol}$ in LIGs). Using equation 3.7, the derived total bolometric luminosity for the detected star-forming knots ranges from 10^{10} $L_\odot$ to $10^{11.4}$ $L_\odot$. The typical ULIG which has star- forming knots detected in *any* band has a contribution to the bolometric luminosity of not more than $10^{10.5}$ $L_\odot$. This falls short of the average cool ULIG bolometric luminosity by a factor of 60 (assuming $L_{\rm ir}$ =0.75 $L_{\rm bol}$ and using the measured average $L_{\rm ir}$ = 1.45×10^{12} $L_\odot$for cool ULIGs). It thus appears that *nothing* detected optically or in the near-infrared in the cool ULIGs is capable of generating the high bolometric luminosity assuming the kinds of SEDs we have used here. Whatever the power source, it must be more highly obscured in the cool ULIGs than in the warm, a result supported by the estimated extinctions derived from the optical/near-infrared colors.

4.5. Conclusions

We have presented high spatial resolution images of a sample of "cool" ULIGs. We find that:

1. All of the systems are major mergers, as manifested by tails and other merger-induced extended structure.

2. A large fraction (at least 43% and as high as 72%) have resolvable double galactic nuclei.

3. Most of the "cool" ULIGs have evidence for compact star-forming knots, with the exception of the systems with the widest separations. This may indicate that clustered formation begins in earnest only during the end stages of the merger, just before nuclear coalescence, although this result may also partly be due to the limited ground-based resolution.

4. The nuclear colors of most of the cool ULIGs appear similar to that of a mixture of stars and extinguishing dust with a total optical depth of 30–50 $A_{\rm V}$, or of young stars with a modest amount of the K'emission (30%) originating in hot (800 K) dust. This host dust emission is then further extinguished by a uniform dust screen 1–5 $A_{\rm V}$ thick. Unlike the "warm" ULIGs, the optical/near-infrared emission from the nuclear regions of the cool sample is probably stellar in nature.

5. The dereddened H-band luminosities of the cool ULIG host galaxies lie in the range 0.9–2.5 L^*, and are thus essentially identical to that of the warm ULIGs and are consistent with their apparent merger origin. There are, however, no systems with $L_{\rm H} > 3$ L^*, unlike the warm ULIGs.

6. Very few of the star-forming knots are detected in the near- infrared, nor are any new knots (much like the "warm" ULIGs). Constraints imposed by the limits of their (I-H) colors imply very young ages ($<$ 5– 7 Myrs) for many of these knots. They cannot be

extinguished by more than a very mild foreground reddening screen ($< 2\ A_V$), and any additional knots must be very deeply embedded.

7. As in the "warm" ULIGs, it appears that in most cases the star- forming knots are insufficiently luminous to be the source of the high bolometric luminosity, although in some cases they may provide a significant fraction. Although the constraints are found to be very model dependent, using assumptions similar to those used in the warm ULIGs, the observed optical/near-infrared observable knots provide typically only about 2% of the high bolometric luminosity, ranging from less than 1% to about 20%. This is very similar to the results found for the warm ULIGs. It appears unlikely that anything seen in the optical or near-infrared is related to the high bolometric luminosity, unless it has an SED much more biased towards the far-infrared.

4.6. Notes on Individual Objects

IRAS 00091−0738 — a system very similar in appearance to IRAS 12112+0305 with an extremely complex nuclear core 3.5 kpc in diameter bifurcated N-S by dust lanes. A thick, perhaps edge-on tail extends 19 kpc (projected distance) to the south, while another plume-like tail extends 20 kpc to the north. At near-infrared wavelengths the core becomes a single source 0.7″ in diameter, with a tidal tail to the north. This connects to and appears to be the base of the optical tidal tail which loops around back towards the south, and appears similar to the structure seen in the core of IRAS 12112+0305. Identified as having HII spectra by Veilleux et al. (1998).

IRAS 01199−2307 — double nucleus system separated by 25 kpc, the largest of any ULIG in this sample. Both nuclei are ellipsoidal in appearance and remain similar to spiral bulges; Veilleux et al. (1998) identifies these as having HII spectra. The NE nucleus is surprisingly faint in the near-infrared compared to the SW; additionally, at K′ it takes on the appearance of two lobes, the SW of which seems to correspond to the optical nucleus, and the NE to the arm extending from it. The western tail is 48 kpc in total length, with an apparent projected linear length of 40 kpc. The fainter eastern tail is 30 kpc long.

IRAS 03521+0028 — double nucleus system separated by 4.3 kpc. Short, stubby tails extend 9 kpc from each nucleus in an E-W direction. No additional star-forming knots or other structure are seen. This galaxy has LINER optical spectra (Veilleux et al. 1997).

UGC 5101 - a nearby system from the BGS, identified as a Seyfert 1.5 by Sanders et al. (1988a). A linear tail stretches 38 kpc to the west from the nucleus. A second tail runs clockwise from a position angle of -90 to form a nearly complete circle 225 degrees around with a radius of 17 kpc and a total length of 65 kpc. The optical morphology seems to suggest that the two sets of tails are actually similar features lying in planes perpendicular to each other. The *HST* images clearly reveal a set of spiral dust lanes to the north of the nucleus; the nucleus itself is dominated by a small (200 pc) size emission region. This spiral structure, along with that in the core of Mrk 273, may resemble that seen in the warm ULIG Mrk 231 (Chapter 2), only rotated out of the plane of the sky.

IRAS 12112+0305 — this galaxy appears to consist of a double-lobed core similar to that seen in IRAS 00091-0738, with a bright tidal tail extending 18 kpc to the north and another arc 30 kpc long loops along the south. The orientation of the tails suggests that the northern tail is parallel to the line of sight, while the southern lies tilted by 45 °. The southern arc has a blue condensation halfway along its length. A red star-like object is located 4 kpc SW of the core. Seen by Carico et al. (1990), this is unlikely to be a supernova since it has not faded noticeably in the intervening 7 years. It is not a foreground star as recent near-infrared spectroscopy (Surace, unpublished) indicates that it is at the same redshift as the nucleus to its north — if it is a starburst knot or AGN then its total lack of U′ emission indicates a line of sight extinction of at least 3 $A_{\rm v}$ (see §6.5). Kim (1995) identifies this ULIG as having a LINER spectrum.

Mrk 273 — a very narrow ($\approx$ 2.5kpc) linear tidal tail extends 41 kpc south of the nucleus. Two diffuse plumes extend north and northeast 40 kpc each. The new deep images suggest that these plumes actually connect to the NE, making a complete ring nearly 100 kpc in circumference. In this respect it may be very similar to UGC 5101, which it strongly resembles. The *HST* image of the galaxy core at I-band clearly shows a pattern of dust lanes running along the long axis of the nucleus, closely resembling those seen in edge-on spiral galaxies. The nucleus is dominated by a small, yet extended emission region. Khachikian & Weedman (1974) identify this as a Seyfert 2.

IRAS 14348−1447 — two nuclei separated by 5.3 kpc. A plume extends north 20 kpc from the NE nucleus. A second plume stretches 17 kpc to the SW from the SW nucleus, where it merges with a fan-shaped plateau of emission extending from the NE to the SW of the galaxy. At least a dozen star- forming knots are seen in the *HST* image. The circular ring of knots surrounding the SW nucleus are well detected in our B & I images, as are the knots in the base of the northern tail. We fail to detect these (or any other) knots in either near-infrared filter. Although Nakajima et al. (1991) claimed detection of a broad-line component in the SW nucleus, Veilleux et al. (1997) fail to confirm this and designate this galaxy as a LINER.

IRAS 15250+3609 — an apparently single nucleus system, this galaxy has at least three other galaxies nearby to the north, south and west. However, it is unclear if these galaxies are physically related to the merger system. A tidal feature appears to emerge from the SW side of the nucleus and loops around on the eastern side to create a closed ring 27 kpc in diameter and 80 kpc long. Another, aparrently shorter arm extends from the northeast of the nucleus. Near-infrared imaging reveals several additional knots of star formation near the nucleus. Veilleux et al. (1995) classify this as a LINER.

Arp 220 — the closest and hence most well-studied of all ULIGs. A short tail extends approximately 30 kpc to the northwest (Sanders et al. 1988; Hibbard 1995). Because this ULIG appears be radically different from all others in terms of its high degree of variable dust obscuration, the registration between our ground-based optical data and the NICMOS data is highly uncertain. Therefore, the 2.5 kpc aperture photometry should be regarded with caution; we have assumed that the bright near-infrared peaks are spatially coincident with the optical dust lane. Kim (1995) classifies this as a LINER galaxy. The reader is

directed towards a wealth of literature on this object (Sanders et al. 1988a, Graham et al. 1990, Skinner et al. 1997, Scoville et al. 1998).

IRAS 20414−1651 — this complex system is somewhat different from the other ULIGs. It has a horseshoe-shaped main body with some sort of extended structure "corkscrewing" 17 kpc to the south, which then bends west and meets with a very blue stellar condensation. Kim (1995) identifies this as having HII spectra.

IRAS 22206−2715 — two nuclei separated by 9.2 kpc. The northern nucleus is circular in shape, perhaps suggesting that it is viewed face on. The southern nucleus is elongated and bar-shaped, suggesting a spiral galaxy inclined by roughly 60 °, an idea supported by the zig-zag nature of the tidal tail emanating from it. Each tail is approximately 20 kpc in total length. Like many of the other galaxies here, this seems to be a collision between two galaxies with high relative inclination, resulting in one broad, almost circular tidal tail, and one that is seen edge-on, or nearly so. Veilleux et al. (1998) find HII spectra.

IRAS 22491−1908 — the most extreme example of clustered star- formation in the sample. At optical wavelengths the knots of star-formation create so much confusion as to preclude identification of the galaxy nuclei. Only in the near-infrared do the two nuclei, separated by 2.5 kpc, stand out. The system has two high surface brightness tails. The first extends 12.5 kpc NE from the main body of the galaxy and is essentially featureless. The second extends NW 16 kpc from the main body, but ends in a complex, face-on circular loop 10 kpc in diameter. This tail has two very red clumps of star formation at its base, and the circular disk at the end of the tail has many blue knots of star formation. The *HST* data seem to suggest that the NE tail may also terminate in a somewhat fainter version of this disk. This galaxy has an HII spectrum (Sanders et al. 1988a, Veilleux et al. 1995).

IRAS 23233+0946 — two nuclei separated by 8.5 kpc. A tidal tail 19 kpc in linear distance and apparently 28 kpc in total length extends to the SE. Both nuclei have colors consistent with an old stellar population. Veilleux et al. (1998) classify this as a LINER.

IRAS 23365+3604 — this galaxy has a single, point-like nucleus embedded in a face-on disk 20 kpc in diameter. Four large star-forming knots are contained in this disk, and are detected even in the near-infrared. The disk itself has a twisting spiral structure. A faint linear tail extends north for 60 kpc from the nucleus. Another, higher surface brightness tail extends 20 kpc due south from the nucleus. This tail has an odd projection halfway along it's length — a short (few kpc) tail jutting west from its side, not unlike the feature seen in the linear tail of Mrk 273. Veilleux et al. (1995) classify this as a LINER.

REFERENCES

Barnes, J.E. 1992, ApJ, 393, 484

Barnes, J.E., & Hernquist, L. 1996, ApJ, 471, 115

Borne, K.D., Bushouse, H., Colina, L. & Lucas, R.A. 1997, BAAS, 191, 2102

Carico, D.P., Graham, J.R., Matthews, K., Wilson, T.D., Soifer, B.T., Neugebauer, G. & Sanders, D.B. 1990a, ApJ, 349, L39

Carico,D.P., Sanders, D.B., Soifer, B.T., Matthews, K., & Neugebauer, G. 1990b, AJ, 100, 70

Condon, J.J., Huang, Z-P., Yin, Q.F., & Thuan, T.X. 1991, ApJ, 378, 65

de Grijp, M.H., Miley, G.K., Lub, J., & de Jong, T., 1985, Nature, 314, 240

Elias, J.H., Frogel, J.A., Matthews, K. & Neugebauer, G. 1982, AJ, 87, 1029

Graham, J.R., Carico, D.P., Matthews, K., Neugebauer, G., Soifer, B.T., & Wilson, T.D. 1990, ApJ, 354, L5

Hibbard, J.E. 1995, PhD. Thesis, Columbia, New York

Joseph, R.D., Meikle, W., Robertson, N.A., & Wright, G.S. 1984, MNRAS, 209, 111

Kent, S.M. 1985, ApJS, 59, 115

Kim, D-C., 1995, PhD. Thesis, University of Hawaii

Khachikian, E.Y., & Weedman, D.W., 1974, ApJ, 192, 581

Knapen, J.H., Laine, S., Yates, J.A., Robinson, A., Richards, A., Doyon, R., & Nadeua, D. 1997, ApJ, 490, L29

Landolt, A. 1982, AJ, 88, 439

Landolt, A. 1992, AJ, 104, 340

Majewski, S.R., Hereld, M., Koo, D.C., Illingworth, G.D., & Heckman, T.M., 1993, ApJ, 402, 125

Murphy, T., Armus, L., Matthews, K., Soifer, B.T., Mazzarella, J.M., Shupe, D.L., Strauss, M.A., & Neugebauer, G. 1996, AJ, 111, 1025

Nakajima, T., Kawara, K., Nishida, M., & Gregory, B., 1991, ApJ, 373, 452

Reike, G.H. & Lebofsky, M.J. 1985, ApJ, 288, 619

Sanders, D.B., Soifer, B.T., Elias, J.H., Madore, B.F., Matthews, K., Neugebauer, G., & Scoville, N.Z. 1988a, ApJ, 325, 74

Sanders, D.B., Soifer, B.T., Elias, J.H., Neugebauer, G.,& Matthews, K. 1988b, ApJ, 328, 35

Scoville, N.Z., Evans, A.S., Dinshaw, N., Thompson., R., et al. 1998, ApJ, 492, L107

Skinner, C.J., Smith, H.A., Sturm, E., Barlow, M.J. et al. Nature, 386, 472

Toomre, A., 1978, in "IAU Symposium: The Large Scale Structure of the Universe", (D. Reidel Publishing Co.: Dordrecht), 79, 109

Veilleux, S., Kim, D-C., & Sanders, D.B, Mazzarella, J.M., & Soifer, B.T., 1995, ApJ, 98, 171

Veilleux, S., Kim, D-C., & Sanders, D.B., 1998, ApJ, *in prep*

Veilleux, S., Sanders, D.B., & Kim, D-C. 1997, ApJ, 484, 92

Chapter 5

Observations of Infrared-Excess Palomar-Green QSOs[1]

ABSTRACT

Ground-based high spatial-resolution (FWHM < 0.3–$0.8''$) BIHK$'$ imaging is presented for a complete sample of optically selected QSOs which have been additionally selected to have infrared excesses similar to those of "warm" ULIGs. In all cases, the host galaxies of the QSOs were detected and have considerable two-dimensional structure. 76% of the QSOs occur in spiral hosts, and 22% are unmistakably the result of a galaxy merger. Another 27% have strong nuclear bars or other nuclear disturbances consistent with (but not necessarily implying) very advanced merger systems. Several of the systems have knots of star formation similar to those seen in other merger systems and in the ULIGs. H-band luminosities of the hosts range from 0.4-7.5 L^* with a mean of 2.2 L^*, and are consistent with those found in ultraluminous infrared galaxies.

5.1. Introduction

Since their initial discovery thirty-five years ago, quasi-stellar objects (QSOs) have been the subject of enormous debate. Chief among these debates has been the question of what mechanism is the source of their enormous luminosities. The observed short-period variability of QSOs, the appearance of collimated radio jets in radio-loud quasars, and the presence of broad emission lines all helped drive the "standard model" of QSO structure, namely one involving accretion disks surround supermassive black holes. However, the size-scale of the accretion disk is relatively small, and it is difficult to drive new material at the required rate into the nucleus from the rest of the galaxy; this problem is known commonly as "feeding the monster" (Gunn 1979).

Early n-body experiments by Toomre & Toomre (1972) had suggested that galaxy collisions might be able to bring large supplies of material deep into the central regions of galaxies. Additional theoretical work has helped support this picture (Hernquist 1989, Bekki & Noguchi 1994, Barnes & Hernquist 1996). Many other studies have implicated various kinds of galaxy interactions as being important to nuclear activity. Stockton & MacKenty (1987) demonstrated directly the presence of merger activity (in the forms of bridges and other extended emission) in a considerable fraction of QSO host galaxies. More recent *HST* results have similarly provided direct evidence of interactions and mergers (Bahcall et al. 1997). A large body of evidence indicates that even minor interactions alone, and not actual mergers, can fuel QSO activity, since the rate of companion galaxies in close proximity to QSOs is abnormally large (Yee 1987, Lake et al. 1998). Some workers have even taken this idea one step further with the claim that perhaps the interactions are all that are required

[1]Chapters 5 & 7 will be submitted to ApJ as " Multiwavelength High Resolution Observations of Infrared-Excess QSO Host Galaxies", by Surace & Sanders

and that an interaction induced super-starburst can produce at least the radio-quiet QSO phenomena without invoking black holes at all (Terlevich 1989).

Many other galaxies (e.g., Seyfert galaxies, radio galaxies) have forms of abnormally energetic behavior lumped under the general heading of active galactic nuclei (AGN). IRAS discovered a new class of AGN: galaxies that had QSO-like bolometric luminosities ($L_{\rm bol} > 10^{12}\ L_{\odot}$) yet which emitted nearly all of their luminosity at far-infrared wavelengths. Many of these galaxies showed evidence for merger activity along with optical line ratios similar to that of other AGN. Tying together the theoretical framework for merger-induced fueling along with an evolutionary timeline, Sanders et al. (1988) proposed that these so-called ultraluminous infrared galaxies (ULIGs) were the immediate progenitors of optically selected QSOs, and that ULIGs represented a stage in QSO evolution where the active nuclei were enshrouded in gas and dust. This dust shroud reradiates the nuclear emission at far-infrared wavelengths; eventually, powerful winds (Heckman et al. 1990) would disperse the dust and reveal an optical QSO nucleus.

Since an understanding of the QSO phenomena seems to hinge critically on understanding the fueling mechanism, much attention has turned to the environment in which the quasar nucleus is presumably embedded. It has long been known that Seyfert active nuclei resemble lower-luminosity optical QSOs in many ways, and are additionally the nuclei of galaxies. Indeed, the distinguishing feature often used to differentiate QSOs and Seyfert galaxies was the morphological difference that QSOs appeared primarily stellar and did not appear to be embedded in luminous galaxies (Schmidt & Green 1983). Since that time, increasing numbers of observations from the ground have demonstrated to the contrary the presence of extended emission around QSOs apparently compatible with being galaxies (Hutchings et al. 1984, Gehren et al. 1984, Neugebauer et al. 1987). More recent imaging from the ground, particularly in the near-infrared, has begun to investigate in detail the galactic environments of QSOs (Hutchings & Neff 1992, McLeod & Rieke 1994a,b, Kukula et al. 1997).

Traditionally, the greatest impediment to detecting QSO host galaxies has been the relatively low surface brightness of the galaxies relative to the QSO nucleus. Under typical ground-based seeing conditions (FWHM $\approx$ 1– 1.5″) and with typical detectors (particularly with photographic methods), the glare (residual PSF contamination due to seeing and scattered light) from the QSO nucleus has been sufficient to obscure the host galaxies. One of the prime motivators of *HST*, equipped with modern CCD detectors and possessing 10–20 $\times$ the spatial resolution of ground-based instruments (at optical wavelengths), was to image QSO hosts. Ironically, the early results from these projects have been mixed at best, and contradictory at worst. Early reports indicated that many of the observed QSOs had no detectable hosts with limits of typically 1 L* (Bahcall et al. 1995), which was surprising in light of earlier studies and was immediately contradicted by ground-based follow-ups (Neugebauer et al. 1995, McLeod & Rieke 1995). Subsequent additional *HST* imaging showed the presence of detectable hosts, but seemed to indicate that they existed in such a diverse number of environments that it was unclear if any common environment existed (Bahcall et al. 1997).

This apparent state of confusion motivated a new ground-based high spatial resolution study of nearby optically-selected QSOs in order to provide a new, uniform set of imaging data to investigate the questions opened by the *HST* controversy. By observing a complete sample with properties similar to those of ULIGs and using the same instruments and techniques, the question of the relationship between the structure of the QSO hosts and the host galaxies of ULIGs could be investigated. The development of high quantum efficiency, large format detectors spanning the wavelength range from the near-ultraviolet to the near-infrared meant that a detailed study could be carried out over a wide range of wavelengths dominated by different emission processes. The advent of adaptive optics techniques coupled with superior ground-based sites also meant that this imaging could be carried out with much higher spatial resolution than ever before possible, making detection of QSO host galaxies and any compact features within them much easier (see Chapter 1).

We report the results of an imaging survey at B, I, H, and K′-band of a complete sample of low redshift ($z<$ 0.16) QSOs selected from the Palomar-Green Bright Quasar Survey (Schmidt & Green 1983). Their morphology, luminosity, and colors are compared to those of the ULIGs in Chapters 2–4, and the implications for the ULIG-QSO evolutionary scenario are discussed.

5.2. Data

5.2.1. Sample

Details of the sample selection were discussed in Chapter 1.4.3. Briefly, this is a complete sample of all Palomar-Green (PG; Schmidt & Green 1983) QSOs with redshifts $z<$0.16, thus placing them in the same space volume as the "cool" and "warm" ULIG samples (see Chapters 2-4). In order to search for transition objects which might bridge the gap between "warm" ULIGs and the general QSO population an additional selection criterion was imposed. Only those PG QSOs with infrared excesses (compared to their blue luminosity) at least as high as those of the warm ULIGs were selected (i.e., $L_{\rm ir}/L_{\rm blue} > 0.46$[2]). $L_{\rm ir}$ and $L_{\rm blue}$ were calculated from the data presented in Sanders et al. (1989). There are 18 such infrared-excess PG QSOs, however, 3 of these (I Zw 1, Mrk 1014, and 3c273) are also "warm" ULIGs and have already been discussed in detail in Chapters 2 & 3.

It is worth noting that there is a strong morphological selection bias built into the Palomar-Green Survey. In particular, the survey states that a QSO " ...should have a dominant starlike appearance on blue prints of the 48 inch (1.2 m) Schmidt Sky Atlas..." (Schmidt & Green 1983). This criterion was then used to distinguish between QSOs and Seyfert galaxies. Objects which might have shown broad lines but had particularly luminous host galaxies were thus discarded as Seyfert 1s. This criterion was then further used to create

[2] $L_{\rm ir} \equiv L(8 - -1000\mu{\rm m})$ is computed using the flux in all four *IRAS* bands according to the prescription given in Perault (1987). $L_{\rm blue}$ is computed from the luminosity at 3200–8400Åand a bolometric correction of -1.75 appropriate for QSOs (Sanders, private communication).

the M_B <-23 luminosity criterion used to define QSOs, as most of the objects below this criterion showed evidence for nebulosity, but those above did not. However, this criterion is flawed; numerous studies have shown that typically the QSO nucleus and its host galaxy are of comparable luminosity (McLeod et al. 1994a,b), although this is wavelength dependent. Therefore, distant objects measured through large apertures might meet the luminosity criterion due to the presence of their host galaxies. Additionally, lower redshift objects whose nuclei might meet the luminosity criterion but whose host galaxies are also very bright and/or extended will be rejected. In short, the PG BQS is biased against QSOs with luminous extended hosts at low redshifts. Other studies (Goldschmidt et al. 1992, Kohler et al. 1997) have indicated quantitatively that the BQS is incomplete and heavily biased. In particular, it seems to be incomplete by at least a factor of 2 for low redshift, low luminosity QSOs ($z< 0.3; -23 > M_B > -24.1$). This morphological bias is likely to skew the results of this study towards finding systems with low luminosity hosts and towards hosts with few recognizable features. Any results found here regarding the fractions of QSOs with luminous, extended (and possibly with interacting morphologies) hosts are likely to be underestimates of the true fraction. On the other hand, Kohler et al. (1997) also finds that the space density of high luminosity QSOs has been severely underestimated in the BQS. The results presented here, particularly in regards to what fraction of the QSO population has what properties, should therefore be interpreted strictly in the light of our sample selection criteria. The question of their relevance to the general QSO population, whatever that might be, may have to wait until a better understanding of the space density of QSOs is achieved.

5.2.2. Observations and Data Reduction

The data was taken with the UH 2.2m telescope at f/31 using a fast tip/tilt guider in the same manner as the "cool" ULIGs discussed in Chapters 4. B & I- band data was acquired with the Tektronix 2048 and Orbit 2048 cameras. In most cases this was by direct imaging at the f/31 cassegrain focus. In these cases, the data was binned on chip 2x2, yielding adopted pixel scales of 0.14 and 0.09″, respectively. In a few cases the data was obtained by reimaging the f/31 beam at f/10 through the HARIS spectrograph using the Orbit 2048 camera, yielding a pixel scale of 0.14″. The near-infrared data was acquired with the QUIRC camera. In all cases exposure times were short enough (60–240 seconds) to prevent saturation of the QSO nucleus, thus allowing PSF subtraction during post-processing. Total exposure times varied from 9 to 45 minutes per filter; details of the observations are given in Table 5.1.

One QSO, PG 1202+281, could not be observed as there were no guide stars sufficiently bright ($m_V < 13$) and nearby ($R < 5'$) to enable the use of guider at the UH 2.2m f/31 focus. This QSO was, however, observed by *HST*. Several other QSOs (PG 1229+204, PG 1402+261, and PG 2130+099) were also observed with *HST*/WFPC2 as part of other's observing programs (Hutchings & Morris 1995, Bahcall et al. 1997), and were available through the STScI archival retrieval system. The three PG QSOs which are also warm ULIGs (I Zw 1, Mrk 1014, and 3c273) have also been observed with *HST* (Surace et al. 1998, Bahcall et al. 1995); since this data appears elsewhere in the literature and in other

Table 5.1. Details of PG QSO Observations

Name	Inst.[a]	Exposure Times (sec)			
		B	I	H	K′
PG 0007+106	QT	2280	2520	1980	1980
PG 0838+770	QT	1920	2520	2520	1800
PG 1001+054	QT	2680	840	2160	2040
PG 1114+445	QO	1440	1080	540	720
PG 1119+120	QT	1080	1860	1680	1440
PG 1126−041	QT	2340	1860	900	1080
PG 1202+281	W	...	...	...	...
PG 1229+204	QH	1200	960	2040	1440
PG 1351+640	QT	2280	1800	1440	1560
PG 1402+261	WQT	3240	1800	2400	1200
PG 1411+442	QO	1440	1200	1200	2220
PG 1415+451	QH	1200	1440	2280	2400
PG 1440+356	QT	1500	1680	1500	1920
PG 1613+658	QT	900	720	2100	2700
PG 2130+099	WQT	2340	1260	2640	2400

[a] Q = UH2.2m f/31 QUIRC, T = UH2.2m f/31 Tektronix 2048, H = UH2.2m f/31 Orbit reimaged at f/10 through HARIS spectrograph, O = UH2.2m f/31 Orbit, W = *HST*WFPC2

chapters, it is not presented here. The WFPC2 images were generally taken through the F606W and F702W filters which correspond roughly to V and R-band, and are therefore not directly comparable to our data. They are, however, valuable for interpreting morphology that is only marginally resolved in our ground-based imaging. This data was reduced in the same manner as that in Chapter 2; i.e., by shifting and rotating according to the astrometric solution provided by STScI, and combined using the GCOMB task in IRAF/STSDAS, along with its cosmic ray-rejection routines.

Point spread functions for the ground-based data were constructed as in Chapters 3 & 4 by modeling the stars seen in the individual combined observations. For the *HST*/WFPC2 data, PSFs were theoretical PSFs were calculated using the TinyTim software (Krist 1994). The PSFs were important in determining the photometry since they provided all of the needed aperture corrections.

The data was flux calibrated through observations of Landolt and Elias standard stars in the optical and near-infrared (Landolt 1983,1992, Elias et al. 1982 ; see Appendix 3). In most cases the nights were photometric with $\sigma_{\rm M} < 0.05$. For data taken on non-photometric nights, we have calibrated the data by using large fixed-aperture photometry already in the literature for the targets. Specifically, the near-infrared data for PG 0007+106 and PG 1001+054 were calibrated using the photometry given in Neugebauer et al. 1987 and the magnitude zeropoints contained therein. Optical data for PG 1119+120, PG 1440+356,

PG 1613+290, and PG 2130+099 were calibrated using the photometry of Neugebauer et al. (1987) and the magnitude zeropoints of Bessel (1979).

5.3. Results

5.3.1. Morphology

5.3.1.1. Large-Scale Features

Host galaxies were detected around every QSO observed. Their morphology is surprisingly diverse. Figure 5.1 presents the wide-scale morphology of all the QSOs (except Mrk 1014, PG 1202+281, and 3c273) at all four observed wavelengths. In each case the images have been stretched in an attempt to emphasize the faint structure in the host galaxies. Figure 5.2 presents the optical data for every QSO except PG 1202+281 and 3c273 as near-truecolor images (we have no optical data for these two objects). These images are the easiest to understand and hence the most instructive for the following discussion.

Of the 18 QSOs, 13 appear to have spiral or spiral-like hosts based on the presence of spiral arms, rings and bars. One galaxy is known to be an elliptical (3c273; Bahcall et al. 1997). Additionally, Bahcall et al. (1997) find that the one galaxy we did not observe (PG 1202+281) is a small elliptical; McLeod et al. (1994b) claim a detection but give no information on spatial structure. The remainder (PG 1001+054, PG 1351+640, & PG 1415+451) are indeterminate and lack any obvious structure in their extended emission. These three indeterminate cases also have very high nuclear luminosity fractions, thus making them hard to classify. Our morphologies generally agree well with existing published data (Hutchings & Neff 1992, Dunlop et al. 1993, McLeod et al. 1994ab) . Adopting the criteria for radio "loudness" of $P_{5GHz} > 10^{24.7}$ watts Hz^{-1} (Woltjer 1990) and the radio fluxes of Kellerman et al. (1994), we find that all of our sample QSOs are radio-quiet except for 3c273. Since at least 76% of the radio-quiet QSOs in our sample occur in spiral hosts, this seem to support earlier claims that radio-quiet QSOs occur most often in spirals, and contradicts some recent claims that elliptical hosts are more predominant (Bahcall et al. 1997). The only radio-loud object, 3c273, is known to have an elliptical host. This may be a result of the way the sample was selected: our QSO sample was chosen specifically to have an infrared excess. It is known that infrared-selected samples of galaxies are biased strongly against ellipticals; for example, elliptical galaxies are vastly under-represented in *IRAS* surveys, presumably due to a lack of dust (Sulentic 1988, see Appendix A.3.2).

5 hosts (PG 0838+770, PG 1119+120, PG 1126-041, PG 1229+204, and PG 1402+281) have strong nuclear bars ranging from 10–22 kpc in length. These thick bars may have been detected previously and been thought to be elliptical hosts; deeper imaging reveals spiral arms and rings attached to them. The fraction of barred systems (27% 5/18) is similar to that usually found for intermediate-type field spirals and early-type spirals found in the field or in groups (Elmegreen et al. 1990).

The host galaxies of PG 0007+106, Mrk 1014, PG 1411+442, and PG 1613+658 have tidal tails and arms and are unmistakably recent merger systems. Thus, at least 22%

(4/18) of the far-infrared excess PG QSOs occur in merger systems. This is similar to the ≈15% interaction fraction found by Bahcall et al (1997). Moreover, Hutchings et al. (1992,1994,1995) classified PG 1229+204 as a merger involving a small companion resulting in the observed bar and ring structures. Hutchings & Neff (1992) also propose that PG 2130+099 may also be in a post-interaction state, although it is not clear if it's disturbed morphology necessarily implies that. None of the four merger systems with obvious tidal tails is one of the barred systems.

5.3.1.2. Star-Forming Knots

Compact high surface brightness emission regions are detected in 33% (6/18) of the QSO hosts. In particular, "knots" of star formation like those found in the ULIGs are detected in PG0007+106, I Zw 1, Mrk 1014, PG 1119+120, PG 1229+204, PG 1411+442 and PG 1613+658. Four of these are also the same systems that show evidence for merger activity; a fifth is also postulated to be a merger remnant (Hutchings & Neff 1992). Of the remainder, PG 1119+120 shows evidence for a very red off-nuclear knot, as well as several very blue knots embedded in structure of the outer arms. I Zw 1 has evidence for knots embedded in its spiral arms. Figure 5.4 shows some of the small scale-scale nuclear structure, enhanced by a variety of techniques. In most cases the observed PSF had insufficient S/N to be used for a high quality point source subtraction. In Figure 5.4 radial profile models have been fitted to the QSO nuclei using the ELLIPSE and BMODEL routines in IRAF/STSDAS. The models were then subtracted from the raw data, leaving just the non-radially symmetric component of the QSO host galaxy behind. Even with this technique, structure within a radius of 1–2″(2–4 kpc) of the nucleus generally cannot be recovered at optical wavelengths. In the near-infrared the situation is considerably better, as illustrated by the detection of the "jet"-like feature in PG 1411+442. Unfortunately, the host galaxies have much less structure at these wavelengths. In several cases a modified version of this technique was used. Models were fit using the JIP imaging package; only in this case the radial models were based on specific position angles, allowing exclusion of obvious structure such as stars from the model. This generally results in a more accurate model which has less tendency to oversubtract from the host galaxy.

The small scale structure is displayed in Figure 5.4. The optical data for I Zw 1 and Mrk 1014 appear in figure 5.2, while the near-infrared data appear in Chapters 3. The nuclear subtracted I-band image of PG 0007+106 clearly shows an arc or tidal tail similar to that in Mrk 231. The nuclear-subtracted image of PG 1229+204 shows the galactic bar, as well as the condensations both in the bar and near it's ends. The data for PG 1411+442 shows a north-south structure extending both north and south in each direction from the nucleus. Since the northern extension seems to be the base of the tidal tail, it is possible the southern one is actually the base of a fainter counter-tail. There are many bright condensations or knots in the northern tail itself. The image to it's right shows the bright knot (or possibly jet-like) feature to the southwest. The bottom two panels show PG 1613+658. On the left is the nuclear-subtracted wide-field image, showing the long tidal tail to the east and what appears to be a counter-tail extending west. The right hand panel shows a deconvolved K′image of the nuclear regions. To the northeast is the bright

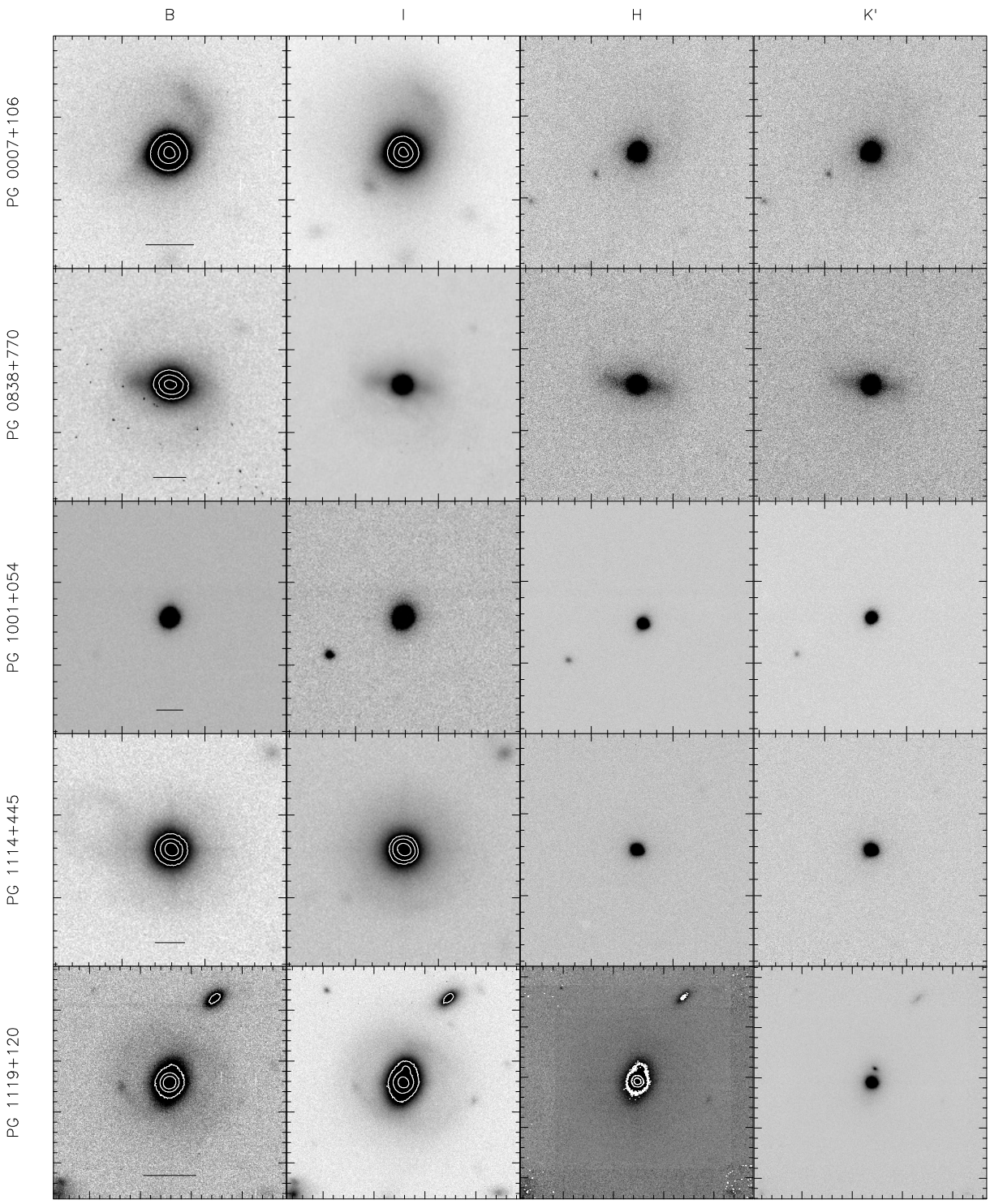

Fig. 5.1.— BIHK′ data for the infrared-excess PG QSO sample. Image intensities have been scaled to accentuate the low surface brightness features in the host galaxies. Ticks are every 1″, with major ticks every 10″. The scale bar is 10 kpc.

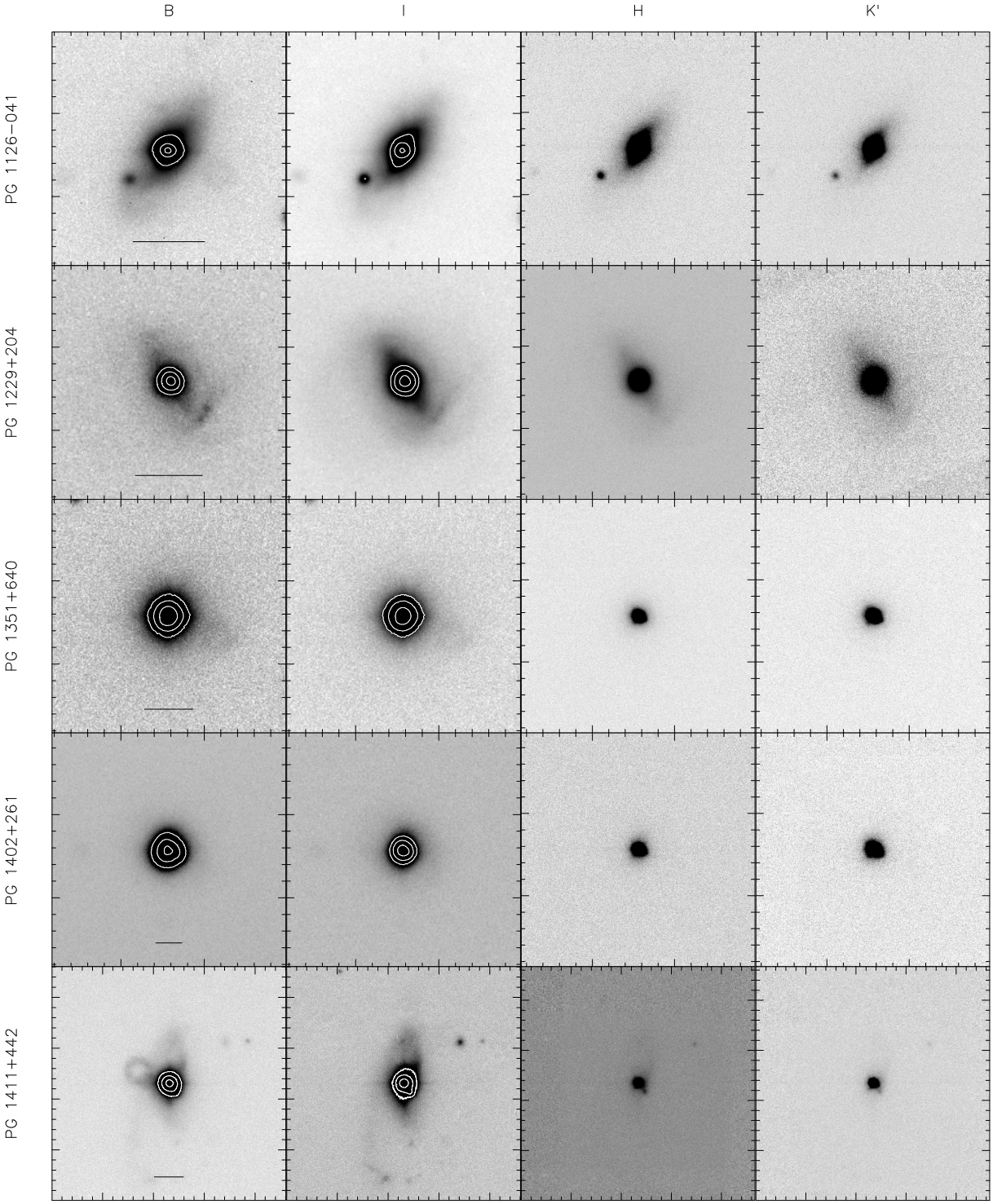

Fig. 5.1.— (continued)

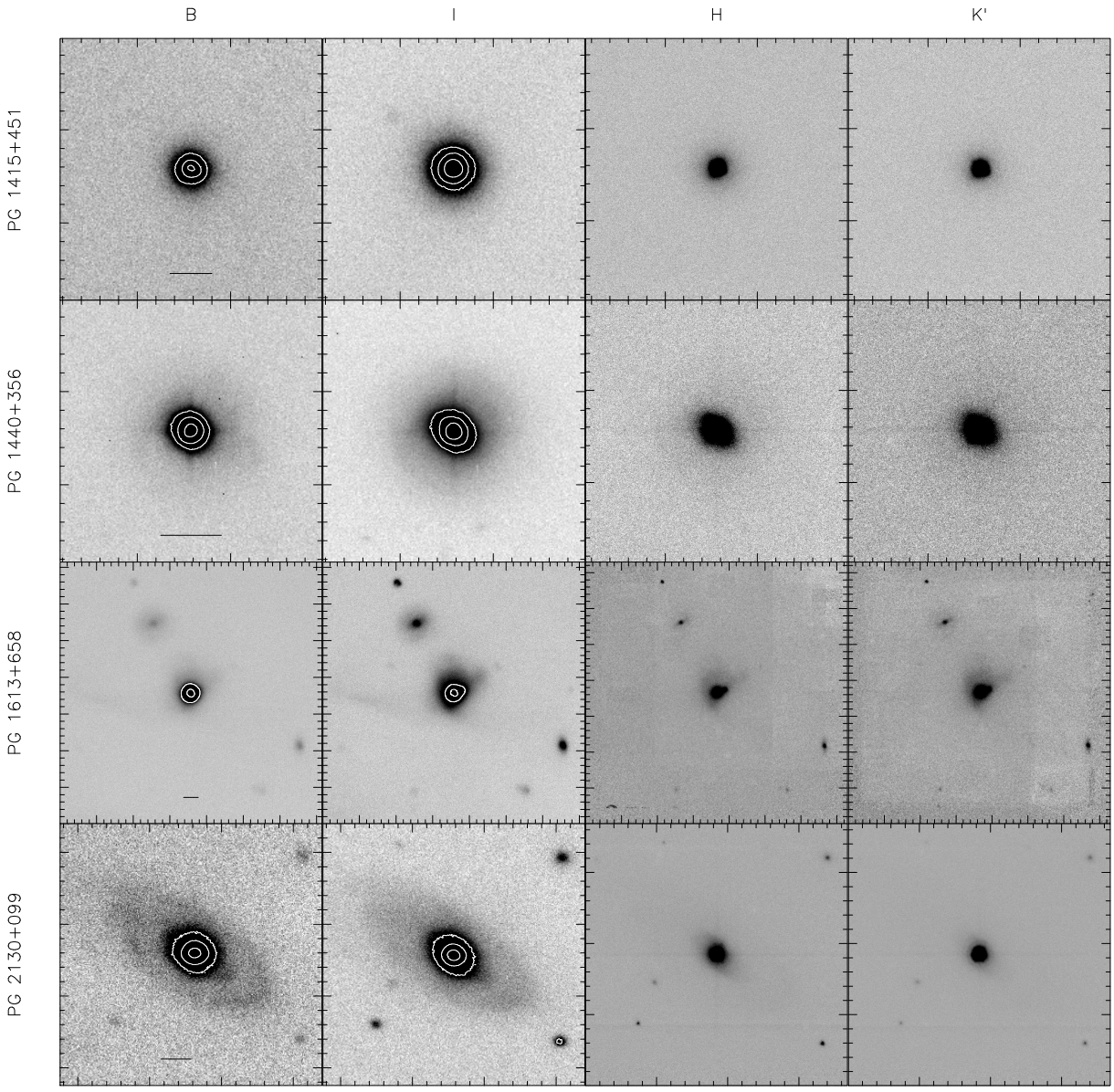

Fig. 5.1.— (continued)

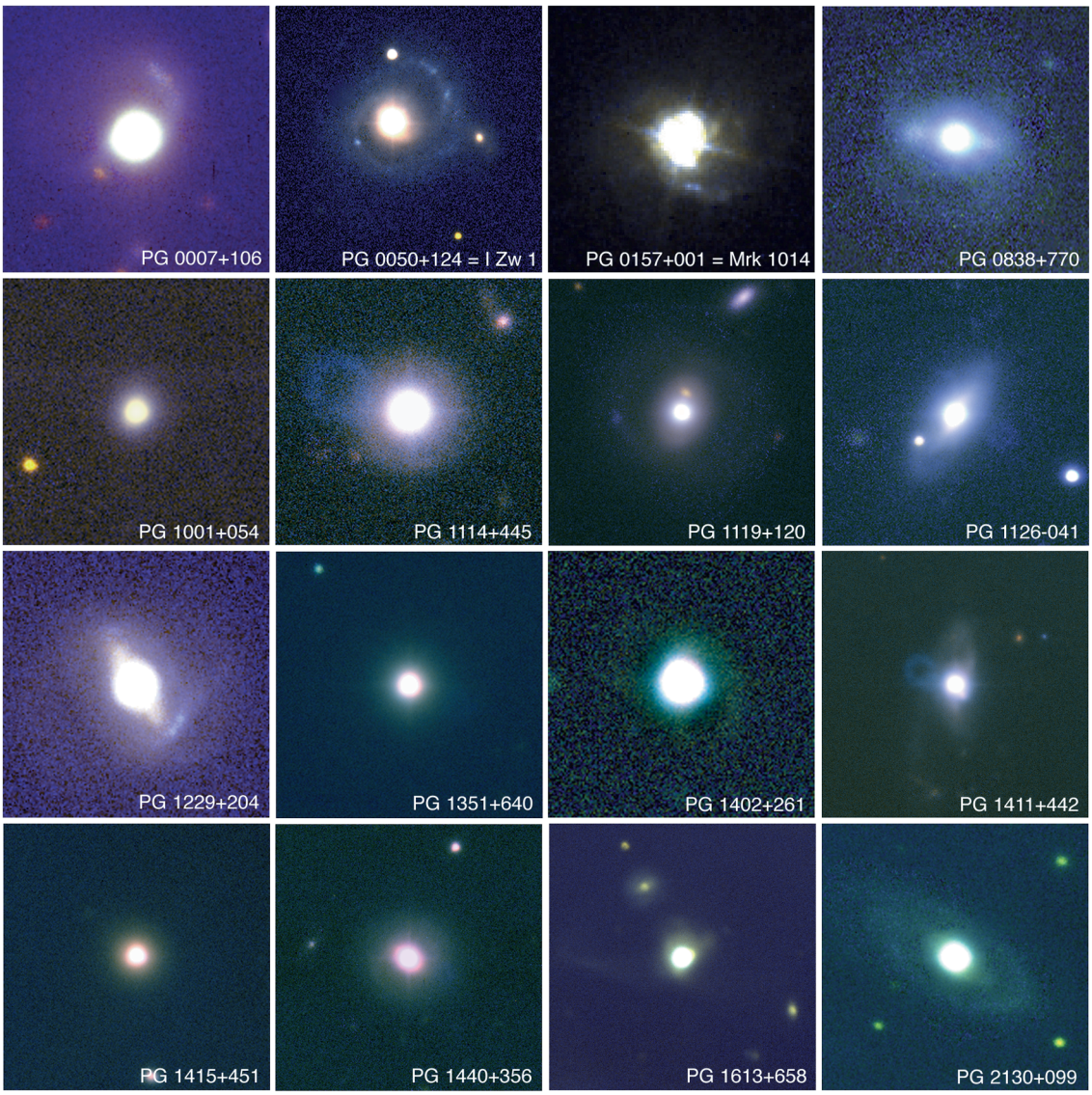

Fig. 5.2. - Near-truecolor images of the infrared-excess PG QSO sample, made by extrapolating the B and I-band images as described in Figure 2.3. PG 1202+281 and 3C273 are not pictured since we have no data for them.

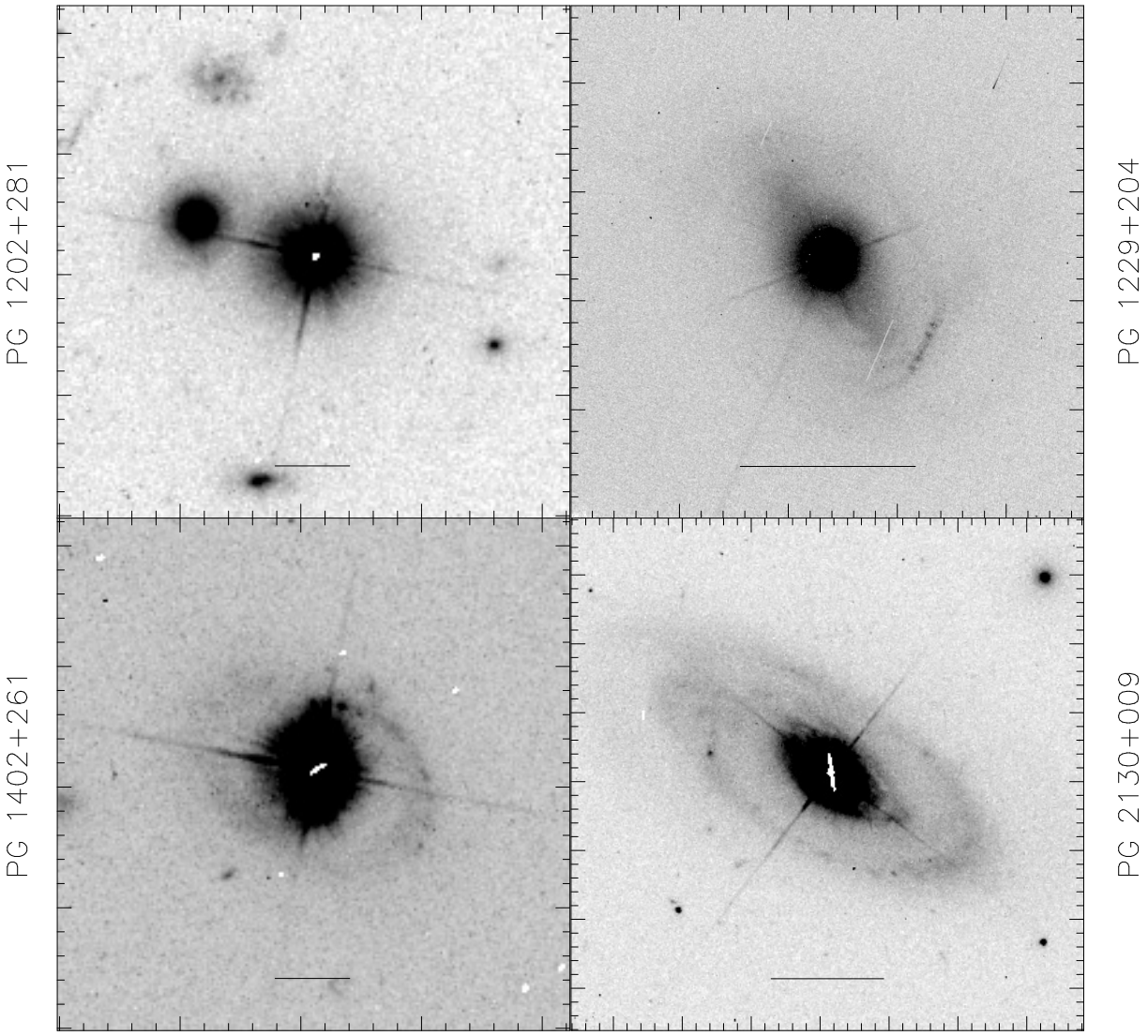

Fig. 5.3.— Archival images of infrared-excess PG QSOs taken with *HST*/WFPC2 in the V and R filters as part of other programs (Bahcall et al. 1997, Hutchings & Morris 1995). Tick marks are $1''$, and the physical scale bar is 10 kpc.

nuclear knot described by Hutchings & Neff (1992). Additionally, there is a less luminous high surface brightness region to the southwest.

5.3.2. Luminosities

Table 5.2 gives BIHK′integrated photometry for all of the QSOs as well as nuclear and host galaxy luminosities and nuclear fractions. These were derived by measuring the total flux of the QSO/host system in a very large aperture, and then subtracting the contribution of the QSO nucleus and any high surface brightness features (e.g., star forming knots). As in Chapter 3, the luminosity of the QSO nucleus was determined in two ways: measuring the flux in a 2.5 kpc aperture and then correcting this with an aperture correction derived from the observed PSF, and also by fitting the observed PSF to the nucleus. Generally, these results were the same to within 10%. This is not surprising; since the surface brightness of the QSO nucleus is so much higher than that of the underlying galaxy, small aperture photometry will mostly be sensitive to the QSO nucleus as the underlying host contributes only a small fraction of the total flux inside the aperture.

Table 5.2. Global and Nuclear Photometry of PG QSOs

Name	m_B		m_I		m_H		$m_{K'}$	
	Int.	Nuc.	Int.	Nuc.	Int.	Nuc.	Int.	Nuc.
PG 0007+106	15.77	16.20	14.30	15.12	11.81	12.51	10.78	11.32
PG 0838+770	16.28	16.56	15.12	15.73	13.32	14.43	12.66	13.26
PG 1001+054	16.15	16.18	15.50	15.58	14.48	14.81	13.41	13.80
PG 1114+445	16.06	16.17	14.78	14.92	13.34	14.18	12.32	12.92
PG 1119+120	15.09	15.33	13.55	14.33	12.19	12.56	11.63	11.83
PG 1126-041	14.92	15.14	13.53	14.00	11.92	12.28	11.12	11.34
PG 1202+281	...	...	...	...	...	...	...	...
PG 1229+204	15.55	16.03	13.96	15.08	12.33	13.23	11.72	12.39
PG 1351+640	14.63	14.82	13.65	13.92	12.74	12.99	11.89	12.12
PG 1402+261	15.51	15.78	14.98	15.07	13.22	13.39	12.07	12.28
PG 1411+442	14.79	15.06	13.88	14.11	12.42	12.89	11.67	12.08
PG 1415+451	15.90	16.24	14.70	15.17	12.98	13.38	12.14	12.56
PG 1440+356	15.15	15.29	13.77	14.14	11.83	12.18	11.08	11.37
PG 1613+658	15.67	16.06	13.98	14.53	12.19	13.03	11.44	12.12
PG 2130+099	14.56	14.76	13.48	14.01	11.63	11.99	10.78	11.04

The observed underlying host galaxies vary in absolute magnitude from M_H=−22.99 (PG 1119+120) to M_H=−26.10 (3c273), with a mean value of M_H=−24.39±0.90 and a median of M_H=−24.27. The H-band luminosities range from 0.4 to 7.5 L^*, with a median of 1.3 L^* and a mean of 2.2 L^*. This is almost identical to the result found by McLeod and Rieke (1994a,b), who found a mean M_H=−24.3 for all PG QSOs with $z < 0.3$. McLeod & Rieke split their data into two samples, a high luminosity sample ($M_{\rm total\ B} < -23.1$; Mcleod & Rieke 1994b) and a low luminosity sample ($M_{\rm total\ B} > -23.1$; Mcleod & Rieke 1994a).

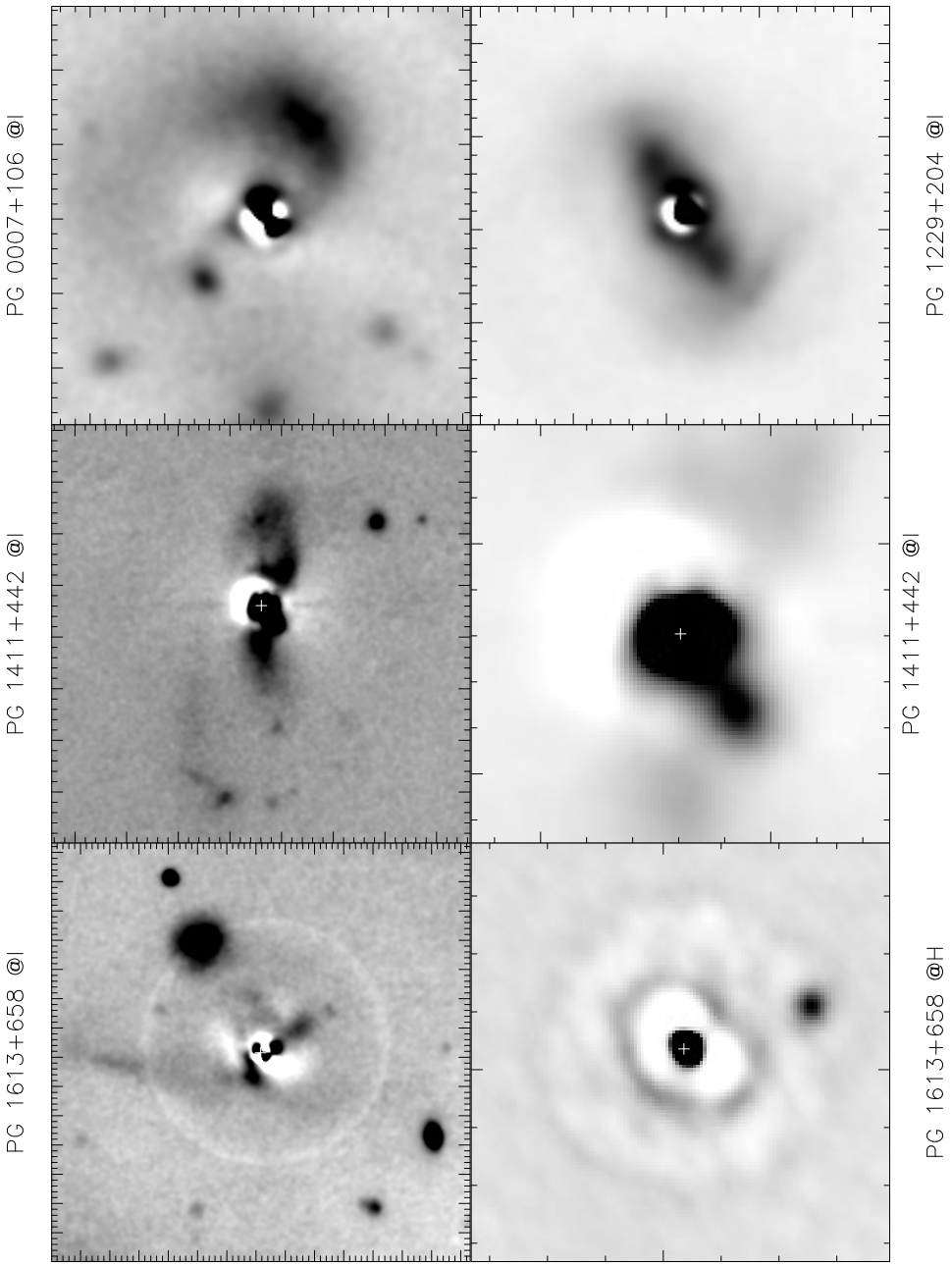

Fig. 5.4.— Enhanced images of PG QSOs showing small-scale structure. All of the images have had a radial model of the QSO light subtracted from them, except for the bottom right, which has been deconvolved with the Richardson-Lucy algorithm. The middle right panel is a close-up of the middle left panel showing the emission very close to the QSO nucleus. The location of the QSO nucleus in all cases is marked with a cross; the structure within a few arcseconds of this location (except in the middle panel) is residual error from the PSF subtraction.

These samples had mean H-band luminosities of $M_{\rm H}$=−24.6 and −23.9, respectively, and they postulated that this implied that high luminosity QSOs were found in high luminosity hosts (McLeod & Rieke 1994b). In this case it is fair to compare the H-band nuclear luminosity against the B-band total integrated luminosity since the B-band luminosity is dominated by the QSO nucleus (see below) and to first order may be taken as indicative of the QSO nuclear luminosity. Unsurprisingly, our data show a very tight correlation between B-band nuclear and total luminosity. We do not, however, actually see a correlation between $M_{\rm B}$ and $M_{\rm H}$ in our data, nor is there is any significant correlation between the H-band luminosity of the host galaxy and either the total or nuclear B-band luminosity. Similarly, there is no statistically significant correlation between nuclear and host luminosity in B or I-band, as well. However, we note our small sample size vs. that of McLeod et al. (1995b; 14 vs. 50) which may prevent such a correlation being observed. Even in the data of McLeod et al. (1995b), the effect is sufficiently weak that it requires binning all of the luminosities into just two groups to be detected. There *is* a statistically significant correlation between K-band luminosities of the host and nuclei at better than the 0.995 level. This may support the notion that more luminous QSOs are found in more luminous host galaxies. This correlation may break down at short wavelengths, as seen in our data, due to contamination of the host galaxy light by emission from star formation, contamination by the QSO nucleus, and extinction by dust. A similar, albeit weaker, result was found by Taylor et al. (1996).

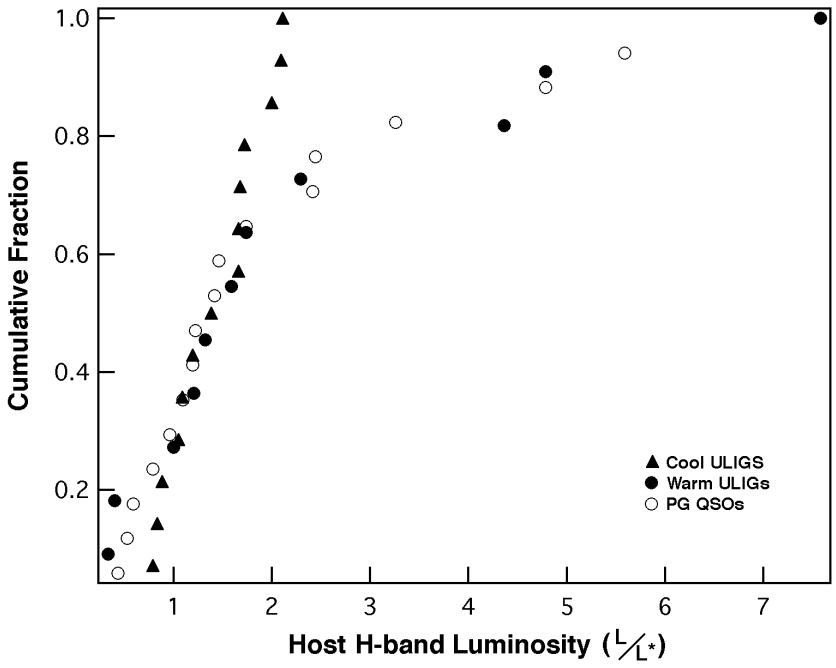

Fig. 5.5.— Cumulative distribution functions of the host galaxy luminosity at H-band for the three ULIG and QSO samples.

The QSO host galaxies have a median H-band luminosity very similar to that of both samples of ULIGs, but have a mean luminosity and span a total range more similar to that of the warm ULIGs. Figure 5.5 shows the H-band host luminosity cumulative distribution

functions (CDFs) of the three samples. In these cases, we have subtracted from the total integrated emission all of the light attributable to QSO nuclei, putative AGN, and clustered star formation; the residual should only be emission from old starlight. As expected from their similar median values, all three samples have nearly identical distribution functions below the 80% number fraction. Both the infrared-excess QSOs and the warm ULIGs have identical distribution functions, suggesting that the same underlying population of galaxy luminosities and hence galaxies make up the hosts. While to some extent this is due to the overlap (16% of QSOs, 25% warm ULIGs) between the two samples, removal of the overlap objects leaves the two CDFs still very similar. As was noted in Chapter 4, the cool ULIG sample seems to have a dearth of the very highest luminosity hosts, and as a result it's CDF deviates from the other two. There are several interpretations: first, and most importantly, the deviation is not statistically significant. Kolomogorov- Smirnov statistics indicate that we can reject the null hypothesis that the cool ULIG sample is drawn from the same underlying population as the warm ULIG and QSO samples at only the 50% level, mostly due to the small number statistics involved. Second, the warm ULIG and infrared-excess QSO samples are truly complete, i.e. they contain every object meeting the selection criteria, while the cool ULIG sample is only *statistically* complete, as it was drawn randomly from a much larger sample of objects meeting the selection criteria. As a result, it consists of only about 30% of the entire cool ULIG population. While the warm ULIG and QSO samples necessarily contain any existing systems with high luminosity hosts, there is a small likelihood that the cool ULIG subsample will fail to contain any such systems. It is of course also possible that this difference in CDFs is actually real, i.e., there is a difference in the populations of the host galaxies. If this were the case, then the distributions of host luminosities are consistent with the infrared-excess QSOs having evolved from warm ULIGs, but that only 80% of the warm ULIG/QSO populations could have evolved from an earlier cool ULIG state. The remaining warm ULIGs and QSOs either arose from a different process, by nature of their massive hosts never passed through a cool ULIG state, or that any such cool state was unusually short-lived.

Of the 4 QSO hosts with direct evidence for merger activity, 3 have the highest H-band luminosities in the sample ($L_{\rm H} > 3.2L^*$; PG 0007+106, Mrk 1014, and PG 1613+658) while the fourth (PG 1411+442) is more nearly 1.3 L^*. This is consistent with their interpretation as mergers of two galaxies.

The fraction of the total system luminosity due to the QSO nucleus is given in Table 5.3. The average nuclear fraction is (BIHK′)=(0.79, 0.67, 0.60, 0.71)±(0.08, 0.16, 0.15, 0.10). As expected from previous studies (Sanders et al. 1989, McLeod & Rieke 1995), the minimum nuclear fraction occurs somewhere near 1 μm, which is a result of the comparative SEDs of QSOs and galaxies. There is a considerable range in nuclear fractions: the QSO nucleus at H-band accounts for anywhere from 36% to 85% of the total luminosity. On average, though, the QSO nucleus and the underlying host galaxy are roughly similar in total magnitude at H. At shorter wavelengths such as B, the QSO nucleus is roughly 4 times more luminous than the host.

Table 5.3. Nuclear Luminosity Fraction in PG QSOs

Name	B	I	H	K′
PG 0007+106	0.67	0.47	0.52	0.61
PG 0838+770	0.77	0.57	0.36	0.58
PG 1001+054	0.97	0.93	0.74	0.70
PG 1114+445	0.90	0.88	0.46	0.58
PG 1119+120	0.80	0.49	0.71	0.83
PG 1126−041	0.82	0.65	0.39	0.82
PG 1202+281	...	...	...	...
PG 1229+204	0.64	0.36	0.44	
PG 1351+640	0.84	0.78	0.79	0.81
PG 1402+261	0.78	0.92	0.85	0.82
PG 1411+442	0.78	0.80	0.65	0.68
PG 1415+451	0.73	0.65	0.69	0.68
PG 1440+356	0.88	0.71	0.72	0.77
PG 1613+658	0.70	0.60	0.46	0.53
PG 2130+099	0.83	0.61	0.72	0.79

5.3.3. Colors

Optical/near-infrared colors were derived for the QSO nuclei. Figures 5.6 and 5.7 illustrates the ($B-I$, $I-H$, $H-K'$) colors of the QSO nuclei, using the two rotations of the optical/near-infrared color cube used in chapters 3 & 4. The mean QSO nuclear colors are ($B-I, I-H, H-K'$) = $(0.99, 1.56, 0.96)\pm(0.23, 0.52, 0.17)$. These colors are similar to those derived in Chapter 3 for UVSX QSOs, and seem to continue to support the large observed intrinsic scatter in QSO colors. All of the observed infrared-excess PG QSOs have ($H-K'$) colors redder than those of the modeled synthetic QSO or derived observationally from the UVSX sample (§3.3.3.1). This reddening is not consistent with any appreciable (>1 A_V) foreground dust screen; instead, it is most consistent with varying small contributions (10– 20%) at K' from hot (600–1000 K) dust. This contribution from hot dust is less extreme than that found in the warm ULIGs, and they are therefore found predominantly between the regions in the 3-color diagram occupied by synthetic optical QSOs and the warm ULIGs. Since a smaller fraction of the luminosity at K' seems to originate in hot dust, and any foreground reddening screen is much thinner, this lends support to the idea that the infrared-excess QSOs are transition objects between warm ULIGs and optical QSOs and that as they age, much of the dust in the vicinity of the active nucleus is dissipated or destroyed.

Table 5.4 presents photometry derived for the star-forming knots and other structures seen in some of the QSO hosts. The ages derived from the colors are difficult to constrain, primarily due to high detection limits in the near- infrared. However, in most cases the constraints that can be made indicate young ages for most of the knots (less than $\approx 10^8$ years). The arc in PG 0007+106, while apparently bluer than it's surroundings, is essentially unconstrained due to a lack of a clear near-infrared detection. The nuclear knot in PG

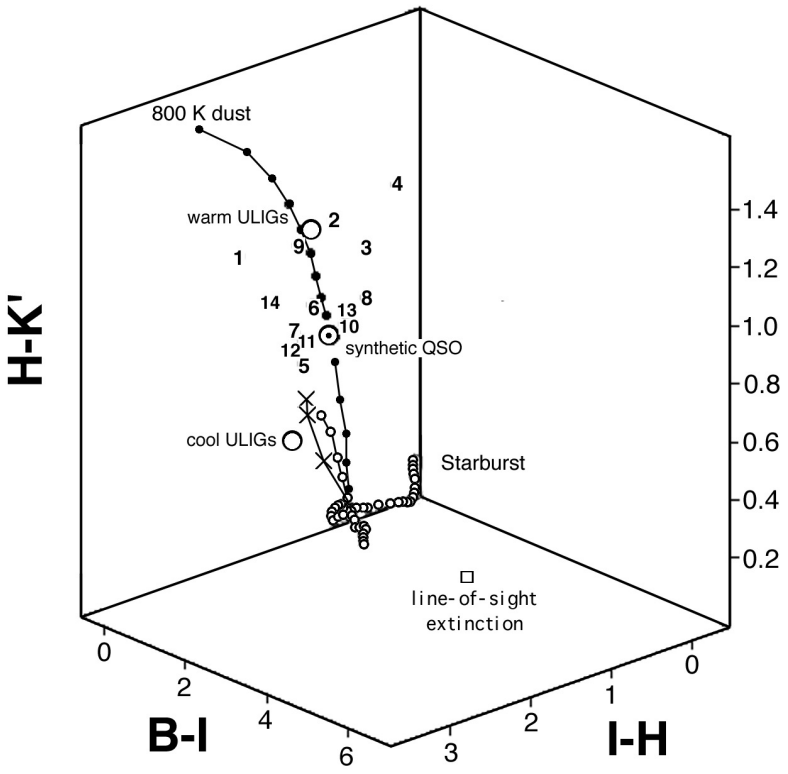

Fig. 5.6.— $(B-I)$,$(I-H)$,$(H-K')$ color cube as in Figure 3.6 illustrating the colors of the QSO nuclei. For clarity, the nuclei have been marked with numbers: (1) PG 0007+106 (2) PG 0838+770 (3) PG 1001+054 (4) PG 1114+445 (5) PG 1119+120 (6) PG 1126-041 (7) PG 1229+204 (8) PG 1351+640 (9) PG 1402+261 (10) PG 1411+442 (11) PG 1415+451 (12) PG 1440+356 (13) PG 1613+658 and (14) PG 2130+099.

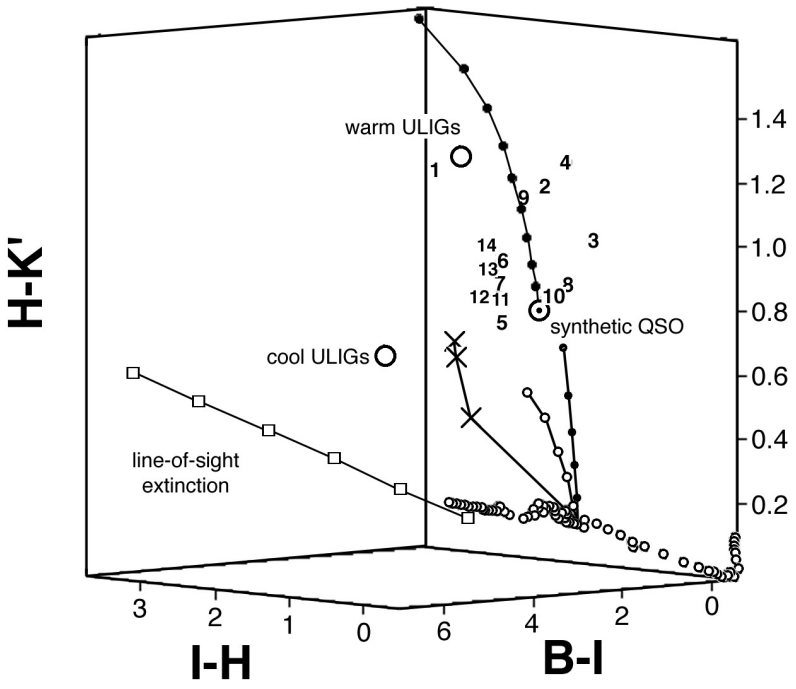

Fig. 5.7.— Same as Figure 5.6, but rotated as to be parallel to the reddening vector. Most of the QSO nuclei have colors similar to the synthetic QSO colors, albeit with high values of $(H-K')$. This near-infrared excess, however, is less than that of the warm ULIGs.

1119+120 is quite red, with a considerable K′ excess, while the knot in the spiral structure appears quite young and blue. Similarly, the knots in PG 1229+204 are blue and have ages of less than 100 Myrs old. The knots in PG 1411+442 are ill-constrained due to large measured uncertainties, but they are probably less than 100 Myrs. The nuclear knot has colors similar to many of the star-forming knots seen in the ULIGs. Finally, the nuclear knot in PG 1613+658 is most prominent at H-band. While actually quite red optically, it's near-infrared colors are typical of star formation.

Table 5.4. Details of PG QSO Small Structure

Name	Δ RA[a]	Δ Dec	m_B	m_I	m_H	$m_{K'}$
	arcseconds					
PG 0007+106 arc	−2.8	6.4	20.80	18.37	>15.80	>17.60
PG 1119+120 knot 1	−0.7	2.8	>19.10	16.93	16.64	15.39
PG 1119+120 knot 2	9.5	−1.0	22.30	21.25	>20.70	>20.70
PG 1229+240 SW knots	-4.1	-4.1	20.78	19.37	>18.80	>18.80
PG 1411+442 knot 1	3.5	−18.6	23.53	20.70	>20.70	>20.20
PG 1411+442 knot 2	−0.2	8.3	22.07	20.13	>20.00	>20.10
PG 1411+442 knot 3	−1.1	−1.7	20.18	18.91	16.35	15.88
PG 1613+658 knot	−2.4	0.7	>22.80	19.74	15.95	15.71

[a] offsets given relative to the QSO nucleus

The colors of the host galaxies themselves as determined from the global and nuclear photometry are poorly determined. This is primarily because the nuclei dominate the luminosity, particularly at very long and short wavelengths. Since the average QSO nucleus is anywhere from 1.5 to 4 times more luminous than the host at B, relatively small errors in the determination of the QSO nuclear luminosity result in disproportionately large uncertainties in the QSO host luminosity. The mean colors so derived are $(B-I, I-H, H-K')$ = (1.66, 1.86, 0.65)±(0.79, 0.65, 0.36). These colors are appreciably redder at K′ than expected for a normal stellar population. This same result was found in Chapter 3 for the three warm ULIGs that are also PG QSOs. This may be a result of residual QSO light (which is much redder in the near- infrared than starlight) contaminating the colors of the hosts. The surface brightnesses were measured in small apertures at the apparent half-radius point in the host galaxies (these mean surface brightnesses appear in Figure 5.8). The colors derived from these representative surface brightnesses are $(B-I, I-H, H-K')$ = (2.16, 2.14, 0.65). This is also a considerable $(H-K')$ excess, considering that these values were measured far enough from the nucleus that residual nuclear contamination should be quite small. On the other hand, these colors are also very similar to those observed in the "nuclei" of the cool ULIGs, and may represent a near-infrared excess due to recent star-formation activity. McLeod & Rieke (1994a) note a similarly high value of $H-K$ when comparing their results to those of Dunlop et al. 1993. They note, however, that typical K-corrections to normal galaxy color may result in $H-K \approx 0.45$ (their sample being similar in redshift to ours). If this were combined with modest reddening (1 A_V) and hot dust emission, the

observed colors could probably be accounted for, considering the uncertainties introduced by the host/nucleus decomposition.

5.3.4. Detectability of QSO Hosts

It is commonly held that near-infrared observations are optimal for detecting QSO hosts (McLeod et al. 1995, Dunlop et al. 1993). This is motivated primarily by the comparative SEDs of typical spiral galaxies and QSO nuclei; the peak of the galaxy SED is very near the minimum of the QSO SED, and therefore H-band observations yield the highest possible contrast between the galaxy host and the QSO nucleus. This was based on the assumption that the greatest difficulty in detecting QSO hosts was trying to differentiate the extended, low-surface brightness galaxy emission from the wings of the PSF of the extremely bright point-like nucleus.

However, our observations run counter to this — it is actually much easier to detect the QSO hosts at shorter wavelengths like B and I-band. Both our observations and those of others (Hutchings & Neff 1992, Hutchings & Morris 1995) indicate that typical QSO hosts are similar in gross properties to most galaxies. At redshifts of z<0.16, a typical host galaxy 30 kpc in diameter is likely to be 5–10″ in radius. This is sufficiently large that at a stable site like Mauna Kea under good conditions (0.5″ FWHM at 5000 Å or 0.3″ at 1.6μm) the wings of the PSF do not extend measurably to such large radii. Therefore, at low redshift ($z < 0.4$) *the limiting factor in QSO host galaxy detection at low redshifts is background noise* (both instrumental and poisson noise from background sky emission). With modern instruments, the poisson noise from the background sky emission is generally higher than the instrumental noise, although eventually flat-fielding errors become significant. The 2 magnitude increase in host galaxy surface brightness from *I*-band to *H*-band cannot offset the 6 magnitude decrease in sky brightness under a dark sky (this increases to a 9 magnitude difference in sky brightness from *B* to *H*). Space-based observations, which have nearly negligible sky brightnesses, would not be so affected; and hence the increase in host luminosity at near-infrared wavelengths would then increase detectability. Although the decrease in spatial resolution at long wavelengths with instruments like NICMOS would in theory decrease detectability versus optical instruments like WFPC2, as noted above the very large spatial scales of the QSO hosts at low redshift effectively renders this point moot. Only at higher redshifts ($z > 0.5$) would this become important.

Another reason for the increase in detectability lies in the relative morphology of galaxies at long and short wavelengths. At near-infrared wavelengths galaxies are relatively smooth, reflecting the distribution of old stars. At short wavelengths galaxies show much more complex morphologies due to emission from young stars and differential extinction by dust. Features such as spiral arms are much more easily detected at short wavelengths, and therefore QSO host galaxies are more *recognizable* in filters such as *B* and *I*. At near-infrared wavelengths the smooth distribution of old stellar light in the host galaxies is more difficult to detect due to confusion with flat- fielding errors, the wings of the QSO nuclear PSF, etc., while at short wavelengths the high spatial frequency features are more easily separated from large-scale extended background variations.

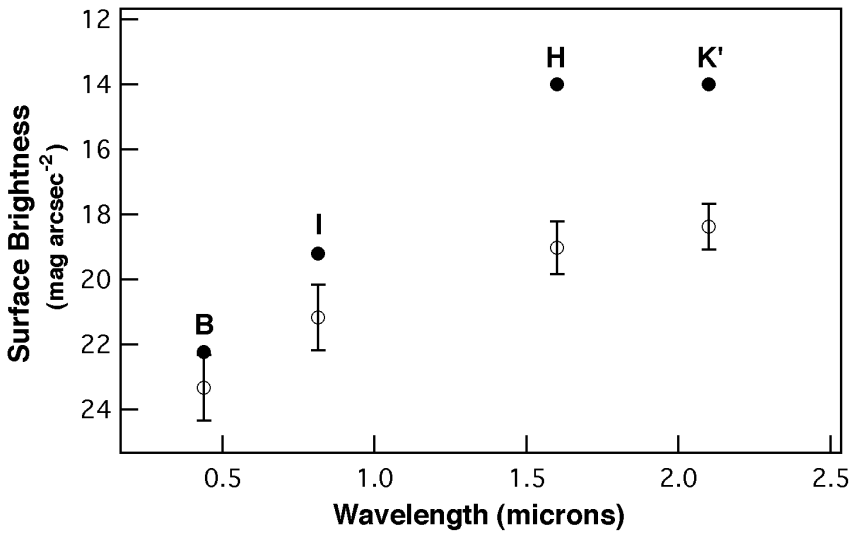

Fig. 5.8.— A comparison of the surface brightnesses of the night sky (closed circles) on Mauna Kea (CFHT Observer's Manual 1990; Wainscoat & Cowie 1992) vs. the observed mean surface brightnesses of QSO host galaxies (open circles) as a function of wavelength. The surface brightnesses were measured at the apparent half radius of the galaxies. Host galaxies are easier to detect at optical wavelengths such as I due to the much lower sky brightness.

5.4. Conclusions

1. Host galaxies were detected in all 17 observed infrared-excess PG QSOs. The one QSO not observed (PG 1202+281) was already known to have an elliptical host. In many cases these galaxies had observable 2-dimensional morphology. At least 76% have features indicative of spiral structure, 27% have strong nuclear bars, and 22% appear to be on-going merger systems.

2. The underlying host galaxies have H-band luminosities, which are believed to indicative of the size of the underlying old stellar population, ranging from 0.4 L^* to 7.5 L^*, with a mean of 2.2 L^*. These luminosities are consistent with those of ULIGs.

3. The QSO nuclei and their host galaxies are similar in total luminosity at H-band, but this ratio increases to an average of 4:1 at B.

4. Contrary to many expectations, QSO host galaxies at low redshift are easiest to detect at optical and not near-infrared wavelengths. This is due primarily to the low background emission of the sky at optical wavelengths coupled with the large projected size of the extended hosts.

5.5. Notes on Individual Objects

The following are descriptive notes explaining various features of the individual QSO hosts. These features are most easily seen in the near-truecolor images of Figure 5.2.

PG 0007+106 = Mrk 1051 = III Zw 2 — a single tidal arm or arc extends 22 kpc to the north. This arm has several knots of star formation in its far end. Another galaxy is seen directly to the south. Although there is no apparent connecting structure between the two, there does seem to be some extended low surface brightness emission surrounding all of the galaxies in the field, suggesting that perhaps there are multiple interactions.

PG 0050+124 = I Zw 1 — this is also a "warm" ULIG and is discussed in more detail in Chapters 2 & 3. It has two asymmetric spiral arms, both of which have knots of star formation. The galaxy disk is 30 kpc in diameter.

PG 0157+001 = Mrk 1014 — this QSO is also a "warm" ULIG and is discussed in detail in Chapters 2 & 3.

PG 0838+770 — a strong nuclear bar 22 kpc in projected length runs E-W through the host galaxy. Condensations are seen near each end of the bar. A single spiral arm extends clockwise from each end of the bar. The galaxy itself is elongated perpendicular to the axis of the bar, although this may be a projection effect.

PG 1001+054 — small and uniform, with no distinguishable features.

PG 1114+445 — the host galaxy is diffuse and uniform, but shows some evidence to the south of having a small, tight spiral arm, suggesting that this is a face-on disk galaxy.

PG 1119+120 — a very red compact emission source lies inside the host galaxy envelope to the NW; with high spatial resolution it appears tangentially elongated. The host galaxy consists of a tilted central elliptical condensation which may be a 15 kpc long bar, with an apparent disk 28 kpc in diameter rotated perpendicular to it. There are at least 5 additional smaller galaxies located within a projected distance of 25″ of the QSO.

PG 1126−041 = Mrk 1298 — an elongated, elliptical host approximately 30 kpc in diameter. There are projections from the nucleus parallel to the long axis of the host which suggest that this may be a bar structure.

PG 1229+204 = Mrk 771 = TON 1542 — a strong nuclear bar 14 kpc in projected length runs NE-SW through this host. A very blue, linear chain of star-forming knots extends nearly perpendicular to the bar axis at one end. Hutchings et al. (1992, 1994, 1995) claim that this is due to tidal disruption with a small companion; however, it seems more likely that these knots are associated with the bar itself, considering that there appears to be a similar blue region visible on the opposite end of the bar (Figure 5.2).

PG 1202+281 = GQ Comae — we were unable to observe this QSO due to the sensitivity limitations of our fast tip/tilt guider. However, Bahcall et al. (1997) have observed this system with *HST*/WFPC2 and claim that the host galaxy appears to be a small elliptical E1.

PG 1351+640 — no features are discernible in the ground-based images.

PG 1402+261 — Bahcall et al. (1997) describes this as an SBb(r). The *HST/WFPC2* images show a clear bar with very open arms extending from their ends, a morphology common to several other QSO hosts (e.g., PG 0838+770, PG 1119+120). The ground-

based images are just capable of showing this structure (this panel in Figure 5.2 has been enhanced by unsharp-masking).

PG 1411+442 — a tidal loop 88 kpc long extends to the north, then wraps around to the east and extends south. In the model-subtracted image a counter-tail is seen extending south and curving to the west. In the near- infrared, a linear structure is seen extending to the SW from the nucleus which may be a jet. This same jet-like feature can be seen in the optical images after subtraction of a radial model.

PG 1415+451 — no distinguishable features.

PG 1440+356 = Mrk 478 — the galaxy nucleus is elongated NE-SW, and the body of the galaxy is elongated perpendicular to this, a morphology common to many other QSO hosts. There is some faint evidence of shells or arms.

PG 1613+658 — first described in detail by Hutchings & Neff (1992). A very obvious tidal tail extends 88 kpc to the east. In the near-infrared a second bright peak appears 2.4″to the NW and is most easily seen at *H*. There is a companion galaxy nearby; it is unclear if it has anything to do with the QSO host since there is no detection of emission linking the two. There is at least one other small galaxy nearby (33″to the SW).

PG 2130+099 = UGC 11763 = Mrk 1513 = II Zw 136 — this appears to be a spiral galaxy 30 kpc in diameter and inclined 60 ° from face-on. The *HST* images reveal the spiral structure in the host which resembles two concentric rings in the ground-based data. There is an odd asymmetry in the NE part of the host, lending to it's overall peculiar appearance.

REFERENCES

Bahcall, J.N., Kirhakos, S., Saxe, D.H., & Schneider, D.P. 1997, ApJ, 479, 642

Bahcall, J.N., Kirhakos, S., & Schneider, D.P. 1995, ApJ, 450, 486

Barnes, J. & Hernquist, L. 1996, ApJ, 471, 115

Bessell, M.S. 1979, PASP, 91, 589

Bekki., K. & Noguchi, M., 1994, A&A, 290, 7

Canada-France-Hawaii Telescope Observer's Manual, 1990, 5-2

Dunlop, J.S., Taylor, G.L., Hughes, D.H., & Robson, E.I., 1993, MNRAS, 264, 455

Elmegreen, D.M., Elmegreen, B.G., & Bellin, A. 1990, 364, 415

Gehren, T., Fried, J., Wehinger, P.A., & Wyckoff, S., 1984, ApJ, 278, 11

Goldschmidt, P., Miller, L. La Franca, F., & Cristiani, S., 1992, MNRAS, 256, 65P

Gunn, J.E., *Active Galactic Nuclei*, 1979, (Cambridge University Press: Cambridge), 213

Heckman, T., Armus, L., & Miley, G, 1990, ApJS, 74, 833

Hernquist, L., 1989, Nature, 340, 687

Hutchings, J.B., Crampton, D., Campbell, B., Duncan, D., & Glendenning, B., 1984, ApJS, 55, 319

Hutchings, J.B., Holtzman, J., Sparks, W.B., Morris, S.C., et al. ApJ, 429, L1

Hutchings, J.B. & Morris, S.C. 1995, AJ, 109, 1541

Hutchings, J.B. & Neff, S.G. 1992, AJ, 104, 1

Kellerman, K.I., Sramek, R.A., Schmidt, M., Green, R.F., & Shaffer, D.B. 1994, AJ, 108, 1163

Kohler, T., Groote, D., Reimers, D., & Wisotzki, L. 1997, å, 325, 502

Krist, J. 1994, *The Tiny Tim User's Manual*, (StScI: Baltimore)

Kukula, M.J., Dunlop, J.S., Hughes, D., Taylor, G., & Boroson, T., 1997, in *Quasar Hosts*, 1997, (Springer: Berlin), 177

Lake, G., Katz, N. & Moore, B., 1998, ApJ, 495, 152

McLeod, K.K. & Rieke, G.H. 1994a, ApJ, 420, 58

McLeod, K.K. & Rieke, G.H. 1994b, ApJ, 431, 137

McLeod, K.K. & Rieke, G.H. 1995, ApJ, 454, L77

Neugebauer, G., Green, R.F., Matthews, K., Schmidt, M., Soifer, B.T., & Bennett, J. 1987, ApJS, 63, 615

Neugebauer, G., Matthews, K., & Armus, L. 1995, ApJ, 455, L123

Schmidt, M, & Green, R.F. 1983, ApJ, 269, 352

Sanders , D.B., Phinney, E.S.,,Neugebauer, G., Soifer, B.T., & Matthews, K. 1989, ApJ, 347, 29

Sanders, D.B., Soifer, B.T., Elias, J.H., Madore, B.F., Matthews, K., Neugebauer, G., & Scoville, N.Z. 1988a, ApJ, 325, 74

Stockton, A., & MacKenty, J.W., 1987, ApJ, 316, 584

Sulentic, J. 1989, AJ, 98, 2066

Taylor, G.L., Dunlop, J.S., Hughes, D.H., & Robson, E.I., 1996, MNRAS, 283, 930

Terlevich, R. in *Dynamics and Interactions of Galaxies*, 1989, (Springer-Verlag: Berlin), 465

Toomre, A., & Toomre, J. 1972, ApJ, 178, 623

Yee, H.K.C., 1987, AJ, 94, 1461

Wainscoat, R.J. & Cowie, L.L. 1992, AJ, 103, 332

Woltjer, L. in *Active Galactic Nuclei*, 1990, (Springer-Verlag: Heidelberg), 1

Chapter 6

U′-band Imaging of Three Samples

ABSTRACT

We present the first ground-based U′($\lambda_{central}$ =3410Å, Δ_λ=320Å) images of selected systems from three complete samples of ultraluminous infrared galaxies (ULIGs) and infrared-excess PG QSOs. The U′ emission originates primarily in young massive stars and active nuclei; as such it allows a direct examination of the sites of recent high- mass star formation. Strong U′emission is seen in many systems, particularly in the extended tidal features of the ULIGs. The PG QSOs, however, have very little extended U′emission and almost no high surface brightness U′features (other than their active nuclei), suggesting that the QSO host galaxies are deficient in high mass stars in clusters relative to the ULIGs. This may be because they have older (possibly merger-induced) starburst systems than the ULIGs, or that they never had starbursts of the kind found in the ULIGs. Additionally, it is found that star-formation in the tidal tails is largely confined to those ULIGs which have double nuclei, suggesting that the time- scale for star-formation in the tails is brief and confined to the time prior to the actual coalescence of the galaxy nuclei.

6.1. Introduction

Many recent observations have shown the prevalence of clustered star- formation in interacting galaxies (Whitmore et al. 1995, Meurer et al. 1995). Other observations have shown that both ultraluminous infrared galaxies (ULIGs) and QSO host galaxies often have extended morphologies consistent with being advanced mergers (Sanders et al. 1988, Murphy et al. 1996, Clements et al. 1996, Stockton & MacKenty 1987, Hutchings & Neff 1992, Bahcall et al. 1997). In Chapters 2–5 it was shown that these same systems have evidence for clustered star-formation on physical scales of ≈100 pc distributed over their central several kpc and along their extended tidal features. Estimated ages for these clusters based on optical/near-infrared colors were in the range of 10–800 Myrs.

There are several advantages to working at shorter wavelengths. As noted in Chapter 2, there is an ambiguity in interpreting broad-band colors of starbursts following a burst age of 10–100 Myrs, as their colors in all filters redder than B are degenerate during this time period. This can be disentangled through the use of U-band imaging; ($U-B$) colors evolve almost montonically throughout the life of the starburst. Although reddening will still prevent a precise starburst age estimate since it is most severe at short wavelengths, the ($U-B$) colors will help constrain the upper age limits of the starbursts more accurately.

Few if any of the ULIGs have been imaged at short wavelengths before. Integrated photometry exists for a few systems, taken with single beam photometers (Neugebauer et al. 1987, Young et al. 1996). This is primarily because of the formerly presumed nature of the ULIGs. Since the bulk of the luminosity in ULIGs is radiated at 25–100μm as a result of dust absorption and reradiation, the assumption has always been that the galaxies

themselves are intrinsically dusty and that extinction must therefore be very high. In short, no one thought there would be anything to see. However, ground-based and *HST* imaging (Surace 1998, Chapters 2 & 4) have revealed the presence of luminous clustered star formation at optical wavelengths. These observations have shown that extinction is likely to be highly localized, and that many of the active star formation regions have already shed or blown away much of the surrounding dust. As a result, it is possible to actually detect emission at wavelengths as short as U′. Similarly, while all of the PG QSOs have single-beam photometry available at wavelengths very near U′(Neugebauer et al. 1987, Elvis et al. 1986), few have images available.

We present U′imaging data for selected ULIGs and PG QSOs drawn from the three complete samples discussed in Chapter 1. Colors and luminosities are used to derive starburst knot ages assuming a simple starburst model. Implications for the history of star-formation in these systems and their possible relation to each other are discussed.

6.2. Data

The data were taken on December 26–29, 1997 and March 23–24, 1998 at the f/31 focus of the UH 2.2m telescope using the Orbit 2048 camera. The Orbit camera is a backside-illuminated, thinned CCD that is UV-flooded for normal operation; it's quantum efficiency at U′(based on laboratory tests) is as high as 80%. At the f/31 focus this camera is oversampled, and hence the data was binned on chip 2x2 yielding a pixel scale of 0.09″ pixel^{-1}. The UH U′filter ($\lambda_{central}$ =3410Å, Δ_λ=320Å) was used for all observations. This filter has a shorter central wavelength than the standard Johnson U filter (see Appendix C). Total exposure times were typically 30–90 minutes, the long exposure times being necessitated by the narrowness of the U′filter. A sequence of five or more frames was taken in order to allow post-processing rejection of the high cosmic ray incidence. These frames were dithered to further decorrelate structured pixel-to-pixel noise in the CCD itself (such as blocked rows, flat- fielding errors, etc.). The data were reduced in a manner similar to that of the optical data in Chapters 4 & 5. Pixel-to-pixel response variations were corrected by dividing the data by a high S/N median twilight flat, and the CCD bias pattern was removed by subtracting a median bias frame constructed from 20–30 bias frames (zero-time exposures). In both cases the expected poisson noise in the calibration frames was below 0.005%. On the second run this camera developed severe dark current instabilities. This was calibrated by taking 4–5 hours of dark current (closed shutter integration) data at the beginning and end of each night in an attempt to compensate. High S/N dark current images were made for each half of the night, scaled to the exposure times used for the science data, and subtracted from them. In most cases the dark integrations had the same exposure times as used for the actual science observations, thus helping eliminate time-dependent dark current variations. Generally, this strategy seems to have been effective. The individual frames were then rotated to the normal orientation (northeast at upper left), aligned using IMALIGN, and medianed using IMCOMBINE and an algorithm that rejects cosmic rays based on the CCD noise characteristics.

Because of the limited telescope resources available, not all of the objects in the three complete samples could be observed. Since all the objects had already been observed at B and I-band, those that showed evidence of complex structure at these wavelengths, possibly indicative of star-forming activity, were reobserved at U′. In particular, the QSO systems which showed evidence of star formation and merger activity were observed at U′, since they may represent a critical transition between the "warm" ULIGs and the larger optical QSO population. Since extinction is higher at U′ than it is at B, and stars have $(U-B) > -1$, it is likely that any system that showed no structure at B would also show no structure at U′. Due to RA constraints imposed by the time of year of the observations, a few complex systems could not be observed (e.g., IRAS 22491−1808). A total of 25 objects were observed: (11/12) "warm" ULIGs, (8/14) cool ULIGs, and (6/15) PG QSOs that were not in the other two samples.

The data were flux calibrated by observing optical standard stars (Landolt 1983, 1992) with a wide range of colors and at different airmasses, allowing the derivation of accurate zero-point offsets and color terms relating the U′ filter to the standard Johnson U-band filter (see Appendix 3). This also allowed the atmospheric extinction to be measured and corrected; this can be as high as 0.2–0.6 magnitudes per airmass at such short wavelengths. In general, the photometric calibration appears to be accurate to 0.04 magnitudes. Possibly the largest uncertainty is the conversion from U′ to Johnson U-band; the relatively large color term can introduce uncertainties as high as 0.05–0.1 mag, depending on the underlying SED of the thing being measured. Throughout this chapter quoted magnitudes will be on the Johnson U calibration.

Calibration of the point spread function (PSF) is problematic at U′ because most stars are not very luminous at such short wavelengths, thereby decreasing the likelihood of achieving PSF S/N comparable to that of the target objects. In some cases it was possible to estimate the PSF directly from the combined science images in the same manner as in Chapters 3 & 4. In the remaining cases the PSF was derived instead from the standard star observations taken immediately before and after each set of science data. Most of the image degradation at short wavelengths is due to high-order atmospheric turbulence, and hence the quality of the off-axis tip/tilt guiding is largely irrelevant to the achieved PSF; the observed flux standards should therefore provide adequate PSF calibrators. Unfortunately, because of the poor resolution at short wavelengths, aperture corrections tend to be quite large (0.5–1 mag) for sub-arcsecond apertures, and hence knowledge of the PSF is critical. In most cases, in order to derive accurate colors the previous B and I- band imaging had to be re-evaluated in larger apertures than those previously used in Chapters 2–5 in order to compensate for seeing-induced aperture effects. This was particularly necessary for comparison with the WFPC2 data.

6.3. Results

6.3.1. Morphology

Figure 6.1 presents the U′observations of all 25 objects. Many of the systems show considerable structure in their tidal features. In general, the morphology of the ULIGs at U′is very similar to their morphology at B and to a lesser extent at I-band. This is not surprising, as the extinction at U′(1.53 A_V) is only slightly worse than that at B (1.45 A_V), yet is much worse than I (0.48 A_V; Rieke & Lebofsky 1985). Therefore, dust extinction effects are unlikely to significantly alter the relative morphology at U′and B, whereas anything more than a few magnitudes of extinction at I will completely obscure at U′any given feature near the I-band detection limit. Because of the generally poor spatial resolution at U′(0.7–1.5″), any features within a radius of ≈1.5-2 kpc of the luminous point-like nuclei of the PG QSOs and some of the warm ULIGs will be undetectable.

Of the "warm" ULIGs, the two double nucleus systems Mrk 463 (3.8 kpc nuclear separation) and IRAS 08572+3915 (6.2 kpc nuclear separation) have the most spectacular U′features. In both cases up to half a dozen U′knots are scattered along the lengths of the tidal tails. Similarly, Mrk 1014 and Mrk 231 have U′knots embedded in apparent tidal features (the northeastern tidal arm and southern tidal "horseshoe", respectively). I Zw 1 has three prominent knots distributed along its two spiral arms. IRAS 12071−0444 and IRAS 15206+3342 have evidence for marginally resolved knots in their inner 10 kpc diameter "cores". IRAS 05189−2524 has no apparent knots (although there may be some undetected in the extended, unresolved core); however, it's tidal loops are easily recognized. Pks 1345+12 appears to be so red that we cannot achieve adequate S/N in order to detect any high spatial resolution features. However, it does appear that the bulk of the U′emission is associated with the active western nucleus. As noted before in the WFPC2 data, IRAS 01003−2238 shows no evidence of any knots, although it's small spatial size would render any such knots unresolvable in our data. The one warm ULIG which shows no U′knots at all and should, based on our spatial resolution and detection limits, is IRAS 07598+6508.

The cool ULIGs have an equally varied U′morphology. Most of the cool ULIGs' U′activity occurs in their inner 8 kpc. For example, although the single nucleus systems IRAS 00091−0738, UGC 5101, Mrk 273, and IRAS 23365+3604 have long, well-developed tidal tails, none of these tails has the high surface brightness knots found in systems like IRAS 08572+3915 and Mrk 463. The double nucleus systems IRAS 12112+0305 (2.5 kpc nuclear separation) and IRAS 14348−1447 (5.5 kpc nuclear separation), on the other hand, have U′knots located in their tails and also in their nuclear regions. Finally, the very widest separation system examined, IRAS 01199−2307 (24 kpc), has no evidence for U′knots in its barely detectable tails.

The infrared-excess PG QSOs appear deficient in sites of U′emission. Only I Zw 1 and Mrk 1014 have apparent star-forming knots similar to those of the ULIGs, and these two are warm ULIGs anyway. Of the 6 remaining PG QSOs observed at U′, only PG 1229+204 has any appreciable compact U′knots. This is surprising in the cases of PG 1411+442 and PG 1613+658 since both of these systems have clear interaction morphologies in the form of tidal tails like those seen in the ULIGs, yet in both cases the tails are nearly undetectable

and there are no compact knots in them. Similarly, the remaining 3 PG QSOs have luminous central bars with condensations visible in them at other wavelengths (e.g., PG 0838+770), yet these are not detected at U′.

This dichotomy in the appearance of knots along the extended tails may indicate differences in the star-formation history in the tails during different phases of the merger evolution versus the star formation in the nucleus. In particular, the appearance of compact star-forming knots in the tails of every merger system with nuclear separations less than 10 kpc, but not in single- nucleus post-merger systems, may indicate that the tails undergo a relatively unified burst of star formation shortly before the merging of the nuclei, and that no further local bursts occur. Speculatively, this could be due to gas depletion in the tails; the denser nuclear environment may be able to fuel the bursts for much longer, or to fuel a sequence of many bursts as was indicated in Chapter 2. Fading of the starburst knots is very rapid at U'; the knots fade from their peak intensity (which occurs at an age of 30 Myrs) by nearly 5 magnitudes by the time they are only 300 Myrs old. Fading by only 3 magnitudes would make most of the luminous knots observed undetectable; it is therefore likely that most of the knots we observe at U' are between 10- 100 Myrs in age, which is borne out by an analysis of their $(U-B)$,$(B-I)$ colors (see below). Since the nuclear regions of the more dynamically advanced systems (i.e. Mrk 273, UGC 5101) continue to have luminous U' knots, either these knots are intrinsically more luminous (thus allowing them to be detectable for a longer period of time), the time-scale of the burst is much longer than the instantaneous burst modeled here, or there is an on- going generation of new knots.

6.3.2. Colors and Derived Starburst Ages

Table 6.1 lists the photometric data for the U′ observations. We compare the colors of observed features to various modeled colors. The U' colors provide essentially no discriminant between AGN and starburst activity. The synthetic optical QSO model introduced in Chapter 3 yields $(U-B)$,$(B-I)$ colors for a QSO at the sample median redshift of -0.78 and 0.67, which is essentially the same as the instantaneous starburst model with an age of 10 Myrs. From the UVSX sample of Elvis et al. (1994) we similarly derive $(U-B)$,$(B-I)$ = $(-0.82,1.12)\pm(0.16,0.19)$. As discussed in Chapter 3, long wavelength emission therefore remains the best possible color discriminant between AGN and star formation activity. Throughout this analysis we will continue to consider the U′ emission as a result of either starburst activity or AGN depending on the results found at other wavelengths in Chapters 3 and 4. Larson & Tinsley (1978) find typical (U−B) colors for non-interacting galaxies in the RC2 in the range of $-0.2 - 0.6$, and Guiderdoni et al. (1988) finds typical values of $(U-B)$ for spirals of 0.03. Such a wide span of colors is probably due to the variable star formation histories of the "normal" galaxies involved. Perhaps a more meaningful comparison can be made to the $(U-B)$ colors of individual stellar spectral types: $(U-B)$ = -1.15, -1.06, -0.02, 0.07, 0.05, 0.47, and 1.28 for spectral classes O5, B0, A0, F0, G0, K0, and M0, respectively (for stars on the main sequence — the corresponding giant stars are somewhat redder; Allen 1973). Only OB stars can contribute to $(U-B)$ colors significantly less than 0.

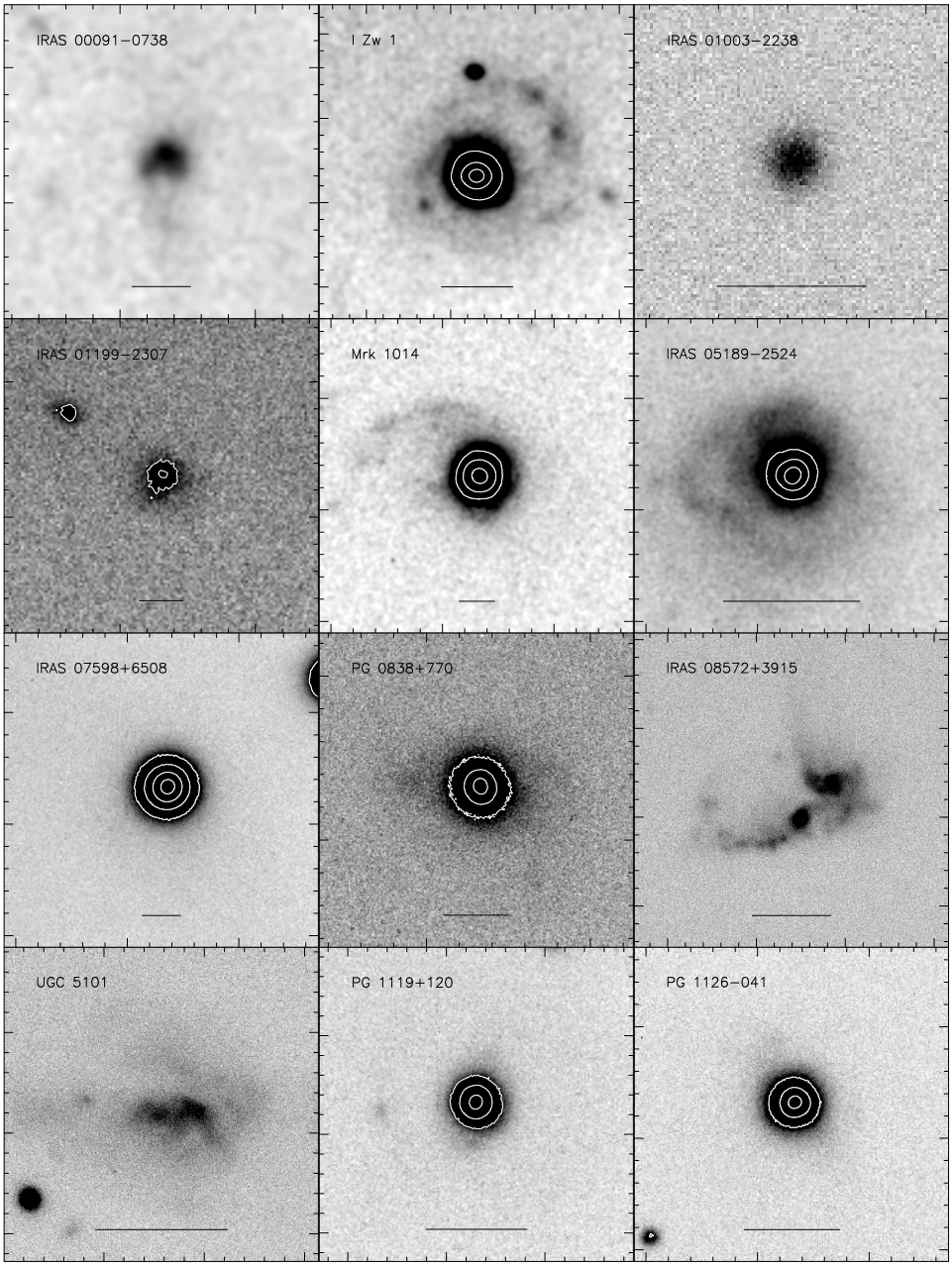

Fig. 6.1.— U′ images of systems selected from three complete samples of ULIGs and QSOs. The images have been smoothed by convolution with a $0.2''$gaussian. Ticks are $1''$, and the scale bars represent a physical scale of 10 kpc.

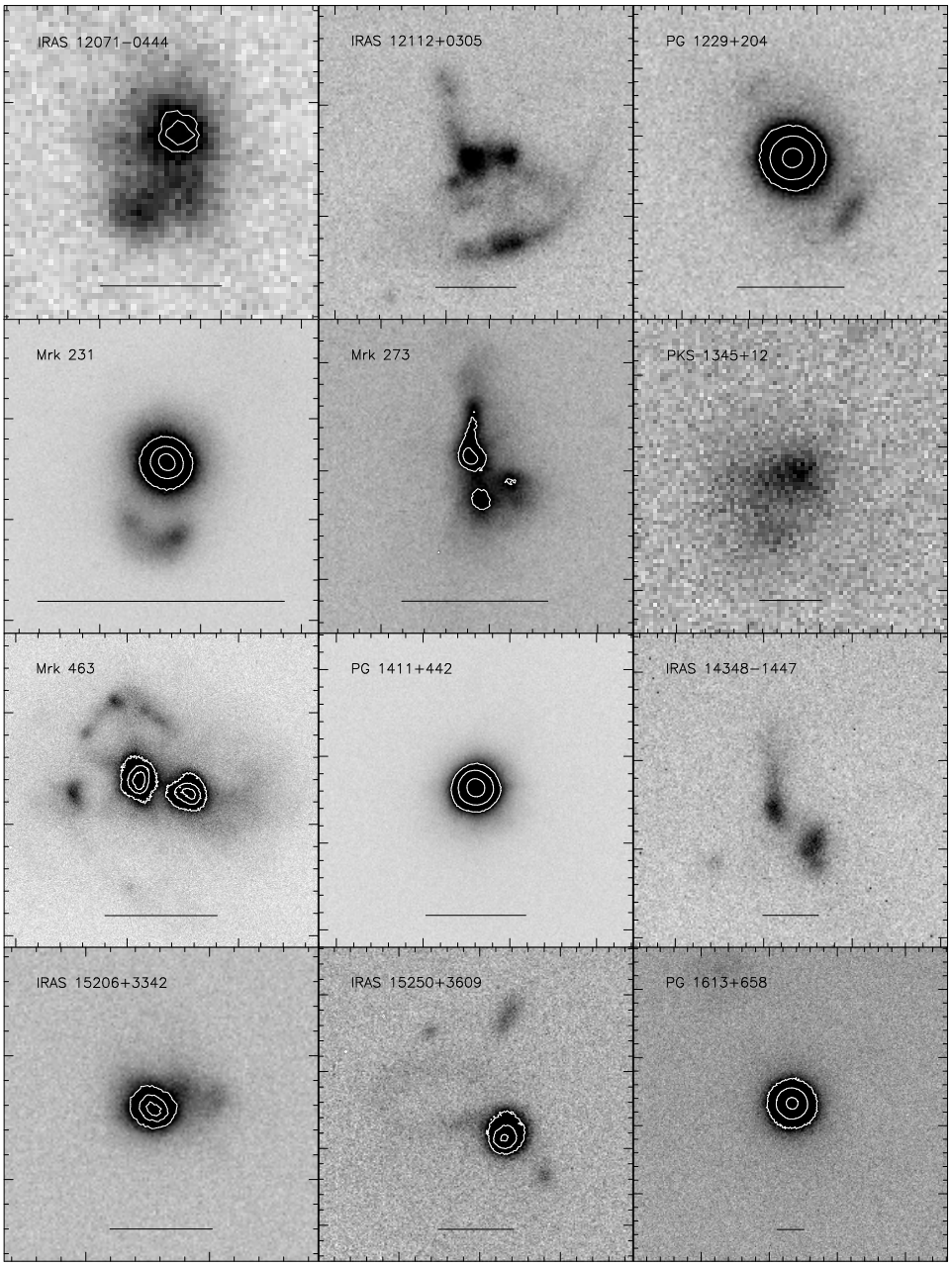

Fig. 6.1.— (continued)

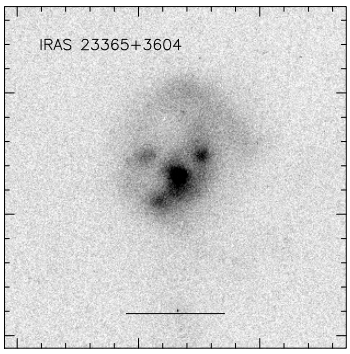

Fig. 6.1.— (continued)

We continue to use the BC95 model with a Salpeter initial mass function (IMF) and upper and lower mass cutoffs of 125 and 0.1 $M_{\odot}$, respectively. It should be emphasized here that the age estimates based on color diagrams of this sort are relatively insensitive to the exact shape of the IMF. This is because the colors of a stellar (starburst) ensemble are dominated by the most luminous stars since what is measured at the telescope is a luminosity- weighted average of all the stars in the burst (Leitherer 1996). It would require very extreme changes in the mass index of the IMF in order for late- type stars to dominate by sheer numbers. The low mass end of the IMF primarily acts as a reservoir for the mass of the burst; most of the luminosity is emitted by only a small ($\approx$ 10%) mass fraction of the burst. Truncation of the lower end of the IMF, therefore, primarily adjusts the luminosity per unit mass of the burst, and thus the rate at which the gas supply is consumed. For example, truncating the IMF at 3 $M_{\odot}$in the model above only increases the bolometric luminosity per unit mass by a factor of 5 and leaves the color evolution almost unchanged until roughly 1 Gyr (at which time the entire stellar population has left the main sequence, and therefore become very red; Charlot et al. 1993). Similarly, adjusting the upper mass cutoff from 120 to 60 $M_{\odot}$ leaves the color evolution unchanged after the first few million years due to the very rapid evolution of the upper end of the IMF. The model we are using is thus likely to be a good one for a typical long-lived stellar population extending from the most massive stars to the least massive. Changing the upper and lower mass cutoffs is likely to only change the bolometric luminosity per unit mass, and even then only by a factor of a few.

The ($U-B$) colors of galaxies as a whole seem ill-determined; as an illustration, the integrated ($U-B$) colors of the cool ULIG sample range from -0.5 (IRAS 12112+0305) to 1.09 (UGC 5101), with a median of 0.51. Such an enormous range in integrated colors is similar to the Larson & Tinsley result (1978), and probably does not constrain the galaxies' stellar populations significantly. Due to the apparent wide range in colors, another approach must be used. It is probably more meaningful to address the colors of the individual features observed in the ULIGs and QSOs.

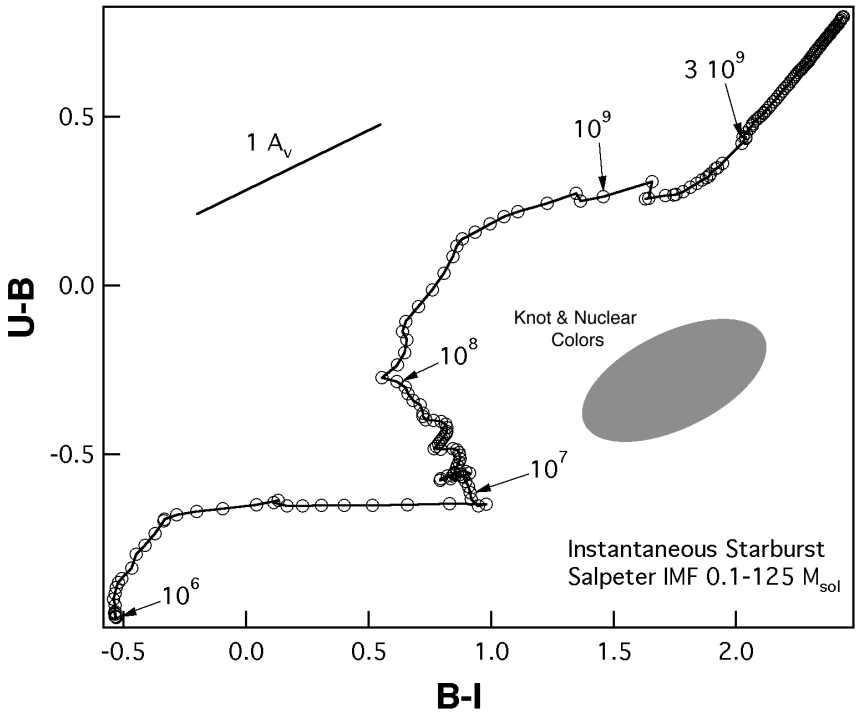

Fig. 6.2.— ($U-B$, $B-I$) colors for a modeled starburst (BC95) with a Salpeter IMF and upper and lower mass cutoffs of 125 and 0.1 $M_\odot$, respectively. The shaded area represents the locus of knot colors observed in all three samples as well as the cool ULIG nuclei.

Table 6.1. U′ Observations of Selected Targets

Name[a]		Exp. Time	m_U
IRAS 00091-0738	Total	2880	18.75
IZw 1	Total	2400	13.68
IRAS 01003-2238	Total	360	17.89
IRAS 01199-2307	Total	7200	14.12
	SE Nucleus		18.92
	NW Nucleus		20.12
Mrk 1014	Total	3240	14.68
	Nucleus		14.91
IRAS 05189-2524	Total	6720	15.64
	Nucleus		16.17
IRAS 07598+6508	Total	4000	13.91
PG 0838+770	Total	3240	15.42
IRAS 08572+3915	Total	5040	16.68
	SE Nucleus		19.18
	NW Nucleus		19.59
	4		22.04
	5		21.71
UGC 5101	Total	4500	16.00
PG 1119+120	Total	3240	14.12
	Nucleus		14.31
PG 1126-041	Total	4720	13.56
	Nucleus		13.71
IRAS 12071-0444	Total	3200	17.66
IRAS 12112+0305	Total	3240	16.50
	N Nucleus		18.67
	S Nucleus		>23.20
	NW knot		19.76
	S knots		19.03
	1		19.28
PG 1229+204	Total	3240	14.38
	Nucleus		14.52
	SE Knots		19.50
Mrk 231	Total	1680	14.11
	Nucleus		14.80
	10,11,12,14,irA		18.36
	5,6		18.83
Mrk 273	Total	4000	15.12
	Nucleus		17.17
	S knot		17.94
	W knot		17.80
Pks 1345+12	Total	3360	17.76
Mrk 463	Total	3240	14.76
	E Nucleus		16.48
	W Nucleus		16.84
	1,2,3,4		19.07
	5,6		19.77
	7		20.57
	8,9,10		20.78
PG 1411+442	Total	3200	13.27
	Nucleus		13.71

Table 6.1—Continued

Name[a]		Exp. Time	m_U
IRAS 14348-1447	Total	3240	16.92
	NE Nucleus		18.65
	SW Nucleus		18.04
IRAS 15206+3342	Total	3480	16.21
	E half		16.53
	W half		18.05
IRAS 15250+3609	Total	2520	16.21
	Nucleus		16.95
PG 1613+658	Total	3720	13.91
	Nucleus		19.62
IRAS 23365+3604	Total	4320	16.77
	1		19.20
	2		19.80
	3		20.72

[a] "Nucleus" values are for a circular aperture 2.5 kpc in diameter. Knot identification numbers refer to those given in Chapters 2-5.

The lack of resolved U′knots among many of the cool ULIGs forces an examination of their "nuclear" colors. In Chapter 4 it was shown that the nuclear regions (defined by a radius of 1.25 kpc) typically had optical/near- infrared colors similar to young star-forming regions with contributions from hot dust and mild (2–4 A_V reddening). The median "nuclear" colors for the cool ULIGs observed at U′are ($U-B$, $B-I$)=(−0.35, 2.07), with ($U-B$) ranging from 0.2 to −0.7. Dereddened, the median nuclear starburst age is 10 Myrs. Although it is not possible to discriminate between AGN and starburst activity based on UBI colors alone, the lack of a K′excess in the cool ULIGs bolsters the interpretation of the blue U−B colors as being indicative of young stars. The presence of young stars in the cool ULIG nuclei (and in particular the single nucleus systems such as UGC 5101) seems to argue in favor of on-going young star formation, as opposed to the apparent brief burst experienced in the tidal tails. In several cases U′knots are resolvable within a radius of 4−5 kpc of the nucleus. In IRAS 12112+0305 the knots flanking the northern nucleus as well as the knots in the southern arc have dereddened ages of 34 and 6 Myrs, respectively. The southern knot in Mrk 273 has colors most similar to a 1 Gyr old burst (although this seems unlikely due to the fading discussed above), while the western knot appears to be about 200 Myrs. Finally, IRAS 23365+3604 has knots ranging between 3–60 Myrs.

Examining the "warm" ULIGs is more problematic, since there is evidence for AGN activity in the nuclei of all of these systems, and since AGN have *UBI* colors very similar to those of a young starburst. It is therefore likely that any examination of the nuclear (radius<2.5 kpc) regions will simply reflect the presence of AGN light. Instead, we break the warm ULIGs into several subcategories. Of the 3 systems with double nuclei, IRAS 08572+3915 and Mrk 463 each have many U′knots, while Pks 1345+12 seems to have few.

Although this latter case may be a result of the low S/N of our observations, the *HST* data (Chapter 2) also shows little in the way of knot structure as well. The knots in the tails of IRAS 08572+3915 appear to have dereddened ages of 5–10 Myrs, while those in Mrk 463 vary from 4-90 Myrs, although the median is only 6 Myrs. The stellar galactic nuclei (based on imaging at other wavelengths) IRAS 08572+3915e and Mrk 463w have ($U-B$, $B-I$) colors of (-0.26, 1.56) and (-0.36,1.54) yielding dereddened ages of 45 and 25 Myrs, respectively. Similarly, it was shown in Chapter 3 that the optical emission from IRAS 08572+3915w is predominantly starlight, since the AGN only begins to contribute at near-infrared wavelengths. For it we derive a starburst age of 37 Myrs. Pks 1345+12 has integrated colors so red ($U-B$, $B-I$)=(0.73,2.54) as to be similar to a very old, late-type stellar population, although this could also be the result of 2–3 A_V of intervening dust. The integrated colors of IRAS 01003−2238 indicate an age of 40 Myrs, although at least some of the knots observed with WFPC2 are at most 5 Myrs in age (Chapter 2). Of the single-nucleus non-QSO systems, Mrk 231, IRAS 12071−0444, and IRAS 05189−2524 have the most well-developed tidal structure, but only the former two have any evidence for resolvable starburst knots. This is probably due to the lower spatial resolution at U′; there is evidence in the WFPC2 data (Chapter 2) for an extended starburst region in the nucleus of IRAS 05189−2524, but which cannot be resolved here. Estimated ages for the southern, presumably stellar, part of IRAS 12071−0444 are 125 Myrs. The northern part in the vicinity of the putative active nucleus contains several knots of star formation which we cannot resolve here, and which may be quite young. IRAS 15206−3342's western half has colors of (-0.41, 1.50), which are similar to those of a 20 Myr old burst. The eastern component shows a peculiarly large U′excess (-0.9, 1.55), which may be indicative of contamination by the putative active nucleus. The same is likely to be true of the nuclear colors of IRAS 05189−2524, whose dereddened colors are similar to a 5 Myr old starburst. Mrk 231's "horseshoe" has dereddened colors similar to a starburst 225 Myrs old. The extended structure in the QSO I Zw 1 appear similar to the spiral arms of a spiral host galaxy; the U′emission is similar to that seen in spirals. Mrk 1014 has several knots embedded in its tidal tails, 2 of which were detected with WFPC2. Unfortunately, they are sufficiently faint that their colors are not well determined; they are likely to be in the age range 3–30 Myrs. Lastly, the extended features to the south and east of IRAS 07598+6502 were not obviously detected; however, these features were of fairly low effective surface brightness due to the seeing. A careful examination of the region as a whole indicates ($U-B$) similar to a stellar population of 5–10 Myrs.

Finally, we examine the colors of the galaxy features of the infrared-excess PG QSOs. Unfortunately, there are very few such features detected at U′. The small arc in PG 1119+120 has a dereddened age of 40 Myrs. The second nuclear knot is undetectable at U′, although given the limited spatial resolution this is not surprising. The knots at the ends of the bar in PG 1229+204 are extremely blue, and have ages of around 3 Myrs.

6.3.3. Luminosities

Again, we consider the bolometric luminosity of the observed knots and nuclear regions. The U-band bolometric correction (BC) is relatively robust against changes in the IMF mass

cutoffs, since the energetics are dominated by the most massive stars. Indeed, adjustments to the IMF mass cutoffs, while changing the bolometric luminosity per unit mass by a few times, have little effect on color as explained above, and hence the bolometric correction remains unchanged. Throughout the starburst age range of 0-1 Gyr, the BC at U varies only from about 0.5 to 2, and is very nearly 1 during the span of 10-600 Myrs for the modeled starburst. The likely bolometric luminosity of the star formation observed at U′was determined by applying the bolometric correction applicable to a given measured emission region based on it's estimated upper age limit, which was in turn based on its *UBI* colors. This was then dereddened by the amount indicated by the *UBI* colors (typically $A_{U'}$ = 1–1.5).

The cool ULIG luminosities were calculated by considering the emission inside the nuclear (2.5 kpc diameter) regions, as well as any observed knots. The estimated $L_{\rm bol}$ ranges from $10^{9.7}L_{\odot}$ (UGC 5101) to $10^{11.3}L_{\odot}$ (IRAS 00091−0738), with a median of $10^{10.7}L_{\odot}$and 75% lying in the range $10^{10.4--10.9}L_{\odot}$. The star-formation observed at U' thus accounts for approximately 3% of the bolometric luminosity in a typical cool ULIG, assuming an average $L_{\rm bol}$ of $10^{12.3}L_{\odot}$. This is extremely similar to the result derived in Chapter 4 from optical/near-infrared wavelengths.

The warm ULIGs' star-formation budget was tallied by adding up all the emission in the observed knots as well as non-AGN nuclear regions (i.e., IRAS 08572+3915e) and all the nuclear regions where star-formation is believed to dominate based on WFPC2 B-band imaging (e.g., IRAS 08572+3915w, IRAS 12071−0444). The warm ULIG luminosities vary from $10^{9.9}$ (IRAS 08572+3915) to $10^{11.7}L_{\odot}$(IRAS 15206+3342), with a median of $10^{10.6}L_{\odot}$. Again, this is similar to results found at other wavelengths. The warm ULIGs (not including 3c273) have a mean $L_{\rm bol}$=$10^{12.26}L_{\odot}$; the average warm ULIG has a contribution of ≈2% by star formation observed at U′to the bolometric luminosity, although this number is as high as 30% in at least one case (IRAS 15206+3342).

Since most of the QSOs have no evidence for star-forming knots, we instead examine the extreme case that *all* the U′emission originating in the QSO host galaxy is due to young star formation. The resulting median bolometric luminosity based on U′luminosity is $10^{10.8}L_{\odot}$, ranging from $10^{10.6}$ to $10^{11.1}L_{\odot}$. Since all of the QSOs have bolometric luminosities in excess of $10^{12}L_{\odot}$, this merely confirms the obvious statement that in the QSOs the majority of the high bolometric luminosity arises in a process other than star formation, i.e., the QSO nucleus. The similarity in luminosity ranges for the QSO hosts and the results derived for the ULIGs is probably more indicative of the similarity in their host masses than anything else; similar sized host galaxies with similar colors have similar derived total luminosities. Counting only the observed luminosities in the small knots of PG 1229+204 and PG 1119+120, the total emission in resolvable star-forming knots is only $10^{9.7}$ and $10^{9.5}L_{\odot}$, respectively. This is an order of magnitude less than is typical for the ULIGs, although it is similar to the emission from individual knot complexes in the ULIGs (i.e. in the horseshoe of Mrk 231). The ULIGs simply have many more knots.

6.4. Conclusions

1. Many ULIGs are luminous at U′and have evidence for considerable small-scale structure. This structure is almost identical to that seen at optical wavelengths.

2. Many of the double-nuclei systems have luminous knots of U′emission in their tidal tails, which seem absent in the single-nucleus systems. If real, this may indicate that the star-formation in the tails is predominantly brief and occurs early during the merger process.

3. Most of the compact knots in the cool ULIGs have estimated upper age limits (based on their *UBI* colors) on the order of 10 Myrs, with a few systems having slightly higher limits. In the "warm" ULIGs these upper limits are also generally slightly higher ($\approx$ 50 Myrs), with several systems having upper limits of several hundred Myrs. Although this could be a result of reddening, it runs counter to that expected based on morphology.

4. Few of the QSOs show evidence for compact U′emission other than in their active nuclei, despite having been predominantly selected for having bright, extended tidal features similar to those of the ULIGs. This is consistent with their being aged versions of the ULIGs. Conversely, it is also consistent with their having never developed compact star-forming regions like those in the ULIGs in the first place, or that these regions had a different luminosity distribution. However, the presence of extended tidal structure in some QSO systems and the prevalence of young star-forming clusters in other merging galaxies argues against this interpretation. Those that do have compact knots have upper age limits of 3–30 Myrs, which either argues against their fitting into the late stages of a merger time sequence or that some star-formation is still on-going.

5. The bolometric luminosity of the star-formation observed at U′is generally only a very small fraction ($\approx$ 3%) of the known bolometric luminosity, a result nearly identical to that derived at optical and near-infrared wavelengths. This implies that "what you see is what you get"; even over a span of a factor of 20 in visual extinction, the star-forming structure remains similar. Most of the star-formation we can detect even in the near-infrared probably occurs in knots that are not heavily extinguished along the line of sight.

6.5. Notes on Individual Objects

IRAS 00091−0738 — the U' emission originates primarily in the stellar "nucleus", with very little emission coming from the dense tidal tail to the south.

I Zw 1 — the U' emission originates almost entirely (90%) in the Seyfert 1 nucleus. Both tidal arms can be traced at U' and closely mirror the B-band morphology. In particular, the two condensations in the NW arm and the bright blue condensation in the SW arm are both easily detected at U'.

IRAS 01003−2238 — no features are discernible, which is expected from the small size scale of the extended structure seen in the WFPC2 images and the poor ground-based resolution. It's colors are similar to a starburst of age 10 Myrs.

IRAS 01199−2307 — both nuclei are detected at U', but the emission is dominated by the SW nucleus by roughly 3.5:1. The tidal arms are undetected at U'.

Mrk 1014 = PG 0157+001 — the eastern tidal arm is very prominent at U', breaking into many smaller clumps. The QSO nucleus accounts for about 86% of the total U' emission. The integrated host galaxy color is $U-B$=0.72, similar to that of old stars.

IRAS 05189−2524 — the U' emission essentially mirrors that at all other wavelengths. The EW and NS loops are easily seen.

IRAS 07598+6502 — the star-forming knots detected at B are undetected at U'. The nucleus accounts for 94% of the emission.

PG 0838+770 — the U' emission arises primarily in the QSO nucleus. The bar is just discernible at U'.

IRAS 08572+3915 — large knots of emission trace the leading edges of all the tidal structures for their entire length. Many small knots are seen in the vicinity of the putative NW active nucleus. The SW nucleus dominates at short wavelengths, perhaps indicating that a strong starburst is taking place there. Both nuclei have $(U-B) < -0.25$ in a 2.5 kpc diameter aperture; this, combined with their $(B-I)$ colors from Chapter 2, indicates the presence of stars that cannot be much more than 100 Myrs old in both nuclei.

UGC 5101 — the U' emission comes from an extended region in the core of the merger system. The tidal tails are barely detectable.

PG 1119+120 — the host galaxy and bar are just barely detectable at U′. The only feature readily recognizable at U' is the knot directly east of the QSO nucleus, which appears elongated in the direction of the (possibly) tidal arm.

PG 1126-041 — the host galaxy has no high surface brightness features.

IRAS 12071−0444 — clearly extended in the same manner as the WFPC2 images. Nearly all the compact U' emission arises from the northern nucleus seen at B. The southern complex of knots is clearly detected at U'.

IRAS 12112+0305 — all of the tidal structure seen at B & I is seen at U'. The condensations in the center of the southern tidal arc are clearly visible. The galactic "nucleus" in the northern part of the system is dominated by a compact knot of emission at U', with another knot located on the short tidal arc extending to the west. Most notable by it's absence is the star-like nucleus in the center of the system, which has completely disappeared between U' and B-band, implying a line-of- sight extinction greater than 3 A_V.

PG 1229+204 — the elongated structure of the bar is visible at U', as are the blue star-forming knots that run in chains at each end of the bar. The contrast between the northern knots and the bar is even greater here than at B, and the presence of the knots argues against the interpretation that the southern knots are the remains of a tidally distorted galaxy.

Mrk 231 — The U' emission comes almost entirely from the active nucleus and from the southern star-forming "horseshoe". The horseshoe has $(U-B)$=0, yielding a maximum age of a few hundred Myrs. The corkscrewing structure extending from the NW of the nucleus

and wrapping around through the west to the extreme south of the nucleus is also detected at U'.

Mrk 273 — Although the tidal tails are clearly detected at U', nearly all the emission arises in the central few kpc, which contains several large knots of U' emission which are not seen in the WFPC2 I-band images or in CFHT K-band images (Knapen et al. 1997) In particular, the extremely prominent southern knot does not appear in either of these images.

Pks 1345+12 — this galaxy is very red ($U-B$=0.73, $B-I$=2.54) and hence difficult to detect with high S/N at U'. However, it appears that most of the U' emission arises in the vicinity of the western nucleus.

Mrk 463 — the eastern nucleus is distinctly elongated N-S, and the western nucleus is elongated E-W exactly as expected from the WFPC2 images. Nearly all of the U′ emission in the eastern nucleus comes from the position of the northern "knot", and not the southern infrared "nucleus", which is consistent with its interpretation as an AGN ionization feature. Although the eastern nucleus is physically smaller, and hence has a higher peak surface brightness, it is the western nucleus that dominates in overall luminosity at U′. All of the "knots" identified in the tidal ring structure are extremely luminous at U′. Their colors indicate ages less than 10 Myrs.

PG 1411+442 — despite having prominent optical tidal tails, almost no features can be discerned surrounding this quasar at U′. A very faint region of the northern tail can just be detected at U′.

IRAS 14348−1447 — again, the U′ emission mirrors that at B. The blue knots seen at B surrounding the southern nucleus contribute heavily to the U′ emission in that nucleus, while the northern nucleus has a chain of knots in the base of the northern tail that contribute to the U′ emission.

IRAS 15206+3342 — closely resembles the WFPC2 optical images (Chapter 2). Most of the U′ emission seems to originate in the compact nuclei in the southern half of the primary "string" of knots, consistent with their blue colors.

IRAS 15250+3609 — the high surface brightness central galaxy component is well detected at U′, as are the tidal features. Surprisingly, what appeared to be two separate features at I-band now appear to be a single arc bending away from the galaxy to the NE. The nearly circular arc to the south is undetected. The U′ emission is emitted by a compact source in the southern half of the central galaxy nucleus.

PG 1613+658 — there is no clear detection of the tidal tails or any other high surface brightness structure. The QSO nucleus accounts for 96% of the U′ emission.

IRAS 23365+3604 — the U′ emission closely mirrors that at B. All of the knots detected at B are luminous at U′, and have derived (U−B) <0, indicating probable ages of 10 Myrs or less. The tails are almost undetectable; the most prominent extended emission at U′ is the arclike extension of the disk to the NW of the nucleus. Overall, the total integrated galaxy colors are similar to those of an old stellar population.

REFERENCES

Allen, C.W. *Astrophysical Quantities*, 1973, (London: Athlone Press)

Bahcall, J.N., Kirhakos, S., Saxe, D.H., & Schneider, D.P. 1997, ApJ, 479, 642

Bruzual, G., & Charlot, S. 1993, ApJ, 405, 538

Clements, D.L., Sutherland, W.J., McMahon, R.G., & Saunders, W. 1996, MNRAS, 279, 477

Charlot, S., Ferrari, F., Mathews, G.J., & Silk, J. 1993, ApJ, L57

Guiderdoni, B., & Rocca-Volmerange, B., 1988, Ap&SS, 74, 185

Elvis, M. 1994, ApJS, 95, 1

Elvis, M., Green, R.F., Bechtold, J., Schmidt, M., et al. 1986, ApJ, 310, 291

Hutchings, J.B., & Neff, S.G., 1992, AJ, 104, 1

Knapen, J.H., Laine, S., Yates, J.A., Robinson, A., Richards, A., Doyon, R., & Nadeua, D. 1997, ApJ, 490, L29

Larson, R.B., & Tinsley, B.M., 1978, ApJ, 219, 46

Leitherer, C. 1996, in From Stars to Galaxies, eds. C. Leitherer, U. Fritze-vonAlvensleben, J. Huchra (San Francisco: ASP), 373

Meurer, G., Heckman, T., Leitherer, C., Kinney, A., Robert, C., & Garnett, D. 1995, ApJ, 110, 2665

Murphy, T., Armus, L., Matthews, K., Soifer, B.T., Mazzarella, J.M., Shupe, D.L., Strauss, M.A., & Neugebauer, G. 1996, AJ, 111, 1025

Neugebauer, G., Green, R.F., Matthews, K., Schmidt, M., Soifer, B.T., & Bennett, J. 1987, ApJS, 63, 615

Rieke, G.H., & Lebofsky, M.J. 1985, ApJ, 288, 619

Sanders, D.B., Soifer, B.T., Elias, J.H., Madore, B.F., Matthews, K., Neugebauer, G., & Scoville, N.Z. 1988a, ApJ, 325, 74

Stockton, A., & MacKenty, J.W., 1987, ApJ, 316, 584

Young, S., Hough, J.H., Efstathiou, A., Wills, B.J., Bailey, J.A., Ward, M.J., & Axon, D.J. 1996, MNRAS, 281, 1206

Whitmore, B., & Schwiezer, F. 1995, AJ, 109, 960

Chapter 7

Conclusions: The Merger Time Sequence

ABSTRACT

Two possible time sequences for cool ULIGS, warm ULIGs, and PG QSOs are presented. The first is a morphological sequence based on comparison to n- body simulations of mergers between similar mass spiral galaxies and characterized by luminosity-normalized tail lengths and nuclear separations. A clear correlation is found between detailed morphology and the appearance of tracers of AGN activity. The second is based on star-formation observed in the three samples. We discuss how the nature of the circumnuclear starburst prevents a detailed interpretation of the galaxy ages based on the apparent ages of the starburst knots, although some general statements may be made. Additional observations that may someday be able to salvage this technique are presented. Final conclusions from the dissertation are then presented.

7.1. Introduction

In Chapter 1, the purpose of this dissertation was outlined as an attempt to determine if an evolutionary sequence exists relating ultraluminous infrared galaxies (ULIGs) and optical QSOs. Chapters 2–6 explored the circumnuclear and extended environments of the three different samples of objects and demonstrated similarities between all of them. In this final chapter, an attempt is made to show an actual *time* sequence, showing that not only are the ULIGs and QSOs inherently similar types of objects, but that they are related to each other temporally, and that their apparent properties change over time. This time sequence must be based on *independent* features of the hosts unrelated to putative AGN features, such as the projected separation of the galaxy nuclei in multiple nucleus systems. Furthermore, these features must be ones that evolve in time, since otherwise they might only suggest a range of properties, and not a time sequence.

Previous attempts have been made to suggest such a time sequence. Originally, Sanders et al. (1988a,b) proposed an evolutionary model linking QSOs and ULIGs via the putative transition objects known as warm ULIGs, due to their "warm" mid-infrared colors. Studies have shown that several properties of infrared galaxies are tied to their luminosity, most notably the fraction of interacting galaxies and the fraction of systems showing AGN-like spectra (Kim 1995). However, these studies have generally concentrated on implicating the presence of merger activity in various phenomena; they have not taken the additional step of placing the galaxies themselves in a time sequence. The most famous attempt to do so, of course, is the Toomre morphological sequence (Toomre 1977), which arranged objects by the degree of coalescence of the progenitor disk galaxies. It did not, however, address specifically the question of ULIGs and was geared more towards the formation of elliptical galaxies. Other recent studies have sought to construct galaxy time sequences by measuring the ages of star-forming knots as determined by their broad-band colors (Whitmore et al. 1997). In this chapter we use both approaches, trying first to demonstrate a time sequence based on morphological features, and then the same task based on age-dating of star-formation.

7.2. Morphological Sequence

We have divided all three samples into several broad categories based on their morphology. Figure 7.1 shows an n-body simulation of the merger of two spiral disk galaxies (Gerritsen 1997), and is instructive for understanding the different phases of the merger process. Note that it is not meant to be taken as a literal description of the merging process during ultraluminous infrared galaxy formation. Many outside factors contribute to the details of the merger: impact parameter, relative velocity, galaxy mass and morphology, rotation, etc. (Barnes & Hernquist 1992, 1996). In particular, the timescale associated with each panel in Fig 7.1 should not be considered absolute. However, in gross properties this model seems to be similar to the observed morphologies of many ULIGs, and hence is useful as an aid in assembling a merger time sequence.

At the earliest stages of interaction, prior to the first close passage of the galaxies, the galaxy disks remain relatively unperturbed and separate and hence do not show evidence for tidal tails or bridges. The is the *first approach* stage (I), and is represented in Fig 7.1 by time-steps 104–209. There are no such unperturbed double galaxy systems in any of the three samples. Such galaxies *do* abound in far-infrared flux limited samples of paired galaxies such as in Appendix A. This indicates that ultraluminous activity is not achieved at such an early stage in the merger process, although some far- infrared enhancement has begun.

Similarly, in the *first contact* stage (II), although the disks overlap, strong bars and tidal tails have not yet formed. These are the primary morphological differences between time-step 313 and the time-step 939 that will be visible in imaging data. All of the galaxies in the two ULIG samples have well-developed tidal-tails, although in some cases these require deep imaging to see. While tails are not found in the majority of the QSO hosts, it is also the case that none of the tailless QSO hosts appear similar to a pair of overlapping disks. It is therefore likely that none of the observed objects is in this stage of merger.

Now we consider all *pre-merger* systems (III), i.e. those that still have two identifiable nuclei and yet also have well-defined tidal tails. This time period corresponds to time-step 417–835 in Fig 7.1. While our imaging observations cannot prove that the multiple nucleus systems will necessarily merge, the presence of ultraluminous activity combined with the prevalence of mergers in ultraluminous galaxies, as well as the presence of tidal tails and other structure interconnecting the nuclei in every case, would seem to strongly indicate eventual merger. Within this category the systems have been arranged according to projected separation; lacking kinematic information, this is an approximation only since we cannot tell if the two galaxies are pre or post-apgalacticon (farthest approach). Of the cool ULIGs, this stage includes IRAS 01199−2307, IRAS 03521+0028, IRAS 14348−1447, IRAS 22206−2715, IRAS 22491−1808, and IRAS 23233+0946. In the warm ULIGs these are IRAS 08572+3915, Mrk 463, and Pks 1345+12. Of the three QSOs with clear tidal tails, only PG 0007+106 might fit into this category. However, it is unclear if the two galaxies to it's south are tidally connected, and hence it will not be included here. Ordered by nuclear separation, they are: IRAS 01199−2307 (24 kpc), IRAS 22206−2715 (8.9 kpc), IRAS 2323+0946 (8.8 kpc), IRAS 08572+3915 (6.2 kpc), IRAS 14348−1447 (5.5 kpc), Pks 1345+12 (4.6 kpc), IRAS 03521+0028 (4.3 kpc), Mrk 463 (3.8 kpc), IRAS 12112+0305

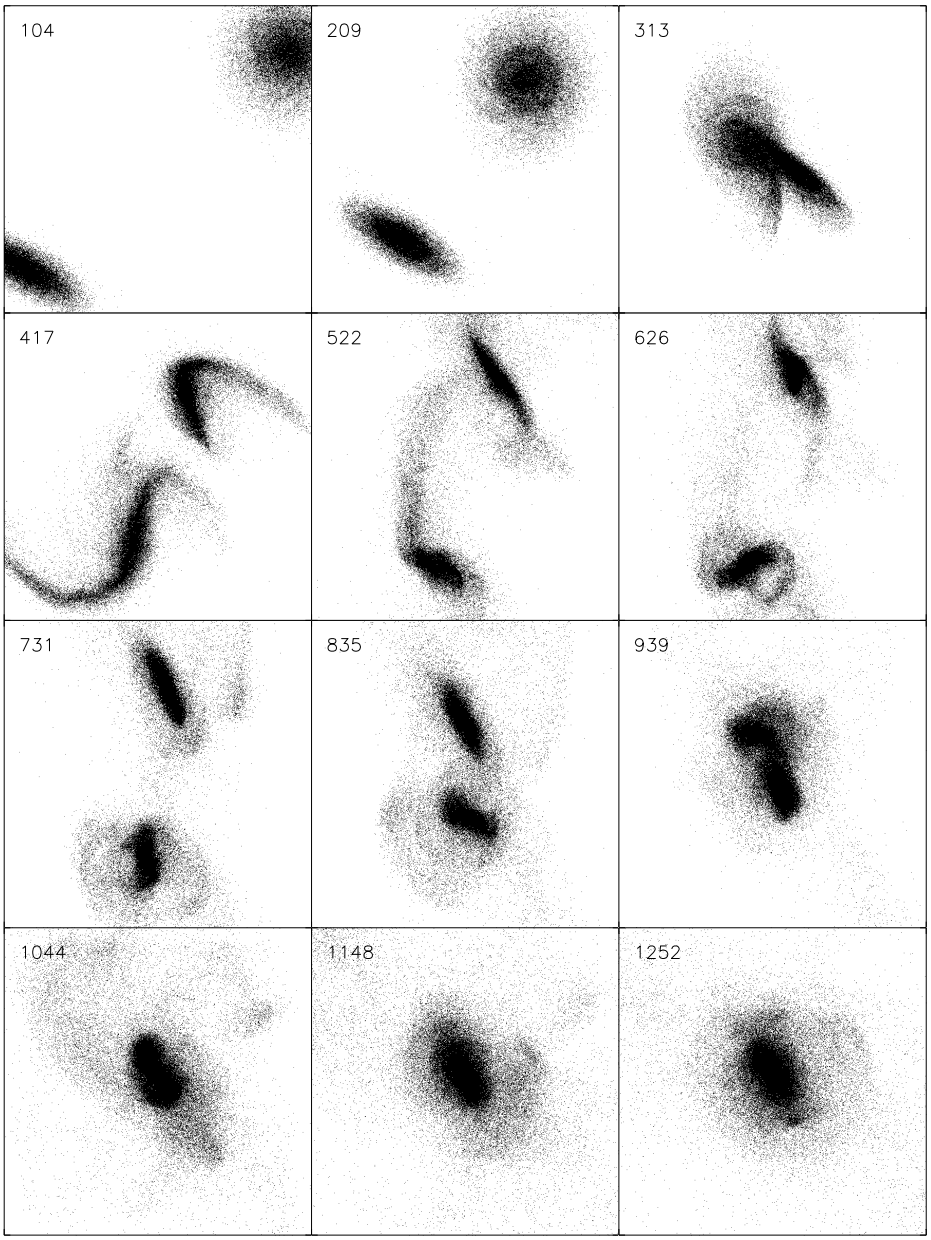

Fig. 7.1.— An n-body simulation of the merger of two spiral disks (Gerritsen 1997; reproduced with permission). Most of the ULIGs correspond to the time period between t=417–1044. Although the time-steps are in Myrs, they should only be considered schematic.

(2.5 kpc), and IRAS 22491−1808 (2.5 kpc). The Stage III systems, ordered by nuclear separation, are shown in Figure 7.2.

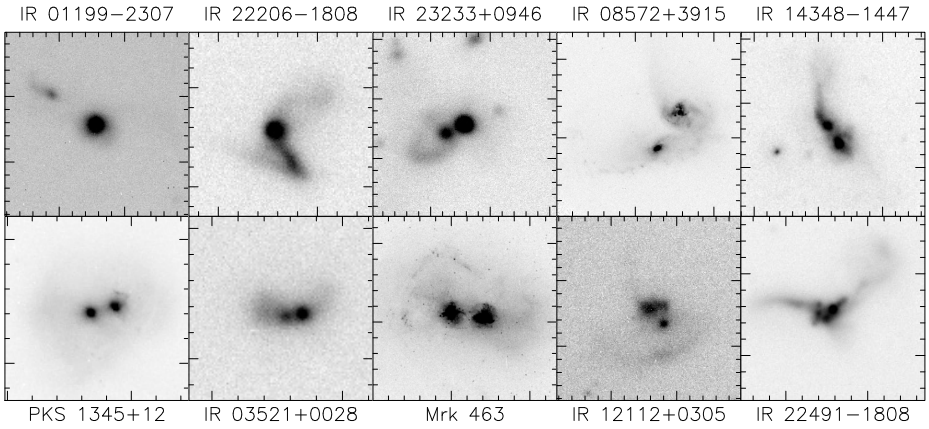

Fig. 7.2.— Stage III pre- merger systems in order of decreasing nuclear separation left to right, top to bottom. I-band images are shown, emphasizing the structure of the tidal tails.

The *merger* stage (IV) occurs after the nuclei have apparently coalesced. These systems have prominent tidal features, but only one nucleus can be detected at optical and near-infrared wavelengths. Additionally, the sole galaxy core is often noticeably extended and tends to be cut by many dust lanes. Most of the ULIGs belong in this category: IRAS 00091−0738, UGC 5101, Mrk 273, IRAS 15250+3609, Arp 220, IRAS 20414−1651, IRAS 23365+3604, Mrk 1014, IRAS 05189−2524, IRAS 12071−0444, Mrk 231, and IRAS 15206+3342. Three QSOs fall into this class: PG 0007+106, PG 1411+442, and PG 1613+658. It is clear that there are two dominant morphologies in this class. The first group, which we will call stage IVa, consists of systems that have diffuse, extended central regions typically composed of several smaller extended emission regions which appear to be cut by dust lanes. Stage IVa includes IRAS 00091−0738, Arp 220, IRAS 20414−1651, IRAS 12071−0444, IRAS 05189−2524, and IRAS 15206+3342. The second stage, IVb, consists of systems that are dominated, particularly at long wavelengths, by a single point-like source, and includes all other stage IV objects. However, there is no a priori reason to believe that the stage IVb systems are any older than the stage IVa systems, other than the fact that stage IVa resembles stage III, and stage IVb resembles stage V, and that stage V is older than stage III based on the appearance of tidal structure.

Finally, we arrive at the *old merger* stage (V). These are systems which do not show any direct *unmistakable* signs of tidal tails, yet have disturbed central morphologies similar to those of the merger stage IV systems, particularly those with knots of star formation. Essentially, this implies that the surface brightness of any tidal features has fallen below our detection limit, leaving nothing but the high surface brightness relaxed merger remnant core visible. No cool ULIG fits into this class, since they all have tails. Among the warm ULIGs, the most likely representative of this class is IRAS 07598+6502, which apparently has patches of tidal debris. Other candidates for this stage are PG 1229+204 (with a strong nuclear bar and star- forming knots), PG 0838+770, PG 1119+120, PG 1126-041, and PG 2130+099 (see Chapter 5).

Figure 7.3 shows a schematic representation of the merger time sequence based on the extended morphology of the host galaxies. This figure extends from Stages I-V, and shows selected ULIGs and QSOs. It additionally illustrates stage I with some of the objects from Appendix A, which are not ULIGs.

It is apparent that a critical morphological transition seems to be occurring in stage IV (as illustrated by the differentiation between stages IVa and IVb), and it is unfortunate that we do not have more objective means for evaluating the system ages. While it should be possible to use the detailed structure of the tails as a means of measuring the dynamical ages of the systems, this is difficult to put into practice due to orientation effects. The surface brightness of the tails is difficult to determine, because the tails themselves are not solid structures but instead resemble thin curved sheets. As a result, when seen edge-on (e.g., UGC 5101, Mrk 273) their surface brightness is higher than if they were face- on. Similarly, because the tails are curved and actually comprise full loops in some cases (e.g., UGC 5101, IRAS 15250+3609), it is difficult to evaluate their full length, especially in those cases where the tails are seen length-on. In any case, their length may be set by the particulars of the interaction. Nonetheless, due to lack of anything better, we will attempt to use the lengths of the tails as a crude age diagnostic as they are the easiest merger feature to quantify. Due to the scalability of the mergers, we expect larger galaxies to raise longer tails. In order to correct for this, we consider the length of the tails divided by the total H-band luminosity of the host galaxy. Thus, for each system we derive a luminosity-normalized tail length in kpc per L_{H*}. As a first test, we examine the lengths of all the tails of the stage III and IV objects. The average tail length in stage III is 17 ± 10 kpc$\cdot L_*^{-1}$, with a median of 14 kpc$\cdot L_*^{-1}$. For stage IV, the mean is 31 ± 18 kpc$\cdot L_*^{-1}$, with a median of 26 kpc$\cdot L_*^{-1}$. Figure 7.5 shows the cumulative distribution functions of luminosity-normalized tail lengths for the Stage III and Stage IV systems. Kolomogorov-Smirnov statistics indicate that we can reject the null hypothesis that the two CDFs are drawn from the same parent set at the 95% level; small sample statistics are the primary cause of the low significance of this result. It thus appears that there is a difference in the lengths of their tidal tails, and since stage IV must be more evolved than stage III by virtue of having fully merged nuclei, this difference in tail length probably reflects the difference in their dynamical age. The increasing disparity between the two CDFs at large tail lengths is expected due to orientation effects. Given a random distribution of projection angles on the sky, both distributions of tail lengths must necessarily meet at tail lengths of zero when they lie nearly orthogonal to the plane of the sky.

Extending this to within Stage IV, we find for stage IVa that the mean is 27 ± 17 kpc$\cdot L_*^{-1}$, while for stage IVb it is 33 ± 20 kpc$\cdot L_*^{-1}$. Therefore, there does not seem to be a statistically significant increase in tail length between the two dominant nuclear morphologies in Stage IV. On the other hand, given the small significance of the difference between Stages III and IV, which are obviously different dynamical ages, it is unlikely that a statistically significant result could be derived from the extremely small sample sizes of Stages IVa and IVb (5 and 10 objects, respectively).

We can now examine the question of whether the appearance of active nuclei is tied to the dynamical time sequence. First, we examine when the appearance of AGN diagnostics appear in the optical spectra; it has been shown by Goldader et al. (1995) and Veilleux

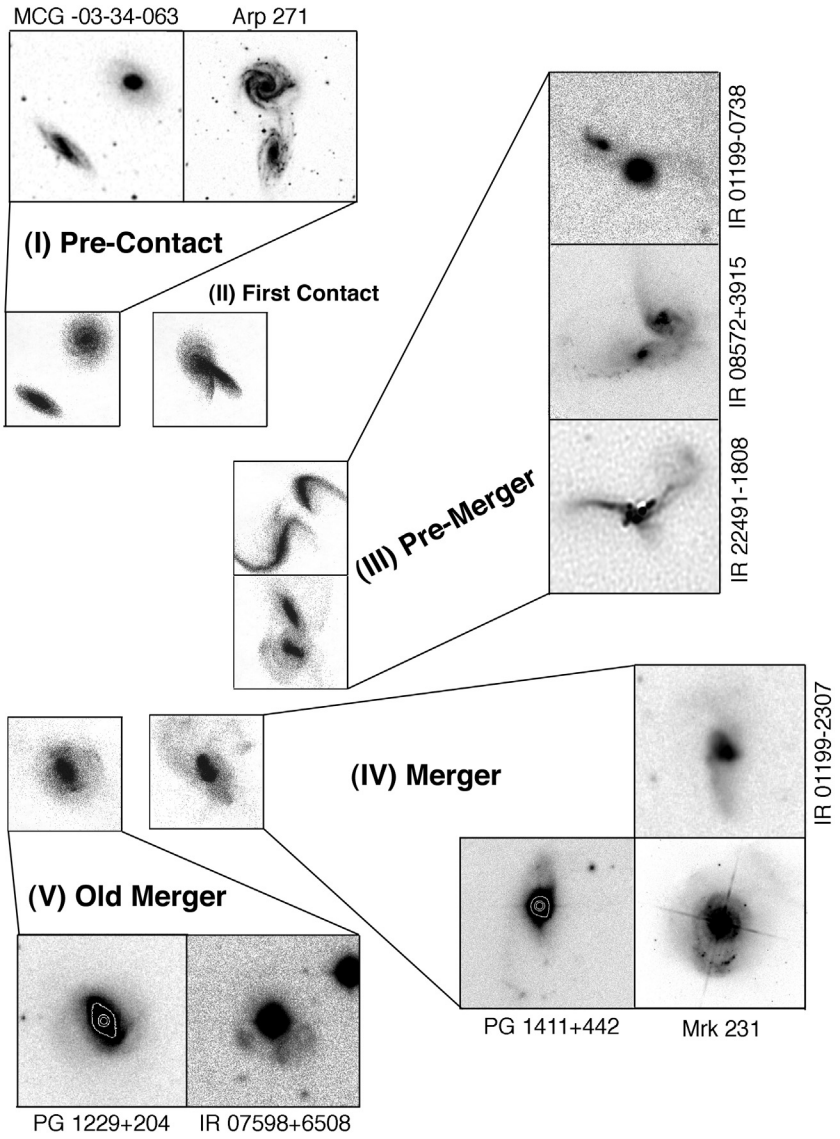

Fig. 7.3.— Schematic representation of the 5 merger sequence stages illustrated with n-body simulations taken from Fig 7.1. and selected ULIGs and QSOs. Also shown are interacting galaxies from Appendix A used to illustrate stage I. These two systems are not ULIGs.

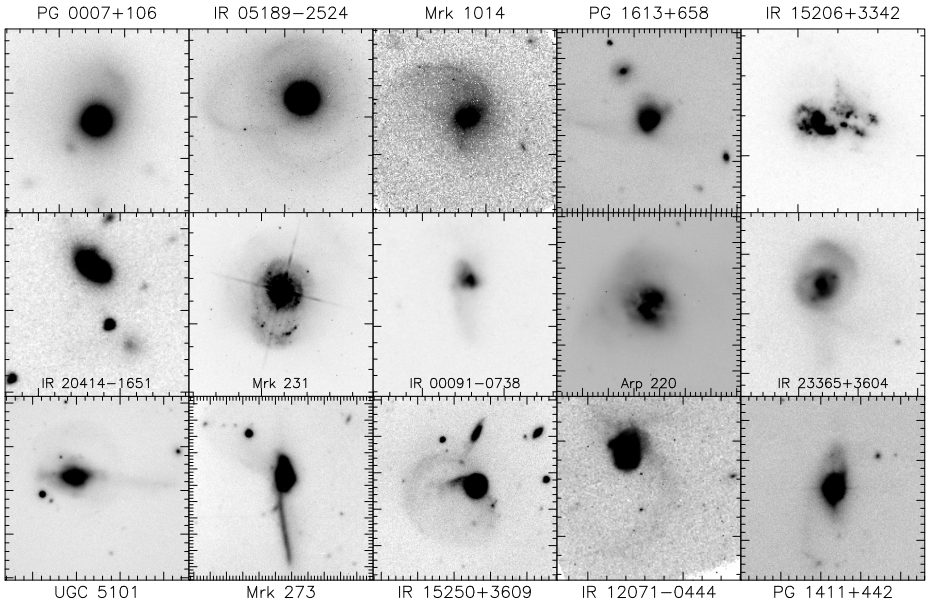

Fig. 7.4.— I-band images of stage IV (single nucleus merger) systems, arranged by length of tails normalized by the host galaxy H-band luminosity. The images have been stretched in an attempt to show the tail structure, at the expense of the central regions.

et al. (1997) that while near-infrared spectra are capable of finding broad line regions in those systems known to be Seyfert 2s from optical spectra, the non-Seyfert systems are too obscured to be uncovered even at near-infrared wavelengths. Therefore, the optical classifications are as useful as those in the near-infrared for detecting AGN. Since the appearance of AGN spectra is believed to be tied to a dust-expulsion unveiling process, the more evolved systems should have a greater likelihood of AGN-like spectra visible at short wavelengths. We use the optical spectral classifications of Sanders et al. (1988a,b), Kim (1995), Veilleux et al. (1997), and Veilleux et al. (1998). We find that stage III has an active nucleus fraction (Seyfert 1 or 2) of 20%, while the stage IV systems have an active nuclear fraction of 60%. 40% of Stage IVa systems contain optically identifiable active nuclei, while 70% of stage IVb systems do. This holds even if we consider only the ULIGs (since it is unclear how the selection of the QSOs may affect this result), in which case Stage III still has an AGN fraction of 20%, as opposed to 45% for the Stage IV ULIGs. Stages IVa and IVb for ULIGs have AGN fractions of 40% and 50%, respectively. There is therefore an increasing amount of optically identifiable Seyfert activity in the more dynamically old Stage IV systems, supporting the claims of Sanders et al. (1988). This also indicates that the more nucleated systems with single nuclei dominating I- band have a slightly increased likelihood of Seyfert activity.

Finally, all of the stage V systems are QSOs or Seyfert 1s. However, given that the morphological classification for stage V (disturbed morphology and lack of well-defined tails) can also be interpreted as indicative of no merger at all, this result is perhaps suspect.

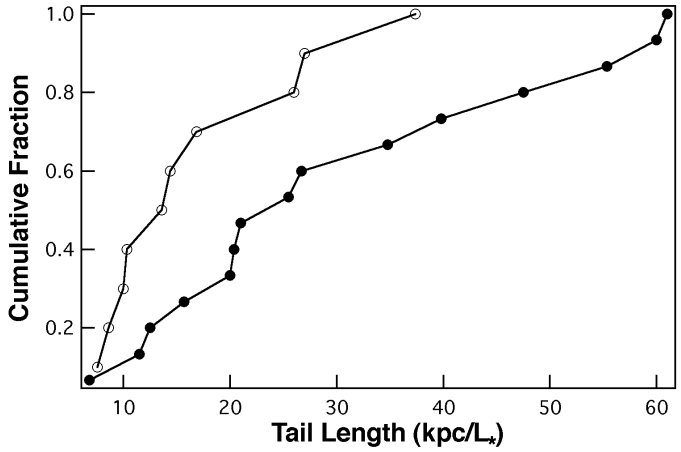

Fig. 7.5.— Cumulative distribution function of luminosity-normalized tail lengths for merger stages III & IV. The lengths of the tails have been normalized by the H-band luminosity, and are in units of kpc$\cdot L_*^{-1}$.

Table 7.1. Properties of ULIG/QSO Merger Stages

Stage		# Objects	% AGN[a]	% Warm	Tail Length[b]
I	Pre-contact	0	...	...	...
II	First Contact	0	...	...	...
III	Pre-merger	10	0.20	0.30	30±17
IV	Merger	15	0.60	0.30	50±30
IVa	diffuse single nucleus	5	0.40	0.60	27±17
IVb	nucleated merger	10	0.70	0.20	33±20
V	Old Merger	6	1.00	1.00	...

[a] determined from optical spectroscopy [b] total projected length along each tail normalized by host galaxy luminosity at H-band (in units of kpc$\cdot L_*$)

7.3. Star-Formation Sequence

Constructing a merger time-sequence based on the star-formation histories of the galaxies is considerably more problematic. At the time this dissertation was started, it was hoped that the clustered star formation then being discovered in the warm ULIGs (Chapter 2) and in other, lower luminosity interacting galaxies might be used as "clocks" to precisely date the merger systems. However, the underlying assumption was that star-formation initiated in the merger systems at roughly the same point in their dynamical evolution, and that this burst of star formation was *brief*. Based on the observations presented here and elsewhere (Whitmore et al. 1997, Meurer 1995), this is now known to generally be false — while burst-mode star formation begins in most cases shortly after first apgalactic passage, *it continues for as long as several hundred Myr afterwards* (based on the apparent

dynamical ages and on the observed properties of the starburst knots) in the form of local knotty bursts.

This is effectively demonstrated by examining the five dynamical stages outlined in section 7.2. Knots with extremely young (<10 Myr) upper age limits are found in many of the stage III systems, particularly in the tails of the wider separation systems (e.g., Mrk 463) and in the cores of smaller separation systems (e.g., IRAS 22491−1808). But, such knots are also found in the stage IVb systems like IRAS 23365+3604 and Mrk 231, and stage V systems like PG 1229+204. Thus, a simple interpretation of the knot ages is not possible, since it appears that, particularly in the central regions of the galaxies, the presence of very young stars in knots seems to imply that new star-forming knots are being created long after the merger of the two nuclei. This is not a particularly surprising result; the timescale for the merger process can actually be quite long — up to 500 Myrs from first apgalactic encounter. The plausible timescale for starburst ultraluminosity, however, is comparatively quite short, being on the order of 10 Myrs. As detailed in Sanders et al. (1988a), the mean molecular gas (H_2) content for the nearby ULIGs is $10^{10.45}$ $M_\odot$, which is already many times that of the Milky Way. Assuming that a similar amount of gas has been converted to stars, this provides an immediate estimate of the luminosity/mass ratio in the ULIGs. For nearby ULIGs with molecular gas measurements, the mean ratio of $L_{\rm ir}/M(H_2)$ is 84 $L_\odot$/ $M_\odot$. Given that $L_{\rm bol} > L_{\rm ir}$, then the actual value may be slightly higher. However, such a high L/M is very difficult to achieve. Some authors argue for an IMF with a truncated lower mass cutoff (Wright et al. 19988; Rieke et al. 1993); by eliminating the lower end of the IMF, which contributes little to the total luminosity but contains a large fraction of the mass, L/M can be immediately raised. Figure 7.6 illustrates this point with the BC95 instantaneous starburst models. In order to achieve the very highest luminosities per unit mass requires the presence of both very massive stars and truncation of the IMF at low stellar masses. An instantaneous burst, wherein all the stars are created simultaneously, maximizes L/M since subsequent aging and fading of the stars decreases their luminosity. However, for the instantaneous burst such high values are achieved for only 10 Myrs or so. Some authors have argued for an extended time-scale for the starburst with on-going star-formation in order to account for observed short-wavelength emission (Rieke et al. 1980), although it now appears that these may actually be the result of scattering (see Chapter 3). Figure 7.6 illustrates the difficulty with extending the starburst lifetime by showing an extreme example of an exponentially decaying burst with τ = 1 Gyr. By extending the timescale of the burst, the demand for mass to sustain an ultraluminous starburst increases dramatically well beyond what could be maintained by the apparent gas mass. If the entire observed galaxy-wide starburst were coeval, then it would fade to the point of undetectability within a fraction of a dynamical timescale. The presence of a wide range of dynamical ages with apparently young starbursts in the ULIGs therefore strongly argues that while individual starburst knots may have short lifetimes, the overall starburst timescale, at least in the nuclei, must be comparable to the dynamical timescale. Some recent n-body simulations have also argued that the burst time-scale must be very short in order to achieve such high luminosities (Mihos 1994a,b).

As was pointed out in Chapter 2, even the knots detected with WFPC2 are likely to be aggregates of smaller clusters. It seems likely that the integrated starburst appears

more similar to one with a longer characteristic time-scale and lower peak luminosity, being the unresolved aggregate of many smaller, possibly instantaneous bursts. If so, then the knots themselves will not be useful for age-dating. As discussed in Chapter 6, the bolometric luminosity is dominated by the most massive stars and that at optical wavelengths the knots fade very rapidly. If there are young massive stars present in an unresolved stellar ensemble (and on-going knot star-formation seems indicated in these galaxies), then the luminosity-weighted observations will always detect the presence of these young stars preferentially and thus derive a young burst age, even if a large mass fraction of the burst is bound into much older, physically distinct yet spatially unresolved knots. Perhaps the simplest statement that can be made about this effect based on the observations in Chapters 2-5, which helps to underscore this point, is "if you look for young stars, you will find them". The only way to salvage this technique is to determine the ages of the oldest star-forming knots in the hope that at some point a size-scale is reached at which the stars in the knot are coeval. Unfortunately, this is difficult due to knot fading since the oldest knots that can be detected will be those at the detection limit, unless either the system itself is young or the detection limit is very low. Similarly, extremely high spatial resolution is required; possibly such a task could be achieved from space-based observations.

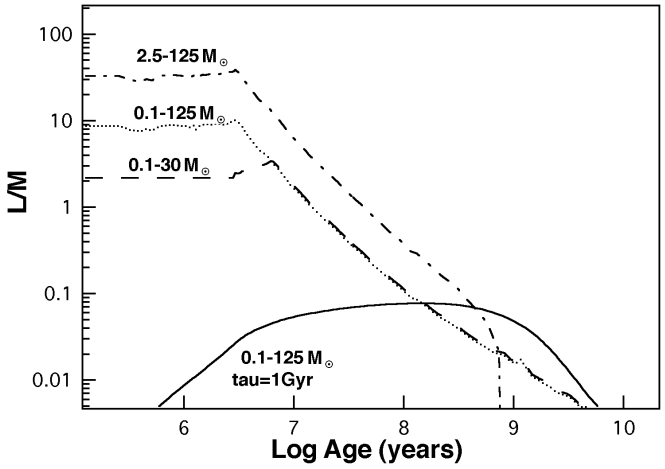

Fig. 7.6.— BC95 starburst models showing the value of L/M (bolometric luminosity in units of $L_\odot$ and total starburst mass in $M_\odot$) as a function of age. All models are for an instantaneous starburst with a Salpeter IMF and the specified upper and lower mass cutoffs, except for the model indicated with a solid line, which has an exponentially decaying star formation rate with an e-folding time of 1 Gyr. Note the low efficiency of the extended-timescale starburst.

Additionally, reddening is the bane of this entire process. Simple colors like ($B-I$), as discussed in Chapter 2, are incapable of establishing anything more than an upper limit to the age of the starburst knots; the effects of reddening very closely mimic the effects of stellar aging. From Chapter 4 it is apparent that at least in the cool ULIGs there may be several visual magnitudes of reddening present. In principal, the three-color ($B-I$, $I-H$, $H-K'$) approach described in Chapter 3 allows one to compensate for reddening effects. An examination of figure 3.7, however, shows that in the reddening orthogonal basis the three-color space occupied by stars with ages 10–800 Myrs is very small and the uncertainties

in colors are large enough to prevent a meaningful age determination. Since the SEDs of the starburst knots are inconsistent with a simple naked burst and a foreground dust screen, even using this diagnostic is clouded by the additional complications of warm dust mixed with the stars. Only high spatial resolution spectroscopy of the individual coeval knots would allow an independent measurement of their ages and simultaneously avoid the age/strength degeneracy.

However, it may still be possible to address the issue in very broad strokes using the information derived from U′ observations. Namely, it appears that while star-formation in the nuclear regions is a long-lived phenomena, the star-formation occurring in the tails is not. If the knots in the tails could still be detected even after a long period of time, then they could conceivably be used as an age-dating method. Unfortunately, our ground-based observations lack the required sensitivity, and as such we can currently only argue based on detections and non-detections of knots, as was done in Chapter 6. As noted in Chapter 6, it appears that star-formation in the tails begins in earnest sometime after the first close passage of the galaxies. However, star-forming knots are not generally detected in the tails of the infrared-excess QSOs, nor in the single nucleus ULIGs; the most likely interpretation is that they are older, and hence have faded at U′ by this time. Assuming that the knots detected in the tails are near their peak U′ luminosity, then to have faded to undetectability will require approximately 45 Myrs. Likewise, the dearth of knots found in the QSOs versus the single-nucleus ULIGs would imply an additional age difference of 50–100 Myrs. Similarly, as noted in Chapter 4 the prevalence of stars that must be very young (< 10 Myrs) is much greater in the cool ULIGs than in the warm ULIGs and that infrared-excess QSOs have no knots that must be so young. While inconclusive, this result does suggest a rough star-formation sequence.

7.4. Implications for the Evolution of Star-Formation in ULIGs and QSOs

The presence of young stars visible at optical and near-infrared wavelengths has been demonstrated in many of the ULIGs. In particular, a large fraction of systems have direct evidence based on imaging for clustered knots of star- formation whose colors are consistent with young stars 10–100 Myrs in age. In the remaining systems, most of which have inferior spatial resolution, the nuclear regions have integrated colors consistent with the presence of young stars. This supports many other lines of evidence that have suggested the presence of young stars in ULIGs. This also demonstrates that clustered star formation is the dominant mode of star formation in ULIGs, just as it appears to be in other interacting galaxies. However, the question of the rate of evolution of star formation in the ULIGs is only partially answered. In regards to timing, the bulk of the star-forming knots in the tails appear shortly after the tails do, and then this activity seems to cease. This may be a result of the decreasing mean density in the tails, which makes collapse increasingly less likely. Gas depletion may also play some factor. In the nuclei, however, star formation continues for a much longer fraction of the dynamical time-scale. These observations cannot directly address the issue of the shape of the IMF, and as a result are unable to constrain the mass of stars in the burst beyond that predicted for a given model. In general, we are most sensitive to the presence of massive stars, which dominate the energetics of the burst anyway. In the

extremely old bursts where lower mass stars play a key role in the burst energetics, cluster fading is likely to have made the clusters undetectable.

Of the 26 ULIGs observed, 10 (38%) had obvious double nuclei, with 25% having separations greater than 4 kpc, which is sufficient to still be able to identify the galaxies as separate coherent structures. This implies that in a significant number of cases, ultraluminous activity has begun well before final merging of the nuclei. This would seem to argue against the claims of Mihos & Hernquist (1994a,b). Based on n-body simulations, they concluded that interactions between disks with massive bulges would be stable against most star formation until very near the final merger state (IV-V), at which time a very brief yet intense ultraluminous starburst would occur. However, they also found that disk interactions without massive bulges underwent a longer-lived, yet less intense, burst of star formation during the dynamical stage III. An alternative interpretation, therefore, to our finding ultraluminous galaxies in both stages III and IV would be that our luminosity selection criterion has selected two similar, yet separate, types of systems: bulgeless interactions whose upper end of their luminosity distribution make up our double nucleus (III) systems, and another sample of disk/bulge systems which make up the population of single nucleus (IV) systems. However, more recent modeling work including radiative and pressure feedback (Gerritsen 1997) seems to indicate that a more complex treatment of the star formation results in much longer, less intense starbursts, which is more similar to the interpretation that the stage III and IV ULIGs are a single dynamically evolving population with many continuously forming, low luminosity starburst knots. Our observations cannot by themselves differentiate between these two interpretations; it would require an additional study of the lower luminosity LIGs.

7.5. Implications for the Evolution of AGN in ULIGs and QSOs

In section 7.1 it was shown that the incidence of optically detectable spectroscopic evidence for AGN increases dramatically with dynamical age. This leaves open, however, the question of whether this indicates that AGN fueling and activation begins at later times in the ULIGs' history, or whether this represents an unveiling process by which an AGN fueled during the early stages of the merger process is revealed at progressively shorter wavelengths. This is important because if the AGN are actually fueled only at late dynamical times, then a second energy-production mechanism is needed to account for the less dynamically evolved ULIGs (i.e., an ultraluminous starburst). The imaging of Chapters 2-5 suggest that this is most likely an unveiling process.

In Chapters 2 & 3 it was shown on the basis of imaging that all of the warm ULIGs have evidence for AGN being present, and that these AGN are similar in properties to QSOs. This result is further supported by spectroscopic observations (Sanders et al. 1988b, Kim 1995). Two important points are made. First, evidence for AGN is found in the form of compact emission sources with AGN-like broad-band colors even in those warm ULIGs that do not have spectroscopic evidence for AGN (e.g., IRAS 15206+3342). The small-scale structure of these systems indicates that spatial confusion is the cause of this lack of detection. Therefore, AGN are likely to always be present in warm ULIGs, and they are

simply easier to detect at later dynamical times, indicating a time-related simplification of the small-scale structure in the ULIG nuclei. The second point is that the optical/near-infrared colors of the warm ULIG putative nuclei appear similar to QSOs, but with a strong hot dust component, indicating the presence of dust which might be associated with the obscuration of the AGN.

In chapter 4 it was shown that the cool ULIGs predominantly do not have any evidence based on optical/near-infrared imaging for the presence of AGN. However, they do not have any evidence in the optical or near-infrared for anything else that could produce the high bolometric luminosity, either. The heating source in these galaxies, whether starburst or AGN, must be hidden at these wavelengths. Although radio observations of these systems indicate the presence of a compact emission source, ultraluminous starburst models predict similar results (Condon et al. 1991). However, there are two cool ULIGs (UGC 5101 and Mrk 273) which do have Seyfert spectra. Recent HST observations show them to have compact nuclei similar to those found in the warm ULIGs. Moreover, IRAS 22491−1808 also has evidence based on optical/near-infrared colors for a QSO-like nucleus; optical confusion hides any spectral indicators of its presence. This, combined with the results of Chapters 2&3 are strongly suggestive that the AGN are in fact present already in all the ULIGs, and that the process seen in the morphological time sequence is likely to be one of unveiling, and not fueling.

Finally, whether it is star formation or active nuclei that powers the ULIGs, the presence of merger activity in nearly every ULIG serves to underscore its importance in the fueling of the high bolometric luminosity . Given that the morphological time sequence extends well into Stage V which is dominated by QSOs, it appears that the lifetime of the active phase is at least as long as the merging timescale from stage III to V, and likely to be slightly longer, depending on the fraction of QSOs that form via this method. Based on dynamical simulations of merger systems, this is on the order of 500–1000 Myrs (Mihos & Hernquist 1994, Gerritsen 1997). This is similar to other estimates of the ULIG lifetime which are based on observations of the relative fractions of the objects and also on theoretical fueling timescales for black holes (Murphy et al. 1996). If the time sequence presented above is actually one of fueling and not unveiling, then this will only increase the total "active" lifetime, as the ULIGs may be powered by star formation early in their lifetime, yet switch over to AGN as time progresses and thus remain infrared- luminous for that much longer. Finally, the implications for QSO formation are as yet unclear. It appears that at least 25% of infrared-excess QSOs are consistent with formation via this ULIG-merger scenario, based on their similarity to evolved ULIGs. This number may be as high as 40%, depending on the interpretation of the QSO host morphologies.

7.6. Things That Don't Fit into Either Sequence

It is clear that a number of ULIGs and QSOs *cannot* readily be made to fit into the ULIG-QSO evolutionary paradigm. In the warm sample, IRAS 01003−2238 in particular stands out. It is underluminous and shows only the barest hint of structure even under the high spatial resolution of *HST*, indicating that it is unlikely to be a merger system like the

other ULIGs. It is also known to be a powerful Wolf-Rayet galaxy — it thus seems to be the clearest case of a possible ultraluminous starburst. Similarly lacking in a merger morphology consistent with the other ULIGs is the warm ULIG/QSO I Zw 1. Its host galaxy appears to be dominated by spiral structure; while it appears that it may be interacting with a small companion to the west, it is clearly different from the extremely disruptive encounters that have befallen the other ULIGs.

Similarly, in many of the QSOs the evidence regarding where they fit into this scheme is ambiguous at best. In particular, most (78%) of the QSO host galaxies do not show direct evidence for tidal structure that can implicate the presence of a major merger in the same way that it can for the ULIGs. However, this lack of a "smoking gun" cannot demonstrate whether or not a merger has taken place, since very evolved mergers are expected to appear similar to elliptical galaxies. Unfortunately, the lack of evidence for merger activity is not any more compelling an argument in favor of mergers than it is an argument for no mergers at all. Similarly, there is evidence for other kinds of tidal interactions besides major disk mergers being somehow connected with QSO activity; it is far beyond the scope of this dissertation to comment on these.

That not all ULIGs appear to necessarily result from mergers, and that a large fraction of the QSOs cannot be directly implicated in merger activity like that found in most ULIGs, supports the idea that there may be alternative mechanisms for producing each of the associated phenomena. It is therefore more correct to state that in the vast majority of cases the evolution of merger systems can explain the activity seen in the ultraluminous galaxies and in a considerable fraction of QSOs. Unfortunately, this complicates any understanding of the relative fueling lifetimes. Given that PG QSOs and ULIGs have similar space densities, if ULIG/merger evolution is responsible for only one-quarter of QSOs, then this would indicate that the lifetime of the active phase is likely to only be slightly longer than the ULIG phase, or several hundred Myrs.

7.7. Summary of Conclusions from Dissertation

1. Merger activity has been implicated in the vast majority ($> 90\%$) of ULIGs as well as a large fraction ($> 22\%$) of QSOs.

2. This merger activity results in the formation of knots of star formation both in the inner nuclear regions and in the tidal features.

3. These knots of star formation are insufficiently luminous to account for more than a small fraction ($< 10\%$) of the high bolometric luminosity of these systems.

4. While predominantly young (10–100 Myrs) these star-forming knots have a formation history that may span most of the dynamical interaction lifetime.

5. The warm ULIGs all have evidence for active galactic nuclei. Similarly, several of the cool ULIGs do.

6. These active nuclei, in most cases, could produce most of the high bolometric luminosity.

7. There is a clear correlation between the appearance of indicators of AGN and dynamical lifetime.

8. It is likely that this correlation is due to an unveiling process associated with the aging merger remnant.

9. These results are consistent with the idea that roughly one- quarter of the infrared-excess QSO population examined here is derived from the aging ULIG population.

10. Not all ULIGs are a result of this process, nor are all QSOs necessarily a result of it. This suggests the existence of alternative paths for producing similarly energetic phenomena.

7.8. Epilogue

In the beginning, I thought this dissertation would "write the book" on ULIG evolution. Ultimately, it appears instead to have raised many more questions than it answered by revealing a whole new range of phenomena previously unsuspected or not wholly understood in the ULIGs. In particular, we had not anticipated (perhaps foolishly, in hindsight) the discovery of clustered star formation in interacting galaxies. The circumnuclear starbursts that had been previously postulated in ULIGs based on multi-aperture photometry are now understood to be extended "knots" or "clumps" of star formation scattered about not only the inner core of the galaxy merger, but along its tails and other tidal features as well. It remains unclear as to whether there is any interaction between this star formation and any AGN present, or whether they are parallel, yet otherwise unrelated, phenomena.

The imaging of the central cores of the ULIGs has also, in my mind, underscored how complicated their small-scale morphology is. In particular, we have always known that thick dust absorption must be important in these galaxies, since the very presence of the enormous far-infrared excess necessitates this. However, we now know that this is not any sort of simple dust screening or veiling process. In reality, the light that we observe is a complicated mixture of scattered and extinguished light. This underscores the importance of high spatial resolution polarimetry studies such as can be done with HST/WFPC2 or planned instrumentation on the Next Generation Space Telescope (NGST); only this way can we try to sort out where any given emission is originating.

The same dilution effect that has so hampered ground-based polarimetry has also been the bane of ground-based spectroscopy. Confusion resulting from the small scale structure in the ULIGs has muddied their interpretation. Also, many of the star-forming regions are inherently too faint to be easily observed from the ground with the required high spatial resolution. Again, NGST may be the only hope to achieve the required sensitivity. Another alternative may be the new generation of 8m class telescopes being built on Mauna Kea. Coupling of their large apertures with adaptive optics may provide the needed sensitivity and spatial resolution.

Finally, it appears there is the very real possibility that attempts to "pry open" the dust shroud surrounding the central power source in the ULIGs may ultimately prove to be futile. Increasingly, the size scale of the hypothetical ultraluminous starburst has been

reduced until it now rivals that of the AGN model in compactness. Unless we can "peek around the corners and through the cracks" using polarimetry and high spatial resolution in the manner described above, it may be that the dust shroud is simply too thick to penetrate directly with *any* observation at any wavelength. Indeed, this thesis has shown that whatever the central engine, it must exist on size scales of 100 pc or less, a result which is now being corroborated by mid-infrared imaging by others. However, this is similar in size to the minimum theoretical size for the far-infrared emission region (Condon 1991). Even if we can find an AGN, it may not be clear it is what is actually providing the dust heating. In this case, we may be forced to continue in the direction followed in this thesis, so succinctly stated by Doyle's infamous Sherlock Holmes: if we can eliminate what is *not* the central power source in the ULIGs, then whatever is left must be the truth.

Finally, this dissertation was a little too ambitious from the beginning. In particular, the inclusion of spectroscopy would have made it entirely intractable in a typical graduate student lifetime. Fortunately (!), instrumentation problems pushed the timeline for the spectroscopy sufficiently far back as to fall outside this dissertation.

REFERENCES

Barnes, J.E., & Hernquist, L. 1992, ApJ, 393, 484

Barnes, J.E., & Hernquist, L. 1996, ApJ, 471, 115

Condon, J.J., Huang, Z-P., Yin, Q.F., & Thuan, T.X. 1991, ApJ, 378, 65

Gerritsen, J. 1997, PhD. Thesis, Kapteyn Astronomical Institute, Groningen

Goldader, J., Joseph, R.D., Doyon, R., & Sanders, D.B., 1995, ApJ, 444, 97

Kim, D-C., 1995, PhD. Thesis, University of Hawaii

Mihos, J.C., & Hernquist, L. 1994, ApJ, 425, L13

Mihos, J.C., & Hernquist, L. 1994b, ApJ, 431, L9

Meurer, G. 1995b Nature, 375, 742

Sanders, D.B., Soifer, B.T., Elias, J.H., Madore, B.F., Matthews, K., Neugebauer, G., & Scoville, N.Z. 1988a, ApJ, 325, 74

Sanders, D.B., Soifer, B.T., Elias, J.H., Neugebauer, G.,& Matthews, K. 1988b, ApJ, 328, 35

Rieke, G.H., Lebofsky, M.J., Thompson, R.I., Low, F.J., & Tokunaga, A.T., 1980, ApJ, 238, 24

Rieke, G.H., Loken, K., Rieke, M.J., & Tamblyn, P., 1993, ApJ, 412, 99

Toomre, A. 1977, in *The Evolution of Galaxies and Stellar Populations*, (Yale: New Haven), 401

Veilleux, S., Sanders, D.B., & Kim, D-C. 1997, ApJ, 484, 92

Veilleux, S., Sanders, D.B., & Kim, D-C. 1998, in prep.

Whitmore, B.C., Miller, B.W., Schweizer, F., & Fall, S.M. 1997, AJ, 114, 1797

Wright, G.S., Joseph, R.D., Robertson, N.A., James, P.A., & Keikle, W.P.S., 1988, MNRAS, 233, 1

Appendix A

A HIRES IRAS Atlas of All Close Interacting Galaxies in the IRAS Revised Bright Galaxy Sample [1]

ABSTRACT

The importance of far-IR observations in our understanding of extreme activity in merging galaxies has been illustrated by many studies. However, the normal spatial resolution of the IRAS all-sky survey is insufficient to resolve the emission from individual galaxies in most interacting galaxy pairs, and hence previous studies of their far-IR properties have had to concentrate either on global system properties or on the properties of very widely separated and weakly interacting pairs. Using the HIRES image reconstruction technique, it is possible to achieve a resolution ranging from 30″to 1.5′ (depending on wavelength and detector coverage). This is sufficient to resolve many interacting galaxy systems into individual galaxies, thus providing valuable information on the far-infrared activity within a particular galaxy.

We present high-resolution 12, 25, 60, and 100 μm images of 100 interacting galaxy systems contained in the IRAS Revised Bright Galaxy Sample (RBGS) (Sanders et al. 1998), a complete sample of all galaxies having a 60μm flux density greater than 5 Jy. These systems were selected to have at least two distinguishable galaxies separated by less than three average galactic diameters, and thus we have excluded very widely separated systems and very advanced mergers. Additionally, some systems have been included which are more than three galactic diameters apart, yet have separations less than 4′ , and which are thus likely to suffer from confusion in the RBGS.

We examine the effects of morphology (Hubble type) on far-infrared activity. Contrary to some theoretical models, we find no apparent difference in the far-infrared activity of late and early-type spiral galaxies. Based on the far-infrared luminosity and colors we conclude that star formation rates are slightly elevated (by 50%) after first galaxy contact relative to before the first contact. We also find small enhancements in far- infrared activity in multiple galaxy systems relative to RBGS non-interacting galaxies with the same blue luminosity distribution.

A.1. Introduction

In the last two decades it has become apparent that interactions between galaxies can play a significant role in their evolution. From the early dynamical simulations of Toomre & Toomre (1972) to more modern works by Barnes, Hernquist, and others (Barnes et al. 1992 and references therein) it has become apparent that interactions and mergers between galaxies can radically alter their morphology by inducing shells, bars, tails, and other tidal features. Perhaps more importantly, cancellation of angular momentum during the merger process can lead to a radical redistribution of the gas content of the galaxies, with very

[1] This appendix will be submitted to the ApJSupp. as "A HIRES IRAS Atlas of Interacting Galaxies in the IRAS Revised Bright Galaxy Sample", by Surace & Sanders

rapid gas inflow into the galaxy cores. This supply of fresh material could possibly fuel an active galactic nucleus, or provide the high gas densities needed to lead to a sudden burst of star formation.

There is considerable evidence that enhanced star formation is associated with interacting galaxies (Sulentic et al. 1990 and references therein). The most classic study is Larson & Tinsley (1978), who found that morphologically peculiar galaxies have large dispersions in their *U-B* and *B-V* colors compared to normal field galaxies, and that this could be explained by episodes of rapid star formation involving up to 5% of the total galaxy mass. The young OB stars that dominate the starburst radiate primarily in the optical and ultraviolet, but surrounding gas and dust reprocesses this radiation and thus strongly radiates at thermal wavelengths in the far-infrared. Far-infrared luminosity is thus indicative of the magnitude of recent star formation activity (Telesco 1988, Lonsdale et al. 1984). Additionally, due to the increased temperature of the heated dust, we expect the far-infrared colors to be a good diagnostic of enhanced star formation. Many studies have therefore concentrated on the far-infrared properties of interacting galaxies.

Several studies have also discussed the incidence of multiple bright galaxies being found within a given interacting galaxy system. Haynes & Herter (1984) found that for galaxy pairs separated by 2-10´ , approximately 10% have multiple components brighter than an 0.5 Jy at 60μnm and 1 Jy at 100μm. Xu & Sulentic (1991) also concluded that in the majority of interacting systems, only one galaxy is infrared bright. These results agree with an earlier work by Joseph et al. (1984) which concluded, based on near- IR colors, that most often only one galaxy in a pair showed signs of unusual activity. This becomes an interesting question in that this probes the specific properties of the interacting galaxies that determine whether or not they become strong far-IR emitters.

Recent computational models by Mihos & Hernquist (1994a & 1994b) have predicted that the presence of a large central bulge in a galaxy will help stabilize it against tidal perturbation. Specifically, they found that in major mergers of galaxies the presence of a central bulge inhibits the flow of gas into the central few kiloparsecs of a galaxy, thus preventing high gas densities from being quickly reached and suppressing any period of rapid star formation until the end of the merger (Mihos et al. 1994b). Thus, late-type spirals are expected to experience starbursts during the initial stages of merger, while early-type spirals undergo strong starburst activity only during the completion of the merger process. This provides a mechanism to delay the onset of starburst activity in some systems until very advanced merger stages are reached, as otherwise it is difficult to invoke a starburst model for ultraluminous infrared galaxies (which appear to be very advanced mergers) given the expected timescale for starbursts. Since very evolved mergers have such disturbed morphologies that it is difficult to determine the form of the merger progenitors, the most viable observational test is to examine young merger systems which have not evolved as far away from their original forms and look for evidence for the onset of enhanced far-IR activity in bulgeless galaxies.

The canonical figure used by many authors to delineate interacting versus non-interacting systems is a projected separation of three average galactic diameters, as presumably galaxies this close to one another are also close enough to exert a considerable

gravitational effect (Dahari 1984; Byrd et al. 1987; Surace et al. 1993). However, for most IRAS galaxies this typically corresponds to an angular separation of a few arcminutes. This is less than the resolution normally achieved by IRAS using the 1-d coadder ADDSCAN or the 2-d FRESCO imaging process. As a result, it has been impossible to study the far-infrared properties of the individual galaxies, and most studies have either made assumptions about the distribution of flux between galaxies within the interacting system (Bushouse et al. 1988) or have concentrated on widely separated pairs (Haynes & Herter 1988; Xu & Sulentic 1991). Since previous studies of very widely separated galaxy pairs indicate that in a substantial fraction of interacting systems only one galaxy is unusually active in the far-IR (Xu & Sulentic 1991), it is necessary to resolve these galaxies in order to properly study those properties such as morphology which are unique to the individual galaxies. Additionally, Xu et al. (1991) found evidence that at smaller separations (and hence greater interaction strengths) there was a greater enhancement of far-IR activity. Therefore it would be valuable if these studies could be extended to smaller separations where more observable changes are taking place.

Development of the Maximum Correlation Method algorithm (Aumann et al. 1990) for use in IRAS image reconstruction significantly increased the resolution of IRAS observations. As implemented in the HIRES process, MCM is an iterative deconvolution technique that involves using the known detector response functions of the IRAS detectors to scan simulated image estimates which are then compared to the actual detector data. In this way, a high resolution image estimate is formed. The result is typically a five-fold increase in resolution, varying from roughly $30''\times45''$at 12μm to $72''\times130''$at 100μm, with the actual achieved resolution being highly dependent on the geometry of the detector coverage (Surace et al. 1993). Unfortunately, the HIRES process is extremely computer intensive. In its earlier incarnation on a CDC Cyber, a single field typically took a day or more. As a result, the earlier work by Surace et al. (1993) was rather limited in scope, with only 23 systems being resolvable. On a Sparc 10, this computing time was reduced to approximately 1 hour, thus making feasible the processing of a substantially larger sample.

A.2. Data

A.2.1. Sample

All of the targets were selected from the IRAS Revised Bright Galaxy Sample (Sanders et al. 1998). The RBGS consists of all galaxies detected by IRAS having a 60μm flux density greater than 5 Jy, and is thus similar to and includes all of the well-studied Bright Galaxy Sample (Soifer et al. 1987), but extends coverage to the entire sky, and not just the northern hemisphere above the galactic plane.

The following criterion was applied in order to select close pairs from the RBGS:

$$\frac{2S_{12}}{D_1+D_2} \leq 3 \tag{A.1}$$

where S_{12} is the distance between galaxies' centers and D_1 and D_2 are their optical diameters. This criterion therefore selects all systems where the galaxies are separated by less than three times their average diameter. Note that this excludes very advanced mergers such as Arp 220, where the individual galactic disks can no longer be distinguished. This also has the additional benefit of selecting systems that are sufficiently separated as to be resolvable with HIRES. As such, the sample includes all of the galaxies listed in Table 1 of Surace et al. (1993). Additionally, in an attempt to resolve sources listed in the RBGS which were likely to be confused due to small separations, we included all small galaxy pairs with apparent separation less than $4'$. This separation was determined by the normal survey resolution of $4'$, which in turn is set by the 100μm detector size.

A.2.2. Data Reduction

The IRAS data were processed in a manner similar to Surace et al. (1993). The raw detector scans were initially extracted from the IRAS database using the SNIPSCAN process. These raw detector scans were then flattened using an iterative fitting technique that removed the detector baselines, and they were then deglitched in order to remove artifacts such as cosmic ray hits using the LAUNDR process. The HIRES process was then applied to the detector scans. Restoration was done on $1\square°$fields in order to improve detector baseline coverage, with a pixel size of $15''\text{pixel}^{-1}$, which is sufficient to adequately sample the restored IRAS beam. In most cases the algorithm was iterated 20 times as further iterations tend only to increase noise amplification with little improvement in resolution, although in a few cases the algorithm was allowed to iterate further in an attempt to increase resolution.

In order to aid in the interpretation of the IRAS data, optical images were extracted from the Digital Sky Survey (DSS) and the IRAS data were overlaid on them (Figure A.1). This was particularly valuable since many of the IRAS galaxies lack optical identifications and accurate coordinates. The optical images have a pixel size of $1.7''$. The astrometry of the optical images is based on a linear approximation to the polynomial plate solution provided by STScI, and yields positions accurate to roughly $2''$ (Laidler et al. 1994). The astrometry of the IRAS images is limited by the pointing accuracy of the satellite, which was approximately $2''$ in the in-scan direction and $10''$ cross-scan (Beichmann et al 1988). Furthermore, the astrometry of point-like sources produced by the HIRES technique is known observationally to be approximately $20''$ (Laughlin et al. 1990). Thus, registration of the images should be accurate to within one or two HIRES pixel elements, and certainly should be better than the typical IRAS beam size. Optical identifications were made using the coordinates and names given in the Nasa Extragalactic Database (NED), which are in turn derived from the Third Reference Catalogue of Bright Galaxies (3RC) (de Vaucouleurs et al. 1991). When no identifications were available, the galaxies were identified directly from the DSS images and are labeled from northeast to southwest.

Photometry was accomplished in two ways. When the galaxies were cleanly separated, aperture photometry was performed using polygonal apertures of a size sufficient to insure that all of the galaxy flux was measured. In those cases where components appeared to

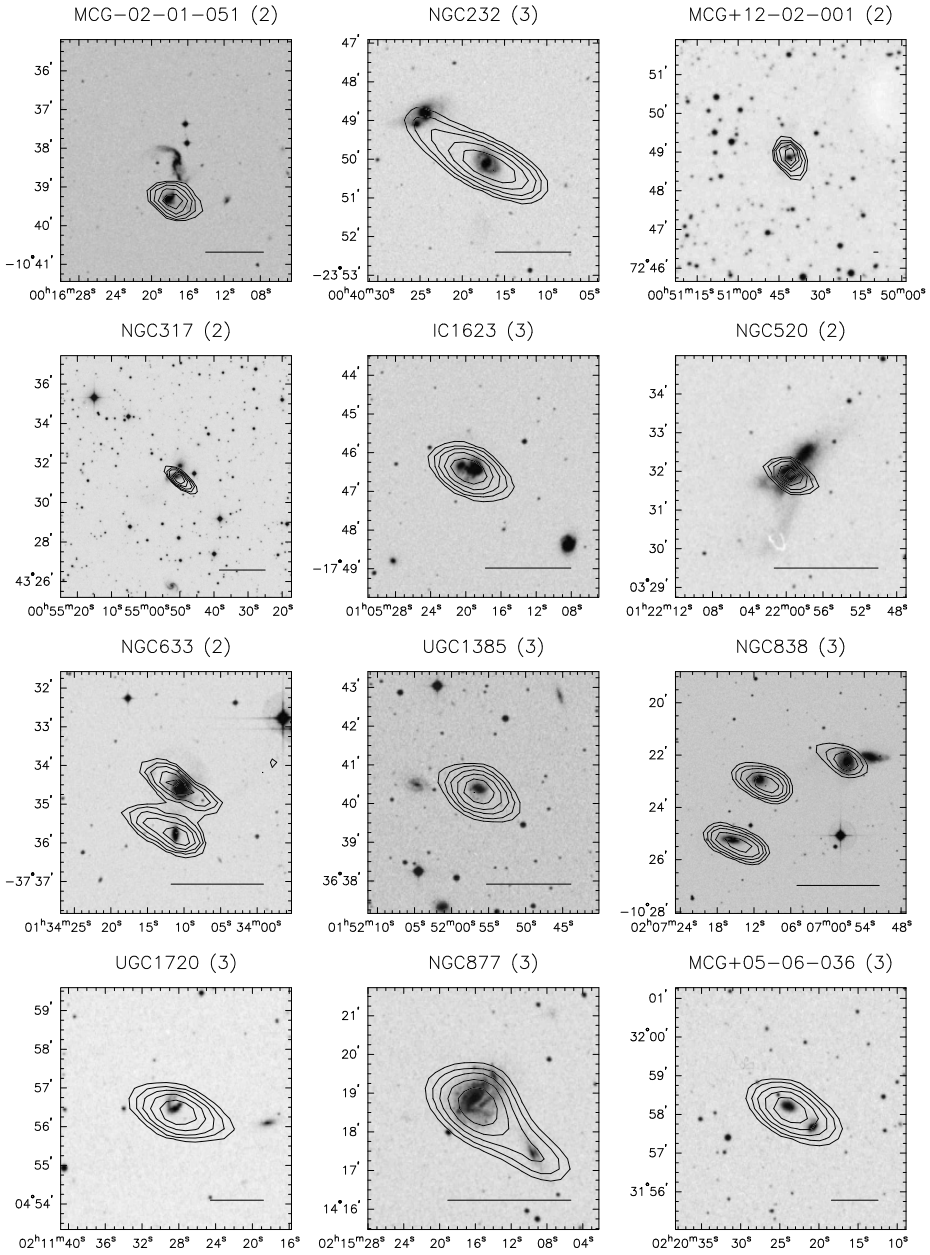

Fig. A.1.— Selected HIRES data for each of the close pair RBGS systems overlaid on grey-scale images taken from the DSS. The contours are at intervals of 10, 16, 25, 40, and 63% of the peak flux, and represent 20 iterations (occasionally more) of the MCM algorithm, and represent the highest achievable IRAS resolution. The scalebar seen at the lower right of each 100μm image is 50 kpc long, except in the following cases where it is 25 kpc: Arp 245, Arp 270, Arp 279, Arp 283, Arp 286, Arp 306, Arp 317, NGC 1097, NGC 2366, NGC 3511, NGC 3893, NGC 4038, NGC 4273, NGC 4572, NGC 4631, NGC 4647, NGC 5078, NGC 5915, NGC 5953, NGC 7552, NGC 7590, UGC 5617, and UGC 7776. For Arp 269 and NGC 2146 it is 12.5 Kpc. The name of the system as given in Table A.1 is listed, along with the IRAS filter (1,2,3,4 = 12, 25, 60, 100 μm).

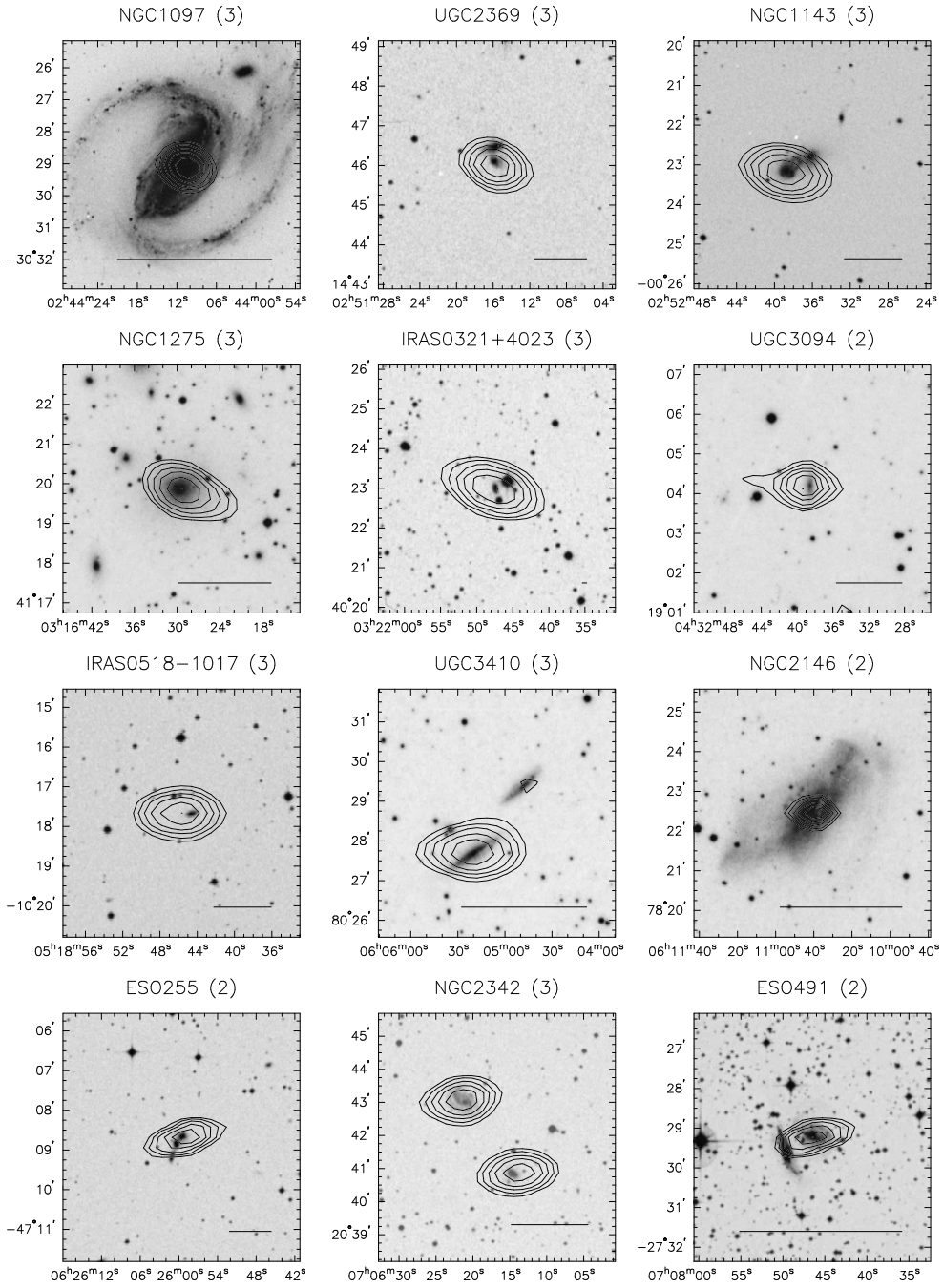

Fig. A.1.— (continued)

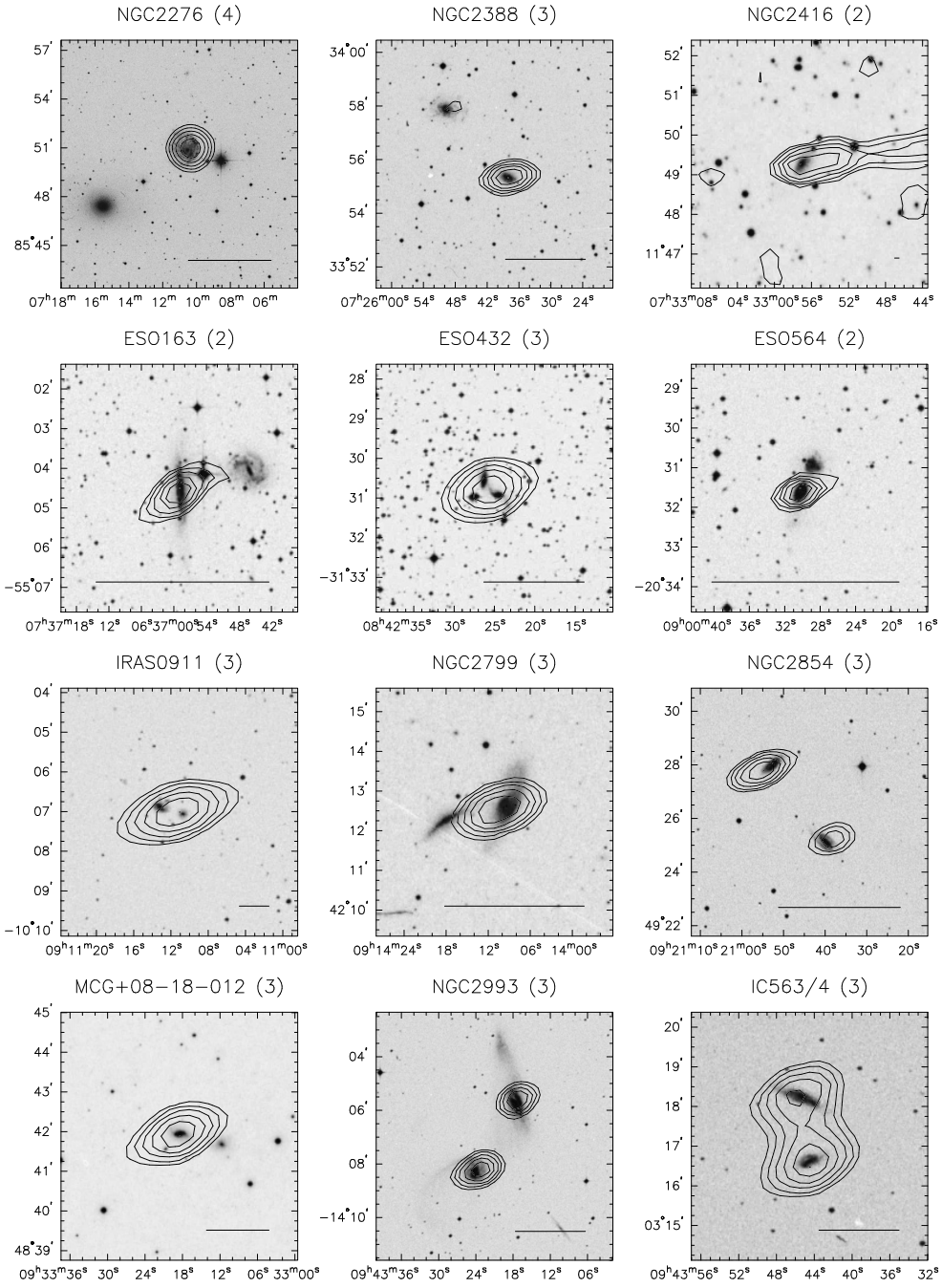

Fig. A.1.— (continued)

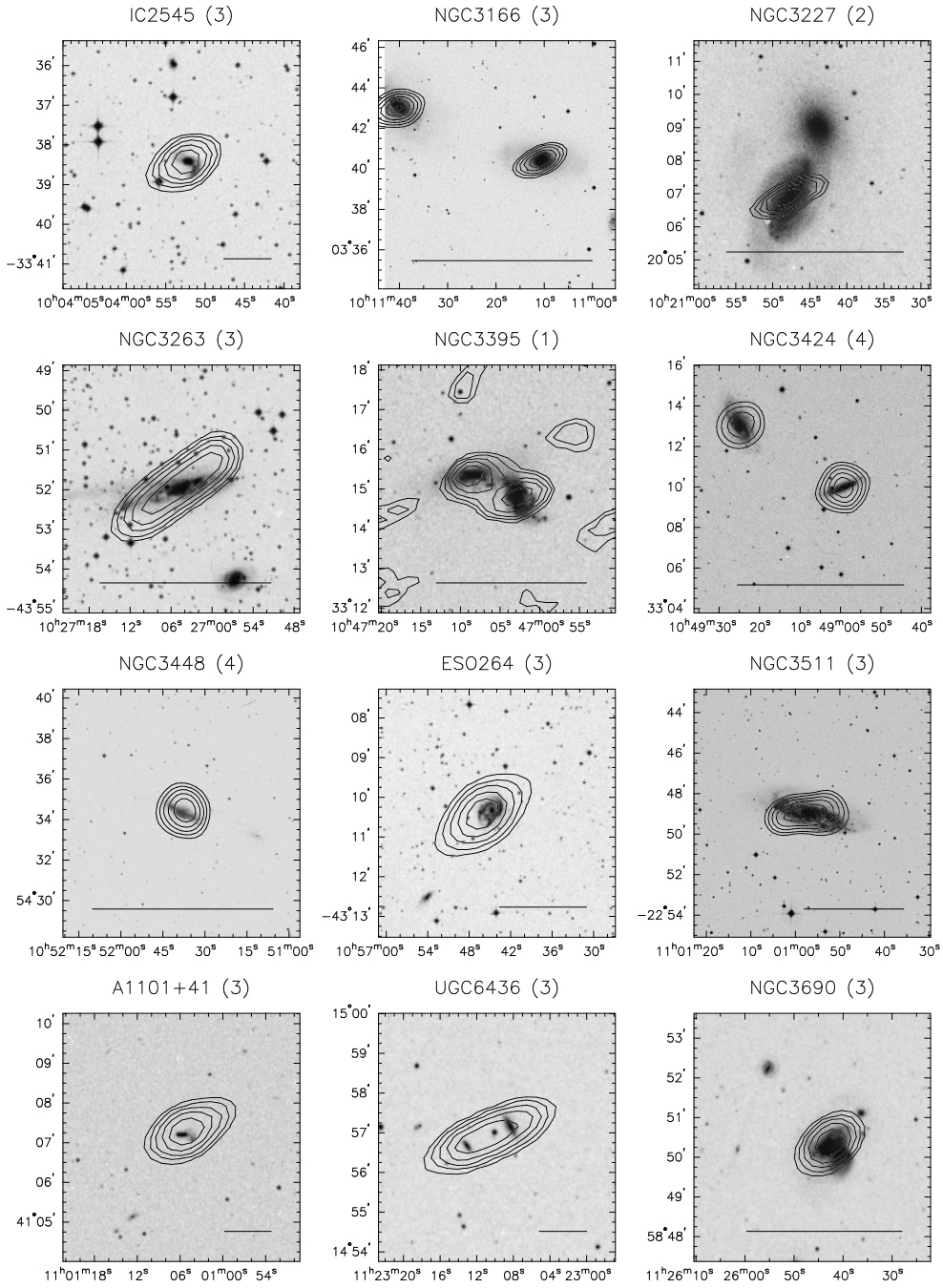

Fig. A.1.— (continued)

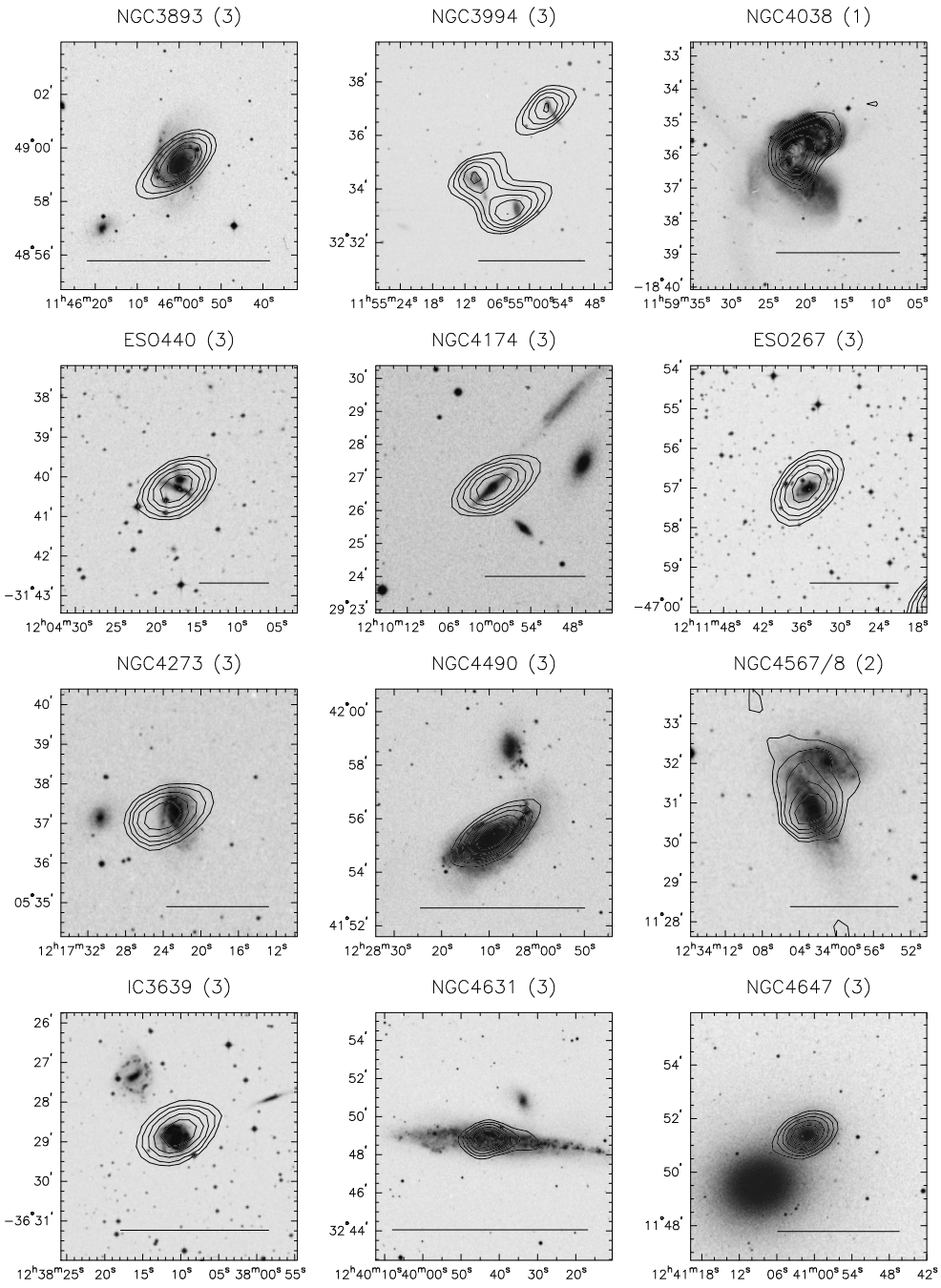

Fig. A.1.— (continued)

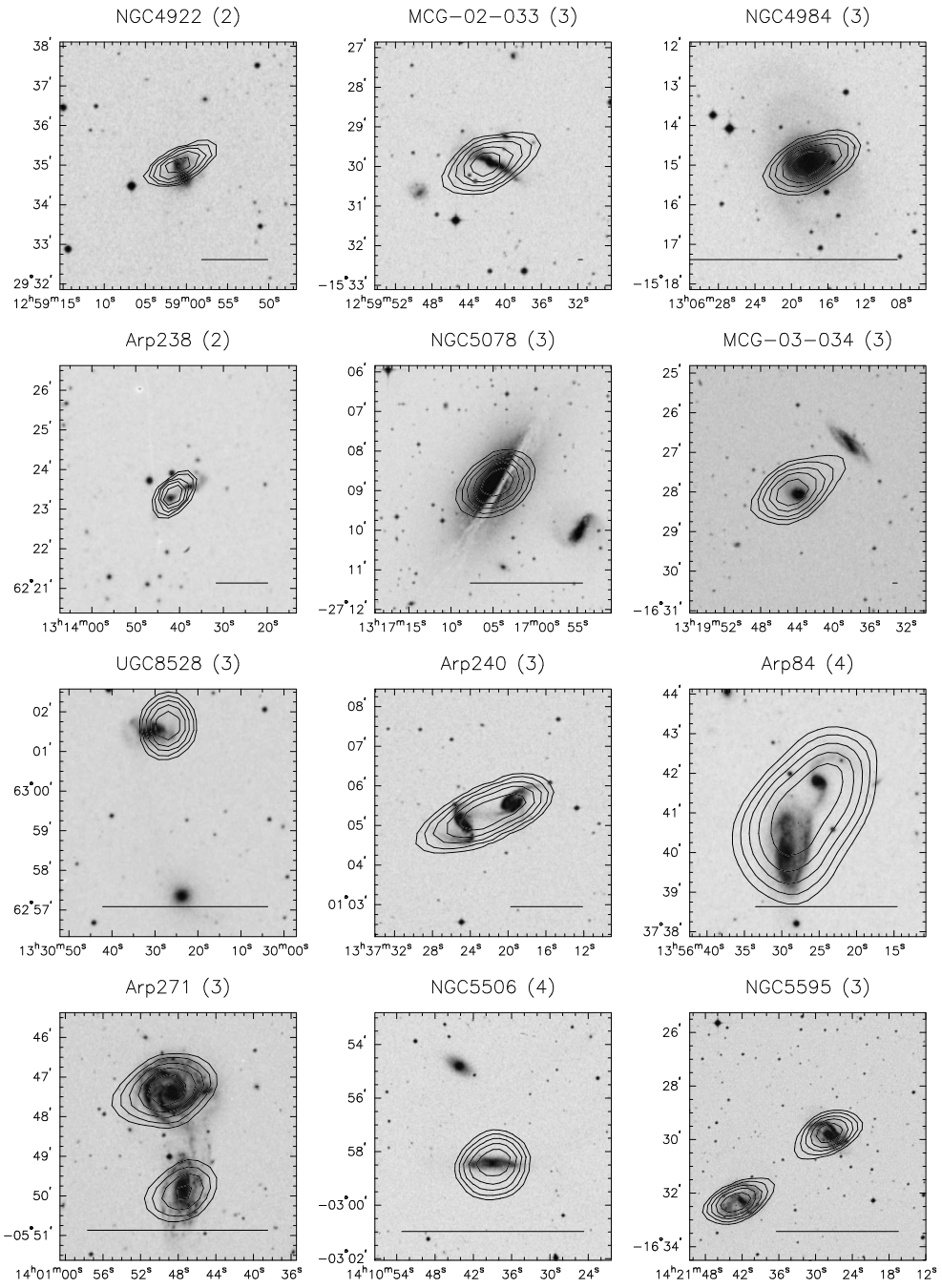

Fig. A.1.— (continued)

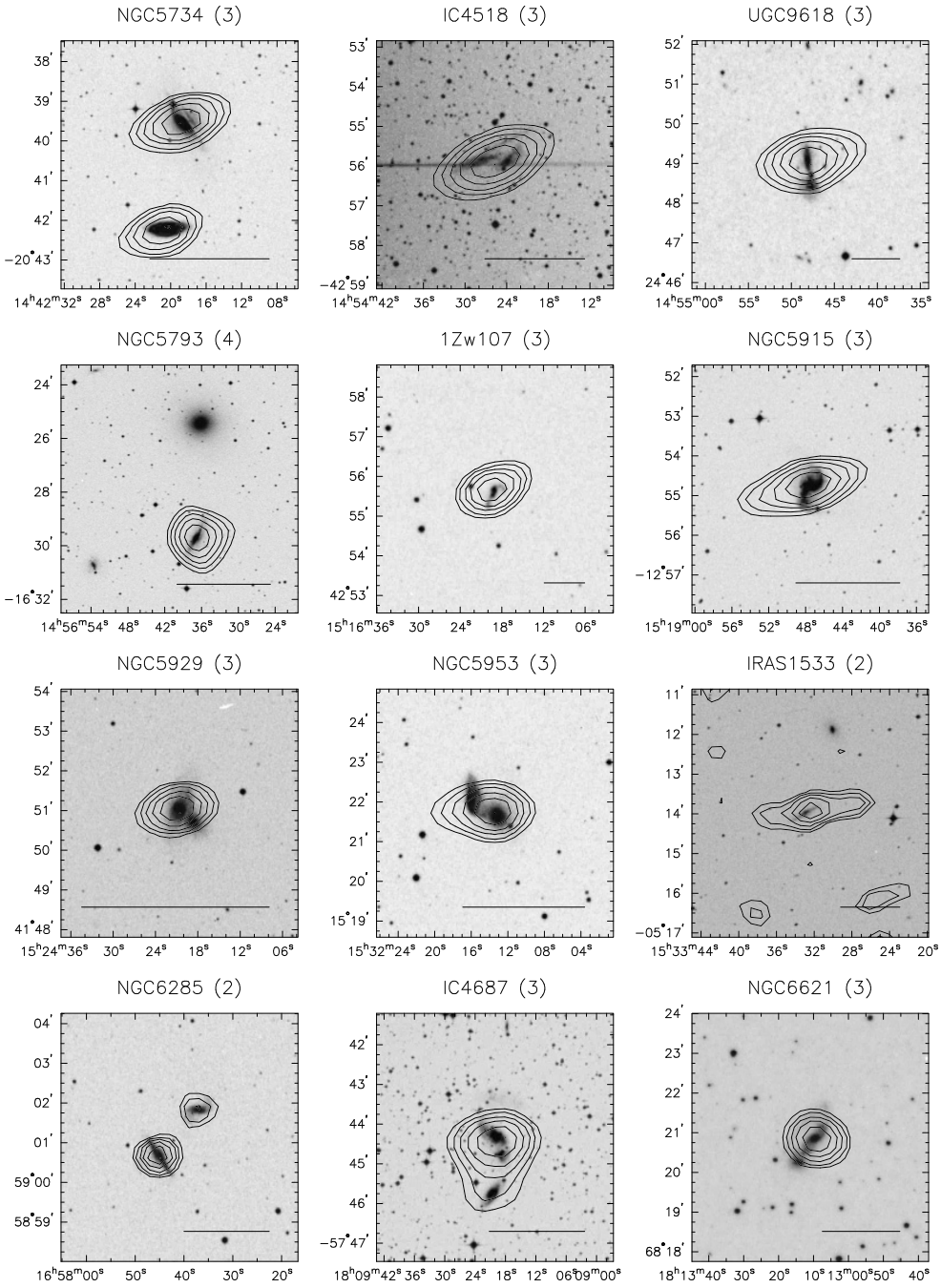

Fig. A.1.— (continued)

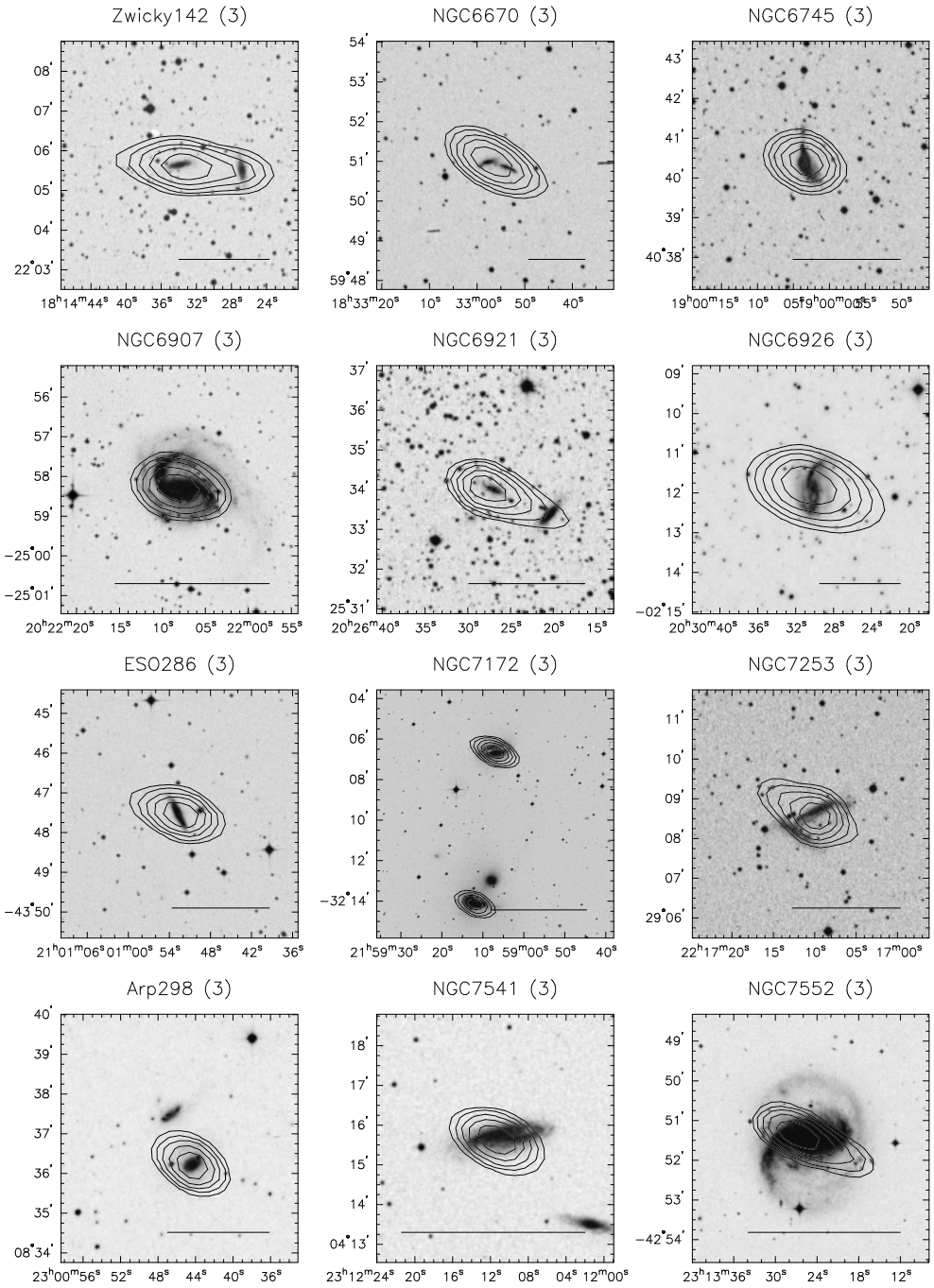

Fig. A.1.— (continued)

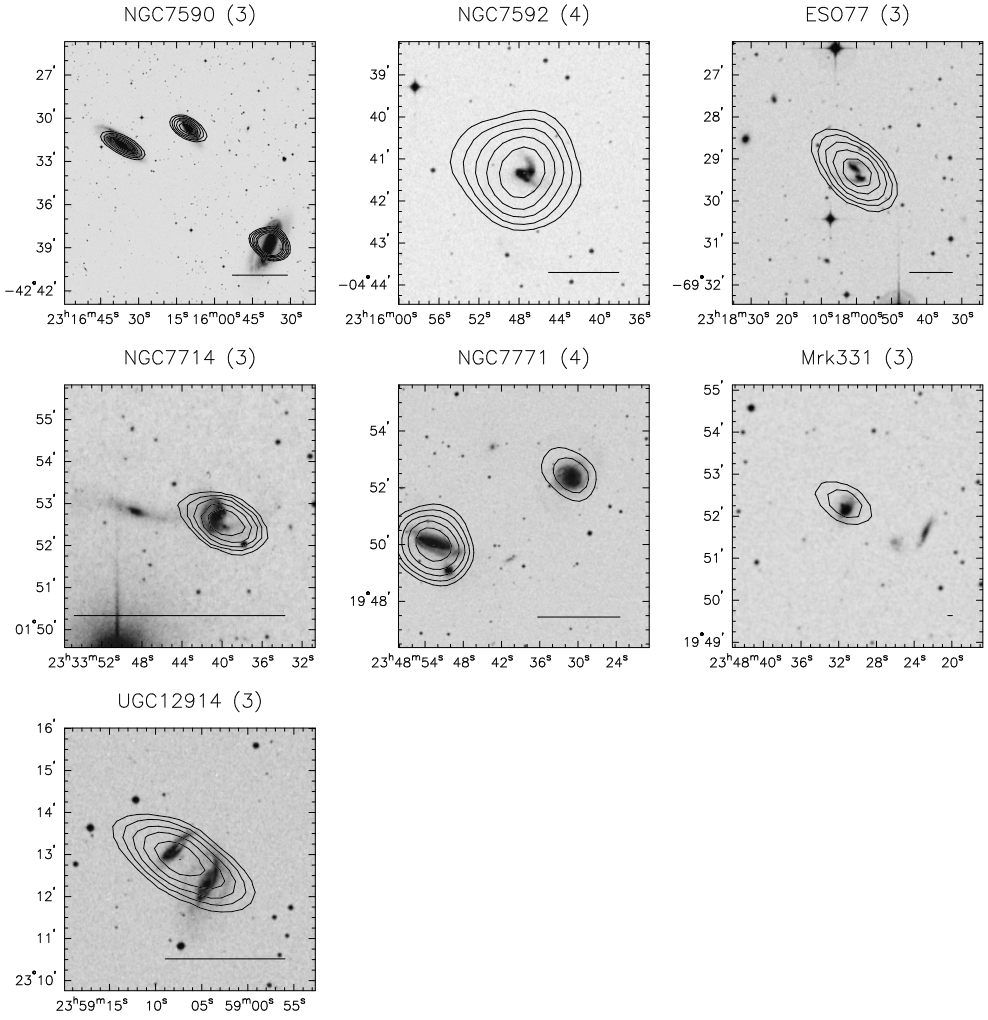

Fig. A.1.— (continued)

be resolved but not separated, the data were modeled with 2-d elliptical gaussians using the AIPS IMFIT and JMFIT routines. This is justified in that although the geometry of the IRAS beam is variable, it usually has roughly the form of an elliptical gaussian who exact size and orientation depend on the detector scan geometry. Peak positions were constrained to the position indicated by the nearest separated IRAS wavelength. If none of the IRAS data were able to supply positions, then the gaussian centers were constrained to the locations of the optical peaks as given by the 3RC, where possible, and otherwise according to positions measured directly from the DSS.

Table A.1 presents the measured global photometry for each of the galaxies identified in the IRAS images from the RBGS sample. In some cases the galaxies were still unresolved. When no level of improvement was gained over Surace et al. (1993), the numbers quoted from that paper are given. In cases where one or more components remained unresolved, but some components were resolved, the first unresolved component gives the flux of all the components, and subsequent unresolved components are marked with ellipses. The columns are as follows:

Column 1 - The galaxy name. Names are given in order of preference from the NGC, UGC, Catalog of Galaxies and Clusters of Galaxies (CGCG), Morphological Catalogue of Galaxies (MCG), and Markarian (Mrk) catalogs. Relevant cross-id's are also given. The given names are those associated with a specific coordinate as given by the 3RC, NED, or the Arp atlas. The Arp name associated with a given galaxy group is assigned to the first (westernmost) object, and no special significance is indicated by it.

Column 2,3 - Epoch 1950 coordinates. The given coordinates are those of the centroid of the infrared emission in cases where there was an infrared detection. Otherwise, the optical position from the 3RC is listed. If the 3RC listed no coordinates, then the coordinates are those measured directly from the DSS. The B1950 epoch was chosen due to the IRAS positional calibration.

Column 4 - Radial velocity in km $\cdot$ s^{-1}.

Column 5 - Total optical magnitude as given by the 3RC. In most cases this is the blue magnitude.

Column 6-13 - 12, 25, 60, and 100 μm integrated fluxes in Jy, and the associated uncertainties.

Column 14 - Log of the far-infrared luminosity, in units of solar luminosities. This is the luminosity from 40-122μm (Helou et al. 1988). H_o = 75 km s^{-1} mpc^{-1} is assumed.

Table A.1. Integrated Flux Densities of RBGS Interacting Galaxies

Name	RA H M S	DEC d m s	cz km/s	m_z	12μm Jy	σ_{12}	25μm Jy	σ_{25}	60μm Jy	σ_{60}	100μm Jy	σ_{100}	L_{fir} $L_\odot$
MCG -02-01-052	00 16 17.2	-10 38 21	8112	13.6	< 0.24		< 0.15		< 0.25		< 0.50		...
MCG -02-01-051	00 16 18.0	-10 39 16	8193	14.8	< 0.24		1.18	0.06	7.23	0.10	10.18	1.50	11.13
NGC 232	00 40 17.0	-23 50 06	6673	14.4	0.30	0.06	0.97	0.08	7.81	1.80	13.43	4.60	11.02
NGC 235	00 40 24.0	-23 48 54	6664	13.3	< 0.18		0.25	0.04	2.25	0.52	3.40	1.20	10.46
MCG +12-02-001	00 50 40.7	72 48 47	...	16.0	0.84	0.10	3.84	0.48	22.93	3.50	31.75	4.50	...
NGC 317a	00 54 49.8	43 31 51	5293	15	< 0.20		< 0.25		...		...		...
NGC 317b	00 54 51.1	43 31 23	5334	13.8	0.28	0.04	1.15	0.15	9.34	1.00	13.95	1.40	10.88
MCG +07-03-011	00 54 52.9	43 25 47	5413	15.1	< 0.20		< 0.27		0.78	0.90	1.97	0.20	9.91
IC 1623 a/b	01 05 21.0	-17 46 23	6016	14.0	0.92	0.11	3.86	0.50	23.85	3.60	31.53	4.40	11.37
IC 1622	01 05 09.0	-17 48 18	...	14.5	< 0.30		< 0.20		0.50	0.09	1.25	0.20	...
NGC 520[b]	01 21 59.6	03 31 51	2261	12.4	1.07	0.13	3.08	0.34	31.62	3.20	47.76	4.90	10.67
NGC 633	01 34 10.6	-37 34 33	5148	13.5	0.22	0.03	0.72	0.08	2.01	0.54	2.32	1.00	10.15
ESO 297-G012	01 34 12.3	-37 35 41	...	14.9	0.34	0.02	0.96	0.07	6.24	1.40	11.01	4.20	...
UGC 1385	01 51 56.3	36 40 18	5621	13.9	0.39	0.06	1.15	0.14	5.92	0.70	9.27	1.10	10.74
MCG +06-05-047	01 51 59.1	36 37 08	4919	15.2	< 0.28		< 0.20		0.51	0.07	< 0.76		...
NGC 833	02 06 53.3	-10 22 09	3977	13.7	< 0.30		< 0.30		< 0.12		< 0.40		...
NGC 835	02 06 57.3	-10 22 19	4152	12.9	0.27	0.03	0.38	0.07	6.33	0.65	11.54	1.20	10.53
NGC 838	02 07 11.1	-10 22 57	3851	13.6	0.76	0.10	2.08	0.30	12.96	1.40	16.96	1.50	10.72
NGC 839	02 07 15.6	-10 25 11	3847	13.9	0.58	0.08	2.31	0.30	12.80	1.40	12.90	1.40	10.68
UGC 1720b	02 11 18.9	04 56 06	...	...	< 0.18		< 0.30		< 0.30		< 0.60		...
UGC 1720	02 11 29.2	04 56 28	9061	...	0.33	0.04	0.68	.08	5.58	0.65	9.23	1.00	11.14
NGC 876	02 15 10.0	14 17 26	3860	16.5	...		...		4.62[d]	1.40	...		...
NGC 877	02 15 15.3	14 19 01	3913	12.6	1.14	0.15	1.94	0.22	8.82[d]	1.60	29.55	3.50	10.75
MCG +05-06-035	02 20 20.8	31 57 42	10083	15.4	< 0.21		< 0.20		< 1.60		...		...
MCG +05-06-036	02 20 23.6	31 57 56	10121	15.0	0.30	0.08	0.69	0.11	6.83	1.10	12.15	1.20	11.33
NGC 1097	02 44 10.6	-30 29 02	1275	10.2	4.16	0.42	9.27	0.95	58.29	6.00	114.82	14.00	10.48
UGC 2369 Ned 02	02 51 15.7	14 46 25	...	15.5	...		< 0.40		< 1.00		...		...
UGC 2369 Ned 01	02 51 15.9	14 46 03	...	15.5	0.37	0.04	1.62	0.20	8.27	0.90	11.75	2.00	...
NGC 1143	02 52 36.2	-00 22 47	8459	13.2	< 0.30		< 0.10		< 1.10		< 1.50		...
NGC 1144	02 52 38.6	-00 23 11	8647	13.8	0.44	0.05	0.85	0.08	5.70	0.68	11.75	1.72	11.14
NGC 1270	03 15 39.6	41 17 19	4871	14.3	< 0.20		< 0.50		0.38	0.05	< 0.80		...
NGC 1272	03 16 02.8	41 18 35	4021	12.9	< 0.20		< 0.40		< 0.40		< 0.40		...
NGC 1273	03 16 08.2	41 21 34	5351	14.3	< 0.20		< 0.40		< 0.80		< 0.50		...
UGC 2665	03 16 08.6	41 27 15	7806	15	< 0.20		< 0.40		0.72	0.10	1.23	0.15	10.12
IC 1907	03 16 15.6	41 23 58	4420	15.4	< 0.20		< 0.40		< 0.40		< 0.50		...
NGC 1274	03 16 21.9	41 22 05	6447	15.1	< 0.20		< 0.40		< 0.30		< 0.30		...
NGC 1275	03 16 28.7	41 19 48	5260	12.6	0.93	0.10	3.02	0.31	7.09	0.75	7.60	0.90	10.70

Table A.1—Continued

Name	RA H M S	DEC ° ′ ″	cz km/s	m_z	12μm Jy	σ_{12}	25μm Jy	σ_{25}	60μm Jy	σ_{60}	100μm Jy	σ_{100}	L_{fir} $L_\odot$
NGC 1277/8	03 16 34.8	41 23 12	4982	13.2	< 0.20		< 0.40		0.52	0.05	< 0.70		...
NGC 1281	03 16 47.2	41 26 58	4201	14.5	< 0.20		< 0.40		< 0.90		< 0.90		...
NGC 1283	03 16 57.0	41 13 06	6749	14.7	< 0.20		< 0.40		0.43	0.05	< 0.40		...
IRAS 0321+4023	03 21 47.6	40 23 01	7007	...	0.28	0.04	1.12	0.20	7.92	0.86	13.19	1.70	11.07
MCG +07-08-004	03 22 07.5	40 21 50	...	14.9	< 0.18		< 0.30		0.80		1.61		...
UGC 3094	04 32 39.0	19 04 12	7408	16.5	0.60	0.06	1.10	0.10	7.16	0.72	16.39	1.70	11.13
IRAS 05187-1017	05 18 45.8	-10 17 41	8474	...	< 0.08		0.20	0.05	5.33	0.50	9.30	1.00	11.07
UGC 3405	06 04 45.3	80 29 15	3791	15.3	0.14	0.05	0.20	0.04	1.93[d]	0.3	6.08[4]	1.80	
UGC 3410	06 05 19.2	80 27 44	3887	15.0	0.49	0.05	0.90	0.07	7.69[d]	1.15	18.32[4]	5.10	10.61
NGC 2146	06 10 40.1	78 22 23	893	11.4	7.36	0.80	21.66	2.40	154.12	16.00	217.44	24.00	10.54
ESO-LV 2550070/1/2	06 26 01.0	-47 08 48	11637	...	0.38	0.04	1.57	0.20	10.38	1.10	12.52	1.60	11.57
NGC 2341	07 06 14.4	20 41 05	5227	13.8	0.66	0.06	1.13	0.12	7.62	1.22	9.88[d]	2.97	10.75
NGC 2342	07 06 17.4	20 43 10	5276	13.1	1.00	0.10	1.76	0.19	7.99	1.30	16.66[d]	4.40	10.86
ESO 491-G020	07 07 47.0	-27 29 18	3021	...	0.70	0.30	2.30	0.50	16.42	2.00	23.80	2.90	10.63
ESO 491-G021	07 07 49.0	-27 29 36	2847	...	< 0.30		< 0.60		...		...		...
NGC 2276	07 10 18.4	85 51 00	2417	11.9	1.48	0.20	2.23	0.20	14.15	1.23	31.58	1.73	10.45
NCG 2300	07 15 45.1	85 48 31	1963	12.1	< 0.36		< 0.30		< 0.30		< 0.63		...
NGC 2388	07 25 37.9	33 55 21	4134	14.7	0.82	0.09	2.64	0.28	17.42	1.90	25.64[d]	3.80	10.93
NGC 2389	07 25 48.9	33 57 55	3957	13.4	0.53	0.07	0.73	0.10	3.40	0.35	5.85[d]	0.88	10.20
CGCG 058-004	07 32 41.6	11 49 46	4884	15.6	0.22		0.6		1.68		2.68		
NGC 2416	07 32 55.7	11 43 34	5101	14.1	<0.20		<0.30		1.35		3.16		
CGCG 058-009	07 32 56.9	11 49 16	4881	15	0.33		1.05		9.08		12.88		
ESO 163-G010	07 36 46.7	-55 04 08	2798	...	< 0.20		< 0.21		1.76	0.02	...		...
ESO 163-G011	07 36 59.4	-55 04 38	2822	11.9	0.37	0.04	0.63	0.00	5.32	0.70	14.64	1.50	10.20
ESO 432-IG006	08 42 25.6	-31 30 48	...	...	0.88	0.09	1.14	0.11	7.15	0.73	9.91	1.00	...
ESO 564-G010	09 00 29.0	-20 31 00	...	...	< 0.20		< 0.30		9.17	1.00	11.85	1.20	...
ESO 564-G011	09 00 30.0	-20 31 36	2596	...	0.38	0.05	1.45	0.17	...		...		...
IRAS 0911-1006e/w	09 11 10.7	-10 07 03	16449	...	< 0.20		0.67	0.07	7.39	0.70	13.31	1.40	11.79
NGC 2798	09 14 10.0	42 12 35	1739	13.0	0.87	0.09	3.20	0.40	19.29	2.20	27.98	3.10	10.22
NGC 2799	09 14 17.7	42 12 14	1755	14.3	< 0.30		< 0.40		< 1.50		< 1.00		...
NGC 2854	09 20 38.5	49 25 15	2741	13.8	0.20	0.05	0.41	0.10	2.49	0.25	5.29	0.42	9.79
NGC 2856	09 20 54.6	49 27 48	2638	14.1	0.43	0.04	1.24	0.07	6.27	0.69	11.57	0.93	10.13
NGC 2857	09 21 13.3	49 34 36	4887	12.9	0.15	0.03	0.22	0.08	0.91	0.10	2.78	0.25	9.94
MCG +08-18-012 Ned01	09 33 12.0	48 41 41	...	...	< 0.10		< 0.24		< 1.00		...		...
MCG +08-18-012 Ned02	09 33 18.5	48 41 56	...	...	0.20	0.03	0.79	0.09	6.23	0.80	9.34	1.60	...
NGC 2992	09 43 17.3	-14 08 39	2314	13.1	0.74	0.07	1.57	0.17	7.34	0.80	11.60[d]	3.00	10.06
NGC 2993	09 43 23.6	-14 08 12	2420	13.1	0.58	0.06	1.88	0.20	10.92	1.10	14.64[d]	3.80	10.24

Table A.1—Continued

Name	RA H M S	DEC ° ′ ″	cz km/s	m_z	12μm Jy	σ_{12}	25μm Jy	σ_{25}	60μm Jy	σ_{60}	100μm Jy	σ_{100}	L_{fir} $L_\odot$
IC 563	09 43 44.6	03 16 34	6093	14.8	0.38	0.05	< 0.18		2.41[d]	0.20	5.87[4]	0.60	10.50
IC 564	09 43 45.3	03 18 07	6056	14.1	0.30	0.05	0.24	0.04	3.07[d]	0.25	6.56[4]	0.70	10.57
IC 2545[e]	10 03 52.2	-33 38 23	10230	15.0	0.38	0.05	1.29	0.18	9.71	1.10	9.60	1.10	11.41
NGC 3165	10 10 55.8	03 37 25	1332	14.5	< 0.15		< 0.30		0.10	0.05	...		...
NGC 3166	10 11 09.3	03 40 25	1345	11.3	0.33	0.30	0.40	0.06	6.10	0.04	14.00	0.14	9.58
NGC 3169	10 11 38.7	03 43 03	1233	11.1	1.09	0.04	1.12	0.04	7.90	0.03	21.90	0.12	9.66
NGC 3226	10 20 43.2	20 09 06	1151	12.3	< 0.27		< 0.18		< 0.60		...		...
NGC 3227	10 20 47.3	20 07 03	1157	11.1	1.11	0.12	2.04	0.21	9.01	1.00	19.11	2.00	9.60
NGC 3262	10 26 58.0	-43 54 18	2864	14.	<0.50		<0.30		<0.21		< 0.7		
NGC 3263	10 27 04.8	-43 51 55	2842	12.5	1.1		1.01		8.9		21.1		
NGC 3395	10 47 02.6	33 14 44	1620	12.4	0.28	0.05	0.72	0.08	6.79[d]	2.10	13.00[4]	3.00	9.74
NGC 3396	10 47 08.9	33 15 18	1625	12.6	0.23	0.04	0.98	0.11	6.15[d]	2.10	9.56[4]	3.00	9.67
NGC 3413	10 48 34.0	33 01 56	645	13.1	< 0.15		0.31	0.04	1.09	0.40	2.01	0.10	8.15
NGC 3424	10 49 00.1	33 09 54	1501	13.2	0.48	0.04	0.88	0.04	8.80	0.09	17.40	0.21	9.80
NGC 3430	10 49 25.2	33 13 03	1585	12.2	0.36	0.40	0.75	0.05	13.90	0.07	9.60	1.00	9.91
UGC 6016	10 51 12.1	54 33 13	1493	17.0	< 0.10		< 0.15		< 0.50		< 0.50		...
NGC 3448	10 51 39.6	54 34 27	1350	12.5	0.34	0.04	0.76	0.09	6.74	0.75	12.17	1.40	9.58
ESO 264-G057/8	10 56 44.8	-43 10 18	5156	14.8									
NGC 3511	11 00 57.0	-22 49 00	1106	11.5	0.88	0.40	0.89	0.03	8.61	0.05	22.54	0.21	9.59
NGC 3513	11 01 19.2	-22 58 28	1194	11.9	< 0.12		0.34	0.04	3 .30	0.06	7.84	0.23	9.22
A1101+41[e]	11 01 04.3	41 07 06	...	...	...		...		...		...		...
MCG +08-23-019 Ned02	11 01 05.7	41 07 11	10356	...	< 0.30		0.42	0.05	6.50	0.70	11.38	1.30	11.33
UGC 6436a	11 23 08.4	14 57 08	...	...	< 0.25		0.35	0.07	5.10[d]	1.00	...		...
UGC 6436b	11 23 13.0	14 56 39	10251	14.9	< 0.25		0.41	0.07	2.1[d]	1.00	...		...
NGC 3690	11 25 42.0	58 50 17	3131	11.8	3.90	0.40	24.14	2.40	121.64	12.50	122.45	12.50	11.48
NGC 3893	11 46 01.8	48 59 13	973	11.2	1.70	0.20	2.09	0.23	15.76	1.70	38.38	4.00	9.72
NGC 3896	11 46 26.8	49 01 39	869	13.9	< 0.21		< 0.18		< 0.33		< 0.30		...
NGC 3991	11 54 54.0	32 36 00	3111	14.2	< 0.40		0.24	0.04	2.61	0.28	4.22	0.45	9.87
NGC 3994	11 55 02.3	32 33 23	3096	13.3	0.35	0.04	0.53	0.05	5.00	0.50	10.31	1.20	10.19
NGC 3995	11 55 10.3	32 34 24	3254	12.7	< 0.40		0.68	0.07	3.27	0.30	6.63	0.68	10.05
NGC 4038/9[b]	11 59 20.0	-18 35 49	1642	10.9	2.92	0.38	7.11	1.13	46.88	1.70	85.69	8.20	10.59
ESO 440-IG058	12 04 17.3	-31 40 17	6818	16	0.37	0.06	0.97	0.09	7.30	0.78	13.40	1.50	11.02
NGC 4169	12 09 47.0	29 27 30	3784	13.2	< 0.35		< 0.30		< 0.33		< 0.80		...
NGC 4170	12 09 50.2	29 28 57	1127	13.6	< 0.30		< 0.10		< 0.30		< 0.80		...
NGC 4174	12 09 54.9	29 25 36	3980	14.3	< 0.24		< 0.33		< 0.21		< 1.20		...
NGC 4175	12 09 58.6	29 26 52	3956	14.2	0.40	0.05	0.77	0.10	5.70	0.70	10.58	1.20	10.44
ESO 267-G029	12 11 14.9	-46 59 45	5445	14.2	0.37		0.97		5.68		10.31		

Table A.1—Continued

Name	RA H M S	DEC ° ′ ″	cz km/s	m_z	12μm Jy	σ_{12}	25μm Jy	σ_{25}	60μm Jy	σ_{60}	100μm Jy	σ_{100}	L_{fir} $L_\odot$
ESO 267-G030	12 11 35.0	-46 57 00	5543	14.2	0.46		0.89		5.95		12.39		
IC 3153	12 17 03.8	05 40 33	...	14.8	< 0.20		< 0.20		0.60	0.08	0.94	0.12	...
NGC 4270	12 17 08.2	05 49 06	2495	13.1	< 0.20		< 0.30		0.31	0.05	2.09	0.30	9.10
NGC 4268	12 17 13.9	05 33 40	2374	13.8	< 0.20		< 0.20		< 0.30		< 1.20		...
NGC 4273	12 17 23.6	05 37 13	2378	12.4	1.05	0.13	1.35	0.17	11.27	1.20	21.87	2.50	10.31
NGC 4277	12 17 30.5	05 37 07	2516	13.4	< 0.20		< 0.20		< 0.60		< 1.20		...
NGC 4281	12 17 48.6	05 39 54	2711	12.3	< 0.20		< 0.40		0.83	0.12	1.78	0.25	9.31
NGC 4485	12 28 03.3	41 58 26	493	12.3	< 0.90		0.53	0.10	2.16	0.70	3.83		8.21
NGC 4490	12 28 08.9	41 55 26	578	10.2	2.74		5.34	0.80	50.86	6.00	88.29		9.71
NGC 4567/8[b]	12 34 02.3	11 31 06	2260	11.1	2.10	0.22	2.93	0.32	21.11	2.30	56.77	6.50	10.60
ESO 381-G008	12 38 10.2	-36 28 45	3285	13	0.82	0.10	2.87	0.30	8.27	1.00	15.22	1.80	10.21
ESO 381-G009	12 38 16.5	-36 27 05	3050	13.9	< 0.16		0.32	0.10	1.17	0.15	...		9.30
NGC 4627	12 39 33.5	32 50 51	765	13.1	< 0.27		< 0.24		< 0.50		< 1.80		...
NGC 4631	12 39 40.7	32 48 54	606	09.8	6.81	0.80	11.24	1.20	99.69	10.00	193.26	24.00	10.07
NGC 4647	12 41 01.0	11 51 20	1414	11.9	0.68	0.08	0.47	0.16	...		...		...
NGC 4649	12 41 08.4	11 49 35	1114	9.8	0.30	0.05	0.32	0.11	...		...		...
NGC 4922 a/b	12 59 01.7	29 35 00	7071	14.2	0.20	0.04	1.67	0.23	6.01	0.75	7.78	0.80	10.91
MCG -02-033-098	12 59 41.6	-15 29 54	4773	14.5	0.33	0.05	1.70	0.24	7.82	0.80	10.29	1.15	10.69
MCG -02-033-098b	12 59 49.1	-15 30 36	...	...	< 0.10		< 0.30		< 0.20		< 0.50		...
NGC 4984	13 06 17.9	-15 14 57	1206	12.3	0.95		2.56		11.23		16.31		
UGC 8335b	13 13 36.3	62 23 32	9453	15	< 0.30		< 0.50		...		...		...
UGC 8335a	13 13 41.4	62 23 21	9313	15	0.49	0.05	2.08	0.20	11.45	1.30	12.90	1.30	11.41
IC 879	13 16 55.2	-27 10 12	1969	14.0	0.23	0.05	0.52	0.08	0.74	0.08	< 0.29		...
NGC 5078	13 17 04.6	-27 08 51	2168	12	1.20	0.13	1.36	0.15	10.37	1.10	35.84	5.70	10.32
MCG -03-34-063a	13 19 38.3	-16 26 50	5150	···	< 0.45		< 0.40		3.03[d]	1.00	3.9[4]	1.00	10.34
MCG -03-34-063b	13 19 43.6	-16 28 05	5150	···	0.84		3.08		4.63[d]	1.20	2.8[4]	0.90	10.43
NGC 5216	13 30 23.0	63 01 32	2949	13.6	< 0.09		< 0.18		0.19	0.03	< 0.05		...
NGC 5218	13 30 27.1	63 01 32	2860	13.1	0.36	0.03	0.92	0.08	7.14	0.70	14.38	1.44	10.28
NGC 5257	13 37 19.7	01 05 33	6798	12.9	0.52[d]	0.16	1.18[4]	0.30	8.10[4]	2.00	13.63[4]	3.00	11.05
NGC 5258	13 37 24.6	01 05 06	6757	12.9	0.25[d]	0.10	0.78[4]	0.30	3.94[4]	1.00	7.27[4]	1.80	10.75
NGC 5331[b]	13 49 43.4	02 20 60	...	...	< 0.3		0.64	0.70	6.27	0.70	10.71	1.10	...
NGC 5394	13 56 22.5	37 42 00	3427	13.7	0.52	0.05	1.19	0.11	5.62[d]	1.41	10.43[4]	3.10	10.31
NGC 5395	13 56 29.3	37 40 03	3487	12.1	0.40	0.04	0.48	0.06	6.86[d]	1.50	14.21[4]	3.10	10.43
IC 4356	13 56 36.6	37 43 59	...	16.2	< 0.20		< 0.27		< 0.45		< 0.10		...
NGC 5426	14 00 47.7	-05 49 47	2621	12.7	< 0.70		< 0.90		3.30	0.37	...		9.61
NGC 5427	14 00 48.6	-05 47 27	2730	11.9	0.74	0.09	0.96	0.10	7.50	0.80	15.45	2.00	10.01
NGC 5506	14 10 39.1	-02 58 26	1815	12.8	1.30	0.03	4.30	0.06	8.76	0.08	8.60	0.12	9.86

Table A.1—Continued

Name	RA H M S	DEC ° ′ ″	cz km/s	m_z	12μm Jy	σ_{12}	25μm Jy	σ_{25}	60μm Jy	σ_{60}	100μm Jy	σ_{100}	L_{fir} $L_\odot$
NGC 5507	14 10 43.9	-02 54 55	1852	13.5	< 0.12		< 0.27		< 0.45		< 0.65		...
NGC 5595	14 21 28.4	-16 29 55	2691	12.6	0.61	0.04	0.71	0.05	9.02	0.04	16.59	0.14	10.31
NGC 5597	14 21 42.2	-16 32 19	2619	12.6	0.56	0.04	1.82	0.06	8.95	0.06	17.05	0.16	10.29
NGC 5734	14 42 19.0	-20 39 36	4091	13.7	0.47	0.03	0.81	0.07	...		...		...
NGC 5743	14 42 20.0	-20 42 12	4074	13.8	0.35	0.04	0.90	0.08	...		...		...
IC 4518a/b	14 54 26.0	-42 55 54	4921	15.0	0.53	0.05	1.52	0.15	9.59	1.00	22.22	2.30	10.90
UGC 9618 Ned 02	14 54 47.8	24 49 05	10173	14.6	0.45[b]		0.55	0.8	7.08	2.00	15.48	5.00	11.39
UGC 9618 Ned 01	14 54 48.1	24 48 21	9776	15.3	...		< 0.21		< 1.50		< 5.00		...
NGC 5793	14 56 37.1	-16 29 40	3491	14.3	0.17	0.04	0.45	0.07	6.43	0.05	8.50	0.19	10.33
NGC 5796	14 56 36.5	-16 25 30	2962	12.7	< 0.21		< 0.33		< 0.36		< 0.54		...
IZw107	15 16 19.7	42 55 36	12043	...	0.31	0.05	1.47	0.20	9.57	1.20	10.75	1.20	11.56
NGC 5915	15 18 47.7	-12 54 56	2291	12.8	0.47	0.04	1.30	0.05	11.00	0.05	14.60	0.22	10.20
NGC 5916a	15 18 28.9	-12 55 29	2338	15	< 0.60		< 0.90		1.16	0.04	2.50	0.17	9.32
NGC 5916	15 18 52.0	-12 59 37	2338	14.2	< 0.15		< 0.24		0.75	0.06	...		...
NGC 5929	15 24 18.9	41 50 41	2561	14.1	< 0.24		< 0.30		< 1.00		...		...
NGC 5930	15 24 20.7	41 51 00	2672	13.6	0.45	0.05	1.84	0.20	9.71	1.00	14.71	2.00	10.30
NGC 5953	15 32 13.7	15 21 43	1965	13.3	0.65	0.10	1.57	0.20	12.00	1.60	21.18	2.50	10.15
NGC 5954	15 32 15.7	15 22 10	1959	13.7	< 0.15		< 0.40		...		...		...
NPM1G -05.0557	15 33 30.2	-05 11 59	...	16.6	< 0.30		< 0.27		< 0.30		< 0.80		...
IRAS 15334-0514	15 33 32.6	-05 13 55	8186	...	< 0.23		0.88	0.10	5.83	0.60	10.10	1.00	11.07
NGC 6285	16 57 36.1	59 01 53	5696	15.3	0.20	0.05	0.27	0.05	2.60[d]	0.60	6.60[d]	2.30	10.48
NGC 6286	16 57 45.0	59 00 41	5501	14.1	0.45	0.06	0.55	0.06	8.03[d]	2.00	18.30[d]	4.00	10.92
ESO 140-IG009/10[e]	18 09 19.4	-57 44 28	5200	13.8	0.94	0.14	2.96	0.38	14.78[d]	3.10	28.55	3.00	11.10
ESO 140-IG011	18 09 22.1	-57 45 45	4949	15.0	< 0.25		0.71	0.10	1.54[d]	0.35	...		...
NGC 6621	18 13 09.3	68 20 50	6284	14.0	0.31	0.05	1.02	0.10	7.02	1.20	12.19	2.30	10.93
NGC 6622	18 13 14.4	68 20 15	6230	16.0	< 0.12		< 0.30		< 1.00		< 1.30		...
CGCG 142-033	18 14 24.0	22 05 00	5353	...	< 0.20		< 0.30		< 0.30		< 1.00		...
CGCG 142-034	18 14 32.6	22 05 36	5599	...	0.27	0.06	0.64	0.08	6.55	0.80	13.25	1.60	10.82
NGC 6670	18 32 56.4	59 50 58	8650	...	0.47	0.05	1.10	0.10	9.24	0.90	14.84	1.50	11.31
CGCG 301-032	18 33 32.8	59 49 14	...	15.2	0.15	0.04	0.15	0.04	0.90	0.10	1.64	0.18	...
NGC 6745	19 00 03.3	40 40 23	4545	13.3	0.45	0.05	0.92	0.12	6.84	0.70	13.01	1.40	10.65
NGC 6907	20 22 08.0	-24 58 17	3161	11.9	1.29	0.13	2.42	0.25	14.76	1.50	31.78	3.50	10.69
NGC 6921	20 26 20.8	25 33 23	4391	14.4	< 0.25		0.62	0.07	3.97	0.60	7.48	1.60	10.38
MCG +04-48-002	20 26 26.8	25 34 00	4259	18.0	0.51	0.06	0.71	0.10	8.15	1.60	12.50	3.00	10.63
NGC 6926	20 30 30.1	-02 11 54	5970	13.2	0.68		0.91		8.21		17.15		
NGC 6929	20 30 45.9	-02 12 31	6130	14.4	<0.20		<0.20		<0.60		<0.30		
ESO 286-IG033	21 00 50.6	-43 43 59	4990	...	[a]		0.43	0.08	1.33	0.10	1.42	0.17	9.93

Table A.1—Continued

Name	RA H M S	DEC ° ′ ″	cz km/s	m_z	12μm Jy	σ_{12}	25μm Jy	σ_{25}	60μm Jy	σ_{60}	100μm Jy	σ_{100}	L_{fir} $L_\odot$
ESO 286-IG035	21 00 52.7	-43 47 31	5208	...	[a]		1.12	0.14	8.17	0.90	14.16	1.60	10.83
NGC 7172	21 59 07.1	-32 06 42	2575	12.9	0.72	0.06	1.06	0.11	6.06	0.61	15.10	1.35	10.16
NGC 7174/6	21 59 11.9	-32 14 03	2778	...	0.25	0.04	0.61	0.06	3.65	0.40	10.15	1.00	10.03
NGC 7253[b]	22 17 11.7	29 08 41	4718	...	0.43	0.05	0.70	0.09	6.38	0.70	13.63	1.50	10.67
NGC 7469	23 00 44.4	08 36 19	4916	13.0	1.48	0.19	5.67	0.70	27.40	4.00	39.61	6.00	11.27
IC 5283	23 00 47.0	08 37 26	4894	14.8	0.36	0.07	0.17	0.05	< 0.80		< 2.00		...
NGC 7541													
NGC 7552	23 13 25.4	-42 51 27	1585	11.3	3.49	0.36	12.43	1.40	78.38	8.00	104.85	12.00	10.73
NGC 7582	23 15 38.3	-42 31 54	1575	11.4	2.54	0.30	9.43	1.10	52.25	5.60	87.60	9.30	10.59
NGC 7590	23 16 10.3	-42 30 45	1596	12.1	1.02	0.10	1.23	0.14	8 .54	0.90	19.57	2.40	9.87
NGC 7599	23 16 35.9	-42 31 54	1654	12.1	1.06	0.10	1.40	0.18	6 .95	1.40	19.45	2.00	9.86
NGC 7592	23 15 47.4	-04 41 26	7328	...	0.40	0.04	1.16	0.17	7.81	0.90	10.66	1.40	11.07
ESO 077-IG014 Ned 01/2	23 17 58.5	-69 29 28	11400	16.5	0.23	0.03	0.61	0.07	6.02	0.70	10.62	1.10	11.38
NGC 7714	23 33 41.0	01 52 34	2798	13.0	0.56	0.05	3.15	0.30	10.73	1.10	12.46	1.30	10.34
NGC 7715	23 33 48.5	01 52 48	2770	14.7	< 0.15		< 0.21		< 0.15		< 0.40		...
IRAS 23487+1957	23 48 40.7	19 57 17	...	...	< 0.55		0.60	0.08	1.44	0.15	3.66	0.41	...
UGC 12812	23 48 46.1	20 17 56	5326	15.5	<0.20		<0.30		<2.00		<1.40		
UGC 12812b	23 48 48.9	20 17 46			<0.20		< 0.60		<2.00		< 1.40		
NGC 7771	23 48 51.7	19 49 52	4287	13.1	1.23	0.16	2.90	0.22	20.93	1.78	44.85	3.80	11.11
UGC 12812	23 48 53.6	20 18 24	5349	14.9	0.87	0.13	3.02	0.24	18.43	1.60	22.56	2.50	11.15
KUG 2349+202	23 49 03.3	20 14 49		16.5	< 0.21		<0.35		<0.20		<0.40		
UGC 12914	23 59 04.0	23 12 23	4371	13.1	< 0.20		< 0.60		2.52	0.70	4.05	1.90	10.15
UGC 12915	23 59 08.6	23 12 59	4336	14.0	0.36	0.06	1.16	0.24	5.18	1.70	13.05	2.80	10.54

Note. — Ellipses for fluxes indicate unresolved, for any other value they indicate that the value is unkown. Specific Notes - (a) bad scan (b) flux lies between galaxies (c) dense cluster (d) resolved using component fitting (e) except NGC 7319/7320

A.2.3. Photometric Uncertainties

Evaluating the photometric uncertainties of the HIRES data product is quite difficult. In general, uncertainties arise from three sources, all of which vary in importance depending on the particular field. The integrated flux density uncertainties quoted in Table A.1 are absolute. That is, they contain the accumulated uncertainty in the absolute flux listed, and typically range from 10-30%.

Confusion is the first limitation. The dominant source of noise in HIRES is not photometric background noise, but confusion due to noise spike amplification. High sigma noise peaks are amplified by the deconvolution process; they appear similar to weak point sources with a signal strength as high as 0.1 Jy. In those cases where the target is less than 0.3 Jy, it becomes difficult to differentiate the target from amplified noise. As a result, quoted upper limits are often quite high, as this upper limit is set by the flux contained in nearby noise peaks. Our achieved sensitivity is thus around 0.25-0.3 Jy, depending on the wavelength and field geometry.

The technique used to derive the photometry is the second contributor to the photometric uncertainty. In cases where the galaxies are well separated and aperture photometry could be used, this typically leads to errors of a few percent. In those cases where the galaxies were not well separated and gaussian fitting was used, this becomes the dominant source of error and can range anywhere from 20-50% depending on the degree of resolution of the targets.

Absolute photometric calibration is the third major problem. As noted in Surace et al. (1993), there are certain caveats to the photometric calibration of the HIRES data product. The calibration of the IRAS data is in part dependent on factors due to detector responsivity and dwell time. This correction, known as the AC/DC correction, is well known for point sources, and hence the Point Source Catalog (PSC) is properly calibrated. However, it is slightly different for extended sources, and is a poorly understood function of source extension. In Surace et al. (1993) this issue was avoided by forcing all of the data onto the same scale as the PSC by using the component flux ratios indicated by HIRES to divide up the flux indicated by the BGS, which was produced using the ADDSCAN process which is known to produce the same photometric scale as the PSC. This version of HIRES produces data believed to be on the DC scale, appropriate for point sources. This is appropriate for most of these sources, as in almost all cases the galaxies were on the order of less than 5′ in size. For sources this small, the AC/DC correction is very small. Unlike Surace et al. (1993), this data has not been forced to agree with the BGS, and this is the source of the variations between the fluxes in the previous paper and this work. Testing of HIRES has shown that measured integrated fluxes of essentially unresolved point sources have an intrinsic scatter of about 8-12% compared to those of the PSC (Laughlin et al. 1990). Note that this systematic error commonly contributes much of the uncertainty in absolute flux. Internally, the calibration of the frames is much better; simulations indicate that relative photometry is probably accurate to roughly 5%.

A.3. Results

A.3.1. Far-IR Properties

A comparison sample of galaxies was constructed by selecting a subsample of the BGS which had no visible signs of interaction and were not in close pairs. From these isolated BGS galaxies we selected a subsample so as to have the same distribution of blue magnitudes as the RBGS close pairs. We can therefore compare the far-infrared properties of a far-infrared flux-limited sample of interacting pairs to a similarly flux-limited sample of isolated galaxies with the same distribution of optical luminosities.

The cumulative distribution functions of $L_{\rm fir}$, Log(f_{12}/f_{25}), and Log(f_{60}/f_{100}) for the two samples are given figures A.2, A.3, and A.4. These distributions only include the galaxies actually detected and resolved by HIRES. These distributions are nearly identical to Surace et al. (1993). In particular, the median value of $L_{\rm fir}=10^{10.48}$ $L_{\odot}$ for the interacting galaxies versus $L_{\rm fir}=10^{10.07}$ $L_{\odot}$ for the isolated galaxies is essentially the same as the previous results. In separated galaxy pairs, then, the interaction process enhances $L_{\rm fir}$ by a factor of roughly 2.5. Similar differences are seen in the far-IR colors: median Log(f_{12}/f_{25})=-0.37 for interactors vs -0.21 for isolated galaxies, and median Log(f_{60}/f_{100})=-0.26 vs -0.33.

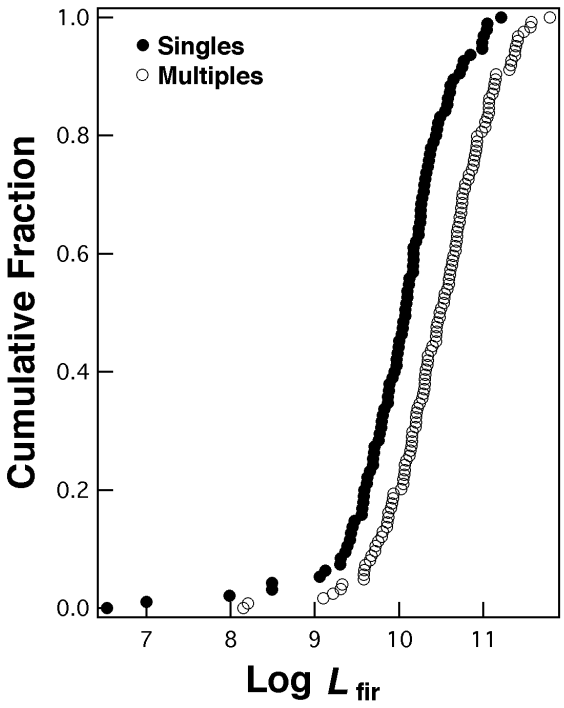

Fig. A.2.— $L_{\rm fir}$ cumulative distribution function for single and double systems in the RBGS. The paired systems show a small ($\approx$2.5$\times$) increase in $L_{\rm fir}$

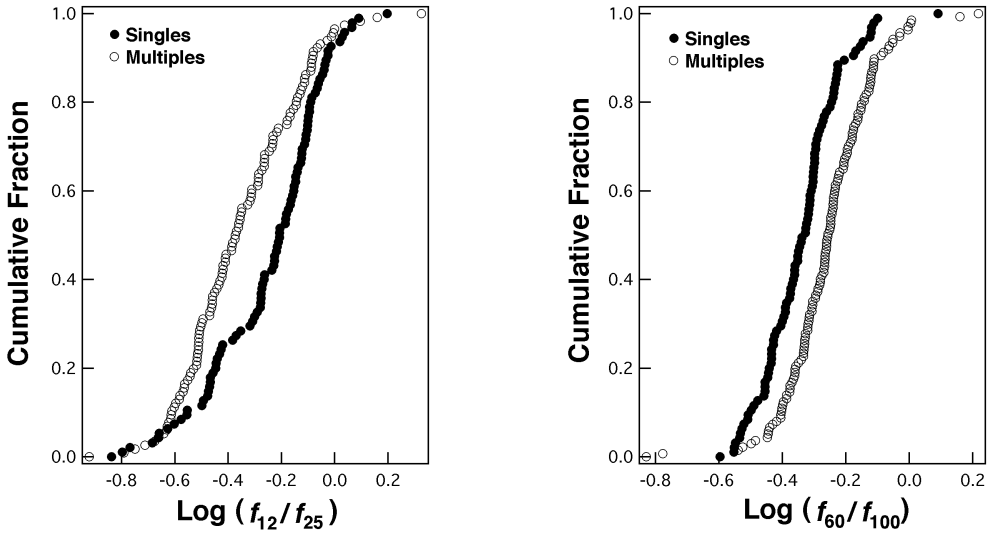

Fig. A.3.— f_{12}/f_{25} and f_{60}/f_{100} ratio cumulative distribution functions for single and double systems in the RBGS.

A.3.2. Optical Morphology and far-IR Enhancement

Hubble types were taken from the 3RC. A fraction of the galaxies either have not been classified at all, or are simply listed as "spiral". All other resolved spiral galaxies that were actually classified were considered to be either "early type" (S0, SB0 through Sa, SBa) or "late-type" (Sb,SBb and higher). Although the specific Hubble type for each galaxy was kept track of, for purposes of this analysis it was felt to be more useful to group the types into broad categories in order to improve the counting statistics.

Only 11 ellipticals are found in the entire RBGS. Of these, none are detected at both 60 and 100μm and only three are detected at all. These numbers agree with what would be expected based on a random pairing of elliptical and spiral galaxies given an elliptical/spiral fraction similar to that of field galaxies, or are perhaps a little low. In particular, this is the number expected for the RBGS if we assume that every system contains one bright spiral galaxy, and that the remaining faint galaxies are distributed according to the field elliptical/spiral ratio. This also agrees with the low detection fractions for elliptical galaxies found by other studies (Sulentic 1989; Haynes & Herter 1988).

An examination of the late and early-type spirals in the RBGS indicates that there are no differences between these populations. The rate of detection for both of the two classes is around 88%, indicating that they have a similar fraction of their distribution above our detection limit. This is further illustrated by Figure 3, which shows the cumulative distribution function of Log $L_{\rm fir}$ for the galaxies which were actually detected in the two classes. They are extremely similar. Results are the same for the color ratios Log(f_{12}/f_{25}) and Log(f_{60}/f_{100}).

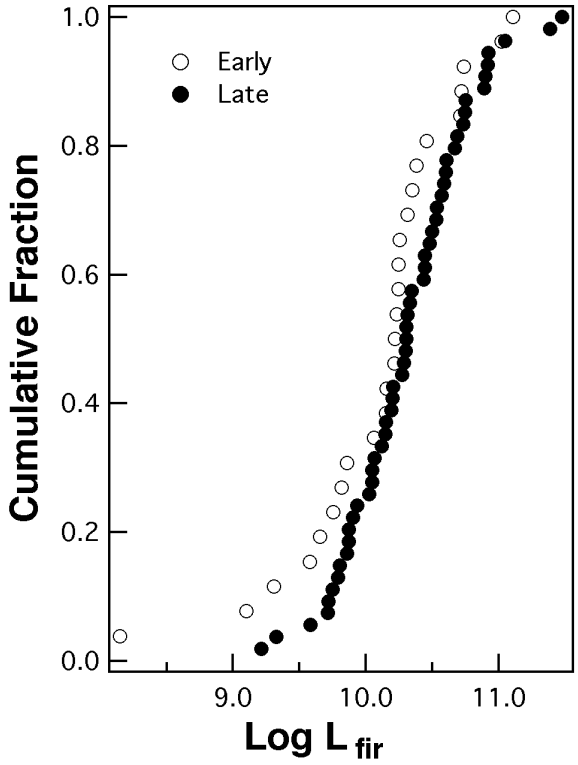

Fig. A.4.— Cumulative distribution function of $L_{\rm fir}$ of late and early type interacting spiral galaxies in the RBGS. There is no measurable difference between the two

Similar results also hold for different combinations of Hubble sub-types. Haynes and Herter (1988) found that the detection rate for isolated spiral galaxies is roughly independent of morphological type. Roberts and Haynes (1994) have confirmed this using large optical samples of isolated galaxies and comparing them against the IRAS data. The median, 25% and 75% percentile values of the distribution of $L_{\rm fir}$ for the RBGS spiral galaxies are also very similar to those found by Roberts & Haynes for isolated UGC galaxies. This is unsurprising, since both the results presented here and previous studies have shown that only a small increase in $L_{\rm fir}$ occurs for widely separated (non- overlapping) interacting pairs (Haynes & Herter 1988; Surace et al. 1993), and therefore any enhanced far-IR activity that could distinguish late from early spirals is likely to be slight. This enhancement would be further diluted by the presence of systems that have not yet reached first perigalcticon, and hence have not yet reached the point at which the two classes would separate themselves (Mihos et al. 1994b), and by the presence of close systems which are unlikely to actually merge or otherwise strongly interact with each other.

A.3.3. Pairing in the far-IR

Figures A.5 and A.6 give the measured flux ratio and lower limits between the brightest component and the average value of the remaining components as a function of L_{fir} and $\mathrm{Log}(f_{60}/f_{100})$. There is no significant correlation between either of these properties and the component flux ratio. There is therefore no increased tendency in far-infrared luminous systems for both components to be infrared luminous. Since both components in an interacting system are presumably undergoing a similar degree of tidal disruption, it seems that at this early stage of interaction the details of the interaction itself are not the dominant factor determining far-IR luminosity.

There has been considerable confusion in the discussion of component flux ratios and pairing. Surace et al. (1993) claimed that in approximately 2/3 of interacting pairs, both galaxies were IR-bright. However, this was taken to mean that 2/3 of galaxy pairs have component flux ratios less than ten. By the same criterion, an examination of Figures A.5 and A.6 confirm that 69% of galaxies have flux ratios less than 10. Since it appears that intrinsic properties of the galaxies, and not the details of the interaction, dictate the level of far- infrared activity in these widely separated systems, then it must be the intrinsic underlying flux distribution that dictates the details of the pairing. Figure A.8 presents the cumulative distribution functions of 60μm fluxes above and below the 5 Jy selection limit. These are the underlying flux distributions at 60mum in the RBGS. Note that we have presented these separately; because the sample is 60μm selected, the CDF is naturally biased above the selection cutoff. There are indications that the interacting galaxies found in the Arp Atlas, as well as several other interacting galaxy samples, have this same flux distribution (Surace & Sanders 1998).

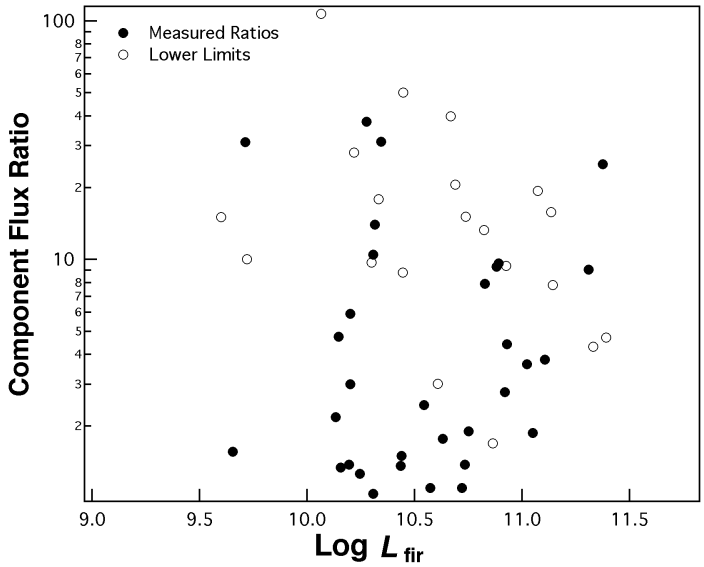

Fig. A.5.— Log $L_{\rm fir}$ versus the component flux ratio. No correlation is seen. The distribution of lower limits is distributed somewhat randomly, since there was a fixed lower flux limit for the dim component, while the bright component could span a wide range of detected brightnesses.

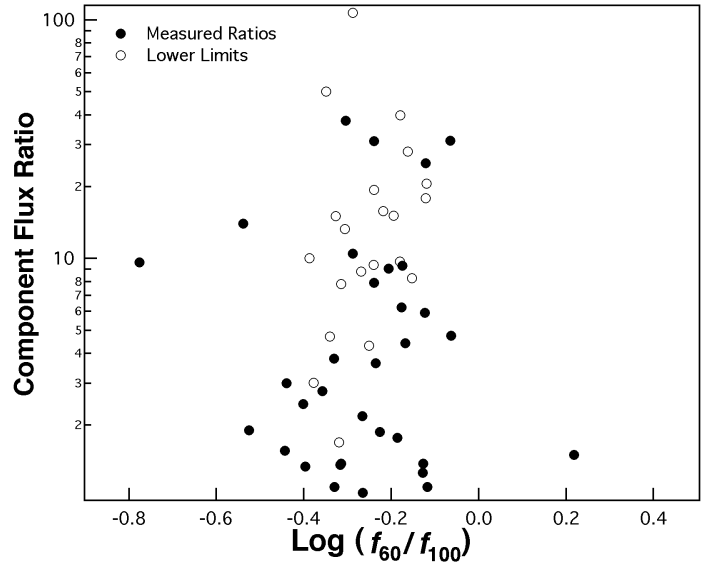

Fig. A.6.— Log f_{60}/f_{100} versus component flux ratio, as in the previous figure. No correlation is seen.

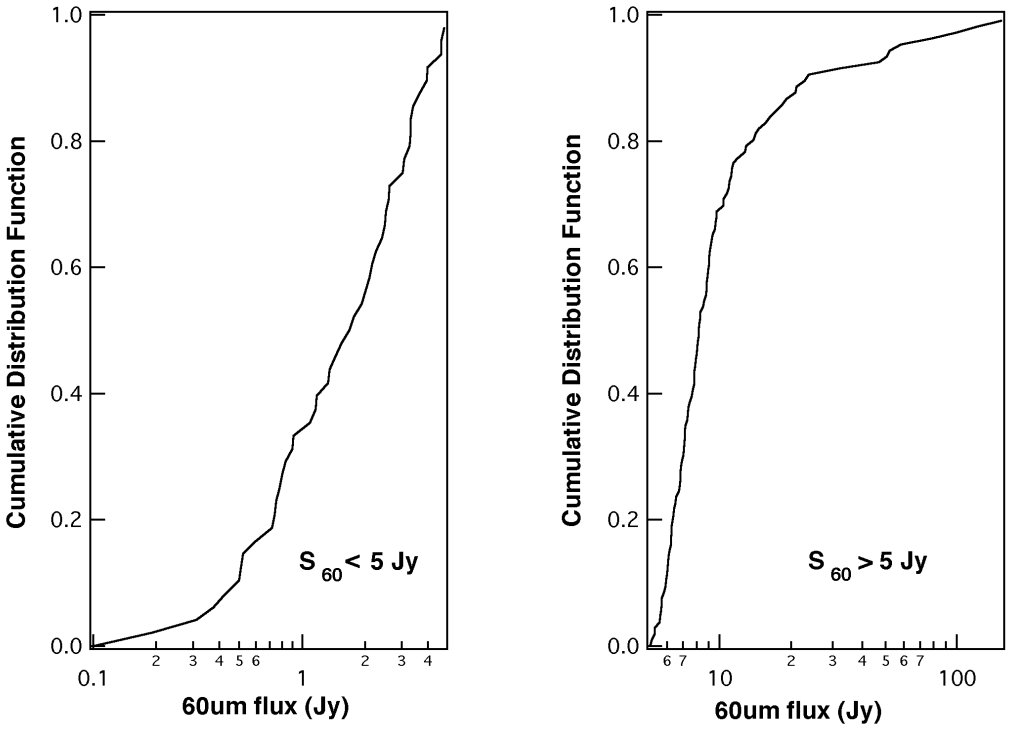

Fig. A.7.— Integrated, spatially resolved 60 μm flux cumulative distribution functions for galaxies detected in the RBGS. The CDF has been split above and below the 5 Jy selection criterion.

A.3.4. CO in Close Interacting Pairs

Twenty of the galaxies with far-infrared detections have published CO fluxes (Young et al. 1995, Elfhag et al. 1996). The correlation coefficient between the far-IR flux Log($F_{\rm ir}$) and the CO flux Log($S_{\rm co}$) is 0.70, which is significant at a greater than 0.995 level. Figure A.8 shows $L_{\rm fir}$ vs m(H_2), where m(H_2)=12×10^3 S_{co} $(\frac{cz}{H_0})^2$. A fit to this data yields

$$L_{\rm fir} = 3162\ m({\rm H_2})^{0.72\pm0.14} \tag{A.2}$$

or, converting to other units

$$L_{\rm ir} = 3.4 \times 10^8\ L_{\rm co}^{0.72} \tag{A.3}$$

which is similar to the result found by Young et al. (1986) for galaxies with dust temperatures 30 K $< T_{\rm dust} <$ 40 K. Since the paired galaxies in the RBGS continue to follow the CO/far-IR relation found in other galaxies, it is the case that at this early stage of interaction it is the size of the molecular gas reservoir that ultimately determines the far-IR luminosity (i.e., galaxies with more CO are more IR-luminous). This is similar to results found elsewhere (Combes et al. 1994).

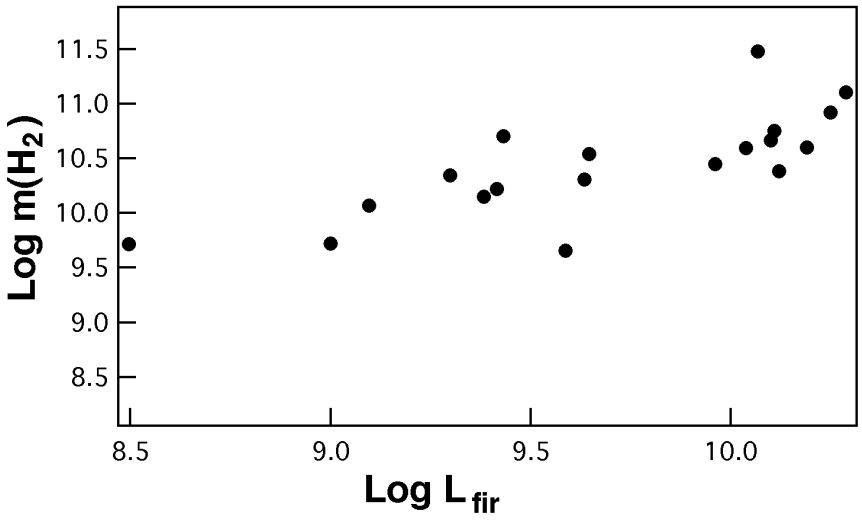

Fig. A.8.— $L_{\rm fir}$ vs. m(H_2) in RBGS interacting galaxies, showing the relationship between the two. Both quantities are in solar units. Although much of the correlation apparent in this figure is due to distance effects, these quantities were plotted since they are more physically meaningful.

A.4. Activity during Different Interaction Phases

Many studies indicate that the enhanced star formation which is presumed to generate the far-infrared activity in these galaxies first begins sometime after the galactic crossing during the merger process. The initial approach between the galaxies can be recognized by the relatively undisturbed nature of the galactic disks. N-body simulations indicate that after this first approach, morphological tidal features such as bridges and tails begin to form. On the second galactic passage the two galaxies usually merge. The presence of these tidal features should therefore be indicative of whether the two galaxies have already made a close approach.

In an attempt to understand the point at which enhanced star formation "turns on", we have separated the galaxy pairs in Table A.1 into two categories, "pre-contact" and "pre-merger", corresponding to merger stages I and III in Fig 7.2. This was done by examining the DSS images for evidence of tidal tails and bridges, for the second category, or for apparently undisturbed galaxy morphologies in the first case. This was severely hampered by the low spatial resolution and depth of the DSS images. Therefore, only systems that could be unambiguously placed in either category were counted. This effectively selects for low-z and therefore low-luminosity systems. However, this should only affect the relative numbers of galaxies in each category; any relationship between luminosity and morphology should remain unaffected.

The pre-merger stage III systems show a statistically significant 50% increase in $L_{\rm fir}$ relative to the pre-contact stage I systems, as well as an increase in their scatter, which once more mirrors the Larson & Tinsley (1978) result.

A.5. Conclusions

We have presented an atlas of high resolution IRAS observations of all 100 of the paired and in many cases interacting systems with a 60μm flux density greater than 5 Jy.

We conclude that there is no difference between late and early-type spirals in terms of their far-IR properties. In particular, no significant enhancement is seen in the far-infrared luminosity or color of the late-type spirals as compared to the early-types. There are several possible explanations for this. If most of the galaxies in the sample are in their first approach towards each other, then there may well be no significant difference between the populations. This is because the n-body simulations indicate that enhanced star formation begins, at the earliest, after initial perigalacticon. Thus, the initial starburst in the bulgeless galaxies which would separate their far-infrared properties from the bulge dominated galaxies has not yet occurred.

We would like to thank Ron Beck and John Fowler for their assistance in setting up our HIRES processing facility, and in particular Diane Engler for her speedy work in extracting the detector scans from the IRAS database. We would also like to thank Joe Mazzarella for his advice about the effects of morphology on galactic properties.

This work has made use of the NASA/IPAC Extragalactic Database (NED) which is operated by the Jet Propulsion Laboratory, California Institute of Technology, under contract with the National Aeronautics and Space Administration. It has also made use of the Digitized Sky Survey, produced at the Space Telescope Science Institute under U.S. Government grant NAG W-2166. This was based on photographic data obtained using the Oschin Schmidt Telescope on Palomar Mountain, operated by the California Institute of Technology, and the UK Schmidt Telescope, which was operated by the Royal Observatory Edinburgh and the Anglo-Australian Observatory.

REFERENCES

Arp, Halton. 1966, Atlas of Peculiar Galaxies. (Pasadena: California Institute of Technology)

Aumann, H.H., Fowler, J.W., & Melnyk, M. 1990. AJ, 99, 1674

Barnes, J. & Henrquist, L. 1992. ARA&A, 30, 705

Beichmann, C.A., Neugebauer, G., Habing, H.J., Clegg, P.E., & Chester, T.J. editors. 1988. IRAS Catalogs and Atlases, Explanatory Supplement. (U.S. GPO, Washington, D.C.) IV.

Bushouse, H.A. 1986a. AJ, 91, 255

Bushouse, H.A. 1986b. Ph.D. Thesis. University of Illinois

Bushouse, H.A., Lamb, & Werner, M.W. 1988. ApJ, 335, 74

Byrd, G.G., Sundelius, B., & Valtonen, M. 1987, A&A, 171, 16

Combes, F., Prugniel, P., Rampazzo, R., & Sulentic, J.W., 1994, å, 281, 725

Dahari, O. 1984, AJ, 89, 966

Elfhag, T., Booth, R.S., Hoglund, B., Johansson, L., & Sandqvist, A. 1996, A&A Supp. Ser., 115, 439

Gerritsen, J. 1997. "Star Formation and the Interstellar Medium in Galaxy Simulations". PhD. Thesis. Kapetyn Astronomical University, Groningen

Haynes, M.P. & Herter, T.1988, AJ, 96, 504

Helou, G., Khan, I.R., Malek, L., & Boehmer, L. 1988, ApJS, 68, 151

Joseph, R.D., Meikle, W.P., Robertson, N.A., & Wright, G.S. 1984, MNRAS, 209, 111

Karachentsev, I. 1972, Commun. Spec. Astrophys. Obs. 7,1

Kennicutt, R.C., Keel, W.C., van der Hulst, J.M., Hummel, E., & Roettoger, K.A. 1987, AJ, 93, 1011

Laidler, V.G., Rehner, D.M., & Sturch, C.R. 1994. The Digitized Sky Survey, (Space Telescope Science Institute)

Larson, R.B., & Tinsley, B.M. 1978, ApJ, 219, 46

Laughlin, G., Engler, D., & Rice, W. 1990, HIRES Product Validation: I. Point Sources. (Infrared Processing and Analysis Center Memo 701-90-077/2).

Lonsdale, C.J., Persson, S.E., & Mathews, K. 1984. ApJ, 287, 95

Mihos, J.C., & Hernquist, L. 1994, ApJ, 425, L13

Mihos, J.C., & Hernquist, L. 1994b, ApJ, 431, L9

Roberts, M. & Haynes, M.P. 1994, ARA&A, 32,115

Sanders, D.B., Egami, E., Lipari, Mirabel, & Soifer, B.T. 1995, ApJ, in press

Smith, B.J. 1989 Optical Imaging of IRAS Galaxies: The Evolution of Infrared-Bright Galaxies.(University of Massachusetts)

Soifer, B.T., Rowan-Robinson, M., Houck, J.R., de Jong, T., Neugebauer, G., & Aumann, H.H. 1984, ApJ, 278, L71

Soifer, B.T., Sanders, D.B., Madore, B.F., Neugebauer, G., Danielson, G.E., Elias, J.H., Lonsdale, C.J., & Rice, W.L. 1987, ApJ, 320, 238

Sulentic, J. 1988, AJ, 98, 2066

Sulentic, J., Keel, W.C., &Telesco, C.M. 1990. Paired and Interacting Galaxies. NASA Conference Publication 3098

Surace, J.A., Mazzarella, J.M, Soifer, B.T., & Wehrle, A.E. 1993, AJ, 105, 864

Surace, J.A. & Sanders, D.B., 1998, in prep.

Telesco, C.M. 1988, ARA&A, 26, 343

Toomre, A., & Toomre, J. 1972, ApJ, 178, 623

Young, J.S., Schloerb, F.P., Kenney, J.D., & Lord, S.D., 1986, ApJ, 304, 443

Young, J.S., Xie, S., Tacconi, L, Knezek, P. et al. 1995, ApJS, 98, 219

Appendix B

Deconvolution of Ground-Based Optical/Near- Infrared Images

ABSTRACT

The limitations of the arcsecond seeing normally experienced at ground-based sites has severely limited our ability to understand the structure of a wide range of phenomena. Since the only significant populations of certain types of objects (such as ULIGs and QSOs) exist at $z > 0.05$ and the structures we are interested in may be only a few hundred pc in size, the need for high spatial resolution ($< 0.4''$) imaging has been very great. While this situation has been partially alleviated by space-based observations, the demand for high spatial resolution is far greater than can be addressed solely by extremely costly space telescopes. The use of adaptive optics techniques and image restoration will therefore become increasingly commonplace as astronomers continue to strive to extract more information from their data.

B.1. Introduction

The use of image restoration techniques has had a long history of application in fields such as radio astronomy, where the complex spatially extended beam pattern has generally produced unrecognizably confused raw data. Optical astronomers, however, have generally been reluctant to apply deconvolution methods to their own data for two reasons: (a) they have been suspicious of the additional layer of (often *non-linear*) processing and it's associated uncertainties, and (b) the relatively simple point-spread-function (PSF) encountered in optical astronomy results in cosmetically acceptable (albeit blurry) images, thus eliminating much of the impetus for deconvolution found in other branches of astronomy.

Ironically, the aberrations of the flawed primary mirror of the *Hubble Space Telescope* (*HST*), while representing a major setback in the telescope's designed performance, almost single-handedly created a new field in the application of deconvolution algorithms to astronomical data as astronomers clamored for tools with which to restore the degraded *HST* images (White & Allen 1990 and references therein). While the servicing mission and installation of COSTAR has eliminated much of the drive for deconvolution that once existed, the techniques developed during that time period are still relevant to many ground-based observations.

B.2. Why deconvolve?

There are two primary reasons to deconvolve one's data. The first is to cosmetically improve the image by making it less blurry. More precisely, by eliminating the broad wings of the PSF, one vastly increases the detectability of high spatial frequency features by producing higher contrast (i.e. a larger peak/background ratio). Figure B.1 shows a raw image of Saturn taken at 1.6μm by the author with the UH 2.2m telescope. Figure B.1 also

shows the same image after 25 iterations of the Richardson-Lucy deconvolution algorithm. Many features, particularly in the rings, are now visible. In galaxy and stellar images this often results in an increase in point source detectability of 1 magnitude or more, which (as noted earlier) is much more effective than increasing the telescope aperture or total integration time.

Fig. B.1.— Raw (top) and Richardson-Lucy deconvolved (bottom) H-band images of Saturn taken at the UH 2.2m. Additional structure can be seen in the rings and cloud bands, as well as the moon Dione, can be clearly seen in the deconvolved image.

The second reason to deconvolve one's data is to improve point source photometry by helping to eliminate confusion. In particular, as discussed in Chapter 3, the PSF encountered with adaptive optics systems tends to consist of a broad disk of scattered light and a high S/N core. Application of deconvolution can help eliminate photometric confusion that occurs when objects lie closer than 1″apart. Figure B.2 shows the total encircled energy as a function of radius both before and after deconvolution with Richardson-Lucy. Almost all astronomers unwittingly perform deconvolution already in order to improve their photometry when they apply "aperture corrections". This is essentially a single pass of the CLEAN algorithm (see below) with the gain set to 1, making the implicit assumption that

all of the flux for a given measurement lies in a single point source located in the center of the aperture.

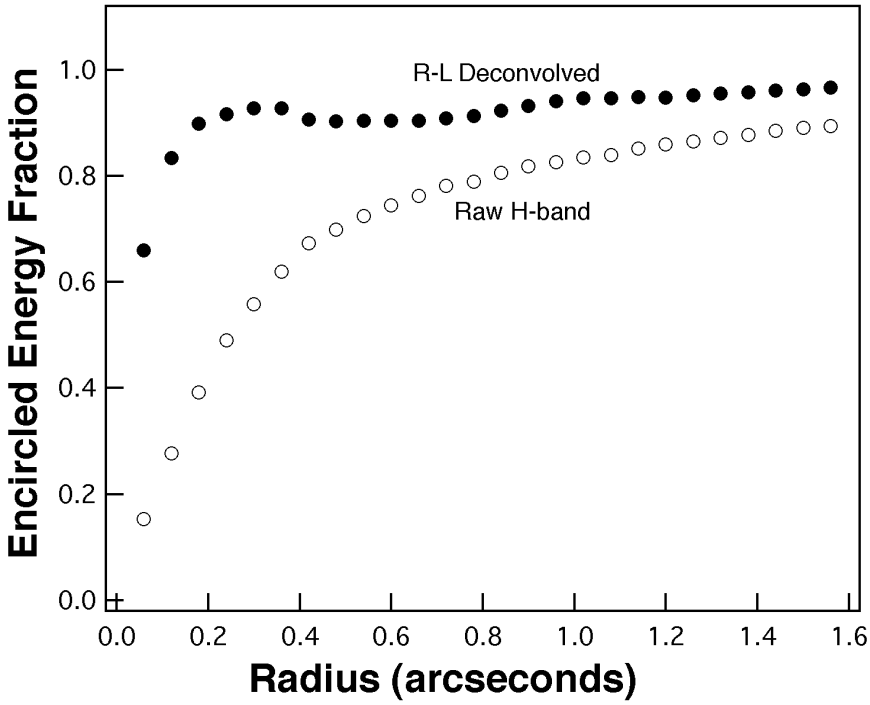

Fig. B.2.— Fractional encircled energy for *H*-band data before and after R-L deconvolution. After processing, more than 80% of the energy is inside a nearly diffraction limited spot. This is similar to the expected atmosphere-free performance of the telescope.

All of the data in this dissertation has been deconvolved, usually with several different techniques, in an attempt to better understand the photometry and morphology of the high spatial frequency structure. This appendix discusses some of the issues encountered in deconvolution of astronomical data at optical and near-infrared wavelengths.

B.3. Requirements for Deconvolution

There are several requirements for successful deconvolution of data:

Adequate Spatial Sampling - a common rule of thumb used in the design of astronomical cameras is that the FWHM of the typical achieved PSF should be 3 pixels. This has been motivated primarily by a need to balance cosmic ray rejection considerations which require higher spatial sampling rates (cosmic ray hits tend to produce profiles narrower than the PSF) and the demand for an adequate field of view (dictated by the total pixel dimensions of the imaging array). However, this sampling is inadequate for deconvolution purposes. Sub-pixel shifts in the true centroid of the emission relative to the center of the pixel may create large changes in the apparent PSF. A more adequate sampling has been found to be 5-7 pixels FWHM. For WFPC1 *HST* images, which have an aberrated PSF nearly 20 pixels

across, this is not a problem. Post-servicing WFPC2 PSFs, however, may be only 1-2 pixels FWHM, and deconvolution efforts are generally of limited value. At the UH 2.2m f/31 focus, the sampling of the QUIRC near-infrared camera (0.06″/pixel, best seeing typically 0.3″) and the Orbit near-ultraviolet/optical camera (0.09″/pixel when binned 2x2, best seeing typically 0.5″) are typically 5 pixels or more FWHM, ensuring adequate sampling all the time.

Isoplanicity - at the time of this writing, nearly all deconvolution algorithms assume a spatially invariant (isoplanatic) PSF. Current attempts to tackle non-isoplanicity generally involve breaking an image up into smaller isoplanatic subimages, each of which is then deconvolved separately. The most serious source of non-isoplanacity in conventional astronomical images is that produced by off-axis telescope aberrations. However, when both the target and the PSF calibration source are near the central axis, as is enforced by the small field-of-view of the detectors at the UH 2.2m at f/31, this is fairly negligible. For much larger fields of view, like that of the UH 8k camera, field distortions may prove to be a serious impediment to deconvolution.

Note that this is completely different from the isoplanacity issues normally encountered in adaptive optics. This is because adaptive optics is concerned with isoplanacity of *short time-scales* induced by the atmosphere, typically less than 0.01 seconds. Although at this time the size of the isoplanatic patch on Mauna Kea is not well-understood, it is believed to be roughly 1′ in the near-infrared for tip/tilt aberrations. However, the problem we are addressing is isoplanacity of the *time-averaged* PSF on *long time-scales* of 120-1200 seconds. Examination of the PSF on large- scale optical (B & I) images show essentially no PSF variation within a radius of 120″ of the target.

Adequate S/N - both the PSF and the data must have adequate S/N in order for deconvolution to produce good results. In particular, after many iterations of fourier-based algorithms like R-L, high-σ noise outliers are amplified into noise spikes, as background flux is concentrated into these high-σ points. This, combined with the smoothing effect of the first few iterations of the algorithms, produces a mottled background. While the noise in the original image is essentially uncorrelated from pixel to pixel, the background noise in the deconvolved image will be correlated on spatial scales similar to that of the PSF. Also, for some algorithms the PSF itself must have S/N at least as high as the actual data. This is discussed below in relation to the CLEAN algorithm.

B.4. Algorithms

The following algorithms (Richardson-Lucy, CLEAN, and MEM) are among the most common in use today. Additionally, they are all implemented in IRAF/STSDAS, thus making them convenient to use, as well readily and freely available. Many other algorithms exist: Fractal Pixon Reconstruction, the Maximum Correlation Method, Wiener Filtering, etc. Most of these are rather esoteric and in practice do not produce such good results as the following methods.

Richardson-Lucy - developed independently by Richardson (1972) and Leon Lucy (1974), R-L has become the algorithm of choice among optical astronomers. It has several advantages over competing techniques. The nature of the solution is surprisingly robust against small variations in the PSF. It is also computationally fast. Using R-L is quite simple: generate a PSF (either observed or theoretical), input proper guesses at the background values and CCD noise characteristics, and then start the algorithm. While it is possible to specify an *image prior* (i.e., a first guess) in order to accelerate convergence of the algorithm, this isn't necessary and is usually irrelevant since convergence is very rapid. Because this is a fourier-based algorithm, it behooves the user to make both the image and the PSF a power of 2 in each dimension. This allows the use of FFTs, which speed things up by factors of 20 or more.

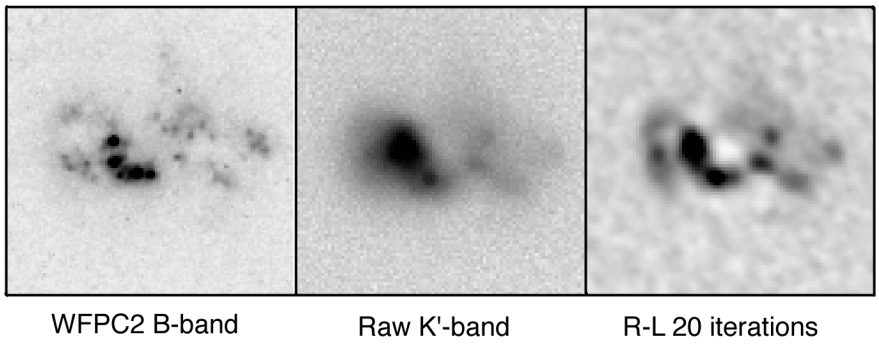

Fig. B.3.— A comparison between WFPC2 B-band data, raw tip/tilt data taken from the UH 2.2m telescope at K', and the results of deconvolution by 20 iterations of the Richard-Lucy algorithm. Most of the star-forming knots seen in the *HST* data are now visible in the resolution-enhanced image. Total processing time was about 1 minute on a Sparc 10.

There are several artifacts encountered when using R-L. The most notable of these is "ringing". Bright point sources embedded in extended emission will produce rings of alternating bright emission and negative flux, a result of the fourier-based algorithm attempting to reproduce high spatial frequency structure (i.e., point sources) when it has no information about such high frequencies. This is a general fourier deconvolution issue based on the fact that there is an upper and lower limit on the spatial frequencies in the image set by the image size and pixel size. Related to this is an issue of photometric instability; bright point sources tend to "steal" flux from their surroundings. There is also a tendency for variable spatial resolution. Before the image has converged to the maximum likelihood solution, the high S/N regions will have a higher effective spatial resolution than the low S/N regions. Fortunately, this is not as severe as the corresponding problem with CLEAN. Finally, there is the problem of noise amplification. High σ outliers in the background noise are interpreted as point sources and then flux is "borrowed" from the surrounding background and pushed into these points. This problem has to some extent been alleviated through use of damping algorithms (White 1992); in general, one stops iterating before this becomes too severe.

One of the more difficult issues is deciding when to stop the algorithm. In theory, the algorithm simply approaches the maximum likelihood solution and should simply be allowed to continue until it has reached a point of diminishing returns. In practice, however, noise amplification and other forms of artifacting becomes quite severe and eventually degrade the image restoration. Originally, a mathematical definition of convergence towards the maximum-likelihood solution was defined, but in practice it became apparent that this was not completely applicable. More recently, some authors have attempted to define new stopping criteria for the algorithm (Perry & Reeves 1992). Realistically, until a more precise understanding of how R-L works is reached, it is likely that no simple stopping criterion will be found. In actual practice one iterates until the noise amplification or ringing become too severe to be acceptable. Often it becomes apparent that the rate of convergence (i.e, the rate of change in the image as characterized by the X^2 value) slows dramatically; usually this is a good point to stop the algorithm. In general 20-40 iterations seems most appropriate for galaxy data with moderate S/N. For planetary data with high S/N extended features (such as figure B.1) this may be as high as 100.

Finally, a more unusual application of R-L is that it can be used as a kind of adaptive smoothing algorithm. The first few iterations of R-L are essentially a convolution of the original data with the PSF, which smoothes the data and correlates the noise over several pixels. By setting the CCD noise estimate to several times it's actual value, the algorithm is damped or slowed down. The first few iterations smooth the data, thus eliminating pixel to pixel noise. The next few iterations then enhance the spatial resolution, returning it to it's original value. This takes advantage of what is normally a flaw in R-L and most other deconvolution algorithms, namely that high S/N features in the image converge to the high spatial resolution solution faster than low S/N regions. The end result is an image whose high S/N features have a resolution equal to or greater than the original data, but with much lower background noise. Note that this will not actually allow detection of fainter features than before; such faint features are also smoothed by this process.

So called "P-Lucy" is an interesting variant of the R-L algorithm that is beginning to see some application. This is the so-called "photometric- channel" version of R-L; it is essentially a hybrid CLEAN/R-L algorithm which attempts to suppress the ringing around bright point sources common to fourier-based algorithms by alternatingly fitting all of the (user-specified) bright point sources in the image, subtracting them out, and then using R-L on the residual (Hook & Lucy 1994). The process is then repeated on each iteration. Not surprisingly, the algorithm was developed in part to tackle the problem of deconvolving the nebulosity of QSO host galaxies where the bright QSO nucleus causes severe ringing artifacts. Current incarnations of P-Lucy suffer from the considerable drawback of being very labor-intensive in terms of preparation. Both the data and the PSF must be carefully prepared. In particular, both the PSF and the data should be resampled onto a finer pixel scale in order to improve the centering of the point sources. This is critical because the point source subtraction is very sensitive to the centroiding of the point sources; if the positions for the points are even slightly off-center this results in a characteristic "half moon" background pattern. In spite of these drawbacks, this algorithm does have two enormous advantages: it can deconvolve faint structure around bright point sources, and at the same time can determine accurate photometry for point sources embedded in nebulosity.

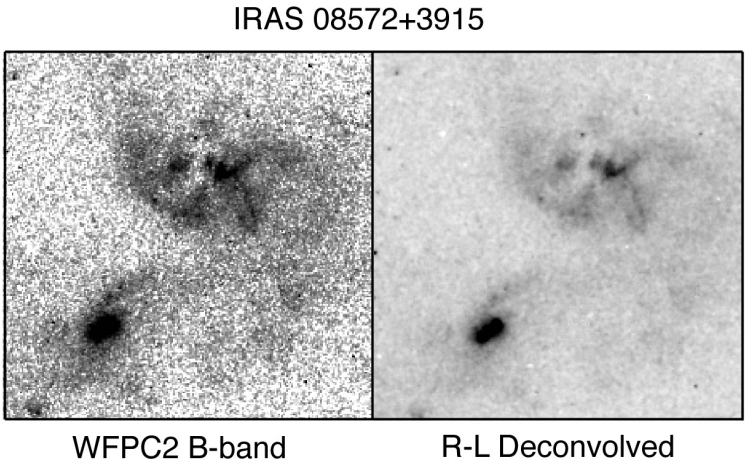

Fig. B.4.— An example of using the R-L algorithm for smoothing and cosmetic image enhancement. The image on the left is the raw WFPC2 *B*-band data for IRAS 08572+3915. On the right is the result of 10 iterations of the algorithm with the CCD noise estimates increased. The stretch is the same in both cases. The pixel to pixel noise has been nearly eliminated, without sacrificing the spatial resolution of the high S/N regions.

CLEAN - a favorite of radio astronomers, CLEAN (Hogbom 1974) works in the image plane and as such is not a true deconvolution algorithm; by definition deconvolution occurs in the fourier plane. CLEAN works by locating the brightest point in an image and subtracting a scaled model of the PSF from it (see Perley et al. 1989 and references therein). This process is then repeated for as many as a thousand iterations. The resulting map of point sources is then reconvolved with a narrow beam and added back to the residual image to produce the final deconvolved image. The primary controls in CLEAN are setting the "damping factor" γ which is the scaling factor of the PSF, the number of iterations, and the characteristics of the final beam. CLEAN is generally not used so much as a resolution enhancement algorithm but as a means of cleaning a dirty (irregularly shaped) beam. The final beam that is convolved with the point source map is usually chosen to be something simple such as a gaussian with a FWHM equal to the telescope diffraction limit. Other packages, such as IRAF/DAOPHOT, are very similar in philosophy to CLEAN in that they also work by a kind of PSF-fitting. In the case of DAOPHOT the locations of all the points are fixed and are iteratively fit together.

Although it enjoys the great benefit of being conceptually simple, CLEAN is not very well suited for most conventional optical and near-infrared applications; there are several major pitfalls to using it. The first is that the underlying assumption made by CLEAN is that the data is well-represented by point sources. This is often unrealistic, and use of CLEAN on extended emission will result in it being reconstructed as a grid of point sources. Therefore CLEAN is really most suitable for use on objects like star clusters where this underlying assumption may be applicable. Second, the final CLEANed image suffers from variable spatial resolution since high S/N regions are preferentially restored

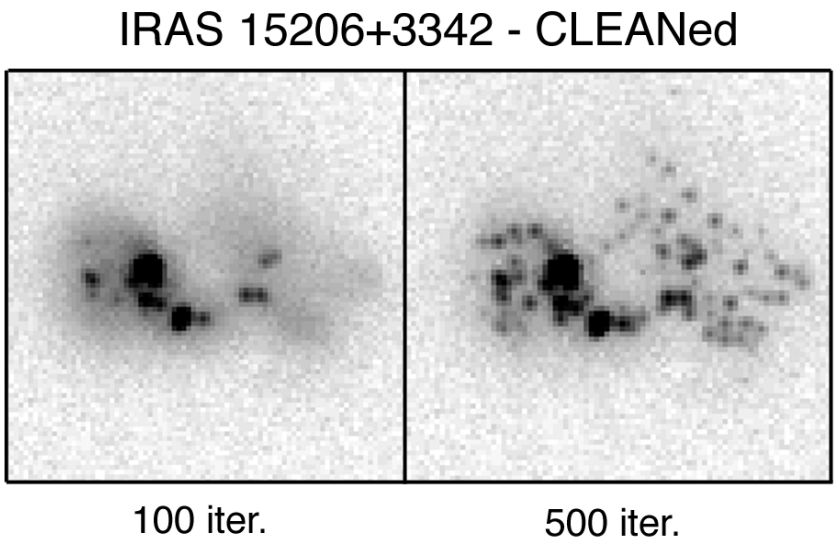

Fig. B.5.— An example of the CLEAN algorithm applied to the K'-band data for IRAS 15206+3342 seen in figure B.3. The left hand image is 100 iterations of the algorithm, and illustrates the problem with variable resolution in CLEAN images. While the brightest knots have been reconstructed with very high resolution, the fainter ones remain blurry. The right hand panel illustrates the pitfall of letting the algorithm iterate too many times; the smooth extended background has been unrealistically reconstructed as many small points, even though this is not actually the case.

first. Although this is a problem common to many deconvolution algorithms, it is much more severe in CLEAN. The CLEANed image will have a very sharp S/N break above which the image has been fully restored to the final beam shape, and below which the data has not been restored at all. The resulting CLEANed data will therefore represent the low S/N regions as unrealistically smooth in comparison to the high S/N regions. Finally, CLEAN is extremely sensitive to irregularities in both the image data and the PSF. Cosmic ray hits, blocked rows, etc. in the raw data tend to "hang" the algorithm, producing severe artifacting.

Because of the subtractive non-fourier nature of the algorithm, a low S/N PSF immediately introduces low S/N regions into the data, thus destroying the quality of the actual data and ruining the image restoration. In radio work this is often circumvented by having extremely high S/N and using theoretical beam patterns, neither of which may be available with optical/near-infrared data. Many of the problems associated with CLEAN can be eliminated by using a modeled, noise-free PSF. The simplest way to do this is with the ISOPHOTE package in IRAF/STSDAS. The observed PSF (extracted from any existing stars using DAOPHOT) can be fitted with elliptical isophotes, and a model constructed from these fits. The resulting PSF, while lacking any non- radially symmetric structure found in the real PSF, will have the considerable benefit of being noise-free.

Maximum-Entropy (MEM) - MEM suffers from the considerable drawback that it is very computationally intensive compared to R-L, usually with very little gain. Since

experimentation is often necessary in the art of image restoration, the computation time of MEM hinders an adequate exploration of the algorithm's parameters. Additionally, MEM has many of the drawbacks of R-L: severe ringing, noise amplification, etc. Most users would be better off investigating R-L before attempting to use MEM.

B.5. Post-Processing Data Reliability

Due to the non-linear nature of these algorithms, estimating the uncertainties of the algorithms tends to be problematic. In raw data most of the noise is uncorrelated on scale lengths of one pixel. In the deconvolved images, however, this noise is correlated on scale lengths similar in size to the PSF. It is no longer possible to determine the uncertainties in a mathematical fashion. Since detection limits are generally limited by confusion with deconvolution- induced artifacts, the confusion limit can often be estimated by measuring the flux from the artifacts themselves. As a general rule of thumb, if a feature cannot be seen in any way at all in the raw data, even after you know to look there, then it probably shouldn't be considered real in the deconvolved data.

Estimation of the uncertainties in measured photometry are much more difficult, since the deconvolution algorithm shifts flux from pixel to pixel. Simulations tend to be the best possible method for evaluating these uncertainties. One takes the raw data and embeds in it artificial features of known flux values. An easy way to do this is with the ARTDATA package in IRAF, which can model a variety of astronomical objects, with a full noise treatment. The artificial frame is then processed by the deconvolution algorithm in exactly the same way the real data was, and an attempt is made to extract photometry from it in order to compare it to the input data. This technique was described in more detail in Chapter 2. Other checks that can be made are to ensure that the flux inside large apertures remains constant before and after deconvolution, thereby ensuring that flux has not been moved into the target from the background. Similarly, as a check on photometry derived from deconvolved data, it is possible to carefully examine the aperture-corrected fluxes from the raw data for believability.

B.6. Low-Order Adaptive Optics: The UH 2.2m f/31 tip/tilt guider

Without the f/31 tip/tilt guiding system on the UH 2.2m telescope, this dissertation would not have been possible. The guider uses a pickoff mirror to send the light from a guide star to a small CCD, which acts as a quad sensor. The guide signal is then used to rapidly tip and tilt the secondary mirror, which is attached to a piezo stack hexapod. Details on the design of this guider can be found in Jim (1995).

B.6.1. Notes on Practical Usage

In theory, since a dichroic mirror supplies the guider CCD with the guide signal, it should be possible to guide directly on-axis when observing in the near-infrared. In reality

this is not particularly practical due to the high limiting magnitude of the guider camera. Generally, the guider can provide some tip/tilt compensation with stars of m_V=13.5. Under a bright sky (i.e., full moon), the optical sky brightness is sufficiently great as to prevent guiding on guide stars fainter than m_V=12.5. Since none of the quasars are much brighter than m_V=15, the quasar nuclei could not be used as guide stars. Similarly, none of the objects has a suitably bright guide star sufficiently close by as to allow on-axis guiding at a rate fast enough to noticeably improve the image over higher-rate off-axis guiding.

When guiding off-axis, a much larger area some 4´ in size becomes available for guide star acquisition. Even so, as many as one-eighth of the systems had no guide stars brighter than m_V=12 in the normal guider acquisition area. This surprising paucity of guide stars out of the galactic plane creates considerable problems in successfully guiding. Under many circumstances, it is possible to rotate the cassegrain focus of the telescope in order to acquire better guide stars. In a few cases, however, it was not possible to guide at all (i.e., IRAS 12071-0444, PG1202+281). In the latter case, no observations were made due to this problem.

B.6.2. Achieved Results

Typically, at near-infrared wavelengths at the UH 2.2m using the tip/tilt guider the seeing is better than 0.5″, and 60% of the time is better than 0.3″, although naturally these numbers are very subjective and weather dependent. Performance at optical wavelengths is much worse, with seeing typically 0.8-1″, although at least one night approached 0.3″at B-band. Even though the guider was used off-axis, results were still very good. This implies that either the seeing at the UH 2.2m is nearly diffraction-limited much of the time at K′, or that the isoplanatic patch for tip/tilt is considerably larger than expected. Regardless of its effects on atmospheric seeing which may or may not be present, the tip/tilt system *is* compensating for correlated local image motion. The most important of these is windshake; a 30 mph wind at the UH 2.2m can easily generate 1-2″or more of windshake depending on the relative orientation of the telescope. The very best results, of course, are achieved when the post-processing deconvolution is used in conjunction with the guider. Under these circumstances, the diffraction-limit at K′can be routinely reached.

REFERENCES

Lucy, L.B., 1974, AJ, 79, 745

Hogbom, J.A., 1974, Astron. Astro. Supp., 15, 417

Hook, R.N. & Lucy, L.B. 1994, in "The Restoration of HST Images and Spectra", Space Telescope Science Institute Conf. Proceedings, 86

Jim, K.T., 1995, BAAS, 187, 1394

Perley, R.A., Schwab, F.R., & Bridle, A.H, eds. *Synthesis Imaging in Radio Astronomy*, 1989, ASP Conference Series No. 6

Perry, K.M. & Reeves, S.J. 1994, in "The Restoration of HST Images and Spectra", Space Telescope Science Institute Conf. Proceedings, 97

Richardson, W.H., 1972, J. Opt. Soc. America, 62, 55

White, R.L. 1994, in "The Restoration of HST Images and Spectra", Space Telescope Science Institute Conf. Proceedings, 104

White, R.L., & Allen, R.J., editors *The Restoration of HST Images and Spectra*, 1990, (StScI, Baltimore)

Appendix C

Derivation of Colors

ABSTRACT

This dissertation has relied almost exclusively on broad-band photometry and colors in wavelengths ranging from 0.3 to 2.2 μm. However, these broad- band filters have wavelength coverages between 0.1 and 1 μm in width. In order to investigate broad-band magnitudes and colors, it is necessary to evaluate modeled emission mechanisms (i.e. hot dust) in each of the filters used. Also, since some of the filters like K$'$ are non-standard, modeled broad-band colors in the literature cannot be used and instead new ones must be generated.

C.1. The IfA Filters

The filters used by the IfA differ in some cases from the standard Johnson- Cousins filter set. This is primarily due to the manufacture of the IfA's interference filters; their extremely sharp bandpass cutoffs and high transmissions are quite different from those of the colored glass used by Johnson and others.

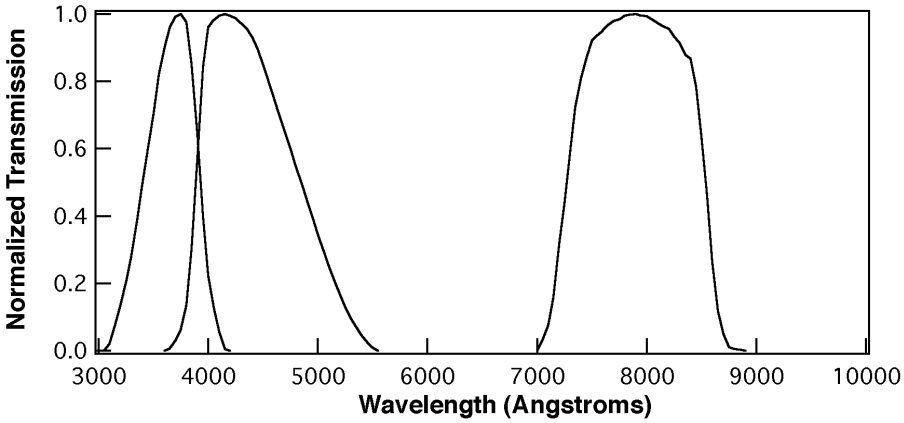

Fig. C.1.— The Johnson-Cousins optical filter system and the filter bandpasses of the U, B, & I filters (Bessel 1990). Because the filters are colored glass, they have very broad wings to their transmission curves.

Near-infrared observations suffer from not having as standardized a filter system as the optical Johnson-Cousins system; several different filters systems exist, usually defined by the observatory where they are used. Perhaps the most common such filter system, which we have chosen to use here, is the *CIT* filter system defined by the photometry of Elias et al. (1982). Additionally, most of the ULIG studies have already been calibrated to these filters and it is in our interest to conform to past measurement systems for ease of comparison. The IfA H-band filter closely resembles the CIT H filter. We have also used the IfA K$'$ filter, described by Wainscoat & Cowie (1992). This is a 2.1μm filter, as opposed to the CIT K filter, with a central wavelength of 2.2μm. It's primary advantage is

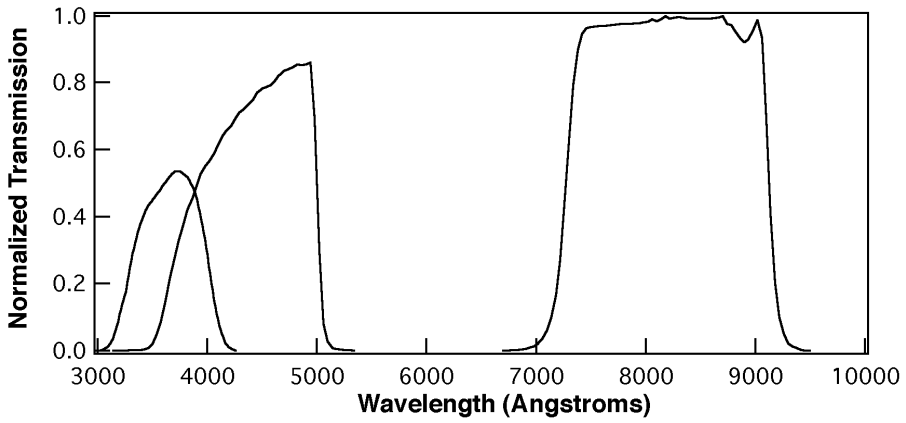

Fig. C.2.— The IfA U′, B, and I-band filters. The interference filters have extremely sharp wavelength cutoffs.

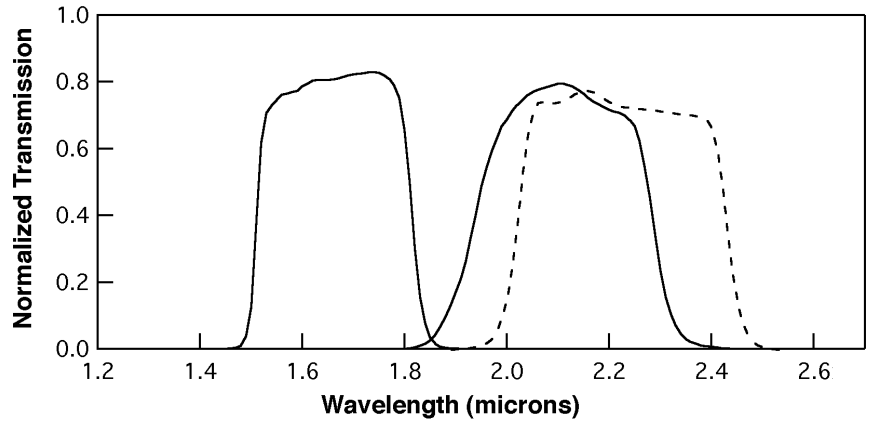

Fig. C.3.— The IfA H and K′ (solid-line) filters. The *CIT* K-band filter is also shown for comparison (dotted line).

lower thermal background; the resulting decrease in noise results in a nearly 1 magnitude improvement in faint source sensitivity.

C.2. Filter Calibration and Transformation to Standard Filters

In order to facilitate comparisons to other works, and to make this work accessible to others, all of the observations have been transformed from the IfA filter system to standard filter systems: Johnson U, Johnson B, Cousins I, and *CIT* H. Only the K′ filter has not been transformed; instead, all the models were recomputed in K′. In all cases the same set of IfA U′BIHK′ filters were used for all of the observations.

The observations were calibrated by observing the Elias et al. (1982) and Landolt (1990, 1992) standard stars. Typically, standards were observed before and after each science target at airmasses similar (whenever possible) to the science target. Two to three dithered images were taken in each filter. These images were reduced in the same manner as the science data, and aperture photometry was used to determine the magnitudes of the standard stars. Apertures were selected to be large enough to encompass all of the flux from the stars (typically 4-6″in radius). The background was set to the median value in an annulus just outside this aperture. The standard star flux measurements were fitted with a function of the form

$$\mathrm{m}_x = \text{-2.5 Log}\frac{adu}{exptime} + \mathrm{ZP}_x \text{ - (airmass}\cdot\mathrm{extinction}_x) + \mathrm{CT}_x\cdot(X\text{-}Y) \tag{C.1}$$

where *ZP* is the magnitude zeropoint in filter x, *adu* is the total flux in data numbers (counts), *exptime* is the effective exposure time, *airmass* is the airmass of the observation, $extinction_x$ is the extinction per unit airmass at filter x, CT_x is the colorterm, and X-Y is the difference in magnitudes (color).

Table C.1 gives the mean photometric solutions for the different filters and cameras used. Note that during this time QUIRC was upgraded with a new imaging array; the two arrays have been labeled QUIRC and QUIRC2. In general, the color terms for the I and H filters were too small to be reliably measured. Similarly the extinction at I, H, and K′ were generally immeasurably small; primarily this is because almost all of the targets and standard stars were observed at less than 1.25 airmasses. Because K′ was not transformed to K, no color terms were derived for it. As described in Chapter 3, this filter was calibrated by using the filter transformation described by Wainscoat & Cowie (1992) to transform all of the K-band magnitudes for the Elias et al. (1982) standard stars to K′.

C.3. Derivation of Colors from Modeled Spectra

In order to determine the broad-band colors of various emission mechanisms, synthetic spectra were constructed (see Chapter 3 for details). Several of these models are shown in Figure C.4. Each spectral model consists of a set (X,Y) of points corresponding to F_λ and

Table C.1. Photometric Solutions for Different Instruments

Configuration	UH Filter[a]	Trans. Filter[b]	Zeropoint[c]	Extinction	Color Term
QUIRC + f/31	H	CIT H	21.65	0.07	... [d]
	K′	UH K′ [e]	21.18	0.08	...
QUIRC2 + f/31	H	CIT H	22.64	...	...
	K′	UH K′	22.21	...	...
Tek2048 + f/31	B	Johnson B	23.95	0.21	0.14[f]
	I	Cousins I	23.19	0.05	-0.06
Orbit2048 + f/31	U′	Johnson U	23.11	0.27	0.13
	B	Johnson B	25.49	0.14	-0.10
	I	Cousins I	24.86	0.13	0.08
Orbit2048 + f/10 HARIS	B	Johnson B	25.12	...	...
	I	Cousins I	24.46	...	...

[a] the UH/IfA filter name [b] the filter system transformed to [c] zeropoints and extinctions are mean values and may vary with atmospheric conditions [d] term either immeasurably small or already given elsewhere (see text) [e] based on transformation of CIT K standards to UH K′ by Wainscoat & Cowie (1992) [f] Tek 2048 color terms taken from Wainscoat (1995). Tek color terms are function of *B-V*, Orbit color terms are functions of *B-I*

λ, where λ ranged from 1000Å to 20μm. Similarly, for the starburst models we used an updated version of the Bruzual & Charlot (1993) spectral synthesis models (BC95; Charlot, private communication). These models provide synthetic spectra for a starburst population with a variety of IMFs at solar metallicity over a time period of 10^5-$10^{10.3}$ years.

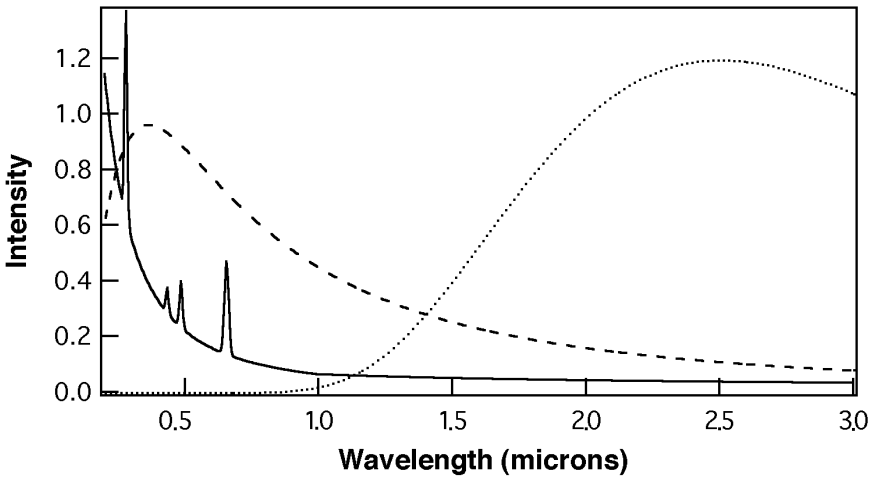

Fig. C.4.— Modeled spectra for free-free emission with an electron temperature of 10000 K (dashed line), 800 K dust with a λ^{-2} emissivity (dotted line), and a synthetic QSO spectrum (solid line). The intensity scaling is arbitrary.

In order to derive the colors, several steps were carried out:

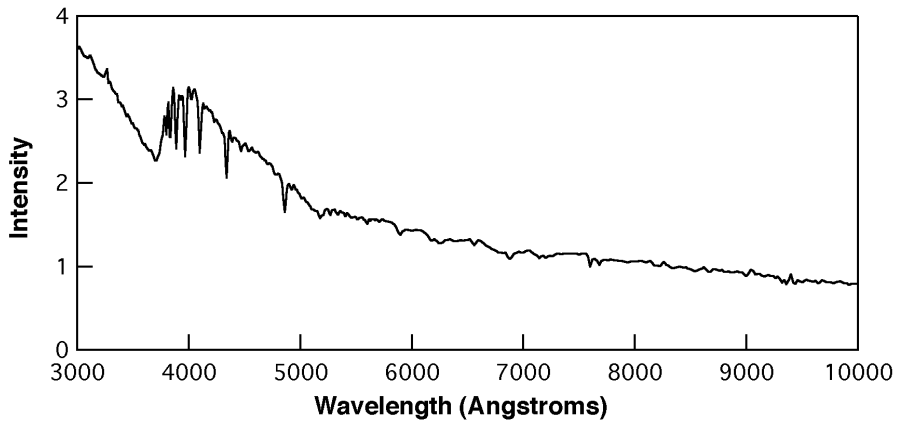

Fig. C.5.— An example of the BC95 model synthetic spectra. This is a spectrum of an instantaneous starburst 28 Myrs old with a Salpeter IMF and a mass range of 0.1-125 $M_\odot$.

1. Each filter was blueshifted to the target rest wavelength, and interpolated to the spectrum model wavelength resolution.

2. The model spectrum and blueshifted filter were then multiplied together. An additional convolution is performed with the known detector responsivity. In the case of the near-infrared an additional convolution is made with a model of the Mauna Kea atmospheric transmission (Tokunaga, private communication); however, since the *JHK* passbands were defined by atmospheric windows in the first place, this has little effect. To some extent the K-correction is dominated by changes in the model SED from rest to redshifted wavelength. The additional "wrinkles" added to the filter shape by the atmosphere and detector are generally second-order effects analogous to the color-terms found in instrumental magnitude calibration. The result of all these convolutions is an estimate of the total emission actually received at the detector.

3. The resulting convolution of the blueshifted filter and model spectrum was then integrated over all wavelengths to derive F_λ.

4. The unshifted filters were then convolved as in step 2 with the Kurucz (1979) model spectrum of Vega to derive F_λ in a given filter for Vega. The unshifted filters are used because even though we are measuring a bluer filter in the rest frame of the galaxy, the zeropoints of the magnitude system are calibrated against the spectrum of Vega which is effectively at $z = 0$.

5. The observed model colors are the difference in instrumental magnitudes of the fluxes derived in step 3 plus a color correction factor based on the spectrum of Vega, which is the difference in instrumental magnitudes derived in step 4. This is essentially a regrouping of the way colors are normally computed; normally, one computes the magnitudes in a given filter first by using the filter zeropoint (from step 4) and the instrumental magnitude (from step 3), and then differencing the resulting calibrated magnitudes. Here we difference the instrumental magnitudes and the zeropoints

separately first, and then apply them to each other. The extra factor of $(1 + z)$ cancels out since we are only computing differences in magnitudes.

Note that because we are only computing colors, this procedure is relatively simple and represents physically what happens at the telescope. Another approach would be to compute full K-corrections, but this is merely adding another layer of obfuscation on what is essentially a semantic difference in approaches. The approach shown here recomputes the colors of the rest-frame models to those that are actually observed in the telescope's reference frame when the model is placed at a given redshift. This way the model colors can be directly compared against the measured galaxy magnitudes. This is opposite in philosophy from the way K-corrections are used, which is to correct the observed galaxy magnitudes and colors to galaxy rest-frame values so that they can be compared to the models in the rest frame. This approach was adopted because it is the model spectra that are perfectly known, whereas the galaxy spectra are unknown; therefore, it makes more sense to recalculate the model colors at a given redshift, rather than try to correct the actual galaxy observables.

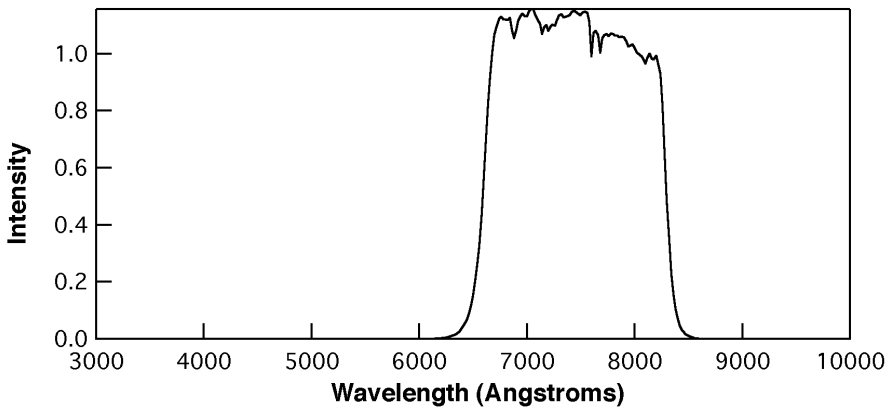

Fig. C.6.— The same synthetic spectrum as Figure C.5 convolved with the IfA I-band filter.

REFERENCES

Bessell, M.S. 1979, PASP, 91, 589

Bessell, M.S. 1990, PASP, 102, 1181

Bruzual, G., & Charlot, S. 1993, ApJ, 405, 538

Elias, J.H., Frogel, J.A., Matthews, K. & Neugebauer, G. 1982, AJ, 87, 1029

Landolt, A. 1982, AJ, 88, 439

Landolt, A. 1992, AJ, 104, 340

Wainscoat, R.J. & Cowie, L.L. 1992, AJ, 103, 332

Errata - April 23,1999

Jason Surace

Nobody's perfect, and this thesis has a few errors as printed. They do not significantly affect it's content. The only major error appears in Section 7.3.

- Figure 7.5 — No legend appears. The open circles are Stage III, the closed circles are Stage IV.
- Table 7.1 — The tail lengths for Stage III and IV should be 17±10 and 31±18, respectively.
- Figure C.2 — The UH U-band filter is depicted, not the UH U′ filter. The correct figure appears below.

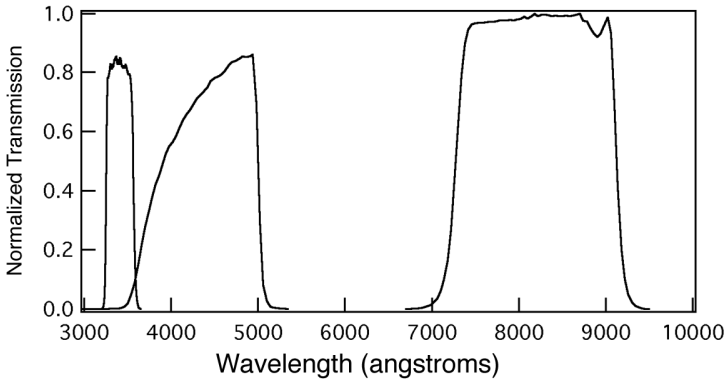

- Table 6.1 — The total magnitude for IRAS 01199-2307 should be 18.12, not 14.12. A future paper will contain a vastly more complete version of both this table and chapter.
- Figure 7.6 — The L/M ratios are too low by a factor of 85 (see below). This was due to a failure to account for the 4.8 magnitude difference between the bolometric magnitudes of Vega and the Sun. The correct figure appears below.
- Section 7.3 — There is an error in this section based on the erroneous Figure 7.6, which partially invalidates the argument made in the second paragraph of this section. The error in computation of bolometric luminosity *does not* propogate backwards into the discussions in previous chapters of the contribution of the star-forming knots to the high luminosity of the galaxy systems. The figure was made using a different computation than used in the previous chapters.

  As discussed in Chapter 2, the minimum mass needed to create an ultraluminous instantaneous starburst is approximately 10^9 solar masses, which is based on the maximum L/M ratio for an instantaneous burst being roughly 1000 (for the 0.1-125 solar mass case).

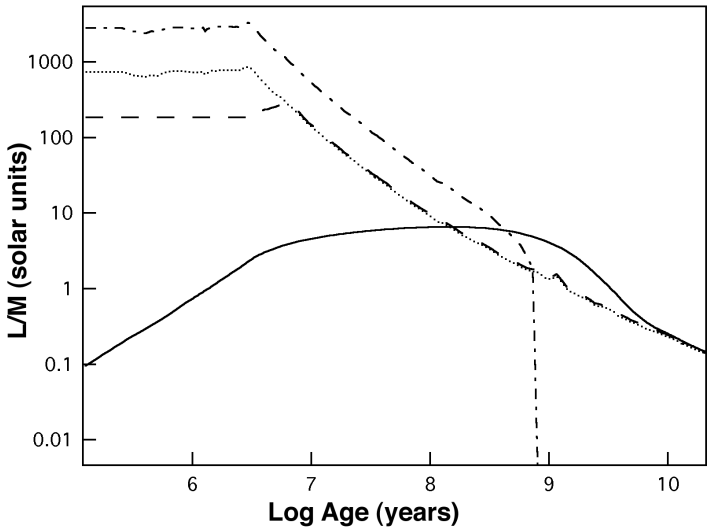

This is easily within the range (by a factor of 30) of the known molecular gas reservoir in ULIGs. However, this high value of L/M can only be maintained for a few million years. As the text correctly states, the ULIGs have an observed L/M of 85 (coincidentally, this is the amount that Figure 7.6 is off, so the vertical axis label "1" is actually the observed L/M for ULIGs). For any normal IMF, such a high L/M can still only be maintained for 10 Myrs, which is drastically less than the dynamical timescale. At this level the text is still correct. However, for a drastic truncation of the lower end of the IMF, the timescale can approach 50 Myrs, which is within a factor of a few of the dynamical timescale. However, it is noteworthy (and stated elsewhere in the text), that although the truncated IMF can sustain an ultraluminous burst for a significant fraction of the dynamical timescale, it undergoes luminosity evolution of nearly a factor of 100×. The lack of any such super-luminous (10^{14} solar luminosity) non-AGN objects argues against this situation.